



PHD

Integral design of non-toxic surfactants for industrial applications

Siddiqi, Areeb

Award date:
2022

Awarding institution:
University of Bath

[Link to publication](#)

Alternative formats

If you require this document in an alternative format, please contact:
openaccess@bath.ac.uk

Copyright of this thesis rests with the author. Access is subject to the above licence, if given. If no licence is specified above, original content in this thesis is licensed under the terms of the Creative Commons Attribution-NonCommercial 4.0 International (CC BY-NC-ND 4.0) Licence (<https://creativecommons.org/licenses/by-nc-nd/4.0/>). Any third-party copyright material present remains the property of its respective owner(s) and is licensed under its existing terms.

Take down policy

If you consider content within Bath's Research Portal to be in breach of UK law, please contact: openaccess@bath.ac.uk with the details. Your claim will be investigated and, where appropriate, the item will be removed from public view as soon as possible.

Integral design of non-toxic surfactants for industrial applications

Areeb Nasir Siddiqi

A thesis submitted for the degree of Doctor of Philosophy

University of Bath

Department of Chemical Engineering

April 2022

Copyright notice

Attention is drawn to the fact that copyright of this thesis rests with the author and copyright of any previously published materials included may rest with third parties. A copy of this thesis has been supplied on condition that anyone who consults it understands they must not copy it or use material from it except as licensed, permitted by law or with the consent of the author or other copyright owners, as applicable.

This thesis may be made available for consultation within the University Library and may be photocopied or lent to other libraries for the purposes of consultation.

Declaration of any previous submission of the work

The material presented here for examination for the award of a higher degree by research has not been incorporated into a submission for another degree.

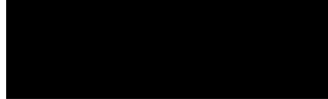
Candidate's signature:



Declaration of authorship

I am the author of this thesis, and the work described therein was carried out by myself personally.

Candidate's signature:



Abstract

Surfactants are chemicals that increase solubility and dispersion of hydrocarbons and oils, and they are widely used in detergents and other cleaning products. After use they are discharged into sewage systems or directly into surface waters, ending up dispersed in the environment polluting the water, the soil and other sediments. The toxic effects of surfactants on various aquatic organisms are known. The vital role surfactants play in modern society means there is no option to stop using them. Thus, non-toxic and biodegradable surfactants are required to decrease their final impact on current water resources.

In this thesis, the approach chosen to discover novel surfactants is to create a computational method, which could act as a screening stage to ensure only the most promising non-toxic and/or biodegradable product formulations make it to experimental testing. This would have the effect of reducing the number of necessary experiments, leading to savings in associated time and costs. Molecular Dynamics (MD) simulations underline the computational method, which represent the system as a collection of particles interacting by mathematical relations termed force fields. This permits the calculation of structural, thermodynamic, and dynamical properties. Therefore, it is an ideal tool for the study of surfactant-water-oil ternary mixtures because the molecular structure is known to strongly influence the surfactant behaviour. Whilst this concept is not new, there has been little progress in applying it to the discovery of non-toxic and biodegradable surfactants.

To simulate surfactants at the molecular scale requires large system sizes that must be run for long durations of time. This demand will be difficult to meet by accounting for all atoms in a molecule. It is for this reason it is chosen to work with models of lower resolution, termed 'coarse-grained' (CG) models. Here multiple atoms are grouped into one bead which interacts via an effective force field. The parameterisation of a CG model is an important step, impacting the model accuracy. In this work recent incarnations of the Statistical Associating Fluid Theory (SAFT) were used to develop the CG force fields used in MD simulations. Here the versatile Mie force field is used to represent the intermolecular interactions with a Coulombic relation used to account for electrostatic interactions in explicitly charged beads. The SAFT approach is a top-down CG method where the force field parameters are determined via a molecular-based equation-of-state. In this thesis a corresponding states version of the equation-of-state was used to find force field parameters for the like-like interactions of the uncharged beads. The SAFT approach allows for faster model parameterisation compared to solely optimising parameters via iterative simulation. There has also been extensive progress in extending SAFT force fields to surfactant-water systems. Despite this, CG MD simulations of surfactant ternary mixtures have not yet been performed using force fields obtained by the SAFT route. Therefore, another key challenge of this thesis is to move the research line forward.

In this thesis SAFT-derived force fields were used to study two different ternary ionic surfactant mixtures: sodium bis (2-ethylhexyl) sulphosuccinate (AOT) in water and cyclohexane, and sodium bis (3-(trimethylsilyl)-1-propanol) sulphosuccinate (AOTSiC) in water and supercritical (sc) CO₂. Derivation of the surfactant models required the study of a variety of fluid systems, including pure esters and binary mixtures comprising methyl acetate and water, AOT and water, and scCO₂ and water. The described systems contain sufficient experimental data to test the SAFT approach. This is a necessary preliminary step which would give more confidence in using SAFT to study properties of promising novel environmentally friendly surfactants for which data may be limited. This could shed light on the impact of structure on product/process performance whilst reducing the number of necessary experiments.

The development of a SAFT model for AOT and its aqueous mixtures was the first objective of this thesis, since a previous one did not exist. The surfactant model is represented in a group contribution manner, where each chemical moiety is represented by a unique bead. By optimising the surfactant-surfactant and surfactant-water intermolecular interactions this allowed the study of phase behaviour and structural properties. MD simulations using these force field parameters showed the formation of a lamellar phase at ambient conditions. At high

temperature a transition to an isotropic phase occurs. The MD simulations do not indicate a structural transition in the middle of the lamellar phase region, instead there is a transition from flexible to rigid bilayers. These observations, as well as the calculated bilayer thickness at room temperature, are in agreement with experimental data. This is encouraging, since only thermodynamic data was included in the force field parameterisation.

Studying the AOT-water-cyclohexane system allowed for the assessment of the SAFT force field to model ternary surfactant mixtures. Due to the group contribution nature of SAFT- γ Mie, many of the intermolecular interactions were simply transferred from the AOT-water model. This model is able to capture both phase morphologies and structural properties. The MD simulations reveal a transition from phase-separated systems to isotropic reversed micelle (RM) phases at low water content. The calculated average cluster size is in good agreement with experimental findings. The relationship between water content and RM morphology was studied. The reduction of water content results in a sharp reduction in average cluster size, highlighting its importance when considering RM stability. When considering the relationship between water content and RM shape, there appears to be little impact since a predominant spherical shape exists for all systems investigated. This has implications for RM experimental investigations, where there are still many differing views regarding the shape of RMs, and where incorrect shape assumptions can affect the accuracy of the results. The advantage of this MD methodology is that no such assumptions about the RM shape must be made for analysis.

Preliminary steps have been completed to study the AOTSiC-water-scCO₂ system using the SAFT-based MD methodology. Due to the similarity in structure to AOT, many of the force field parameters were carried over from the previous model. A model for the water – scCO₂ binary mixture has been created. A single binary interaction parameter was used to optimise the fit to the liquid-liquid equilibrium. These interactions can be transferred to create a preliminary AOTSiC-water-scCO₂ model, which can be tested by comparing to experimental data. Once validated, this would allow the study of the effect of surfactant tail structure and functional groups on the resultant properties of the water-in-scCO₂ RMs. The results of this investigation could then guide the discovery of alternative surfactants to replace expensive and environmentally unfriendly fluorinated surfactants.

Despite their simplicity, the CG models created in this work possess a level of transferability, robustness, and representability. They can be used to predict properties not included in the original parameterisation strategy, with good levels of accuracy. The SAFT theory is hence a suitable approach to parameterise the force fields that could be used in a computational screening method. As has been shown in this work, the methodology requires the prior knowledge of experimental data in order to assess the surfactant structure-performance relationship. This could be obtained from literature or via collaborations with experimentalists both in industry and academia. This approach can be used for the discovery of non-toxic surfactants for a wide range of applications, including drug delivery, food, cleaning products and enhanced oil recovery.

Acknowledgements

There are many people who have helped me to achieve my dream of pursuing a doctorate. First off, I thank my lead supervisor Dr Carmelo Herdes whose door was always open (real and virtual!) for project discussions. I may have chosen this project, but it was because Carmelo saw something in me that I was able to complete it. Prof Tina Düren, my secondary supervisor, was instrumental in my successful application for this PhD, as well as my initial development from Masters student to Doctoral researcher. Thank you so much to both of you.

To my Viva examiners, Prof John Chew and Prof George Jackson, thank you for a very enjoyable discussion. Both of you assuaged any fears I may have had before the Viva.

I would like to extend my thanks to the many people I met at Bath who helped me with my studies as well as getting me away from my desk: Megan, Alistair, Joe, the two Stephens, Mat, Will, Zac, Sam, Mike, Minh and Chris. To borrow a line from Chapter 5 of this thesis: this list is by no means exhaustive. I wish you all the best luck in your future endeavours.

I would like to thank the EPSRC for funding this project, as well as the University Research Computing Team who were responsible for keeping the HPCs up and running.

I would also like to thank my family, who gave so much to enable me to achieve this goal I had set myself.

Project achievements

Published paper

Siddiqi, A. and Herdes, C. Water effect in the reverse micellar formation of docusate sodium. A coarse-grained molecular dynamics approach. *Fluid Phase Equilibria*, 559, (2022), DOI: <https://doi.org/10.1016/j.fluid.2022.113469>

Conferences/Seminars contributions

Siddiqi, A. Integral design of non-toxic surfactants for industrial applications. *Molsim-2019: Understanding Molecular Simulation*. Amsterdam, the Netherlands, 07-18 Jan 2019 (Poster)

Siddiqi, A. Integral design of non-toxic surfactants for industrial applicants. *Chem Eng PhD and Post Docs Symposium*. University of Bath, United Kingdom, 15 July 2019 (Oral presentation)

Siddiqi, A. Water effect in the reverse micellar formation of docusate sodium. A coarse-grained molecular dynamics approach. *ESAT 2021-31st European Symposium on Applied Thermodynamics*. France (100% virtual), 05-09 July 2021 (Oral presentation)

Tutorials

Siddiqi, A. Progress report. University of Bath, United Kingdom, 19 March 2021

Table of Contents

Abstract	i
Acknowledgements	iii
Project achievements	iv
List of Figures	viii
List of Tables	xi
Nomenclature	xiii
Chapter 1 Introduction	1
1.1 Project motivation	1
1.2 Fundamentals of surfactants	3
1.2.1 Definition of a surfactant	3
1.2.2 Aqueous phase behaviour of surfactants	3
1.2.3 Surfactant microemulsion behaviour	7
1.2.4 Environmental aspects of surfactants	8
1.3 Research objectives	10
1.4 Thesis outline	10
Chapter 2 Methodology	12
2.1 Chapter overview	12
2.2 Molecular simulations and modelling	12
2.2.1 Intermolecular force fields	12
2.2.2 Statistical mechanics	17
2.2.3 NVT ensemble	19
2.2.4 NPT ensemble	20
2.2.5 Molecular simulations	21
2.3 Statistical associating fluid theory (SAFT)	25
2.3.1 A brief history of SAFT	25
2.3.2 The M&M correlation	26
2.3.3 SAFT VRE Mie	28
2.4 Analysis methods	30
2.4.1 Surfactant synthesis	30
2.4.2 Density	31
2.4.3 Surface tension	32
2.4.4 Surface excess	35
2.4.5 Liquid-liquid equilibrium	39
2.4.6 Nematic order parameter	39
2.4.7 Relative shape anisotropy	41
2.4.8 Small angle scattering techniques	42

2.5 Coarse-graining	42
2.5.1 Bottom-up approaches	44
2.5.2 Top-down approaches	45
Chapter 3 Modelling the aqueous behaviour of AOT	48
3.1 Chapter overview	48
3.2 Introduction	48
3.3 Model parameterisation strategy	50
3.4 Molecular simulation details	52
3.4.1 Alkane-ester simulations	52
3.4.2 Ester-water simulations	53
3.4.3 AOT-water simulations	53
3.5 Analysis methods	54
3.6 Validation and model creation	54
3.6.1 Alkane-ester interactions	54
3.6.2 Ester-water interactions	58
3.6.3 Remaining cross-interactions	61
3.7 Results and discussion	62
3.7.1 AOT-water phase diagram at room temperature	62
3.7.2 Influence of AOT concentration on bilayer properties	66
3.7.3 Ordered-isotropic transition	69
3.8 Conclusions and outlook	70
Chapter 4 Water effect in the reverse micellar formation of AOT	72
4.1 Chapter overview	72
4.2 Introduction	72
4.3 Cyclohexane model parameterisation strategy	74
4.3.1 Pure interactions	74
4.3.2 Cross-interactions	74
4.4 Molecular simulation details	75
4.4.1 Water-cyclohexane density simulations	75
4.4.2 AOT-water-cyclohexane ternary simulations	76
4.5 Analysis methods	76
4.6 Results and discussion	77
4.6.1 Ternary phase diagram	77
4.6.2 Influence of water content on RM properties	79
4.7 Conclusions and outlook	86
Chapter 5 Conclusions	88
5.1 Conclusions	88

5.2 Future work.....	89
Chapter 6 Toward design of non-toxic surfactants for enhancing scCO₂ as a green solvent	92
6.1 Chapter overview.....	92
6.2 Introduction	92
6.3 Model parameterisation strategy.....	95
6.4 Molecular simulation details.....	96
6.4.1 Water – CO ₂ simulations.....	96
6.5 Validation and model creation.....	96
6.5.1 Water – CO ₂ interactions	96
6.5.2 Remaining cross-interactions	98
6.6 Concluding remarks and future work.....	100
References	101
Appendices	115
Appendix A User-defined functions in Gromacs	116
Appendix B Input interaction parameters	118
Appendix C Example Gromacs input files	125
C.1 NVT simulations.....	125
C.2 Isotropic NPT simulations	127
C.3 Semi-isotropic NPT simulations	130
C.4 NP _{zz} AT simulations	133
Appendix D Example MDTraj script.....	137
Appendix E SO electron density distributions for the AOT – water system at 298.15 K and 1 bar.....	138
Appendix F RM size distributions for the AOT – water – cyclohexane system at 298.15 K and 1 bar	140
Appendix G Balena and Janus technical information	142

List of Figures

Figure 1.1 General structure of a surfactant.	3
Figure 1.2 Images of various micelle shapes: A) Spherical micelle, B) Rod-like micelle, C) Reverse micelle. Taken from ⁽³⁹⁾	4
Figure 1.3 Image of a vesicle formed by surfactants. Taken from ⁽³⁹⁾	5
Figure 1.4 Common surfactant liquid crystalline phases. Taken from ⁽³⁴⁾	6
Figure 1.5 Phase diagram of the C ₁₆ EO ₈ – water binary system. L ₁ and L ₂ refer to the normal and reverse micelle phase respectively. Taken from ⁽³⁴⁾	6
Figure 1.6 Winsor classification of microemulsions. Taken from ⁽⁴⁴⁾	7
Figure 1.7 Ternary diagram representations of two- and three-phase regions formed by simple water-oil-surfactant systems at constant temperature and pressure. Taken from ⁽⁴⁴⁾ ..	8
Figure 1.8 Example of a matrix showing the environmental impact of surfactants. An approved surfactant should lie in the dashed areas. Taken from ⁽³⁹⁾	10
Figure 2.1 The connection between simulation, experiment and theory.	12
Figure 2.2 Common effective pair potentials used in molecular simulations: (a) the Hard-Sphere (HS), (b) Square-well (SW), (c) Lennard-Jones (LJ) and (d) Mie potentials. Taken from ⁽⁶⁵⁾	15
Figure 2.3 Illustration of the types of bonded interactions. Taken from ⁽⁶⁵⁾	16
Figure 2.4 Image of a pycnometer. Taken from ⁽¹¹⁷⁾	32
Figure 2.5 Illustration of the liquid-air surface and the force necessary to increase the surface area. This force is proportional to the surface tension.....	33
Figure 2.6 Illustrative description of a closed system.....	33
Figure 2.7 Schematic diagram of the Drop Volume method. Taken from ⁽¹²¹⁾	34
Figure 2.8 Image of a Drop Volume tensiometer. Taken from ⁽¹²²⁾	34
Figure 2.9 The Gibbs approach to defining surface excess Γ . Taken from ⁽³⁴⁾	36
Figure 2.10 Schematic representation of a surface tension-concentration plot and its transformation into a surface tension-surface excess plot. Taken from ⁽¹⁵⁾	39
Figure 3.1 Experimental phase diagram of the AOT-water binary mixture. Taken from ⁽⁵⁸⁾ ..	48
Figure 3.2 CG representations of the molecules used in this study: AOT (left) and water (right). The underlying atomistic structure is included as a guide to the eye. The hydrogens have been removed from the AOT model for clarity. These images are not to scale.	50
Figure 3.3 Flowchart of the coarse-graining methodology used in this work.....	52
Figure 3.4 Plot of the potential energy between CP and ES beads for the BAC system at 298.15 K. The black line corresponds to the raw (unaveraged data), whilst the red line refers to the running average, every 100 configurations.....	55
Figure 3.5 Plot of surface tension for the BAC system at 298.15 K over the last 20 ns of simulation. The black line corresponds to the raw (unaveraged data), whilst the red line refers to the running average, every 50 configurations.....	56
Figure 3.6 Equilibrated density profile of BAC at 298.15 K.	56
Figure 3.7 Equilibrated MD simulation images at 298.15 K for i) BAC, ii) PAC, and iii) OAC. The colour code is given in Table 3.1	57
Figure 3.8 Plot of potential energy between ES and W beads for the system at 298.15 K. The black line corresponds to the raw (unaveraged data), whilst the red line refers to the running average, every 800 configurations.....	59
Figure 3.9 The particle number density profile of the MAC (black line) and water (red line) system at 298.15 K taken from the last 175 ns of simulation.	60
Figure 3.10 T-x liquid-liquid phase diagram at 1 bar for the binary mixture methyl acetate (x ₁) and water. The SAFT CG model is shown as solid circles while the UA model by Feria et al ⁽¹⁸⁷⁾ is shown as solid squares. Experimental data ⁽¹²⁹⁾ is shown as dashed lines.	60

Figure 3.11 Equilibrated MD simulation images for the methyl acetate – water system at i) 293.15 K, ii) 298.15 K, iii) 303.15 K and iv) 313.15 K. The colour code is provided in Table 3.1.....	61
Figure 3.12 Potential energy between the SO and W beads at 29.39 wt % AOT. The black line corresponds to the raw (unaveraged data), whilst the red line refers to the running average, every 500 configurations	63
Figure 3.13 Time variation of tail-averaged S_2 for the 29.39 wt % system over the last 100 ns of simulation. The black line corresponds to the raw (unaveraged data), whilst the red line refers to the running average, every 300 configurations.....	64
Figure 3.14 Variation of nematic order parameter S_2 for each system studied. The line is added as a guide to the eye.....	64
Figure 3.15 Equilibrated MD simulation images at AOT content of i) 29.39 wt%, ii) 32.22 wt %, iii) 35.36 wt % , iv) 44.53 wt %, v) 53.19 wt %, vi) 61.98 wt %, and vii) 71.18 wt %. The colour code is provided in Table 3.1. Water beads have been removed for clarity.	65
Figure 3.16 Equilibrated MD simulation images for systems with AOT content of i) 80.45 wt% and ii) 89.17 wt%. The colour code is provided in Table 3.1. Water beads have been removed for clarity.	66
Figure 3.17 Variation of nematic order parameter S_2 for Tail 1 (black circles) and Tail 2 (red squares) for all bilayer systems. The lines are added as a guide to the eye.....	67
Figure 3.18 Average electron density distribution of the SO bead across the z dimension of the simulation box at 29.39 wt % AOT.	68
Figure 3.19 Average electron density distribution of the SO bead across the z dimension of the simulation box at 61.98 wt % AOT.	68
Figure 3.20 Average bilayer thickness as a function of AOT weight percentage. The MD simulations are represented by black circles and the experimental data by Fontell ⁽¹³⁹⁾ (red squares) is included for comparison. The lines are added as a guide to the eye.....	69
Figure 3.21 Equilibrated MD simulation images for systems with AOT wt% of i) 29.39 wt% and ii) 71.18 wt% at 433.15 K. The colour code is given in Table 3.1. Water beads have been removed for clarity.....	70
Figure 3.22 The experimental phase diagram for the AOT-water system ⁽⁵⁸⁾ , with equilibrated MD simulation images for 29.39 wt% and 71.18 wt% at 298.15 K and 433.15 K super-imposed.	71
Figure 4.1 CG representation of cyclohexane. The underlying atomistic representation is included for comparison purposes. The hydrogen atoms have been removed for clarity. This image is not to scale.	74
Figure 4.2 Phase diagram of the AOT-water-cyclohexane ternary system ⁽⁵⁹⁾ . The solid continuous curve denotes the phase boundary, obtained by experiment. Included are the approximate positions of each system studied. Compositions are given in weight percentage.	76
Figure 4.3 Plot of potential energy between the SO and W beads for system a. The black line corresponds to the raw (unaveraged data), whilst the red line refers to the running average, every 100 configurations	78
Figure 4.4 Variation of the average nematic order parameter, S_2 , with each system studied. The line is added to guide the eye. The experimental phase diagram ⁽⁵⁹⁾ is included for reference.....	79
Figure 4.5 Equilibrated MD simulation images, from left to right, for the systems a, f, i, j, and k. The cyclohexane beads have been removed for clarity. The colour code is given in Table 3.1.....	80
Figure 4.6 The average cluster size distribution for system k.	81
Figure 4.7 The average cluster size distribution for system p.	82
Figure 4.8 Variation of the average cluster size over the last 30 ns for system k.....	83

Figure 4.9 Plot of potential energy between the SO and W beads for the RM100 system. The black line corresponds to the raw (unaveraged data), whilst the red line refers to the running average, every 500 configurations	84
Figure 4.10 Variation of the relative shape anisotropy over the last 100 ns for the RM100 system. The black line corresponds to the raw (unaveraged data), whilst the red line refers to the running average, every 100 configurations.....	85
Figure 4.11 The experimental phase diagram for the AOT-water-cyclohexane system ⁽⁵⁹⁾ , with equilibrated MD simulation images for systems a, f and p super-imposed.	87
Figure 6.1 CG representations of the molecules used in this study: AOTSiC and CO ₂ . The underlying atomistic representation is included for comparison purposes. In the AOTSiC model the hydrogen atoms have been removed for clarity. These images are not to scale.	95
Figure 6.2 Plot of potential energy between W and CO beads for the system at 200 bar. The black line corresponds to the raw (unaveraged data), whilst the red line refers to the running average, every 200 configurations	97
Figure 6.3 The particle number density profile of the water (red line) and scCO ₂ (black line) system at 200 bar taken from the last 40 ns of the simulation.	97
Figure 6.4 P-x liquid-liquid phase diagram at 383.15 K for the binary mixture scCO ₂ (x ₁) and water. The SAFT CG model is shown as solid circles, while the experimental data ⁽²⁸⁵⁾ is shown as solid lines.	98
Figure 6.5 Equilibrated MD simulation images for the scCO ₂ – water system at i) 200 bar, ii) 300 bar, iii) 400 bar and iv) 500 bar. The temperature is 383.15 K for all systems. The colour code is provided in Table 5.1 and Table 3.1.....	99
Figure A.1 C++ code lines for mie2gmx.cpp.....	117
Figure E.1 Average electron density distribution of the SO bead across the z dimension of the simulation box at 32.22 wt % AOT	138
Figure E.2 Average electron density distribution of the SO bead across the z dimension of the simulation box at 35.36 wt % AOT	138
Figure E.3 Average electron density distribution of the SO bead across the z dimension of the simulation box at 44.53 wt % AOT	139
Figure E.4 Average electron density distribution of the SO bead across the z dimension of the simulation box at 53.19 wt % AOT	139
Figure F.1 The average cluster size distribution for system l.....	140
Figure F.2 The average cluster size distribution for system m.....	140
Figure F.3 The average cluster size distribution for system n.....	141
Figure F.4 The average cluster size distribution for system o.....	141

List of Tables

Table 3.1 List of the names of the CG beads used in the system, with the corresponding underlying chemical, number of CG beads m and the bead colour.	51
Table 3.2 List of the systems studied in this chapter. Note that the water model contains two molecules per bead.....	53
Table 3.3 Comparison of experimental and optimised simulation values of liquid density (in kg m^{-3}) and surface tension (mN m^{-1}) for BAC.....	57
Table 3.4 Comparison of experimental and optimised simulation values of liquid density (in kg m^{-3}) and surface tension (mN m^{-1}) for PAC.....	57
Table 3.5 Comparison of experimental and optimised simulation values of liquid density (in kg m^{-3}) and surface tension (mN m^{-1}) for OAC.	58
Table 3.6 Absolute deviation from the mutual solubility data ⁽¹²⁹⁾ at 298.15 K and 1 bar	58
Table 3.7 List of non-bonded intermolecular interaction parameters	62
Table 3.8 Parameter matrix indicating how each intermolecular interaction was derived.....	62
Table 4.1 List of cyclohexane non-bonded intermolecular interaction parameters.....	75
Table 4.2 Parameter matrix indicating how each cyclohexane intermolecular interaction was derived.....	75
Table 4.3 AOT-water-cyclohexane systems, number of molecules, and estimated dielectric constant ϵ_r , calculated using equation (2.66).....	77
Table 4.4. Average cluster size, taken over the last half of the simulations.	82
Table 4.5 List of all single RM systems studied and estimated dielectric constant ϵ_r , calculated using equation (2.66).	83
Table 4.6 The average anisotropic shape factor for a variety of RM sizes, with the corresponding simulation image.....	84
Table 6.1 List of the new CG beads used in the study, with the corresponding chemical, number of segments m and the colour.....	96
Table 6.2 List of all the water-CO ₂ binary mixtures studied via MD simulation	96
Table 6.3 List of the new non-bonded intermolecular interaction parameters	99
Table 6.4 Parameter matrix indicating how each new intermolecular interaction was derived.	100
Table B.1 Intermolecular interaction parameters for a butyl acetate molecule.....	118
Table B.2 Structure of a butyl acetate molecule	118
Table B.3 Intramolecular interaction parameters for a butyl acetate molecule	118
Table B.4 Intermolecular interaction parameters for a pentyl acetate molecule	118
Table B.5 Structure of a pentyl acetate molecule	118
Table B.6 Intramolecular interaction parameters for a pentyl acetate molecule	119
Table B.7 Intermolecular interaction parameters of an octyl acetate molecule	119
Table B.8 Structure of an octyl acetate molecule	119
Table B.9 Intramolecular interaction parameters of an octyl acetate molecule	119
Table B.10 Intermolecular interaction parameters for the AOT-water-cyclohexane system. The SO and NA beads are assigned a charge of -1 and +1 respectively.....	120
Table B.11 Structure of an AOT molecule. The NA bead is modelled as fully dissociated.	120
Table B.12 Intramolecular interaction parameters for an AOT molecule.....	121
Table B.13 Structure of a cyclohexane molecule.....	121
Table B.14 Intramolecular interaction parameters for a cyclohexane molecule	121
Table B.15 Intermolecular interaction parameters for the ternary AOTSiC – water – scCO ₂ system. The SO and NA beads are assigned a charge of -1 and +1 respectively.....	122
Table B.16 Structure of an AOTSiC molecule. The NA bead is modelled as fully dissociated.	123

Table B.17 Intramolecular interaction parameters for AOTSiC	124
Table B.18 Structure of a CO ₂ molecule.....	124
Table B.19 Intramolecular interaction parameters for a CO ₂ molecule	124

Nomenclature

Symbol	Definition (units)
a_0	Minimum interfacial area occupied by surfactant head group (m^2).
a	Chemical activity (mol m^{-3}).
\mathbf{a}	Acceleration (m s^{-2}) vector
A	Helmholtz free energy (J)
A_{cmc}	Area of the surfactant headgroup at the critical micelle concentration (m^2)
A_s	Interfacial area (m^2).
A_{min}	Minimum area (m^2)
b	Asphericity (-)
\mathbf{b}	Periodic box vector matrix (-)
B	Nosé-Hoover mass parameter (K s^2)
c	Acylicity (-)
c_i	Centre of mass (m)
d	Solvent-dependent dielectric parameter ($\text{m}^3 \text{kg}^{-1}$). In the context of dimensions it refers to diameter (m). In the context of small angle scattering it refers to the separation of lattice planes.
dW	Wiener process
d_T	Solvent-dependent temperature fitting parameter (K)
d_V	Solvent-dependent volume fitting parameter ($\text{m}^3 \text{kg}^{-1}$)
e	Elementary charge (C)
E	Energy (J)
\mathbf{f}	Atomistic force (N) vector
F	Force (N)
\mathbf{F}	Force (N) vector
g	Acceleration due to gravity (m s^{-2})
g_i	Fitting parameter
$g(r)$	Radial distribution function (-)
G	Gibbs free energy (J)
H	Hamiltonian (-)
h	Planck's Constant ($\text{kg m}^2 \text{s}^{-1}$)
I	Ionisation potential (eV)
I^2	Moment of inertia (m^2)
k_{ij}	Binary interaction parameter (-)
k_{angle}	Angle bending constant ($\text{J mol}^{-1} \text{rad}^{-2}$)
k_{bond}	Bond stretching constant ($\text{J mol}^{-1} \text{m}^{-2}$)
$k_{dihedral}$	Dihedral angle bending constant (J mol^{-1})
k_B	Boltzmann constant (J K^{-1})
K	Kinetic energy (J)
K_0	Kinetic energy at set temperature (J)
K_{ow}	Octanol-water partition coefficient (-)
l_c	Maximum extended chain length of surfactant tail in micelle core (m)
L	Length (m). In the context of Force-based methods it refers to the number of reference frames
L_{tail}	Surfactant tail length (-)
m	Mass (kg). In the context of SAFT models it refers to the number of coarse-grained beads (-)
M	Mechanical property (-). In the context of relative shape anisotropy it refers to total mass (kg)
\mathbf{M}	Coordinate mapping (-)
n	Number of moles (mol). In the context of dihedrals it refers to the multiplicity (-)
\mathbf{n}	Molecular director (-)

N	Number of molecules (-). In the context of error analysis it refers to number of data points (-). In the context of Particle Mesh Ewald method it refers to number of charge sites (-).
N_{av}	Avogadro number (mol^{-1})
N_c	Number of components (-)
N_f	Number of degrees of freedom (-)
N_p	Number of phases (-)
P	Pressure (Pa). In the context of statistical mechanics it refers to the probability (-)
P_c	Critical Packing Parameter of a surfactant (-)
p	Momentum (kg m s^{-1})
\mathbf{P}	Pressure (Pa) matrix
\mathbf{P}_{ref}	Reference pressure (Pa) matrix
\mathbf{p}	Set of momenta for all particles in a system
q	Charge (C)
\mathbf{q}	Set of co-ordinates of all particles in a system
Q	Partition function for the NVT ensemble (-).
\mathbf{Q}	Saupe order tensor (-)
r	Position (m)
r_0	Equilibrium bond length (m)
r_c	Molecular cut-off radius (m)
\mathbf{r}	Position (m) vector
R	Universal gas constant ($\text{J mol}^{-1} \text{K}^{-1}$)
R_g	Radius of gyration (m)
S	Entropy (J K^{-1})
S_2	Nematic order parameter (-)
T	Temperature (K)
T_c	Critical temperature (K)
T_r	Reduced temperature (K)
t	Time (s)
\mathbf{u}	Unit vector
U	Internal energy (J). In the context of molecular simulations it refers to the intermolecular or intramolecular interaction energy (J mol^{-1})
v	Volume of surfactant hydrophobic tail (m^3)
\mathbf{v}	Velocity (m s^{-1}) vector
V	Volume (m^3). In the context of intermolecular force fields it refers to potential energy (J)
V_{tail}	Surfactant tail volume (m^3)
w_0	Molar water to surfactant ratio
W	Mechanical work (J)
\mathbf{W}^{-1}	Inverse mass parameter matrix in Parrinello-Rahman algorithm ($\text{bar}^{-1} \text{s}^{-2} \text{m}^{-1}$)
x	Mole fraction (-)
x	Distance (m)
\acute{x}	Salt-free mole fraction (-)
X	Property e.g. surface tension
z	Ionic valence (-)
α	Van-der-waals constant (-). In the context of Cartesian coordinates it refers to an index of Cartesian components (-)
α_0	Electronic polarisability (cm^{-3})
β	Reciprocal temperature (J^{-1}). In the context of molecular simulations refers to the isothermal compressibility (Pa^{-1})
γ	Surface/interfacial tension (N m^{-1})
Γ	Gibbs Surface excess (mol m^{-2})
δ	Kronecker delta function (-)

δt	Time step (s)
Δ	Partition function for the NPT ensemble (-)
ΔG_{ads}^0	Gibbs free energy of adsorption (J)
ε	Well-depth (J)
ε_0	Dielectric permittivity of a vacuum ($F\ m^{-1}$)
ε_r	Dielectric constant (-)
θ	Bond angle (rad). In the context of small angle scattering it refers to angle of diffraction
θ_0	Equilibrium bond angle (rad)
κ^2	Shape anisotropy (-)
Λ	Thermal de Broglie Wavelength (m)
λ	Eigenvalue (-). In the context of small angle scattering it refers to wavelength (m)
λ_{ij}	Square-well attractive range (-)
λ_{ij}^a	Attractive exponent in Mie force field (-)
λ_{ij}^r	Repulsive exponent in Mie force field (-)
μ	Chemical potential ($J\ mol^{-1}$)
ξ	Friction parameter (-)
ρ	Density ($kg\ m^{-3}$). In the context of statistical mechanics refers to probability density. In the context of Particle Mesh Ewald it refers to the charge density ($J\ mol^{-1}\ m^{-2}$)
σ	Interaction parameter (m). In the context of interfaces refers to the interfacial layer
τ_T	Temperature coupling time constant (s)
τ_P	Pressure coupling time constant (s)
ϕ	Dihedral angle (rad)
ϕ_0	Equilibrium dihedral angle (rad)
$\phi(\mathbf{x})$	Reciprocal space potential ($J\ mol^{-1}$)
ω	Acentric factor (-)

Abbreviation	Definition
AA	All-atomistic
AAD	Absolute average deviation
AOT	sodium bis(2-ethyl 1-hexyl) sulphosuccinate
AOTSiC	Sodium bis (3-(trimethylsilyl)-1-propanol) sulphosuccinate
$C_{16}EO_8$	Octaethylene glycol mono-hexadecyl ether
CG	Coarse-grained
CMC	Critical Micelle Concentration
DPD	Dissipative Particle Dynamics
EoS	Equation of State
FFV	Fraction Free Volume
HS	Hard sphere
IBI	Iterative Boltzmann Inversion
IMC	Inverse Monte Carlo
LJ	Lennard-Jones
LLE	Liquid liquid equilibrium
M&M	Mejía and Müller
MD	Molecular Dynamics
MC	Monte Carlo
PMF	Potential of Mean Force
RDF	Radial Distribution Function
RM	Reverse Micelle
SAFT	Statistical Associating Fluid Theory
SANS	Small Angle Neutron Scattering
SAXS	Small Angle X-ray Scattering

SW	Square-well
TMS	Trimethylsilyl
UA	United atom
VLE	Vapour liquid equilibrium
VOC	Volatile Organic Compounds
VR	Variable range
VRE	Variable range electrolyte

Chapter 1 Introduction

1.1 Project motivation

Surfactants are used in a variety of products, spanning from everyday consumer usage encompassing household cleaning (e.g. laundry detergents, hard surface cleaners and window cleaners) and personal care (e.g. shampoo, shaving creams and toothpaste) to various industries including pulp and paper, oil and gas, agrochemicals and pharmaceuticals ⁽¹⁾. Indeed, many products mankind takes for granted would not exist if not for the presence of surfactants. Even products necessary for human development such as milk exist due to surfactants, in this case the surfactant is the milk protein casein ⁽²⁾. The necessity of surfactants is further proved by the global market size which was estimated to be \$41.3 billion in 2019. The market is expected to grow to \$58.5 billion by 2027, and the main factors cited include low prices and easy availability of surfactants ⁽³⁾. It should be noted that the ongoing Covid-19 Pandemic has had significant impact on the market. Whilst hygiene products have been performing well due to public information campaigns, industrial sectors have been negatively affected due to restrictions such as national lockdowns. However, as the economy recovers, it is expected these sectors will rebound strongly ⁽⁴⁾.

After use, surfactants are sent to wastewater treatment plants, where the removal efficiency can vary. One study ⁽⁵⁾ reported average values of 95-99 % based on removal of alcohol ethoxysulphates, alkyl sulphates, and alcohol ethoxylates in various sites within the EU. However, another study ⁽⁶⁾ carried out in Poland found that removal efficiencies ranged from 88-98 % and 56-76 %, dependent on the type of surfactant. Despite the disparities it is guaranteed that a fraction of surfactants, due to their high volume of consumption, will enter the natural environment including surface waters and sludge disposals. A consequence of further unrestricted market growth could be significant concentrations of surfactants in aquatic environments in the future. Many surfactants are toxic to aquatic organisms above a certain concentration. For example, linear alkyl benzene sulphonate surfactants, commonly used in detergent formulation and personal care products, can cause biochemical, pathological and physiological effects on aquatic and terrestrial environments ^{(7) (8) (9)}. This has caused a shift in global regulations to favour more environmentally friendly surfactant formulations, with the environmental profile of surfactant chemistries at the forefront of product formulation and design ⁽¹⁰⁾. Indeed, recognition of the economic and ecological importance of the marine environment and its sensitivity toward anthropogenic impacts is growing, which further increases the emphasis being placed on their protection. This is particularly relevant to surfactants, as the marine environments are considered the ultimate disposal sites of surfactants ⁽⁵⁾. It is for this reason that the design of new environmentally friendly surfactants is the key goal of this work.

An accurate understanding of how the surfactant structure is related to properties including binary and ternary phase behaviour is a pre-requisite for the design of new products and processes. If a new non-toxic surfactant structure is found or proposed, it is important to investigate the phase behaviour as this will have an effect on the product/process performance. This is a non-trivial activity. Experimental techniques used to study the structure-performance relationship include small angle neutron scattering (SANS) ⁽¹¹⁾, nuclear magnetic resonance (NMR) ⁽¹²⁾ and tensiometry ⁽¹³⁾. These methods may yield useful information, but they are not without complications nor limitations. A purely experimental route can become time-consuming and expensive and may be limited by safety and feasibility aspects. This can be due to the product/process containing toxic chemicals or requiring extreme operating temperatures/pressure. An approach that has established itself alongside theory ⁽¹⁴⁾ and experiment ⁽¹⁵⁾ and is popular in the field of soft matter is molecular dynamics (MD) simulation ⁽¹⁶⁾. In this technique molecules are described as particles which interact via a mathematical equation to model the underlying physics which in MD is called a force field. This work aims to use MD simulations as the basis of a screening stage so that only the most promising surfactant mixtures make it to experimental testing. The improvements in intermolecular force

fields, increases in computer speed and memory, and more efficient algorithms are some of the reasons molecular simulations have become widespread⁽¹⁷⁾. Furthermore, MD simulations can be used to calculate structural, interfacial, and dynamic properties which can then be compared to experimental findings for further analysis⁽¹⁸⁾. The application of MD simulations to surfactant structure analysis studies is a logical step, as the structure can be altered by simply changing the number of the specific groups in the molecule. The investigation of new functional groups in the surfactant molecular structure can also be achieved in a trivial manner in molecular modelling. Whilst MD simulations on ternary surfactant-water-oil mixtures are not new⁽¹⁹⁾, there is not much direct work on the discovery of non-toxic surfactants.

To gain insight into the molecular-scale behaviour of surfactants via simulation, large time and length scales need to be explored. Should the atomistic detail of the molecules be fully represented, system sizes and simulation times are limited^(20, 21). The alternative is to work on the coarse-grained (CG) scale, where multiple heavy atoms are incorporated into one super-atom or 'bead'. The next big decision is about how the force field parameters are assigned, to ensure the model is accurate and can represent the underlying physics. This can be a challenging task, especially if the required data is not available or complex interactions are present e.g. hydrogen bonding present in water which results in its unique behaviour⁽²²⁾. One approach is to start with a more detailed atomistic model, and integrate out irrelevant degrees of freedom, termed 'bottom up' CG methods⁽²³⁾. The main issue with these methods is the lack of transferability to other state points. The force field parameters can instead be found by fitting to macroscopically observed thermophysical properties in a 'top-down' approach. This can be achieved by employing an equation of state (EoS), an analytical representation of the free energy, to link the intermolecular potential and macroscopic experimental data⁽²⁴⁾. These methods are limited by the strength of the link between the EoS and intermolecular potential.

In this work the Statistical associating fluid theory (SAFT)⁽²⁵⁾, in particular the SAFT- γ Mie group contribution⁽²⁶⁾ and the SAFT VRE Mie version⁽²⁷⁾ which extends to electrolytes, is the parameterisation method. This is a top-down CG route which uses a free energy perturbation method to provide a strong link between force field parameters and macroscopic data. This allows for a fast model parameterisation where the CG force field can be fit to multiple state points and properties simultaneously. The SAFT- γ Mie equation of state has been expressed in a reduced form using a corresponding states correlation. This approach is called the M&M correlation⁽²⁸⁾, and it has been ported to an online webpage called Bottled SAFT⁽²⁹⁾. This streamlines the model parameterisation process further, as only three parameters of the target molecule need to be specified: the critical temperature, a characteristic liquid density and the acentric factor. More detail is provided on the relevant SAFT theory, the M&M correlation and Bottled SAFT in section 2.3.

Despite SAFT force fields showing an ability to capture binary surfactant-water properties⁽³⁰⁾⁽¹⁵⁾⁽³¹⁾ they have not yet been extended to ternary surfactant mixtures. It is hence important to assess the capability which is accomplished by studying a system for which there exists experimental data to parameterise the model. The sodium bis (2-ethylhexyl) sulphosuccinate (AOT)-water-cyclohexane system at ambient conditions is chosen as a case study. This system is of relevance in applications such as nanoparticle synthesis⁽³²⁾, where controlling phase morphology can influence particle size and shape.

The second ternary system considered in this work was that of sodium bis (3-(trimethylsilyl)-1-propanol) sulphosuccinate (AOTSiC) in water and supercritical (sc) CO₂. This system has been investigated as an approach to improve the physicochemical properties of scCO₂⁽³³⁾, without having to resort to expensive and environmentally unfriendly fluorinated surfactants. A valid model could assist the discovery process by acting as a screening step to identify promising surfactant structures.

Surfactant phase behaviour is due to a delicate interplay between attractive and repulsive interactions. Before studying these ternary mixtures, it is important to ensure the force field parameters are fine-tuned. In this work this is achieved by simulating the constituent binary mixtures and comparing against available macroscopic data.

1.2 Fundamentals of surfactants

1.2.1 Definition of a surfactant

The term surfactant is an abbreviation of 'surface-active agent'. Surfactants represent a diverse range of amphiphilic molecules, meaning they contain both a hydrophilic and hydrophobic moiety. These are usually referred to as the surfactant 'head' and 'tail' respectively ⁽³⁴⁾, and an example is shown in Figure 1.1. The simplest classification of surfactants is based on the nature of the hydrophilic head. Surfactants with ionic heads belong to either the anionic or cationic group if the head group is negatively or positively charged respectively. Surfactants with non-charged heads are simply termed nonionic, and those that contain both a negative and positively charged group in the main surfactant structure are zwitterionic.

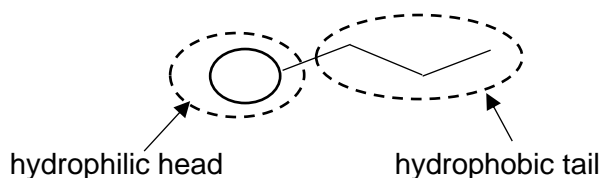


Figure 1.1 General structure of a surfactant.

1.2.2 Aqueous phase behaviour of surfactants

Surfactants when dissolved at dilute concentrations in a solvent will adsorb at the interface altering the physical properties of that interface. The term interface refers to the boundary between liquid/liquid, liquid/solid and liquid/gas systems. In the latter case, the term surface can be used instead. If the air-water surface is considered, this adsorption behaviour can be attributed to the nature of the water and the amphiphilic nature of the surfactant. Water molecules interact with each other via hydrogen bonding, the distortion of this solvent structure by hydrophobic groups in dissolved surfactants is believed to increase the free energy of the system ⁽³⁵⁾, despite the dipolar attraction between the headgroup and water. Less work is required to bring a surfactant molecule to the surface than a water molecule, so the migration of the surfactant to the surface is a spontaneous process, i.e. it results in a reduction in free energy. Surfactants will therefore 'sit' at interfaces so the hydrophilic part is in contact with the water, and the hydrophobic part is in contact with the non-aqueous phase. The surfactants will self-assemble at the interface in the form of a monolayer, which will be in equilibrium with single surfactants (termed 'unimers' ⁽³⁶⁾) in the bulk solution.

Adsorption is associated with significant energetic changes since the free energy of a surfactant molecule located at the interface is lower than that of a molecule solubilised in either bulk phase. Accumulation of amphiphiles at the interface is therefore a spontaneous process and results in a reduction of interfacial tension. Whilst this definition may apply to other chemicals that are surface active, such as medium or long-chain alcohols ⁽³⁷⁾, they are not considered true surfactants. In addition to forming oriented interfacial monolayers, true surfactants aggregate to form micelles, provided their concentration is above a critical concentration, termed the CMC.

At a certain concentration of free unimers in solution, when all the interfaces are saturated with surfactant, surfactant molecules will self-assemble in the bulk forming aggregates of a specific size. These aggregates are called micelles⁽³⁸⁾, and the self-assembly process is called micellisation. The CMC is the concentration at which the first micelle is formed. Further addition of surfactant beyond the CMC will result in more micellisation. The concentration of unimers will remain approximately close to the value of the CMC⁽³⁶⁾.

The shape of micelles can vary from spherical (Figure 1.2 A) to rod-like (Figure 1.2 B). Another classification is whether they are of 'normal' or 'reverse' type. If the micelle is of the former type (Figure 1.2 A and B), then the hydrophilic headgroups form the outer layer of the structure, in contact with water. For a reverse micelle (Figure 1.2 C), the headgroups form the inner layer, in contact with a water core. The number of surfactants constituting a micelle is termed the aggregation number. For a normal spherical micelle, a typical aggregation number is 60-70⁽³⁹⁾. The micelles formed by the surfactant are a function of the geometry⁽⁴⁰⁾, which can be described using the critical packing parameter P_c :

$$P_c = \frac{v}{a_0 l_c} \quad (1.1)$$

where a_0 is the minimum interfacial area occupied by the head group, v is the volume of the hydrophobic tail(s), and l_c is the maximum extended chain length of the tail in the micelle core. The parameter v is a function of the number of hydrophobic groups, chain branching, and chain penetration by other compatible hydrophobic groups. The parameter a_0 is a function of the electrostatic interactions and head group hydration. For example, reverse micelles are formed by surfactants where the tail volume is larger than the headgroup volume, which is usually the case with double-tail surfactants. The surfactant concentration is also a determining factor, normally at low concentrations spherical micelles form which grow and extend as surfactant concentration increases, resulting in an increase of viscosity.

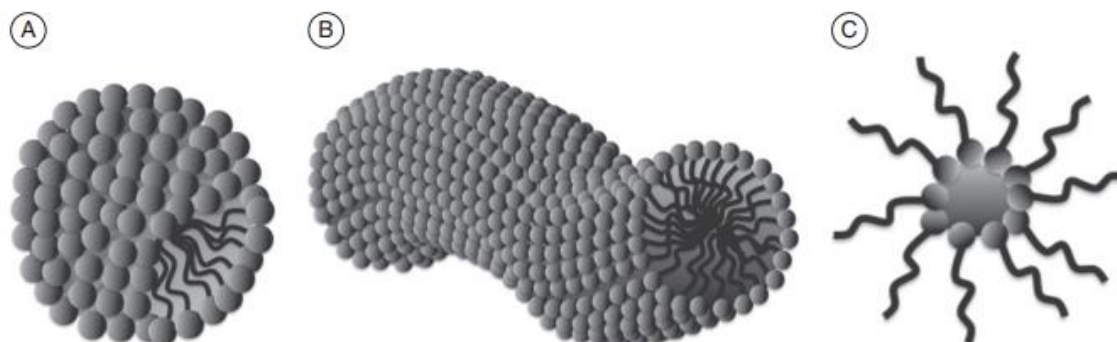


Figure 1.2 Images of various micelle shapes: A) Spherical micelle, B) Rod-like micelle, C) Reverse micelle. Taken from⁽³⁹⁾

Surfactants with two hydrophobic tails will not tend to form micelles, instead self-assembling to form vesicles (also called liposomes) in aqueous solution. These are spherical bilayer structures with two distinct compartments, one forming the core and the other the surrounding medium, as illustrated in Figure 1.3.

The CMC yields important information about the surfactant: a low value indicates that micelles self-assemble in bulk at low concentration, which is relevant because less surfactant will be required for a specific task, for example emulsification, compared to a surfactant with a higher CMC. The CMC is dependent on structure of the surfactant, for example anionic and cationic surfactants will have CMCs about two orders of magnitude higher than those of nonionic or zwitterionic surfactants. This is related to the presence of counter-ions, for which the

accumulation just below the surface involves a non-favourable entropy penalty. Ion-water interactions will lead to counter-ion solvation, which will attract surfactants via Coulombic interactions away from the surface layer. Hence the accumulation of ionic surfactants on the air-water surface is less favourable compared to nonionics.

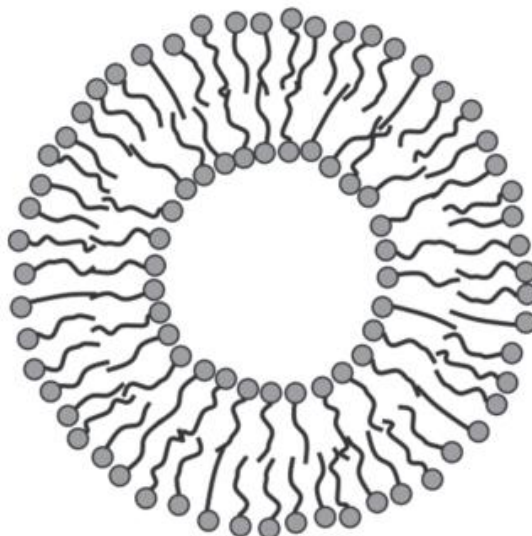


Figure 1.3 Image of a vesicle formed by surfactants. Taken from ⁽³⁹⁾

The CMC of a surfactant occurs at concentrations >1 wt % surfactant. Further addition of surfactant far beyond the CMC, usually at 15-20 wt % surfactant ⁽³⁹⁾, will eventually result in the formation of liquid crystalline phases. These systems consist of extended aggregation of surfactant molecules into large, organised structures. The formation of liquid crystalline phases is due to the repulsive interactions between micellar surfaces, either due to electrostatic or hydration forces. There will also be an entropic contribution, as close contact will lead to limitations in rotational and translational motion. These factors are in addition to avoiding contacts between hydrophobic groups and water. The increase in number of aggregates will mean micelles will become closer to each other, and the subsequent changes in size and shape are thus to maximise the separation. Liquid crystals are characterised by having physical properties between crystalline and fluid structures: the degree of molecular ordering is between that of a liquid and a crystal. In terms of rheology the systems are neither simple viscous liquids nor crystalline elastic solids. Liquid crystals will have at least one direction that is highly ordered, and hence show birefringence. This allows the study of these systems by using scattering techniques such as SANS ⁽³⁴⁾. Liquid crystals can be divided into two different types: lyotropic and thermotropic. In the former class the structure and properties are influenced by temperature, whereas in the latter the main influencing factor is concentration. Most surfactants will typically fall into the lyotropic category.

There are three main types of structures associated with surfactant-water systems: hexagonal, lamellar and cubic. Illustrations of these are provided in Figure 1.4. The hexagonal phase is described as a close-packed array of long cylindrical micelles, arranged in a hexagonal pattern. If the surfactant hydrophilic head groups are located at the outer surface of the cylinder, the term normal hexagonal phase (H_1) is used. If the head groups form the interior, then it is a reverse hexagonal phase (H_2). The lamellar phase (L_α) consists of alternating water-surfactant bilayers. The hydrophobic chains possess a significant degree of randomness and mobility, and the bilayer can range from being stiff and planar to being very flexible and undulating ⁽³⁴⁾. Dependent on the system, the level of disorder may vary strongly or not at all, so that several distinct lamellar phases may occur as the surfactant concentration is varied. The cubic phase consists of a variety of structures, and two examples of these are the micellar cubic phase and the bicontinuous cubic phase. The former is built up of regular packing of small micelles (I_1) or reverse micelles (I_2). The latter are formed by either connected rod-like

micelles or bilayer structures, as before there is a distinction between normal (V_1) and reverse (V_2) structures.

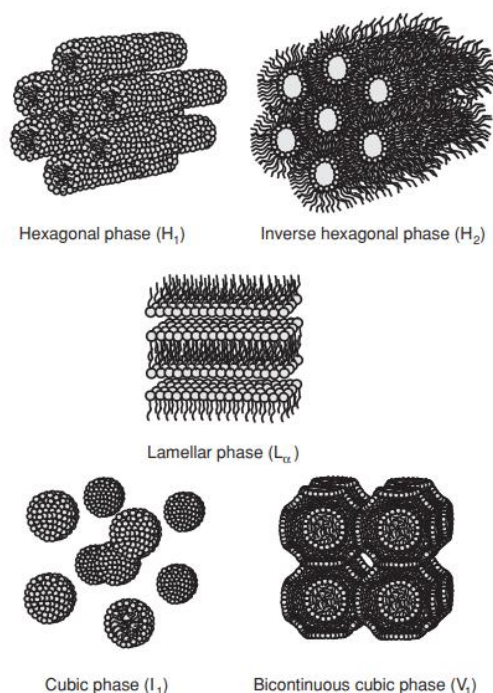


Figure 4.8 Common surfactant liquid crystalline phases. See Table 1.4 for identification.

Figure 1.4 Common surfactant liquid crystalline phases. Taken from ⁽³⁴⁾

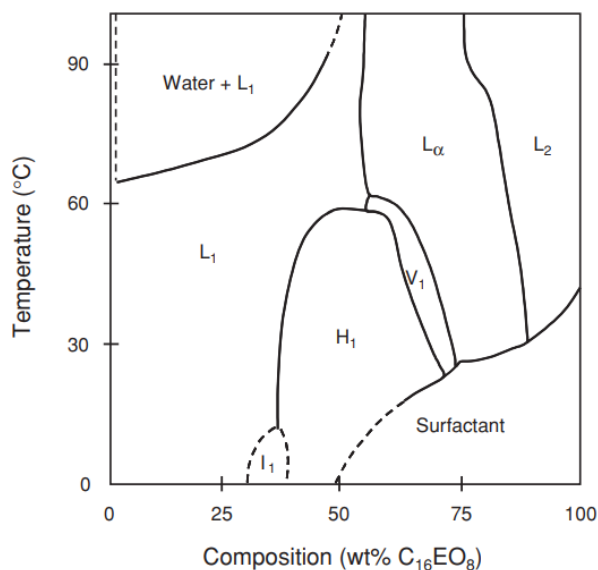


Figure 1.5 Phase diagram of the $C_{16}EO_8$ – water binary system. L_1 and L_2 refer to the normal and reverse micelle phase respectively. Taken from ⁽³⁴⁾

The sequence of mesophases of a surfactant-water system is described via a phase diagram. An example is given in Figure 1.5 for the nonionic surfactant $C_{16}EO_8$ (octaethylene glycol monohexadecyl ether). Boundaries are denoted by either solid or dotted lines, where the latter indicates boundaries not determined accurately ⁽⁴¹⁾. A phase diagram is usually created from experiments where a polarising microscope is used to identify the different phases via an isothermal technique called a phase cut ⁽⁴²⁾. Starting from a small amount of surfactant, a concentration gradient is created by adding water. There will hence be a region of pure

surfactant, and a region of pure water. It is because some liquid crystalline phases are birefringent that they can be identified by polar microscopy. The boundaries between the different mesophases are controlled by the molecular geometry and the inter-aggregate forces, hence the nature and amount of solvent plays an important role. Typically, the phase diagram is reported as a binary temperature-composition diagram.

1.2.3 Surfactant microemulsion behaviour

A microemulsion is defined as a system of water, oil and an amphiphile which is a single optically isotropic and thermodynamically stable liquid solution⁽⁴³⁾. They can be considered, to some extent, small-scale emulsions because they consist of droplet type dispersions either of oil-in-water or water-in-oil with a size range of 5-50 nm in droplet radius⁽⁴⁴⁾. However, as opposed to emulsions, microemulsion droplets form spontaneously. The surfactant will reduce the interfacial tension between the oil and water phases to a sufficiently low level, lowering the energy required to increase the interfacial area. This allows spontaneous dispersion of either water or oil droplets and ensures the system is thermodynamically stable. Microemulsions are typically classified using the notation of Winsor⁽⁴⁵⁾, who identified four general types of phase equilibria: Type I, Type II, Type III and Type IV. The first three are shown in Figure 1.6.

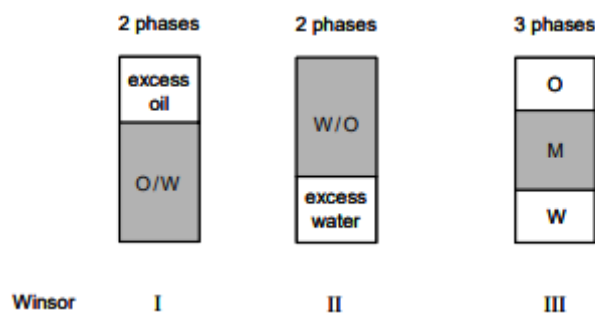


Figure 1.6 Winsor classification of microemulsions. Taken from⁽⁴⁴⁾

In Type I microemulsions, the surfactant is preferentially soluble in water and oil-in-water microemulsions form. The surfactant-rich phase co-exists with the oil phase where the surfactant is only present as monomers at small concentration. In Type II microemulsions the surfactant is mainly in the oil phase and water-in-oil microemulsions form. The surfactant-rich oil phase coexists with the surfactant-poor water phase. In Type III microemulsions a three-phase system is present where a surfactant-rich middle phase co-exists with both excess water and oil phases where the surfactant is present at low concentrations. In Type IV microemulsions a single-phase isotropic micellar solution is present that forms upon addition of sufficient quantity of amphiphiles. As with aqueous systems, the surfactant type and structure will determine the microemulsion formation. The packing parameter P_c ⁽⁴⁰⁾ can also be used to predict microemulsion type by comparing the relative areas of the headgroup (a_0) and the tail group (v/l_c). For example, double tail ionic surfactants such as AOT, where $a_0 < v/l_c$ will preferentially stabilise water-oil microemulsions without the need for co-surfactants⁽⁴⁶⁾.

The phase behaviour of microemulsions depends on the pressure, temperature as well as the nature and concentration of the components. As with binary systems, the determination of phase diagrams and location of the different structures is very important when characterising a system. Several types of phase diagram can be created depending on the number of variables involved⁽³⁹⁾. If the temperature and pressure are held constant, the ternary phase diagram of a three-component microemulsion can be divided into two or four regions and is represented by a triangle as shown in Figure 1.7:

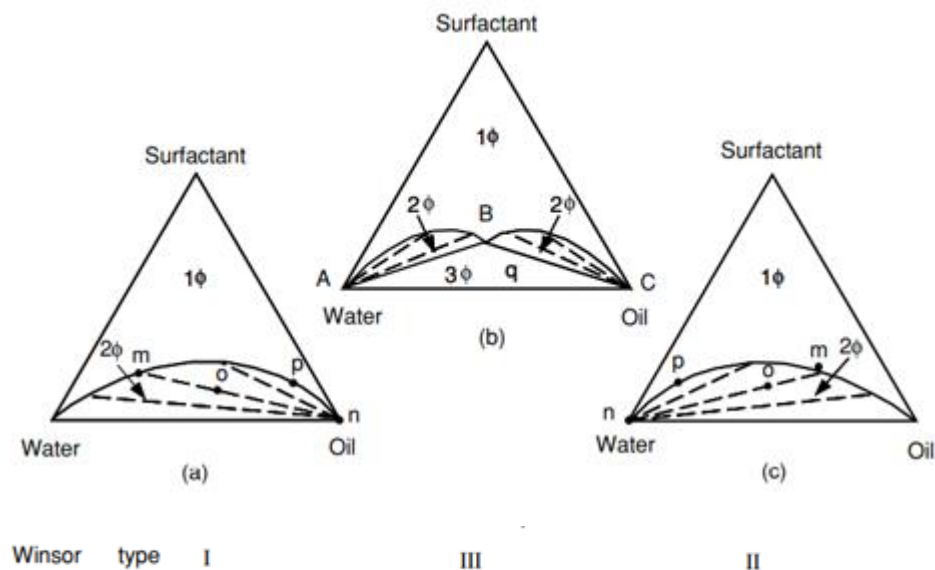


Figure 1.7 Ternary diagram representations of two- and three-phase regions formed by simple water-oil-surfactant systems at constant temperature and pressure. Taken from ⁽⁴⁴⁾

Every composition point within the single phase region above the demixing line corresponds to a microemulsion. Composition points below this line refer to multi-phase regions containing general microemulsions in equilibrium with either an aqueous or organic phase, or both, corresponding to Winsor systems. Any system with composition lying within the two-phase region (e.g. point o in (a) and (c) of Figure 1.7) will exist as two phases whose compositions are represented by the ends of 'the tie-line' (points m and n in the case of point o). Every point on a tie line will have the identical corresponding phases m and n but of different relative volumes. When these two conjugate phases have the same relative volume, this is called the plait (or critical point) p.

1.2.4 Environmental aspects of surfactants

There are four potential factors that can be considered to describe the environmental profile of a surfactant: the biodegradability, aquatic toxicity, the bioaccumulation, and the source of the surfactant raw material. The latter factor can be described in two ways: surfactants synthesised via a renewable route are termed 'bio-based' or 'green' surfactants. Raw materials are from plant-based triglycerides, such as palm, coconut, soy bean, sunflower and rapeseed ⁽⁴⁷⁾. The other, more common type of raw materials are derived from petroleum, for example ethylene obtained from naphtha cracking. There is no guarantee however that a green surfactant will necessarily be non-toxic or biodegrade readily, the preference for these mostly lies in the lower CO₂ emissions related to production. Indeed, green surfactants can also be viewed more preferably by domestic product customers ⁽⁴⁷⁾.

Most surfactants will be sent to a wastewater treatment plant after use, where the surfactant concentration in the water is reduced by a process called biodegradation. Microorganisms are employed to treat the surfactants by biological action, which can involve metabolism of the complex organic substances, converting them to less complex structures via a series of enzymatic reactions ⁽³⁹⁾. The products of these reactions vary depending on whether it is performed under aerobic or anaerobic conditions. In the former case CO₂, water and biomass are produced. On the other hand, anaerobic reactions can proceed through a variety of routes. A substance that will not biodegrade readily in the environment will persist, resulting in concerns about pollution.

Biodegradability of a surfactant can be classified in two ways: primary degradation, which results in the loss of surface activity, and ultimate degradation, defined as the level of degradation achieved when the test compound is totally utilised by microorganisms. The latter can be measured via the closed bottle test. Two bottles are used to which a small amount of sludge has been added. The surfactant to be tested is added into one of the bottles and the difference in amount of CO₂ gas evolved in the bottles is recorded as a function of time. If 60 % of the theoretical amount of CO₂ evolves within 28 days under aerobic conditions, it is considered readily biodegradable according to OECD standards ⁽⁴⁸⁾.

The surfactant tail structure is reported to influence biodegradability, however the relationship is still not understood well. A common case study considered is that of linear alkylbenzene sulphonate surfactants which replaced their branched isomers as it was discovered that the latter did not biodegrade readily ⁽³⁹⁾. However, an emerging view is that the biodegradability is likely to be more determined by the enzyme in question ⁽⁴⁹⁾. To improve biodegradability a cleaveable bond can be incorporated in the surfactant structure. This bond consists of a group that is susceptible to enzymatic hydrolysis, for example an ester bond is catalysed by lipases ⁽⁵⁰⁾. Particular branching patterns have been found to be less harmful than others, for example it is claimed that positioning of the branched groups can affect whether or not the resultant surfactant is more biodegradable or not ⁽³⁹⁾.

The aquatic toxicity of a surfactant relates to the dose that enacts a certain effect on a target organism. The effect can range from death, in which case the metric is the lethal dose, or an inactivation of a function of the species, for example the reproduction rate ⁽⁵¹⁾ termed the effective dose. The organisms studied in toxicity tests can include fish, algae and daphnia ⁽⁵²⁾. Typically, a surfactant is considered environmentally benign if the toxic dose is above 10 mg L⁻¹ after 96 hours testing on fish and 48 hours testing on algae or daphnia ⁽⁵³⁾. Toxic compounds are usually defined as those with values below 1 mg L⁻¹ ⁽⁵⁴⁾.

For a homologous series of surfactants there exists a correlation between aquatic toxicity and the expression $\Delta G_{ads}^0/A_{min}$, where ΔG_{ads}^0 is the Gibbs free energy of adsorption of the surfactant and A_{min} is the minimum area the surfactant occupies when adsorbed at a surface ⁽³⁹⁾. Surfactants adsorb at cell membranes due to their amphiphilic nature, affecting their function due to the presence of xenobiotics ⁽⁵⁵⁾. So, a surfactant with a strong driving force for adsorption (high ΔG_{ads}^0) and that packs tightly at an interface (low A_{min}) will be toxic to aquatic organisms. Therefore, the more efficiently the surfactant packs at an interface, the higher the aquatic toxicity will be. It is noted however that attempts to create structure-toxicity relationships are still in early stages, with issues arising due to limited data, wide variation in readings across different testing sites, and technical difficulties associated with analytical measurements ⁽⁵⁾.

The bioaccumulation of a surfactant refers to how it accumulates in a living organism over time. It is commonly assumed that most surfactants have enough water solubility not to accumulate in lipid compartments of living organisms. The exceptions to this rule include certain hydrophobic fluorocarbon and silicone surfactants as well as regular hydrocarbon surfactants with exceptionally strongly hydrophobic tails and weak polar headgroups ⁽³⁹⁾. Bioaccumulation is commonly determined using a partitioning experiment. The most common procedure is to use octanol and water, and the logarithm of the partition coefficient, $\log K_{ow}$ is calculated. A surfactant is considered to be bioaccumulate if $\log K_{ow} > 3$ ⁽⁵⁶⁾. There are concerns recently about the applicability of $\log K_{ow}$ methods that they have not been fully validated for surfactants and they may not be applicable for due to surfactant phase behaviour ⁽⁵⁷⁾. Hodges et al. recommended in their report that new alternative experimental methods should be sought to avoid these issues ⁽⁵⁷⁾.

It is a common practice to use a matrix, such as in Figure 1.8, where the biodegradability is on one axis and the aquatic toxicity on the other. This allows definition of the minimum criteria for desired properties of new surfactants.

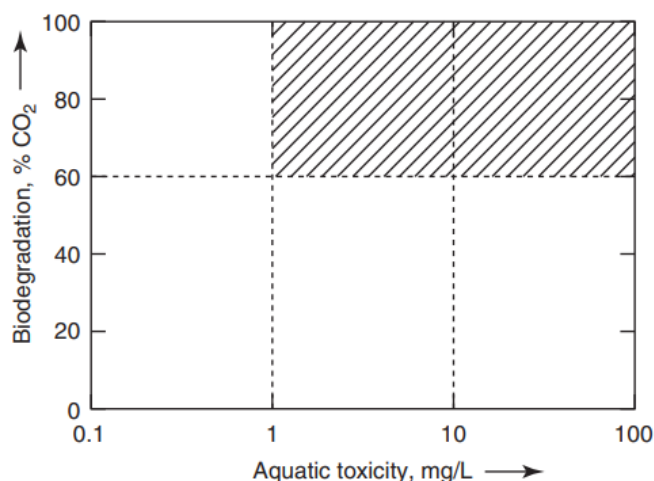


Figure 1.8 Example of a matrix showing the environmental impact of surfactants. An approved surfactant should lie in the dashed areas. Taken from ⁽³⁹⁾

1.3 Research objectives

The specific objectives of this thesis are:

1. Create a SAFT force field for the AOT-water system that is accurate and can capture the underlying physics, as this does not currently exist. The surfactant AOT has been found in an experimental study to be toxic toward aquatic organisms ⁽⁵²⁾. A model that can capture the underlying physics could be used to evaluate the performance of less toxic AOT-derived surfactants. The phase diagram for this system is well established ⁽⁵⁸⁾ and provides target data to reproduce for the SAFT model.
2. By establishing the AOT-water interactions, this will give more confidence to study the more complex ternary system AOT-water-cyclohexane. This system is well-characterised, and this section will assess the ability of the SAFT force fields to study microemulsions at ambient conditions. In particular the phase diagram ⁽⁵⁹⁾ and effect of water contents on reverse micelle morphology ⁽¹¹⁾ will be investigated.
3. Once this SAFT MD methodology has been validated for microemulsions, it can be applied to another industrially relevant ternary system, AOTSiC-water-supercritical CO₂ ⁽³³⁾. This will assess the ability of SAFT force fields to study microemulsions at high pressure. Whilst toxicity data could not be found for AOTSiC, it has been considered in the replacement of fluorinated surfactants which are associated with high costs and negative environmental impacts ⁽⁶⁰⁾. The ability of the model to reproduce the reported phase behaviour ⁽³³⁾ will be assessed.
4. The method can then be used to study the effect of varying the AOTSiC structure on the effectiveness of stabilising water-in-supercritical CO₂ microemulsions. This could lead to the discovery of effective non-fluorinated CO₂-philic surfactants.

1.4 Thesis outline

The layout of the thesis is organised as such: first a background of the methodology is given in Chapter 2. The molecular simulation methods are covered, including intermolecular force fields, and how they are linked to macroscopic properties via statistical mechanics. The different simulation ensembles are then described, followed by an overview of the SAFT theory and in particular the M&M correlation used to find most of the force field parameters. The various analysis methods are described afterwards, including the surface tension, nematic phase order parameter and relative shape anisotropy. A discussion on coarse-graining techniques then follows, highlighting the advantages of using equation-of-state theory to obtain force field parameters in a top-down way. The following chapters cover the development of the MD simulation method and its application to industrial microemulsion

systems, in Chapter 3 the outcomes of objective 1 are presented, namely the development of the SAFT force field for the AOT-water system, including the simulation of pure ester vapour-liquid equilibria and binary ester-water liquid-liquid equilibria. The resultant force fields are then combined with existing force fields in a heteronuclear fashion to simulate the aqueous surfactant mixtures and the simulation results are compared to both phase diagram and bilayer properties to assess how well they match. The results of objective 2 are reported in Chapter 4: the AOT-water-cyclohexane SAFT model predictions are compared to the experimental ternary phase diagram and reverse micelle properties. It is then used to study the effect of water content on the microemulsion properties at the molecular scale, allowing for a comparison to be made with current experimental understanding. The main conclusions of the thesis and recommended future work are presented in Chapter 5. In Chapter 6 the preliminary progress achieved with objectives 3 and 4 are given: the established methodology is used to create a SAFT model that can be used to study surfactant structure effects on the effectiveness of stabilising water-in-supercritical CO₂ microemulsions, as well as the future work required to develop it as a surfactant screening method.

Chapter 2 Methodology

2.1 Chapter overview

The purpose of this chapter is to cover the underlying theory behind the various methodologies encountered in this study. To accomplish this, first an overview of molecular simulations is given which highlights the relationship between simulation, theory, and experiment, and then the theory behind molecular simulation methods is described. This is followed by the basics of statistical mechanics, which provides the link between molecular simulation and macroscopic properties. The statistical associating fluid theory (SAFT) provides the route to obtain the force fields in this study, and so a quick history of SAFT and specifically the M&M corresponding states correlation method is covered. The theory behind the various analysis methods is then presented, including the nematic phase order parameter and the relative shape anisotropy. Since coarse-grained (CG) scale simulations are used in this study, this chapter ends with a section covering the philosophy and various CG procedures employed by researchers.

2.2 Molecular simulations and modelling

2.2.1 Intermolecular force fields

The macroscopically observed thermophysical properties of a system are determined by the intermolecular forces between the constituent molecules ⁽⁶¹⁾. In molecular modelling the purpose of a force field, which is a series of mathematical expressions, is to represent a molecule and its interactions with other molecules ⁽⁶²⁾. The development of a model is a prerequisite for any molecular simulation and is usually done by using data obtained from experiment or theory. Experiments are measurements of nature which quantify the behaviour of the system. Assuming they are carried out carefully, experiments are considered free of significant error. Theories are mathematical models of the underlying physics which relates the force field parameters to macroscopic thermodynamic properties. There is a link between these three concepts which is visualised in Figure 2.1:

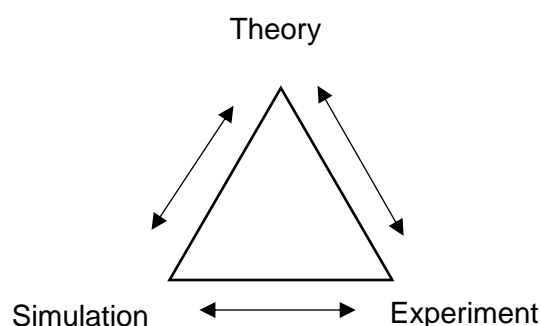


Figure 2.1 The connection between simulation, experiment and theory.

Molecular simulations enable calculation of thermodynamic properties as well as dynamic and structural properties. A molecular model developed from theory can be tested using molecular simulations, and if the theory is accurate the results of both approaches should be consistent. If results from the simulation and theory are not consistent, the theory may not fully capture the underlying physics which can suggest areas for improvement. Simulations can also be used to predict properties not obtainable from the theory, providing further validation of the model by comparison to experiment. Whilst it is possible to fine-tune a molecular model directly to experimental data, this is more time-consuming and expensive due to computational costs of running simulations; it is only a resort when a theoretical approach is not easily available. A simulation with a validated model can then be used to guide experiments, by studying phenomena at the molecular scale experimental phenomena can be interpreted, expanding the research knowledge base.

Understanding the nature of intermolecular force fields is important when interpreting a system's phase behaviour and choosing a molecular model. In simulation methods molecules are described as a set of particles and the Hamiltonian mathematical formulation is used to describe the system ⁽⁶³⁾:

$$H(\mathbf{q}, \mathbf{p}) = K(\mathbf{p}) + V(\mathbf{q}) \quad (2.1)$$

where H is the Hamiltonian of the system, K is the kinetic energy, V is the potential energy, \mathbf{q} is the set of co-ordinates of all particles $i = 1$ to N , and \mathbf{p} is the set of momenta for all particles. Usually, the kinetic energy is evaluated by the following ⁽⁶³⁾:

$$K = \sum_{i=1}^N \sum_{\alpha} \frac{p_{i\alpha}^2}{2m_i} \quad (2.2)$$

where α is an index that includes the different Cartesian (x, y, z) components of momentum p of particle i , m_i is the mass of particle i . It is important to note that equation (2.2) is valid only for point particles, and so does not take into account rotational or vibrational contributions. It is written in this form for illustrative properties. The potential energy V contains information about the intermolecular interactions and is usually the function that must be specified by the user in a molecular simulation. By doing this, the Hamiltonian of the system is fully defined. The full expression of V includes multiple terms including pairs and triplets ⁽⁶³⁾:

$$V = \sum_i U_1(\mathbf{r}_i) + \sum_i \sum_{j>i} U_2(\mathbf{r}_i, \mathbf{r}_j) + \sum_i \sum_{j>i} \sum_{k>j>i} U_3(\mathbf{r}_i, \mathbf{r}_j, \mathbf{r}_k) \quad (2.3)$$

where \mathbf{r}_i is the three-dimensional position of particle i ; i, j, k refer to different particles. No pair is counted twice (i.e. ij and ji), and triplets are treated the same way. U_1 represents the effect of an external field, such as the container walls on the system. The remaining terms represent the particle interactions, where U_2 , the pair potential, is the most important and is dependent on the magnitude of pair separation ⁽⁶³⁾:

$$r_{ij} = |\mathbf{r}_i - \mathbf{r}_j| \quad (2.4)$$

The term U_3 involves triplets of molecules but is only rarely included in computational studies due to it being very time-consuming to compute. It is usually included as average three-body effects in pairwise approximation. This is done by defining an effective pair potential and so equation (2.3) becomes ⁽⁶³⁾:

$$V \approx \sum_i U_1(\mathbf{r}_i) + \sum_i \sum_{j>i} U_{2,eff}(\mathbf{r}_{ij}) \quad (2.5)$$

The above terms model the non-bonded interactions, so termed because they are not associated with the internal bonding of the molecule. These interactions encompass the short-range repulsive, short-range attractive dispersion and electrostatic interactions. The bonded interactions are the ones that constrain the internal structure of the molecule: the bond stretching, bending and torsion. Whilst effective pair potentials are used for the non-bonded

potentials, the bonded potentials can include up to four-body effects. The bonded potentials are usually expressed in terms of a single variable: the bond length, bond angle, or dihedral angle. The total potential energy is then a sum of the bonded and non-bonded terms:

$$V = V_{nb} + V_b \quad (2.6)$$

If the potentials due to an external field are negligible, the non-bonded part of equation (2.6) is then represented as:

$$V_{nb} = \sum_i \sum_{j>i} U_{2,eff}(\mathbf{r}_{ij}) \quad (2.7)$$

There are multiple ways to express the effective pair potentials for the non-bonded interactions and the two-body to four-body bonded potentials. These are described in the remainder of this section.

Non-bonded interactions

The non-bonded interactions describe the force field to capture the short-range repulsive, short-range dispersion and electrostatic interactions between atoms (or CG beads in the case of this study). Common examples of these effective pair potentials are shown in Figure 2.2 and described below ⁽⁶⁴⁾ ⁽⁶⁵⁾.

The Hard-Sphere potential (Figure 2.2a) is described below ⁽⁶⁴⁾:

$$\begin{aligned} U_{HS,ij} &= \infty \text{ if } r_{ij} < \sigma_{ij} \\ U_{HS,ij} &= 0 \text{ if } r_{ij} > \sigma_{ij} \end{aligned} \quad (2.8)$$

where $U_{HS,ij}$ is the non-bonded potential energy between particles i and j . The hard-sphere potential consists of a purely repulsive core of size σ_{ij} . The square-well potential (Figure 2.2b) expands on this by adding a uniform short-range attractive region as shown below: ⁽⁶⁴⁾:

$$\begin{aligned} U_{SW,ij} &= \infty \text{ if } r_{ij} < \sigma_{ij} \\ U_{SW,ij} &= -\varepsilon_{ij} \text{ if } \sigma_{ij} \leq r_{ij} < \lambda_{ij}\sigma_{ij} \\ U_{SW,ij} &= 0 \text{ if } r_{ij} \geq \lambda_{ij}\sigma_{ij} \end{aligned} \quad (2.9)$$

where ε_{ij} is the depth of the square-well and λ_{ij} determines the square-well attractive range relative to σ_{ij} . The discontinuous nature of equations (2.8) and (2.9) makes these potentials difficult to implement in molecular dynamics simulations. As such it is more common to use continuous potentials such as the Mie potential ⁽⁶⁶⁾ (Figure 2.2d) as put forward by Gustav Mie ⁽⁶⁷⁾.

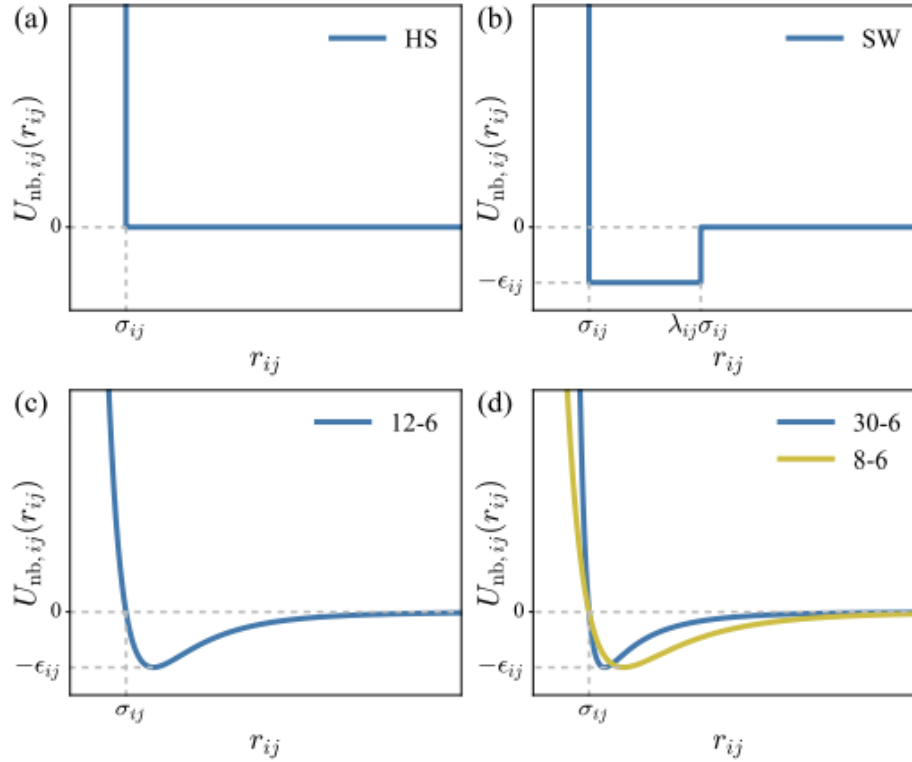


Figure 2.2 Common effective pair potentials used in molecular simulations: (a) the Hard-Sphere (HS), (b) Square-well (SW), (c) Lennard-Jones (LJ) and (d) Mie potentials. Taken from ⁽⁶⁵⁾.

$$U_{Mie,ij} = C_{ij}\epsilon_{ij} \left[\left(\frac{\sigma_{ij}}{r_{ij}} \right)^{\lambda_{ij}^r} - \left(\frac{\sigma_{ij}}{r_{ij}} \right)^{\lambda_{ij}^a} \right] \quad (2.10)$$

where λ_{ij}^r controls the softness/hardness of the sphere, and λ_{ij}^a controls the attractive range. C_{ij} is a parameter that depends on λ_{ij}^r and λ_{ij}^a and is defined as:

$$C_{ij} = \frac{\lambda_{ij}^r}{\lambda_{ij}^r - \lambda_{ij}^a} \left(\frac{\lambda_{ij}^r}{\lambda_{ij}^a} \right)^{\frac{\lambda_{ij}^a}{\lambda_{ij}^r - \lambda_{ij}^a}} \quad (2.11)$$

The value of λ_{ij}^a is typically set at 6 as this gives a good representation of London dispersion forces. Indeed, it was the work of London and Eisenschitz ⁽⁶⁸⁾ which confirmed that, when treated at the quantum mechanical level, the attractive interactions between two non-polar spherical molecules are the result of fluctuating electric dipoles, and give rise to a contribution proportional to r^{-6} . The repulsive exponent value is set to reflect the behaviour of the atom/pair of atoms. Note that if λ_{ij}^r is set to 12, equation (2.10) then becomes the Lennard Jones potential ⁽⁶⁹⁾ (Figure 2.2c).

The potentials described in equations (2.8)-(2.10) represent short-range interactions, and as such are not sufficient to represent long-range interactions which are important when modelling ions. Instead, the approach is to supplement with the Coulomb charge-charge interaction ⁽⁷⁰⁾:

$$U_{Coul,ij}(r_{ij}) = \frac{q_i q_j}{4\pi\epsilon_0\epsilon_r r_{ij}} \quad (2.12)$$

where q_i and q_j are charges on particles i and j respectively. By definition $q = ze$ where z is the ionic valence and e is the elementary charge. ϵ_0 is the permittivity of free space, and ϵ_r is the dielectric constant of the medium. In this work, only the electrostatic contribution of the solvent intermolecular potential is treated implicitly. Mie potentials are used to represent the remaining intermolecular interactions. The total non-bonded potential energy for a Mie fluid with point charges can then be described using the following:

$$V_{nb} = \sum_i \sum_{j>i} \left(\frac{q_i q_j}{4\pi\epsilon_0\epsilon_r r_{ij}} + C_{ij}\epsilon_{ij} \left[\left(\frac{\sigma_{ij}}{r_{ij}} \right)^{\lambda_{ij}^r} - \left(\frac{\sigma_{ij}}{r_{ij}} \right)^{\lambda_{ij}^a} \right] \right) \quad (2.13)$$

Bonded interactions

The bonded interactions refer to those of an atom (or CG bead in this study) in a molecule with its closest neighbours (up to three bonds apart) that constrain the internal structure of the molecule. The bonded terms include two-body bond stretching (as a function of inter-particle distance r), three-body bond bending (as a function of the bond angle θ), and four-body torsion (as a function of dihedral angle ϕ), as shown in Figure 2.3.

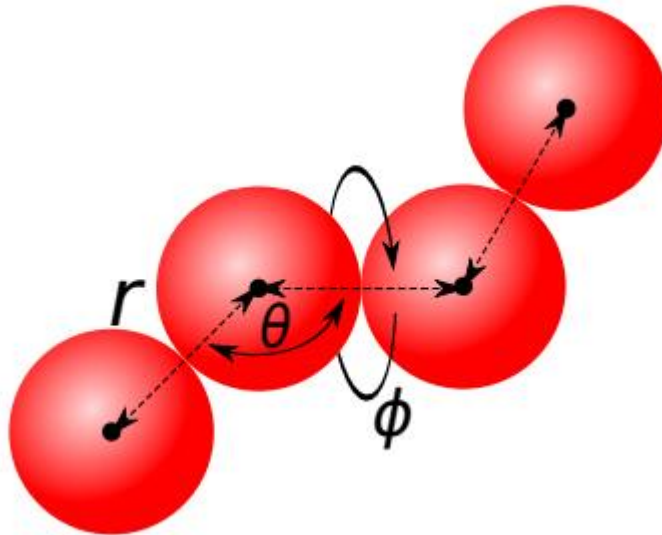


Figure 2.3 Illustration of the types of bonded interactions. Taken from ⁽⁶⁵⁾.

The relative energy (or stiffness) of different types of bonded interactions ⁽⁷¹⁾ is shown below:

$$U_{bond,ij} > U_{angle,ijk} > U_{dihedral,ijkl} \quad (2.14)$$

where $U_{bond,ij}$ is the bond stretching potential, $U_{angle,ijk}$ is the bond bending potential and $U_{dihedral,ijkl}$ is the torsion potential. The bond stretching is typically the most rigid and the torsion is the most flexible of the terms. There are a variety of functional forms to represent bonded terms. In this work the bond stretching is approximated using a harmonic potential:

$$U_{bond,ij}(r_{ij}) = \frac{k_{bond,ij}}{2} (r_{ij} - r_{0,ij})^2 \quad (2.15)$$

where $k_{bond,ij}$ is the bond constant and $r_{0,ij}$ is the equilibrium bond length. The bond bending is approximated as a harmonic oscillator, but as a function of the bond angle θ_{ijk} :

$$U_{angle,ijk}(\theta_{ijk}) = \frac{k_{angle,ijk}}{2} (\theta_{ijk} - \theta_{0,ijk})^2 \quad (2.16)$$

where $k_{angle,ijk}$ is the angle constant, θ_{ijk} is the angle between particles i , j and k , and $\theta_{0,ijk}$ is the equilibrium bond angle. In this work the dihedral potential is approximated using a periodic function:

$$U_{dihedral,ijkl}(\phi) = k_{dihedral,ijkl} (1 + \cos(n\phi_{ijkl} - \phi_{0,ijkl})) \quad (2.17)$$

where $k_{dihedral,ijkl}$ is the dihedral angle constant, ϕ_{ijkl} is the dihedral angle between particles i , j , k , l , $\phi_{0,ijkl}$ is the equilibrium dihedral angle, and n is the multiplicity. The total potential energy contribution due to the bonded interactions is then the sum of the individual two-body, three-body, and four-body interactions:

$$V_b = \sum_{i,j \in I_{bonds}} \frac{k_{bond,ij}}{2} (r_{ij} - r_{0,ij})^2 + \sum_{i,j,k \in I_{angles}} \frac{k_{angle,ijk}}{2} (\theta_{ijk} - \theta_{0,ijk})^2 + \sum_{i,j,k,l \in I_{dihedrals}} k_{dihedral,ijkl} (1 + \cos(n\phi_{ijkl} - \phi_{0,ijkl})) \quad (2.18)$$

where I_{bonds} is the set of all pairs of ij involved in the bonds, I_{angles} is the set of all triplets of ijk involved in the bond angles, and $I_{dihedrals}$ is the set of all quartets of $ijkl$ involved in the dihedral angles. The MD simulation code Gromacs 2019.2⁽⁷²⁾ is used in this study, where the above bonded potentials, equations (2.15)-(2.17) are all available.

2.2.2 Statistical mechanics

An output of molecular simulations is the calculation of the intermolecular potential using the equations listed in section 2.2.1. This gives information of the system at the microscopic level e.g. positions and momenta. In this work the macroscopic description of the system, for example the pressure and temperature, is of interest. This can be obtained by using the concepts of statistical mechanics, as developed by Gibbs, Maxwell, and Boltzmann. These principles are covered in the work of Frenkel and Smit⁽⁷³⁾. Statistical mechanics is the bridge

between intermolecular potentials calculated by molecular simulation and the macroscopic properties that are measured in experiments.

Core to the understanding of statistical mechanics is the concept of the 'ensemble' ⁽⁷³⁾. This is defined as a virtual collection of systems, each one under the same thermodynamic conditions, yet not necessarily the same microscopic properties. The Ergodic hypothesis postulates that a system in thermodynamic equilibrium has visited all the accessible micro-states. Under this assumption, the average of a property X_{micro} over a big number of systems (an ensemble) with all the possible micro-states is identical to the time average \bar{X}_{micro} ⁽⁷³⁾:

$$\langle X_{micro} \rangle = \bar{X}_{micro} \quad (2.19)$$

where the angular brackets represent an ensemble average, and the horizontal upper line represents a time average.

For an isolated system, one that does not exchange heat or material with its surroundings, statistical mechanics also postulates that there is no information to consider any of the micro-states to be more important than any other, so the ensemble can be restricted to follow the principle of equal a priori probabilities. This implies the system can be found in any one of its micro-states with the same probability.

The type of ensemble is differentiated by the thermodynamic conditions that are kept constant. If the number of molecules N , the volume of the system V and the total energy E are chosen then the ensemble is a microcanonical one. The canonical ensemble is described by constant N , V and temperature T . The isobaric-isothermal ensemble is described by constant N , pressure P , and T .

The bridge to macroscopic properties is established by postulating that the average mechanical property corresponds to an average thermodynamic property. For a given ensemble, the average mechanical property M is defined ⁽⁷³⁾ as:

$$\langle M \rangle = \sum_i M_i P_i \quad (2.20)$$

Where P_i is the probability that a system is in the i th micro state, given as the fraction of members of the ensemble in the i th state. The entropy of the system S from this point of view is defined ⁽⁷³⁾ as:

$$S \equiv -k_B \sum_i P_i \ln P_i \quad (2.21)$$

where k_B is the Boltzmann constant. Explicit expressions for the probability can be obtained by entropy maximisation subject to the constraints in each ensemble using the Lagrange method with non-linear constraints. This probability can be written in terms of the partition function, which is expressed differently for each ensemble ⁽⁷³⁾. In practice, thermodynamic potentials and the mechanical properties derived from them are given in terms of the partition function. The expressions for the canonical and isothermal-isobaric ensembles are given in Sections 2.2.3 and 2.2.4 respectively, as these were the ensembles used in this study.

2.2.3 NVT ensemble

If the number of states is large enough, the partition function in the canonical ensemble $Q(N, V, T)$ can be written in continuous variables as a function of the particles positions \mathbf{r}^N ⁽⁷³⁾:

$$Q(N, V, T) = \frac{1}{\Lambda^{3N} N!} \int d\mathbf{r}^N \exp[-\beta U(\mathbf{r}^N)] \quad (2.22)$$

where $\Lambda = \sqrt{h^2 / (2\pi m k_B T)}$ is the thermal de Broglie wavelength, h is Planck's constant, m is the mass of a particle, β is defined as $\frac{1}{k_B T}$, and $U(\mathbf{r}^N)$ is the potential energy of the system.

In equation (2.22), the $\frac{1}{\Lambda^{3N} N!}$ term accounts for the ideal gas contribution, this is the energy distribution due to absence of interactions i.e translational, rotational and vibrational contributions. The remaining integral takes into account the presence of interactions in the system. The average mechanical property can then be represented as:

$$\langle M \rangle = \int d\mathbf{r}^N M(\mathbf{r}^N) \rho_{NVT}(\mathbf{r}^N) \quad (2.23)$$

where ρ_{NVT} is the probability density of the NVT ensemble, and is defined as:

$$\rho_{NVT} = \frac{\exp[-\beta U(\mathbf{r}^N)]}{\int d\mathbf{r}^N \exp[-\beta U(\mathbf{r}^N)]} \quad (2.24)$$

The entropy in the NVT ensemble is defined in terms of $Q = Q(N, V, T)$ as:

$$S = k_B \ln Q + k_B T \left(\frac{\partial \ln Q}{\partial T} \right)_{N,V} \quad (2.25)$$

The Helmholtz free energy $A(N, V, T)$ is the potential whose natural independent variables are those of the canonical ensemble, and is proportional to $\ln Q$:

$$A = -k_B T \ln Q \quad (2.26)$$

This represents the connection between thermodynamics and the canonical partition function. From the purely thermodynamic relation ⁽⁷⁴⁾:

$$dA = -SdT - PdV + \mu dN \quad (2.27)$$

it is possible to obtain the thermodynamic properties, including pressure, chemical potential and internal energy ⁽⁷⁴⁾ as described in equations (2.28)-(2.30):

$$P = k_B T \left(\frac{\partial \ln Q}{\partial V} \right)_{N,T} \quad (2.28)$$

$$\mu = -k_B T \left(\frac{\partial \ln Q}{\partial N} \right)_{V,T} \quad (2.29)$$

$$U = k_B T^2 \left(\frac{\partial \ln Q}{\partial T} \right)_{N,V} \quad (2.30)$$

2.2.4 NPT ensemble

The isothermal-isotropic ensemble is characterised by the partition function $\Delta(N, P, T)$ ⁽⁷³⁾:

$$\Delta(N, P, T) = \frac{\beta P}{\Lambda^{3N} N!} \int dV V^N \exp(-\beta P V) \int ds^N \exp[-\beta U(\mathbf{s}^N, L)] \quad (2.31)$$

where the positions are scaled as $\mathbf{s} = \mathbf{r}/L$, where $V = L^3$ assuming a cubic system. The average of a variable M :

$$\langle M \rangle = \int d\mathbf{s}^N M(\mathbf{s}^N, L) \rho_{NPT}(\mathbf{s}^N, V) \quad (2.32)$$

where ρ_{NPT} is the probability density of the NPT ensemble expressed as:

$$\rho_{NPT} = \frac{V^N \exp\{-\beta[U(\mathbf{s}^N, V) + PV]\}}{\int dV V^N \exp(-\beta P V) \int d\mathbf{s}^N \exp[-\beta U(\mathbf{s}^N, L)]} \quad (2.33)$$

The entropy in the NPT ensemble in terms of $\Delta = \Delta(N, P, T)$ is defined as:

$$S = k_B \ln \Delta + k_B T \left(\frac{\partial \ln \Delta}{\partial T} \right)_{N,P} \quad (2.34)$$

The Gibbs free energy $G(N, P, T)$ is the potential whose natural independent variables are those of the NPT ensemble, and is proportional to $\ln \Delta$:

$$G = -k_B T \ln \Delta \quad (2.35)$$

This is the connection between thermodynamics and the isothermal-isobaric partition function. From the purely thermodynamic relation ⁽⁷⁴⁾:

$$dG = -SdT + VdP + \mu dN \quad (2.36)$$

The volume and chemical potential of the system can then be obtained from ⁽⁷⁴⁾ equations (2.37) and (2.38) respectively:

$$V = -k_B T \left(\frac{\partial \ln \Delta}{\partial P} \right)_{N,T} \quad (2.37)$$

$$\mu = -k_B T \left(\frac{\partial \ln \Delta}{\partial N} \right)_{P,T} \quad (2.38)$$

2.2.5 Molecular simulations

The background to molecular simulations has been covered from sections 2.2.1 to 2.2.4, and in this section the more practical elements are described. In the application of molecular simulations, a series of molecular configurations are generated under constant conditions such as temperature, pressure or total number of molecules, which are known as ‘ensembles’. The average properties of this ensemble are then calculated. There are two techniques associated with molecular simulations: Molecular Dynamics (MD) and Monte Carlo (MC). Both methods originated in the 1950s⁽⁷³⁾ ⁽⁶²⁾, and in both techniques the configuration space is sampled to observe molecular behaviour and calculation of average properties. As is the case in experiments, molecular simulation data contains statistical uncertainties and require time to equilibrate when starting from an initial metastable configuration⁽⁶²⁾. In the MC method new configurations are generated from a starting configuration using probabilistic rules⁽⁷³⁾. Unlike MD, there is no concept of time so dynamical properties cannot be calculated. It is for this reason MD techniques are used in this study. In MD Newton’s Equations of Motion are numerically solved with specified particle interactions and at set conditions⁽⁶³⁾:

$$\mathbf{r}_i = \mathbf{r}_i(t) \quad (2.39)$$

$$\mathbf{v}_i = \frac{d\mathbf{r}_i}{dt} \quad (2.40)$$

$$\mathbf{F}_i = m_i \mathbf{a}_i = m_i \frac{d^2 \mathbf{r}_i}{dt^2} = -\nabla_{\mathbf{r}_i} V(\mathbf{r}^N) \quad (2.41)$$

where \mathbf{F}_i is the force vector acting on particle i , \mathbf{v}_i is the velocity vector of particle i , m_i is the mass of particle i , and \mathbf{a}_i is the acceleration vector of particle i . It should be noted that equations (2.39)-(2.41) are valid for point particles only. It is written this way for illustrative purposes. The simulation can start from a random or ordered configuration, where a configuration close to the equilibrated state is preferable. The initial particle velocities are usually assigned by a Maxwell-Boltzmann distribution set at the desired temperature. The equations of motion are solved numerically using finite difference methods: a small step δt is used which is usually of the order 0.001-0.01 ps, dependent on the force field used⁽⁶²⁾. In this work the numerical algorithm used is the leap-frog algorithm⁽⁷⁵⁾, which is described below⁽⁷³⁾:

$$\mathbf{r}_i(t + \delta t) = \mathbf{r}_i(t) + \mathbf{v}_i \left(t + \frac{1}{2} \delta t \right) \delta t \quad (2.42)$$

$$\mathbf{v}_i(t + \delta t) = \mathbf{v}_i \left(t - \frac{1}{2} \delta t \right) + \mathbf{a}_i(t) \delta t \quad (2.43)$$

where \mathbf{a}_i is obtained by evaluating equation (2.41), knowing that the forces are the derivative of the potential energy. The velocity at time t is expressed as:

$$\mathbf{v}_i(t) = \frac{\mathbf{v}_i\left(t + \frac{1}{2}\delta t\right) + \mathbf{v}_i\left(t - \frac{1}{2}\delta t\right)}{2} \quad (2.44)$$

In a molecular simulation, a few computational techniques are employed to deal with the practical issues of running a simulation program. The first refers to the use of periodic boundary conditions, where the simulation box is replicated throughout space to form an infinite lattice. As a molecule moves in the original box, its periodic image in each of the neighbouring boxes moves in the same way. As a molecule leaves one box, its periodic image will enter through the opposite side. There are no walls at the boundary of the box and no surface molecules. This mimics the presence of an infinite bulk surrounding the system of interest, without having to resort to system sizes that are unpractically large⁽⁶²⁾. It is important to note that the simulation box must be a specific size, as the periodic boundary conditions may artificially stabilise certain phase behaviour leading to results not representative of bulk phase behaviour⁽⁶³⁾.

It is the knowledge of all the velocities and positions in the system that allows the Hamiltonian to be evaluated, and subsequently the properties of the system. The evaluation of the forces from the potential is the most computationally expensive step. If one considers the force calculation of a single molecule in a N molecule system, one will need to include the interactions between this molecule and every other molecule in the system. The summation would include $(N-1)$ terms, but when taking into account all the interactions between this molecule and its periodic images in the surrounding boxes this results in an infinite number of terms, and the calculation becomes impractical. In practice, this summation is restricted by making the minimum image convention approximation⁽⁷³⁾. This states that if a single molecule lies at the centre of a region with same size and shape as the basic simulation box, then it interacts with all molecules whose centres lie within this region, including the closest periodic images of the $(N - 1)$ molecules.

Even with the minimum image convention, the calculation of potential energy due to pairwise-additive interactions involves $\frac{1}{2} N (N - 1)$ terms, which is still a very substantial calculation for systems of even 1000 particles. To improve this situation, a molecular cut-off radius is implemented⁽⁷³⁾. The largest contribution to the potential energy and force comes from neighbours close to the molecule of interest. For short-range forces a spherical cut-off is normally applied where the $U(r)$ is equal to 0 when r is greater than r_c , hence all interaction beyond the cut-off is ignored. The cut-off must be no greater than $\frac{1}{2}$ the simulation box length to ensure consistency with the minimum image convention⁽⁶²⁾.

As mentioned in Section 2.2.1, a Coulombic expression, equation (2.12), is used in molecular simulations to model long range ionic interactions. The long-range nature means these interactions decay very slowly with distance as r^{-1} . This adds two complications to the calculation of non-bonded interactions. First, to calculate all Coulomb interactions over a periodic system results in needing to compute a sum which is conditionally convergent⁽⁷⁶⁾. This means the value of the sum depends on the order in which it is evaluated, otherwise the result will be ambiguous. The second issue is that determining pairwise distances is an expensive computation that grows with the square of the number of atoms involved, despite the importance of long-range interactions. A simple truncation at a particular cut-off radius cannot be applied to electrostatic interactions, as this neglects long-range interaction and can create artificial boundary problems⁽⁶³⁾. In this work the Particle Mesh Ewald (PME) method⁽⁷⁷⁾ is used to handle long-range electrostatic interactions. In this method the charges are

interpolated onto a grid, then a Fast Fourier Transform is used to convert the charges on the grid to their equivalent Fourier space structure factors. The reciprocal space potential is calculated by solving the Poisson equation in Fourier space:

$$\nabla^2 \phi(\mathbf{x}) = -\frac{1}{\epsilon_r} \rho(\mathbf{x}) \quad (2.45)$$

where $\phi(\mathbf{x})$ is the potential at point \mathbf{x} , and $\rho(\mathbf{x})$ is the charge density at point \mathbf{x} . The reciprocal space potential is then stored on the grid. An inverse Fast Fourier Transform is used to convert the reciprocal space potential back to the real space. The force is then calculated from the gradient of the potential. The PME algorithm computational cost increases with $N \log N$, where N is the number of charge sites. This makes it suitable for medium to large systems ⁽⁷²⁾. In these methods a cut-off is still applied, except in this case it relates only to direct space calculations. It is typically kept at the same value as the short-range cut-off ⁽⁶²⁾. The grid dimensions can be specified by the user, where a finer grid can improve accuracy but increase simulation time. Despite this it is usually recommended to use default settings, and only deviate after extensive performance testing ⁽⁶²⁾.

In this work the Gromacs 2019.2 ⁽⁷²⁾ simulation package is used for all simulations. During the simulation, the state variables of the desired ensemble must be maintained at the specified values in a manner that correctly samples the ensemble by capturing the underlying physics. The NVT and NPT ensembles are the ones studied using MD simulations in this work. Variables such as the particle number N and the volume V are trivial to constrain, but variables such as temperature and pressure must be controlled dynamically because they are dependent on the interactions between the system and the surroundings. It is also non-trivial to set the initial velocities and positions to produce a particular temperature or pressure. This necessitates the use of a thermostat and barostat, not to just maintain the desired temperature and pressure, but to bring the system to these desired conditions at the beginning of the simulation. The time necessary to bring the system from its metastable initial state to a stable state is called the equilibration period. In this work, the V-rescale ⁽⁷⁸⁾ ⁽⁷⁹⁾ thermostat is used in the first simulation where the initial configuration is random, to relax the system and assign velocities. This thermostat brings the system to the desired temperature by rescaling the particle velocities to ensure a correct kinetic energy distribution:

$$dK = (K_0 - K) \frac{dt}{\tau_T} + 2 \sqrt{\frac{KK_0}{N_f}} \frac{dW}{\sqrt{\tau_T}} \quad (2.46)$$

where K is the kinetic energy, K_0 the kinetic energy corresponding to the set temperature, t is the time, τ_T is the temperature coupling time constant, N_f is the number of degrees of freedom, and dW is a Wiener process. The Nosé-Hoover ⁽⁸⁰⁾ ⁽⁸¹⁾ thermostat is then used for the rest of the equilibration and then the production run. This thermostat extends the system Hamiltonian by adding a thermal reservoir and a friction term in the equations of motion. The friction force is proportional to the product of each particle's velocity and a friction parameter ξ . This friction parameter can be referred to as the heat bath parameter and is a fully dynamic quantity with its own momentum (p_ξ) and equation of motion. The particle equation of motion is then expressed as:

$$\mathbf{F}_i = m_i \left(\frac{d^2 \mathbf{r}_i}{dt^2} + \frac{p_\xi}{B} \frac{d\mathbf{r}_i}{dt} \right) \quad (2.47)$$

where the equation of motion for the heat bath parameter ξ is expressed as:

$$\frac{dp_\xi}{dt} = (T - T_0) \quad (2.48)$$

where T_0 is the reference temperature, T is the instantaneous temperature and B is the mass parameter of the reservoir which is used to determine the strength of the temperature coupling. In practice, a more intuitive way is to specify τ_T which describes the period of oscillations of kinetic energy between the system and the reservoir. Unlike B , it is not dependent on system size and temperature either. It is directly related to B and T_0 :

$$B = \frac{\tau_T^2 T_0}{4\pi^2} \quad (2.49)$$

The barostat used for the NPT sampling was Parrinello-Rahman ⁽⁸²⁾ and was implemented after the temperature had been equilibrated in a previous NVT run. This barostat can capture the true NPT ensemble and works in a similar fashion to the Nosé-Hoover thermostat. The simulation box vectors as represented by a matrix obeying the matrix equation of motion:

$$\frac{d\mathbf{b}^2}{dt^2} = V\mathbf{W}^{-1}\mathbf{b}'^{-1}(\mathbf{P} - \mathbf{P}_{ref}) \quad (2.50)$$

where V is the box volume, \mathbf{W} is a matrix parameter that determines the strength of the coupling, \mathbf{b} is a matrix that represents the three basis vectors of the periodic box. The matrix \mathbf{P}_{ref} refers to the reference pressure, and the other matrices are at the instantaneous pressure. The particle equation of motion is then expressed as:

$$\mathbf{F}_i = m_i \left(\frac{d^2 \mathbf{r}_i}{dt^2} + \mathbf{M} \frac{d\mathbf{r}_i}{dt} \right) \quad (2.51)$$

$$\mathbf{M} = \mathbf{b}^{-1} \left[\mathbf{b} \frac{d\mathbf{b}'}{dt} + \frac{d\mathbf{b}}{dt} \mathbf{b}' \right] \mathbf{b}'^{-1} \quad (2.52)$$

The extra term is an effect of the Parrinello-Rahman equations of motion being defined with all particle co-ordinates represented relative to the box vectors. The inverse mass parameter matrix determines the strength of the coupling and how the box can be deformed:

$$(\mathbf{W}^{-1})_{ij} = \frac{4\pi^2 \beta_{ij}}{3\tau_P^2 L} \quad (2.53)$$

where β is the isothermal compressibility which in most cases will be a diagonal matrix with equal elements across the diagonal, the value of which is usually not known. It is common to use the value for water at 300 K and 1 atm so that $\beta = 4.6 \times 10^{-5} \text{ bar}^{-1}$ ⁽⁷²⁾. L is the largest box matrix element, and τ_p is the pressure time constant. For simplitude, the values of τ_p and β are the necessary inputs. Both isotropic and semi-isotropic NPT simulations are employed in this work. In the latter the pressure coupling is isotropic in the x and y directions, but different in the z direction. Hence two different values of β and τ_p each are required. Another variation used in this work is the isothermal-isobaric constant area ensemble NP_{zz}AT. In this ensemble only the z dimension fluctuates to maintain the target pressure, hence the value of β for the x/y coupling will be equal to zero.

Once the system has equilibrated, the particle positions and momenta reflect the ensemble conditions, allowing collection of meaningful data and ensemble averages to be calculated. Like with experiments, taking averages over longer time periods will improve the accuracy of the results. In this study, the averages are collected over a time period that is equal to the equilibration period to ensure accuracy, i.e. the production simulation run time is twice the time it takes for the simulation to equilibrate.

2.3 Statistical associating fluid theory (SAFT)

2.3.1 A brief history of SAFT

The SAFT equation of state (EoS) is based on the first order thermodynamic perturbation theory (TPT1) proposed by Wertheim ⁽⁸³⁾, who developed TPT1 to model molecules with strongly anisotropic interactions. Thermodynamic perturbation theories are an approximate solution to the physical description of the system. Perturbation theories take the dominant contribution, the reference state, from a simpler system with an exact solution, such as a hard sphere equation of state. Other behaviour is then captured by adding small perturbations, such as attractive interactions. The SAFT EoS is one such perturbation theory and is firmly rooted in statistical mechanics. Development of the SAFT EoS involved performing molecular simulations to verify the theoretical results ⁽¹⁴⁾. The development of SAFT theory can be described in three generations: the first used the purely repulsive hard-sphere model as the reference system ⁽⁸⁴⁾, the second generation looked at adding more realistic reference systems including square-well ⁽⁸⁵⁾, Lennard-Jones ⁽⁸⁶⁾ and Mie potentials ⁽⁸⁷⁾. See section 2.2.1, 'non-bonded interactions', for a description of these potentials. The third generation is distinguished by employing a group-contribution approach with the continuous Mie potential, called SAFT- γ Mie ⁽²⁶⁾. This has expanded the modelling capacity to more complex systems, including refrigerant gases ⁽⁸⁸⁾, fluoroalkanes ⁽⁸⁹⁾ and non-ionic surfactants ⁽⁹⁰⁾. The general form for the SAFT- γ Mie EoS is given in terms of the Helmholtz free energy A ⁽²⁶⁾:

$$\frac{A}{Nk_B T} = \frac{A_{ideal}}{Nk_B T} + \frac{A_{mono}}{Nk_B T} + \frac{A_{chain}}{Nk_B T} + \frac{A_{assoc}}{Nk_B T} \quad (2.54)$$

where A_{ideal} is the free energy contribution from an ideal gas system, A_{mono} refers to the free energy due to the short-range repulsion and dispersion attractive interactions, and A_{chain} refers to the free energy of the monomers bonding into chain molecules. The A_{assoc} term refers to the contribution from short-range anisotropic interactions, for example hydrogen bonding. Force field parameters are estimated to macroscopic properties of the underlying chemicals via the SAFT EoS using an optimisation procedure, for example minimisation of the squares of the residuals via an objective function ⁽⁹¹⁾. This process can be streamlined by expressing the EoS in reduced units ⁽²⁸⁾. This procedure is sometimes light-heartedly referred to as the 'M&M' correlation due to the names of the authors. It is described in the next section.

2.3.2 The M&M correlation

The corresponding states principle postulates that the behaviour of most common fluids may be described in a general way if the variables that describe their thermodynamic states are scaled accordingly. This principle is used in engineering, for example in EoS modelling where the fluid phase properties can be described in terms of the critical properties, such as the critical temperature and the critical pressure ⁽⁹²⁾. This allows for the development of EoS that can be applied to multiple fluids.

The SAFT formalism permits the modelling of chain fluids as a series of tangentially bonded spherical segments. This introduces another parameter, m , which quantifies the number of segments in a chain molecule ⁽²⁴⁾. The first step of the M&M correlation is to decide the number of CG beads per molecule m , dependent on the desired level of representation. It should be noted that in the SAFT formalism m can be a non-integer, but in CG modelling it is constrained to be an integer. Hence m is the number of tangential CG beads of a molecular model. In SAFT typically a mapping of 3:1 heavy atoms per CG bead is employed. A proportional relationship was noted to exist between the acentric factor ω and the repulsive exponent λ^r , by using a Padé series:

$$\lambda^r = \frac{\sum_{i=0} a_i \omega^i}{1 + \sum_{i=0} b_i \omega^i} \quad (2.55)$$

where a_i and b_i are fitting coefficients, which are unique for each value of m . The van-der-Waals constant α is a function of the Mie exponents ⁽⁸⁵⁾:

$$\alpha = c_{ij} \left[\left(\frac{1}{\lambda^a} - 3 \right) - \left(\frac{1}{\lambda^r} - 3 \right) \right] \quad (2.56)$$

Upon fixing λ^r , a value for the van-der-Waals constant can be determined through the relation:

$$\alpha = \left(\frac{\lambda^r}{\lambda^r - 6} \right) \left(\frac{\lambda^r}{6} \right)^{\frac{6}{\lambda^r - 6}} \left[\left(\frac{1}{3} \right) - \left(\frac{1}{\lambda^r - 3} \right) \right] \quad (2.57)$$

Note that in this case, $\lambda^a = 6$, which takes into account the dispersion scaling of most fluids. It should be noted that other values for λ^a have led to satisfactory reproduction of macroscopic properties, for example with the CO₂ model found in ⁽⁹³⁾, $\lambda^a = 6.66$. Nevertheless, the resulting fluid with $(\lambda^r - 6)$ representation will have a unique critical point, if expressed in reduced units. This reduced critical temperature T_c^* and the van-der-Waals constant α are also related in a linear fashion, and so a Padé expression can be made:

$$T_c^* = \frac{\sum_{i=0} c_i \alpha^i}{1 + \sum_{i=0} d_i \alpha^i} \quad (2.58)$$

where c_i and d_i are fitting coefficients which are unique for each value of m . This relation allows the calculation of the corresponding energy scale ε through the knowledge of the critical temperature of the real chemical T_c , which are related by the following:

$$T_c^* = \frac{k_B T_c}{\varepsilon} \quad (2.59)$$

where k_B is the Boltzmann constant. A similar correlation can be determined for the length scale σ and the saturated liquid density at a reduced temperature $T_r = \frac{T}{T_c} = 0.7$. This property is chosen because the σ values obtained from other critical properties either underestimate (in the case of critical pressure) or overestimate (in the case of critical density) the saturated liquid densities. The size parameter has a relationship to the liquid density in reduced terms:

$$\rho^* = \rho \sigma^3 N_{av} \quad (2.60)$$

where N_{av} represents the Avogadro number. As before, the reduced density ρ^* follows a relationship with the van-der-Waals constant α which can be expressed in terms of a Padé expression:

$$\rho^*|_{T_r=0.7} = \frac{\sum_{i=0} j_i \alpha^i}{1 + \sum_{i=0} k_i \alpha^i} \quad (2.61)$$

where j_i and k_i are the fitting coefficients and $\rho^*|_{T_r=0.7}$ refers to the saturated liquid density at $T_r = 0.7$.

The macroscopic properties required for this method, ω , T_c and $\rho^*|_{T_r=0.7}$ are reported for many chemicals in common databases for example Yaws book of thermodynamical properties⁽⁹⁴⁾. This has allowed for the method to be applied to over 7800 chemicals⁽²⁹⁾. It should be noted that the correlation so far has only been developed for non-ionic species, so in this case the SAFT- γ Mie EoS is the underlying theory. Nevertheless, force field parameters obtained from this correlation have been employed in molecular simulation, and quantitative accuracy in the prediction of vapour-liquid and interfacial properties has been reported^{(95) (15) (96)}.

The main advantage of this approach is that the correlation has been ported to an online database called 'Bottled SAFT'⁽²⁹⁾. This database contains force field parameters for over 6000 chemicals, and so it is just a case of entering the details of the desired chemical. In this database the value of m is constrained to be an integer. No simulations nor trial and error procedures are required to obtain parameters for pure fluids. This strategy therefore offers a way to further streamline the force field parameterisation process.

It should be noted that Bottled SAFT only provides the pure fluid interactions. The final step in creating a CG model is to ensure the interactions between beads of different identity are valid. These are often called the cross-interactions. The SAFT formalism includes combining rules shown in equations (2.62)-(2.64)⁽⁸⁷⁾ to act as a first approximation for interactions between two different Mie fluids, denoted as ii and jj . The unlike size parameters are obtained from a Lorentz combining rule⁽⁹⁷⁾:

$$\sigma_{ij} = \frac{(\sigma_{ii} + \sigma_{jj})}{2} \quad (2.62)$$

The combining rule for repulsive exponent of the unlike interactions is obtained by invoking the geometric mean for the integrated van der Waals energy of a fluid with Sutherland potential⁽²⁶⁾, and by imposing the Berthelot condition⁽⁹⁸⁾:

$$(\lambda_{ij}^r - 3) = \sqrt{(\lambda_{ii}^r - 3)(\lambda_{jj}^r - 3)} \quad (2.63)$$

To satisfy these conditions, a specific geometric relation for the unlike dispersion energy is used, which also accounts for the asymmetry in size:

$$\varepsilon_{ij} = (1 - k_{ij}) \frac{\sqrt{\sigma_{ii}^3 \sigma_{jj}^3}}{\sigma_{ij}^3} \sqrt{\varepsilon_{ii} \varepsilon_{jj}} \quad (2.64)$$

where k_{ij} is the binary interaction parameter used to fine-tune the cross-interactions of a mixture. The form of equation (2.64) is a Berthelot⁽⁹⁸⁾ form relation. This can be obtained by relating the London dispersion potential⁽⁹⁹⁾ to the Lennard-Jones potential⁽¹⁰⁰⁾, invoking the Lorentz combining rule⁽⁹⁷⁾ and assuming that the sizes and ionisation potentials of molecules ii and jj are the same. This is justified by the assertion that this is commonly true, at least of the ionisation potentials. More details on this topic can be found in the work of Haslam et al⁽¹⁰¹⁾ and Hudson and McCoubrey⁽¹⁰²⁾.

If data for the mixture does not exist, an alternative is to model the two different beads as one whole molecule and match the simulation results to the relevant experimental data. An example of this can be found for the parameterisation of a n -dodecylbenzene model⁽¹⁰³⁾. In this case because not only the energetic parameters are varied, k_{ij} is not an appropriate indicator of how non-ideal the system is and is not used to describe the interactions. In this work all cross-interaction parameterisation is carried out by MD simulations, unless a previous study has already been carried out.

2.3.3 SAFT VRE Mie

When representing ionic systems at the CG scale one of the most difficult tasks is accounting for the electrostatic interactions. In the SAFT- γ Mie approach, Mie potentials are found that represent the effective interaction between CG beads, including the net Coulombic interaction. This is not so straightforward for ionic species such as electrolytes and ionic surfactants. Therefore, in many CG approaches the ion-ion interactions are considered separately. Examples include the MARTINI force field⁽¹⁰⁴⁾ and that of Klein et al⁽¹⁰⁵⁾. The SAFT-VRE Mie EoS⁽²⁷⁾⁽¹⁰⁶⁾ was created to model aqueous electrolyte solutions. This EoS adds two additional terms: A_{ion} and A_{Born} to equation (2.54). The first term takes into account the Coulombic interactions between ions, calculated using the primitive implementation of the mean spherical approximation⁽¹⁰⁷⁾⁽¹⁰⁸⁾. Here ions are treated as spherical charged particles which have a distinct size, as the unrestricted model is used. The primitive implementation means the solvent is represented by a continuous medium with a dielectric constant ε_r . In this work, only the electrostatic contribution of the solvent intermolecular potentials are treated implicitly. This treatment simplifies the description of the Coulomb potential between charged ions, while still retaining an accurate description of electrolytes. The A_{Born} term accounts for the thermodynamic effects of ion solvation via the Born model⁽¹⁰⁹⁾ for the free energy of the

solvation of ions, which describes the change in the free energy of the system due to the transfer of ions into a continuous dielectric medium at infinite dilution.

By imposing certain conditions (detailed in Section 2.5.2 'Optimisation by SAFT theory'), the EoS parameters can be related to a corresponding intermolecular potential that can be used in an MD simulation. Taking into consideration the SAFT VRE Mie EoS, the intermolecular potential contains both a Mie, equation (2.10), and a Coulombic, equation (2.12), contribution:

$$U_{ij,tot}(r_{ij}) = U_{Mie,ij}(r_{ij}) + \frac{q_i q_j}{4\pi\epsilon_0\epsilon_r r_{ij}} \quad (2.65)$$

To determine the dielectric constant, the SAFT VRE Mie theory ⁽²⁷⁾ ⁽¹⁰⁶⁾ uses the following relationship to take into account the change with temperature and density of the solvent, which follows the work of Uemetsu and Frank ⁽¹¹⁰⁾:

$$\epsilon_r = 1 + \rho_{solv} d \quad (2.66)$$

where d is a solvent-dependent parameter and ρ_{solv} is the density of the solvent. The parameter d can be expressed as a function of temperature, an accurate description is then expressed as ⁽²⁷⁾:

$$d = d_V \left(\frac{d_T}{T} - 1 \right) \quad (2.67)$$

where d_V and d_T are component specific parameters in units of $\text{dm}^3 \text{mol}^{-1}$ and K respectively.

For a mixed solvent, as in the case of a microemulsion, mixing rules are employed to calculate the d parameter. This is accomplished by using a van-der-Waals one-fluid mixing rule ⁽²⁷⁾:

$$d(\hat{x}_i) = \sum_{i=1}^{n_{solv}} \sum_{j=1}^{n_{solv}} \hat{x}_{i=1} \hat{x}_j d_{ij} \quad (2.68)$$

where the prime refers to salt-free mole fractions, $\hat{x}_i = \frac{N_i}{N_{total}}$, i and j refer to the solvent molecules, N is the number of molecules, n_{solv} is the number of different types of solvent present, and d_{ij} refers to the unlike parameter. The latter can be calculated using the arithmetic mean of the pure component parameters d_{ii} and d_{jj} ⁽²⁷⁾:

$$d_{ij} = \frac{d_{ii} + d_{jj}}{2} \quad (2.69)$$

This definition of d_{ij} then allows the simplification of equation (2.68) to a one summation ⁽¹¹¹⁾ expression:

$$d(\hat{x}_i) = \sum_i^{n_{solv}} \hat{x}_i d_{ii} \quad (2.70)$$

Calculation of $d(\hat{x}_i)$ allows determination of ϵ_r using equation (2.66). This relation requires knowledge of the density of the mixed solvent. Whilst this can be accomplished by using the equation of state, in this work MD simulations are used to calculate the mixed solvent density.

The work of Schreckenberget al ⁽²⁷⁾ and Eriksen et al ⁽¹⁰⁶⁾ sets out the approach to obtain the Mie force field parameters. It should be noted that this procedure was not carried for the systems studied in the thesis but it is covered here for the sake of completion. The like-like ion segment diameters can be selected from the experimentally derived ionic diameters ⁽¹¹²⁾ ⁽¹¹³⁾. These values usually correspond to the ions with a co-ordination number of six in a crystal lattice. The unlike ion-ion and ion-water diameters σ_{ij} are calculated using equation (2.62).

The dispersion energy ε_{ij} between any two unlike ions, and ε_{ii} between two identical ions, is obtained by analogy to the work of Hudson and McCoubrey ⁽¹⁰²⁾ and Haslam et al ⁽¹⁰¹⁾. It is obtained by relating the London dispersion interaction potential ⁽⁹⁹⁾ with the Mie potential model, which was found by following Haslam et al ⁽¹⁰¹⁾. The value for the cross-interaction parameter for any pair of interacting ions can be obtained using:

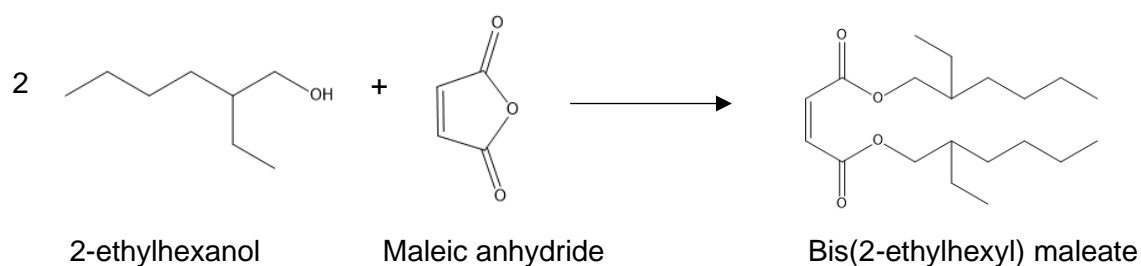
$$\varepsilon_{ij} = \frac{3}{2} \frac{1}{2\sigma_{ij}^6(\lambda_{ij}^3 - 1)} \frac{I_i I_j}{I_i + I_j} \frac{\alpha_{0,i} \alpha_{0,j}}{(4\pi\epsilon_0)^2} \quad (2.71)$$

where I is the ionisation potential, and α_0 is the electronic polarizability of the ionic species. These values can be obtained from the literature (for example references ⁽¹¹⁴⁾ ⁽¹¹⁵⁾ ⁽¹¹⁶⁾). The remaining interactions to parameterise are the energetic cross-interactions ε_{ij} between the ions and water. This can be accomplished by optimising the fit to relevant macroscopic data using the SAFT VRE Mie EoS with a least squares objective function.

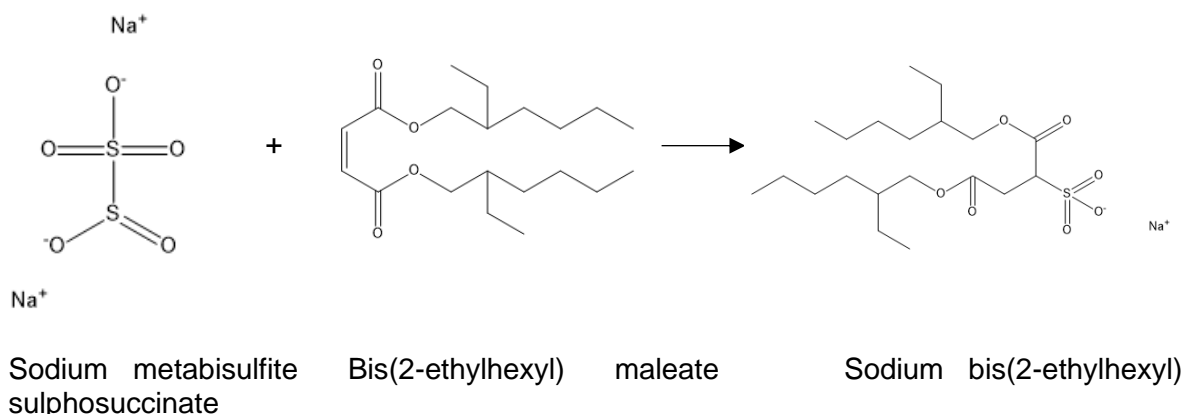
2.4 Analysis methods

2.4.1 Surfactant synthesis

The aim of this section is to give a contrast between the experimental and simulation approach to making a surfactant. First the experimental approach is described, where the example surfactant is AOT (Aerosol OT). It's full chemical name is sodium (bis-2-ethylhexyl) sulphosuccinate, and it is synthesised via two reactions. The first is an esterification reaction between 2-ethyl hexanol and maleic anhydride in a 2:1 molar ratio:



The double bond of this intermediate is then sulphonated by reacting with sodium metabisulfite:



After the two reactions, the product must be purified which can involve Soxhlet extraction, washing, recrystallisation and foam fractionation ⁽¹³⁾. By contrast, the creation of a molecule in a CG simulation simply involves creating a structure file. The positions of each CG bead and the box vectors are specified, taking into account the overall structure. To explore variation in structure (e.g. hydrocarbon tail length) this is simply a case of adding another line in the structure file. The impact of different functional groups is achieved by changing the identity of the specific bead. To do this by experiment would require a separate set of reactions for each structural variant. The more time-consuming activity in CG molecular simulation is assigning the force field parameters so that the model captures the desired phenomena. The relevant techniques are discussed in detail in section 2.5.

2.4.2 Density

The density of a substance is conventionally defined as the amount of that substance divided by its volume. This amount can be in terms of mass, number of moles, number of electrons, or number of particles. The mass density is used in this work to parameterise force fields. An example of an experimental technique to measure the density of a liquid is the use of a pycnometer, which is a glass beaker of defined volume. The pycnometer, pictured in Figure 2.4, is first weighed empty and then again full of the liquid sample. The difference in mass divided by the pycnometer volume is the density of the sample:

$$\rho_{sam} = \frac{m_{pyc+sam} - m_{pyc}}{V_{pyc}} \quad (2.72)$$

where ρ_{sam} is the sample density, $m_{pyc+sam}$ is the total mass of the sample and the pycnometer, m_{pyc} is the mass of the pycnometer and V_{pyc} is the volume of the pycnometer. In Gromacs ⁽⁷²⁾, there are two ways to calculate density. To calculate the density of a bead/molecule as a function of box length (the density profile) the sub-routine *gmx density* can be used. The simulation box is divided into equidistant sections, and the density is calculated in each section:

$$\rho_i = \frac{\langle X_i \rangle}{V_j} \quad (2.73)$$

where X_i refers to the amount of component i , which in Gromacs can be in terms of mass, electron, particle number or charge. The mass, charge and the number of electrons of an atom can be defined by the user. If using particle number, the number of CG beads per molecule must be accounted for when reporting density of a molecule. ρ_i is the density, and V_j is the volume of slab j . This approach is adopted in this work to determine density of components in either vapour-liquid or liquid-liquid systems. The density can be determined from the values of the corresponding bulk regions.

The other option is to calculate the whole box density via the subroutine *gmx energy*, which will report the time-averaged mass density. This route is used in this work for calculating density of a fluid mixture.



Figure 2.4 Image of a pycnometer. Taken from ⁽¹¹⁷⁾

2.4.3 Surface tension

The surface tension is relevant in this work as again it is another parameter used to develop force fields in this work. To understand surface tension a few concepts need to be described first. The term ‘interface’ is commonly employed to describe the boundary in liquid/liquid, solid/liquid, and gas/liquid systems, although in the latter case the term ‘surface’ (hence surface tension) can also be used ⁽⁵⁵⁾. Molecules located at an interface experience an imbalance of forces compared to those in bulk solution, and so an interface is associated with a surface free energy ⁽¹¹⁸⁾. Taking the air-water surface as an example, the imbalance of forces is because water is polar, and air is non-polar. Water molecules at the surface are thus subjected to unequal short-range attraction forces, and undergo a net inward pull to the bulk phase ⁽¹¹⁹⁾. Minimisation of the contact area with the gas phase is therefore a spontaneous process, which is why drops and bubbles are round ⁽¹¹⁸⁾.

The surface energy per unit area, defined as surface tension (γ) is then the minimum amount of work, W , required to create new unit area, A_s , of that interface ⁽¹¹⁸⁾. Another definition of surface tension is given as the force F acting normal to the liquid-gas interface per unit length L of the resulting thin film on the surface ⁽¹¹⁸⁾. This can be expressed as:

$$F = \gamma L \quad (2.74)$$

An illustration of this concept is given in Figure 2.5. The work done by the force F in moving the liquid by distance dx can be calculated as $dW = Fdx$, and the total area of the film increases by $dA_s = Ldx$, and so by multiplying both sides of equation (2.74) by dx , the following relation is derived:

$$dW = \gamma dA_s \quad (2.75)$$

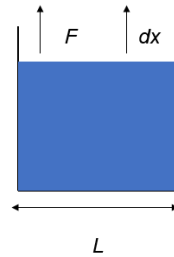


Figure 2.5 Illustration of the liquid-air surface and the force necessary to increase the surface area. This force is proportional to the surface tension.

The surface tension is related to the Helmholtz free energy of the system A ⁽¹²⁰⁾. The Helmholtz free energy is defined as the maximum amount of work that can be performed by a closed system. Therefore, the system is one that can exchange heat and work energy with its surroundings, but not matter, as shown in Figure 2.6.

At constant temperature, volume and number of molecules, the surface tension is the variation in Helmholtz free energy per variation in surface area ⁽¹²⁰⁾:

$$\left(\frac{\partial A}{\partial A_s}\right)_{N,V,T} = \gamma \quad (2.76)$$

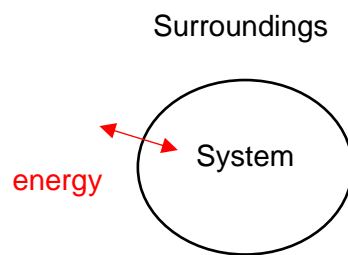


Figure 2.6 Illustrative description of a closed system

In experiments surface tension can be determined by a variety of methods, such as Drop Volume tensiometry. In this method, a liquid (the light phase) is introduced into a bulk phase (the heavy phase) through a capillary. A drop, which tries to move upwards due to buoyancy, forms at the tip of the capillary. As a result of the interfacial tension the drop tries to keep the interface with the bulk phase as small as possible. As a new interface comes into being when the drop detaches from the capillary outlet, it is necessary to overcome the corresponding interfacial tension. The drop does not detach until the lifting force or weight compensates for the force resulting from the interfacial tension on the wetted length of the capillary, which is the circumference. The formula for this relationship is:

$$\gamma = \frac{V_{Drop}(\rho_H - \rho_L)g}{\pi d} \quad (2.77)$$

where g is the acceleration due to gravity, V is the drop volume, d is the inside diameter of the capillary, ρ_H and ρ_L represent the density of the heavy phase and the light phase respectively. This concept is summarised in Figure 2.7, and a picture of an apparatus is given in Figure 2.8.

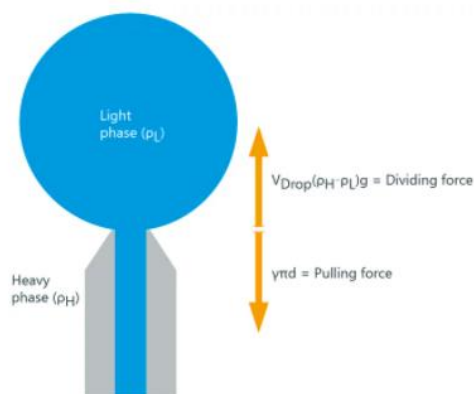


Figure 2.7 Schematic diagram of the Drop Volume method. Taken from ⁽¹²¹⁾



Figure 2.8 Image of a Drop Volume tensiometer. Taken from ⁽¹²²⁾

The vapour-liquid surface tension is a direct output of an NVT MD simulation. The Gromacs sub-routine *gmx energy* employs the mechanical method ⁽¹²³⁾, which requires knowledge of the Cartesian components of the pressure tensor:

$$\gamma = \frac{1}{L} \int_0^z \left(P_{zz} - \frac{P_{xx} + P_{yy}}{2} \right) dz \quad (2.78)$$

where the pre-factor with $L = 2$ refers to the presence of two interfaces in these simulations. The surface tension of a pure fluid is an ideal property to include in model parameterisation, as surface tension reduction is a key description of surfactant behaviour ⁽³⁴⁾.

The capacity of surfactants for lowering the surface tensions of aqueous solutions can be described in two ways: the concentration required to produce a given reduction in surface tension (surfactant efficiency) and the maximum reduction in surface tension that can be achieved regardless of concentration (surfactant effectiveness). A good measure of the efficiency is the concentration required to produce a reduction of 20 mN m^{-1} . At this value, the surfactant concentration is close to the minimum concentration required to produce maximum adsorption at the interface. The surfactant effectiveness is typically measured by either the minimum surface tension or the maximum surface excess (see Section 2.4.4). The effectiveness is determined by the relative size of the surfactant head and tail, therefore surfactant films can either be loosely or tightly packed resulting in different interfacial properties.

2.4.4 Surface excess

A description of the oriented surfactant monolayer at the air-water interface can be obtained by calculating the surface excess, allowing for more in-depth study of the surfactant structure-property relationship^{(13) (124)}. This is defined as the concentration of surfactant molecules in a surface plane, relative to a similar plane in the bulk. It was Gibbs who derived a thermodynamic treatment of the variation of surface tension with composition⁽¹¹⁸⁾.

An important approximation in the Gibbs adsorption isotherm is the exact location of the interface. If a surfactant aqueous phase α in equilibrium with a vapour phase β is considered, then the interface σ is a region of indeterminate thickness τ across which the properties of the system vary from values specific to phase α to those characteristic of phase β . Since properties within this interface cannot be well defined, a convenient assumption is to consider a mathematical plane with zero thickness so that the properties of both phases apply right up to that dividing plane positioned at some specific value X ⁽¹²⁵⁾. The definition of the Gibbs dividing surface XX' is arbitrarily chosen such that the surface excess adsorption of the solvent is zero. This concept is illustrated in Figure 2.9, the Gibbs dividing surface is defined as the plane in which the solvent excess becomes zero i.e. the shaded area on each side of the plane is equal as in (a). The surface excess of component i will then be the difference in the concentrations of that component on either side of that plane (b).

The surface excess concentration of component i is given by⁽¹¹⁸⁾:

$$\Gamma_i^\sigma = \frac{n_i^\sigma}{A_s} \quad (2.79)$$

where n_i^σ is the amount of component i in the surface phase σ over and above that which would have been in the phase if the bulk phases α and β had extended to the dividing surface. Depending on the position of the dividing surface XX' , the value of Γ_i^σ can either be positive or negative.

If the internal energy U of the total system consisting of bulk phases α and β is considered:

$$U = U^\alpha + U^\beta + U^\sigma \quad (2.80)$$

$$U^\alpha = TS^\alpha - PV^\alpha + \sum_i \mu_i n_i^\alpha \quad (2.81)$$

$$U^\beta = TS^\beta - PV^\beta + \sum_i \mu_i n_i^\beta \quad (2.82)$$

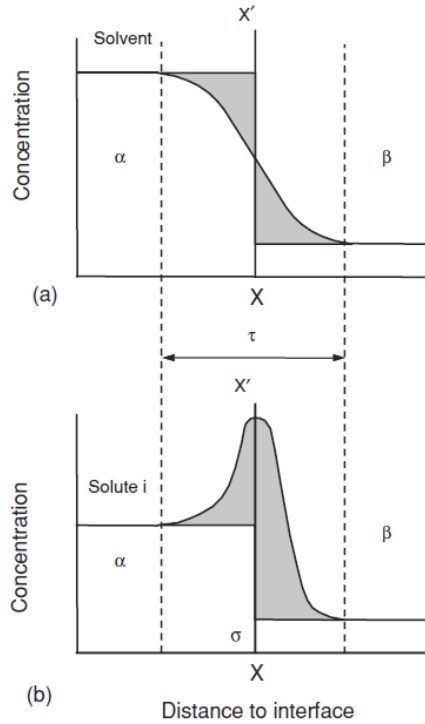


Figure 2.9 The Gibbs approach to defining surface excess Γ . Taken from ⁽³⁴⁾.

In thermodynamics, the internal energy U is the total energy of a system, in particular the total kinetic and potential energy of the molecules in the system ⁽¹²⁶⁾. It is related to the Gibbs free energy via the following equation ⁽¹¹⁸⁾:

$$G = U + PV - TS \quad (2.83)$$

In the case of the bulk phases α and β in equation (2.81) and (2.82) respectively, the first terms (from left to right) is the energy change due to heat transfer. The second term is work done on the bulk volume V of the phase. The energy change due to change in chemical composition of the phase is the third term, where μ_i is the energy that can be absorbed or released due to a change in particle number during phase transition (the chemical potential) of component i . The chemical potential is related to the Gibbs free energy for an isothermal-isobaric system ⁽¹¹⁸⁾:

$$\left(\frac{\partial G}{\partial N_i}\right)_{T,P} = \mu_i \quad (2.84)$$

The corresponding expression for the thermodynamic energy of the interfacial region σ is:

$$U^\sigma = TS^\sigma + \gamma A_s + \sum_i \mu_i n_i^\sigma \quad (2.85)$$

The interfacial region is considered infinitely thin compared to either bulk phase, so the PV term can be considered negligible. However, it is replaced by the work required to expand the interface, which is expressed in equation (2.75)

For any infinitesimal change in T , S , A_s , μ , n , differentiation of the interfacial region U equation (2.85) gives:

$$dU^\sigma = TdS^\sigma + S^\sigma dT + \gamma dA_s + A_s d\gamma + \sum_i n_i^\sigma d\mu_i + \sum_i \mu_i dn_i^\sigma \quad (2.86)$$

For a small, isobaric, isothermal, reversible change the differential total internal energy in any bulk phase is:

$$dU = TdS - PdV + \sum_i \mu_i dn_i \quad (2.87)$$

The equivalent for the interfacial region becomes:

$$dU^\sigma = TdS^\sigma + \gamma dA_s + \sum_i \mu_i dn_i^\sigma \quad (2.88)$$

Subtracting equations (2.86) and (2.88) leads to:

$$S^\sigma dT + A_s d\gamma + \sum_i n_i^\sigma d\mu_i = 0 \quad (2.89)$$

At constant temperature, and considering the definition of the surface excess of component i as in equation (2.79) the general form of the Gibbs equation is:

$$d\gamma = - \sum_i \Gamma_i^\sigma d\mu_i \quad (2.90)$$

If a simple system consisting of a solvent and surfactant is considered, denoted by subscripts 1 and 2 respectively, then equation (2.90) reduces to:

$$d\gamma = -\Gamma_1^\sigma d\mu_1 - \Gamma_2^\sigma d\mu_2 \quad (2.91)$$

Assuming the choice of the Gibbs dividing surface is such that $\Gamma_1^\sigma = 0$, then equation (2.91) further simplifies to:

$$d\gamma = -\Gamma_2^\sigma d\mu_2 \quad (2.92)$$

where Γ_2^σ is the surfactant surface excess concentration. The chemical potential is given by $\mu_i = \mu_i^0 + RT \ln a_i$ so at constant temperature ⁽¹¹⁸⁾:

$$d\mu_i = \text{const} + RT d \ln a_i \quad (2.93)$$

where μ_i^0 is the standard chemical potential of component i , and a_i is the chemical activity of component i . Applying this relation to the surface excess equation gives the common form of the Gibbs equation for non-ionic surfactants, which are non-dissociating in solution:

$$d\gamma = -\Gamma_2^\sigma RT d \ln a_2 \quad (2.94)$$

Or:

$$\Gamma_2^\sigma = -\frac{1}{RT} \frac{d\gamma}{d \ln a_2} \quad (2.95)$$

For ionic surfactants, which are fully dissociating solutes of the form $R^- M^+$, and assuming ideal behaviour below the CMC, the equation takes the form:

$$d\gamma = -\Gamma_R^\sigma d\mu_R - \Gamma_M^\sigma d\mu_M \quad (2.96)$$

If no electrolyte is added, electroneutrality of the interface requires that $\Gamma_R^\sigma = \Gamma_M^\sigma$. Using the mean ionic activities so that $a_2 = (a_R a_M)^{\frac{1}{2}}$ and substituting in equation (2.93) gives the Gibbs equation for 1:1 dissociating compounds ⁽¹²⁵⁾:

$$\Gamma_2^\sigma = -\frac{1}{2RT} \frac{d\gamma}{d \ln a_2} \quad (2.97)$$

If swamping electrolyte is introduced (i.e. enough salt to make electrostatic effects unimportant) and the same counter-ion M^+ is present, then the activity of M^+ is constant and the pre-factor becomes unity, so equation (2.95) becomes valid ⁽³⁴⁾. For materials that are strongly adsorbed at an interface, e.g. surfactants, a dramatic reduction in interfacial (surface) tension is observed with small changes in bulk phase concentration ⁽¹²⁵⁾. The practical applicability of this relationship is that the relative adsorption of a material at an interface, its surface activity, can be determined from the measurement of the interfacial tension as a function of solute concentration. It is important to note that for dilute surfactant systems, the concentration can be substituted for activity in equations (2.95) and (2.97) without loss of generality.

A molecular simulation method was developed by Herdes et al ⁽¹⁵⁾ in which the surface excess – surface tension relationship is modelled to study the pre-CMC region of aqueous surfactant mixtures. It follows from the relationship between surface tension and surface excess, as illustrated in Figure 2.10. The direct study of the pre-CMC region is unfeasible for the foreseeable future, as the dilute surfactant concentrations involved mean prohibitively large numbers of water molecules, and hence system sizes, would be needed. A key assumption of the method, which is referred to as the $\Gamma - \gamma$ method, is that the contribution to the system energetics by the surfactants in the bulk phase are negligible compared to the surfactants accumulated at the free surface. The method was of interest in this work as a potential way to parameterise the molecular models developed more quickly. Whilst this method is applicable to non-ionic surfactants ^{(90) (127)}, it is currently not for ionic surfactants as the presence of counterions results in an entropy penalty, meaning there is significant surfactant concentration in the bulk phase even at pre-CMC conditions. Indeed, an effort during this project was made to adapt the method but more work still needs to be carried out, as discussed in Section 5.2.

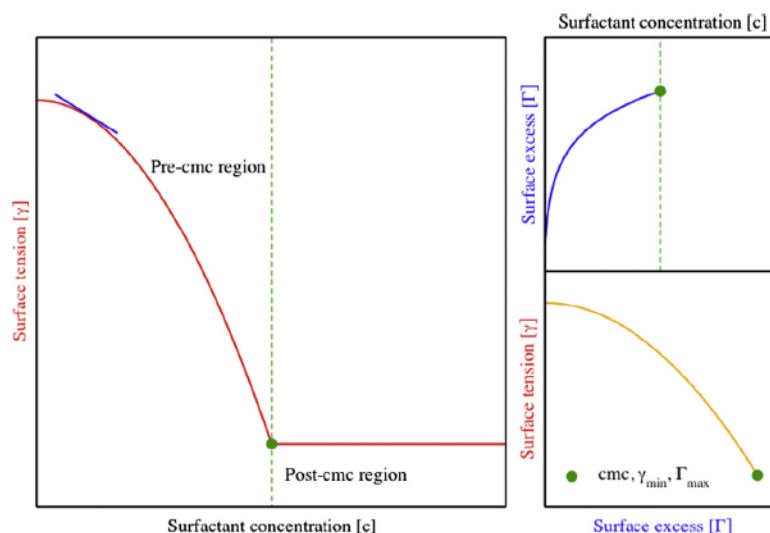


Figure 2.10 Schematic representation of a surface tension-concentration plot and its transformation into a surface tension-surface excess plot. Taken from ⁽¹⁵⁾.

2.4.5 Liquid-liquid equilibrium

This property is used to parameterise the cross-interactions between binary fluid mixtures. When two liquids are mixed together, the equilibrated state is dependent on the miscibility between them. If they are partially miscible, the result will be two co-existing liquid mixtures of different compositions (termed conjugate phases). This difference is referred to as the solubility gap. Despite some liquid mixtures described as such, the state of complete immiscibility is never truly obtained. As an example, if cyclohexane and water are mixed at room temperature, there will be residual amounts of one component in the other phase. Specifically, the mole fraction of cyclohexane in the water-rich phase will be 1.25×10^{-5} , and the mole fraction of water in the cyclohexane-rich phase will be 3.50×10^{-4} ⁽¹²⁸⁾.

The Gibbs phase rule is expressed below ⁽⁷⁴⁾:

$$N_f = 2 + N_c - N_p \quad (2.98)$$

where N_f is the number of degrees of freedom, N_c is the number of components in the mixture, and N_p is the number of different phases. For a two-component, two-phase system the above rule shows that there are only two degrees of freedom. Thus, when the temperature and pressure are fixed, the compositions (usually expressed in mole fraction) are fixed as well.

Experimentally, the liquid-liquid equilibrium can be determined by preparing mixtures of known overall compositions via intense stirring. The phases are then allowed to settle to achieve separation at constant temperature. Samples are then taken from both phases and analytical techniques, for example gas chromatography ⁽¹²⁹⁾, can be used to determine the composition of each phase.

For an MD simulation of the liquid-liquid equilibrium, the initial configuration is a phase-separated one, and when the system reaches equilibrium, the composition of both phases are calculated using the Gromacs ⁽⁷²⁾ subroutine *gmx density* to obtain the density profiles. This then allows the determination of mutual solubility, which in this work is reported in terms of mole fraction.

2.4.6 Nematic order parameter

When a system comprises molecules with one axis of rotational symmetry, an orientational ordered phase can emerge ⁽⁶³⁾. A nematic phase is characterised by a preferred direction for the system alignment. An order parameter is thus the quantification of such organisation,

allowing it to characterise a phase transition. In this work the nematic order parameter is used to determine phase transitions that are observed in surfactant binary and ternary mixtures. To calculate the nematic order parameter, the first step is to define the Saupe order tensor ⁽¹³⁰⁾:

$$\mathbf{Q}_{\alpha\beta} = \frac{1}{N} \sum_{i=1}^N \frac{3}{2} \mathbf{u}_{i\alpha} \cdot \mathbf{u}_{i\beta} - \frac{1}{2} \delta_{\alpha\beta} \quad (2.99)$$

where \mathbf{u}_i is the unit vector that points along the axis of symmetry of the molecule i . In this work \mathbf{u}_i is defined as the end-to-end vector, i.e. the one connecting the hydrophilic head and the end of the hydrophobic tail. N is the number of molecules and δ is the Kronecker delta function. α and β can be equal to x , y , or z positions. Diagonalisation of $\mathbf{Q}_{\alpha\beta}$ gives three eigenvalues λ_+ , λ_0 and λ_- which sum to zero, with $\lambda_+ > \lambda_0 \geq \lambda_-$, and the corresponding eigenvectors. For a uniaxial system the eigenvalues are related by:

$$\lambda_- = \lambda_0 = -\frac{1}{2} \lambda_+ \quad (2.100)$$

The largest eigenvalue λ_+ is the nematic order parameter, termed as S_2 . The corresponding eigenvector is \mathbf{n} , the system director, which denotes the preferred direction of the molecules. In this work, the python package MDtraj ⁽¹³¹⁾ is used to calculate S_2 using the `compute_nematic_order` subroutine. The required input files are the trajectory and structure files of the CG beads that represent the unit vector, which are obtained from Gromacs ⁽⁷²⁾ using the `gmx trjconv` subroutine.

An alternative definition of S_2 is given in terms of the second Legendre's polynomial as:

$$S_2 = \langle P_2(\mathbf{n} \cdot \mathbf{u}) \rangle \quad (2.101)$$

$$= \langle P_2(\cos \theta) \rangle \quad (2.102)$$

$$= \left\langle \frac{3}{2} \cos^2 \theta - \frac{1}{2} \right\rangle \quad (2.103)$$

where $\theta = \mathbf{n} \cdot \mathbf{u}$ is the angle between the molecular axis and the director and $P_2(x)$ is the second Legendre polynomial:

$$P_2(x) = 3x^2 - 1 \quad (2.104)$$

From equation (2.103) it is seen that, with the condition $\cos^2 \theta$ can vary from 0 to 1, the nematic order parameter can vary from -1/2 to 1. A value of -1/2 indicates anti-alignment with the director. If the nematic order parameter is 1, this is indicative of perfect alignment with the director. A value of 0 indicates an isotropic system. An example of such a system is a liquid e.g. pure water, where the molecules have no preferred orientation.

Experimental techniques exist to calculate nematic order parameters; however, they are defined differently from the simulation-based method used in this study. Deuterium order parameters are calculated using deuterium Nuclear Magnetic Resonance (²H NMR), which is a spectroscopic technique used to observe magnetic fields around atomic nuclei. Certain sections of a molecule can be studied by replacing hydrogen atoms with the isotope deuterium. In this case the order parameter values reflect the average orientations of internuclear carbon-deuterium vectors with respect to an external magnetic field ⁽¹³²⁾. This is

not to say that other simulation studies do not use this definition, for example simulations of lipid membranes ⁽¹⁰⁴⁾.

2.4.7 Relative shape anisotropy

Flexible-chain molecules can assume a large number of conformations and shapes due to the many internal degrees of freedom ⁽¹³³⁾. The average shape of a molecule/aggregate is of importance to understand a variety of phenomena. In this work the surfactant micelle morphology, which has been shown to vary with solvent concentration ⁽¹³⁴⁾, is of interest. In this work the principal moments of inertia are used to determine micelle shape. The inertia tensor is defined in this work by:

$$I_{\alpha\beta}^2 = \frac{1}{M} \sum_{i=1}^N m_i (r_i^2 \delta_{\alpha\beta} - r_{i\alpha} r_{i\beta}) \quad (2.105)$$

where r_i is the position relative to the center of molecular mass, m_i is the mass of atom i , and M is the total mass. Transformation to a principal axis system diagonalises the inertia tensor and the principal axis system is chosen so that ⁽¹³³⁾:

$$I = \text{diag}(I_1^2, I_2^2, I_3^2) \quad (2.106)$$

These diagonal elements are the principal moments of inertia. In this work the eigenvalues of I are sorted in descending order, so that $I_1^2 \geq I_2^2 \geq I_3^2$. Knowing these values permits the calculation of the radius of gyration ⁽¹³³⁾:

$$R_g^2 = I_1^2 + I_2^2 + I_3^2 \quad (2.107)$$

which is a measure of the average size of the particular conformation. The asphericity, b , can be calculated ⁽¹³³⁾:

$$b = I_1^2 - \frac{1}{2}(I_2^2 + I_3^2), b \geq 0 \quad (2.108)$$

As well as the acylindricity c , defined as ⁽¹³³⁾:

$$c = I_2^2 - I_3^2, c \geq 0 \quad (2.109)$$

These quantities are useful for characterisation of shape: for shapes of tetrahedral or higher symmetry $b = c = 0$, and for shapes of cylindrical shape $c = 0$. An overall measure of shape anisotropy is the relative shape anisotropy κ^2 ⁽¹³³⁾:

$$\kappa^2 = \frac{(b^2 + \frac{3}{4}c^2)}{R_g^4} \quad (2.110)$$

The relative shape anisotropy can assume values between 0 and 1. A linear array of skeletal atoms (i.e. a rigid rod molecule) is characterised by $\kappa^2 = 1$; for a regular planar array such as masses at the vertices of a regular polygon or a homogeneously filled polygon $\kappa^2 = 0.25$; for structures of tetrahedral or higher symmetry $\kappa^2 = 0$.

In Gromacs ⁽⁷²⁾ the principle moments of inertia can be calculated as a function of time from the trajectory by using the *gmx gyrate* sub-routine. In this case the routine is used to analyse

single aggregate systems. These values can be used to calculate the various shape factors described above via the relevant equations.

2.4.8 Small angle scattering techniques

These methods are important in this study as some of the experimental data included in analysis is generated using these methods. Therefore, a brief description of these techniques will be provided. Scattering techniques in general are based on interactions between incident radiations (e.g. light, X-ray or neutrons) and particles. The desired output of scattering techniques is to determine molecular organisation which allows the relationship between physical properties (size, shape and structure) and molecular structure to be studied. The size range of micelles, microemulsions and liquid crystals is approximately 1 – 10³ nm, so valuable information can be obtained if the incident wavelength, λ , falls within this range⁽¹³⁵⁾. As such, X-rays ($\lambda = 0.05 - 0.23$ nm) and neutrons ($\lambda = 0.01 - 0.3$ nm) can characterise these systems. The Bragg equation defines the angle of diffraction θ of radiation of wavelength λ for a separation of lattice planes d ⁽¹³⁶⁾:

$$\lambda = 2d \sin \theta \quad (2.111)$$

It is clear that small particles, such as microemulsion droplets, will scatter at small angles, which is why small-angle scattering techniques are appropriate⁽¹³⁷⁾.

Scattering events arise from radiation-matter interactions and produce interference patterns that give information about the spatial and/or temporal correlations within the sample. In small angle neutron scattering (SANS) experiments, a beam of neutrons is directed at a sample. These neutrons interact with the atomic radius via strong nuclear forces operating at very short range (ca. 10⁻¹⁵ m) which is much shorter than the incident neutron wavelength (ca. 10⁻¹⁰ m). Different nuclei will show different neutron scattering patterns, which allows the identification of the different structural regions. The aggregation number of a surfactant micelle can then be approximated using SANS results by estimating the micellar volume^{(11) (33)}. This can be accomplished by treating the micelle as monodisperse geometric objects, for example a sphere. The shape itself can be approximated by fitting the neutron scattering pattern to a geometric model.

Small angle x-ray scattering (SAXS) experiments involve a beam of x-rays interacting with the sample, causing scattering of x-rays due to differences in electron density. A fraction of the x-rays will pass through the sample, and a fraction are absorbed and transmitted into other forms of energy such as heat or fluorescence, and a fraction will be scattered in other directions. As observed scattering patterns are due to inhomogeneities in the distribution of electrons in the sample and these differences can be between types of atoms, individual molecules or molecular assemblies, the ability of SAXS to probe distances in the nm range makes it suitable for the analysis of order within the liquid crystal microstructure, for example bilayer repeat distances in surfactant lamellar phases⁽¹³⁸⁾. This permits the calculation of bilayer thickness, which can be calculated from normalised electron density profiles, obtained from Fourier transformation of scattering amplitudes^{(139) (140)}.

2.5 Coarse-graining

In CG models multiple atoms are grouped into one super-atom or 'bead' modelled by an effective force field to capture the behaviour of this group. The opposite approach is to fully model the atomistic detail of a molecule, these models are termed 'all-atomistic' (AA). Examples of such approaches include CHARMM^{(141) (142)}, AMBER^{(143) (144)}, and OPLS-AA^{(145) (146)}. There also exist united atom (UA) models, where hydrogen atoms are grouped with the heavy atom they are bonded to, examples include AMBER UA⁽¹⁴⁷⁾ and CHARMM36 UA⁽¹⁴⁸⁾ and GROMOS⁽¹⁴⁹⁾ yet these are still considered to be at the atomistic scale. With atomistic-scale modelling, system sizes can be up to the nm length scale and simulation times on the order of 10 ns⁽²⁴⁾. The level of information included in these models means they are of limited

use when it comes to simulation of self-assembly processes⁽¹⁵⁰⁾ which can occur on the μs scale and require on the order of 10 nm⁽¹⁵¹⁾. Replacing multiple atoms with a single effective potential is a solution to access the required spatio-temporal scales.

When writing about CG techniques, it is important to acknowledge the dissipative particle dynamics (DPD)⁽¹⁵²⁾ technique, which can be viewed as a more aggressive approach to CG. In this case droplets or clusters of fluid molecules are regarded as soft particles interacting via Newton's Equations of motion (see equation (2.41)). The force between each pair of particles contains three terms: conservative, dissipative and random. The main advantage over MD is that larger time scales (ms) and length scales (100 nm)⁽¹⁵¹⁾ can be accessed. However, such aggressive techniques will ultimately run the risk of losing the connection to the microscopic scale, indeed it has been reported that DPD is appropriate for qualitative studies, but as a predictive tool requires significant refinement⁽¹⁵³⁾. It is for this reason that the standard CG scale is used in this work.

For a true CG representation, multiple heavy atoms must be grouped into a bead. The level of detail is referred to as the CG mapping and is represented as the heavy atoms:bead ratio. In this work, the mapping is set so that is no more than 3:1. Small solvent molecules can also be represented in the CG scale, usually as a single bead.

The advantages of CG models are numerous, for example the computational costs to run simulations of systems are reduced. This can be related to the reduction in resolution: fewer interaction sites mean fewer positions and momenta need to be calculated, and so the number of degrees of freedom of the system are reduced⁽¹⁵⁴⁾. CG models reduce the stiffest degrees of freedom, for example the hydrogen-carbon bonds, which allows for the use of larger time steps⁽¹⁵⁵⁾. In the case of non-ionic CG models, the long-range electrostatic interactions are neglected, leaving only simplified short-range potentials to calculate⁽¹⁵⁰⁾. In contrast, AA models will include all of this detail⁽¹⁵⁴⁾. By integrating out the atomistic detail, the potential energy surface is smoothed⁽¹⁵⁰⁾, which accelerates dynamics allowing for larger time steps to be used and shorter equilibration times.

The potential benefit of CG simulation is that simulation speed may be increased by two orders of magnitude compared to AA simulation⁽¹⁵⁰⁾. This should mean that longer time scales can be explored with the same computational resources. The actual gains in simulation speed will be system dependent, with the simulation conditions, CG models, and settings playing a role⁽¹⁵⁰⁾. Another option to reduce simulation time is using implicit solvent models, where the force fields of the solute represent the effective presence of the solvent⁽¹⁵⁶⁾. This can be especially beneficial for systems where the solvent makes up the bulk of the system (as can be the case in surfactant-water binary mixtures). However, implicit solvent models are disadvantaged in that they cannot be transferred to multicomponent systems⁽¹⁵⁷⁾.

CG models are not without their limitations and disadvantages. Integrating out atomistic detail inevitably leads to loss of information, rendering CG models unable to capture certain behaviour or properties⁽¹⁵⁸⁾. The smoothing of the potential landscape can result in properties such as the diffusion coefficient being orders of magnitude higher than AA or experimental determination⁽¹⁸⁾. As such, CG models are a compromise between reducing simulation time and reduction in accuracy in prediction of system properties or behaviour⁽²³⁾. The method used to parameterise the CG model will also play a big role in how accurate it will be. Overall, the model must capture the underlying physics, otherwise any results obtained will lack meaning and will not provide insight into the physical nature of the system. Indeed, CG models can be used as a research tool to assess how much molecular information must be kept in order to observe certain properties⁽¹⁵⁴⁾.

There are three attributes to judge the quality of CG models: representability, robustness, and transferability⁽²⁴⁾. Representability is a measure of how well the model describes state points outside the range used in the model development. Robustness is the force field's ability to predict structural, thermodynamical and transport properties not usually included in

parameterisation with high accuracy. Transferability is used within a group contribution force field to describe the ability to use a single group in different molecules and maintain accuracy. Therefore, the goal of CG models is to design ones that are accurate over a wide range of state points (representable), for a wide range of properties (robust), and whose groups can be applied to a wide range of molecules (transferable).

Multiple methods exist to obtain CG potentials, and they are categorised into two groups: bottom-up and top-down approaches. The former uses atomistic simulations⁽¹⁵⁰⁾ as the input and the latter requires macroscopic data.

2.5.1 Bottom-up approaches

The bottom-up approaches can be sub-divided into two main groups, structure-based and force-based methods⁽²³⁾.

Structure-based methods

These methods use potentials that are constructed to reproduce the structural characteristics in a CG simulation. The target functions are usually obtained from atomistic simulations but can also be experimentally derived⁽¹⁵⁰⁾. A common structure-based method is the iterative Boltzmann inversion (IBI)⁽¹⁵⁹⁾ where the radial distribution function (RDF) is the target reference function. It is commonly used because of the straightforward implementation and the robustness of the algorithm. This method uses a tabulated potential that is able to reproduce a target radial distribution function $g_{ref}(r)$ from an atomistic simulation through a simple Boltzmann inversion⁽¹⁵⁹⁾:

$$V_{PMF}(r) = k_B T \ln[g_{ref}(r)] \quad (2.112)$$

where $V_{PMF}(r)$ is the potential of mean force (PMF) between pairs of CG beads which can be obtained as a function of their distance r . However, the PMF cannot be obtained by using a pair potential for a CG model, as there are multi-body contributions from all the particles in the system. An iterative procedure is thus used to extract the inter-molecular potential V^{CG} ⁽¹⁵⁴⁾:

$$V_{i+1}^{CG}(r) = V_i^{CG}(r) + k_B T \ln \left[\frac{g_i(r)}{g_{ref}(r)} \right] \quad (2.113)$$

The procedure is initiated and the V_{PMF} is extracted from the simple Boltzmann inversion. The subscript i refers to the iteration number. This method relies on the Henderson uniqueness theorem⁽¹⁶⁰⁾, which states there is only one pair potential that can exactly reproduce a given RDF, thus the IBI method guarantees the theoretical uniqueness of the two-body CG interaction potential for the given g_{ref} .

There exist a number of other structure-based approaches, including the Inverse Monte Carlo (IMC) method⁽¹⁶¹⁾. This method again involves an iterative procedure to reproduce the RDF. However, IMC is non-local i.e. by updating the pair potential at the given distance, one considers the RDF at all distances, hence the number of iterative steps can be reduced. Compared to the IBI method, each step in IMC is more computationally demanding. The structure-based methods can be computationally demanding since they require a simulation at every iteration. Since atomistic simulations are used as the target functions, the accuracy of the resultant model will only be up to this level. The range of properties that can be obtained may only be limited to the radial distribution function that was used to determine the potential. These methods are therefore state dependent and will also suffer from transferability to other molecules and representability across different states unless many states and molecules are optimised together. This will inevitably lead to higher computational cost.

Force-based methods

These methods do not rely on pair-correlation functions, but instead on matching the forces at the atomistic level to the CG interaction sites as closely as possible ⁽¹⁶²⁾. The aim is then to reproduce the many-body PMF with a set of CG interaction functions. The reference forces \mathbf{F}_i^{ref} on the CG beads need to be calculated as a sum of the associated atomistic forces \mathbf{f}_γ ⁽¹⁵⁴⁾:

$$\mathbf{F}_i^{ref} = \sum_{\gamma} \mathbf{f}_{\gamma} \quad (2.114)$$

A model is then constructed in which the CG force field depends linearly on a number of fitting parameters. The fitting procedure is performed by calculating solutions to the following set of $N \times L$ equations ⁽¹⁵⁴⁾:

$$\mathbf{F}_{il}^{CG}(g_1 \dots g_m) = \mathbf{F}_{il}^{ref} \quad (2.115)$$

where $i = 1, \dots, N$, $l = 1, \dots, L$, $g_1 \dots g_m$ are the fitting parameters, N is the number of CG beads, and L is the number of reference frames used for CG. This calculation is repeated for a number of smaller parts of the trajectory and the final result is constructed as an average over the set of solutions.

Relative entropy

In this approach, put forward by Shell et al ⁽¹⁶³⁾ the relative entropy S_{rel} is obtained by minimising the discrepancy between the atomistic and CG distribution functions. S_{rel} can be considered as the amount of information lost in the CG procedure ⁽¹⁶⁴⁾:

$$S_{rel} = \int P_{AA}(\mathbf{r}) \ln \frac{P_{AA}(\mathbf{r})}{P_{CG}(\mathbf{M}(\mathbf{r}))} d\mathbf{r} + S_{map} \quad (2.116)$$

where P_{AA} and P_{CG} are probability distributions in AA and CG ensembles respectively, \mathbf{M} is the coordinate mapping which determines the configuration of the CG model (\mathbf{R}) as a linear combination of coordinates of the underlying atomistic model (\mathbf{r}) along with constants corresponding to the centre of mass c_i :

$$\mathbf{R}_i = \mathbf{M}_i(\mathbf{r}) = \sum_i c_i \mathbf{r}_i \quad (2.117)$$

S_{map} is a measure of the degeneracy of mapping and is given as a logarithm of the average number of AA configurations that can be mapped into a single CG configuration. S_{rel} is either positive or 0, the latter of which would imply the CG model perfectly reproduces the target model. A high value of S_{rel} would indicate a poor correspondence between the CG and AA models. If S_{rel} is at a minimum, then the CG model optimally (but not exactly) represents the underlying model. The IBI and IMC methods described previously can be considered as a subset of this framework.

2.5.2 Top-down approaches

Methods in this category rely on the availability of macroscopic data. There are multiple ways to obtain the necessary data, commonly experimental measurements, equations of state ⁽¹⁶⁵⁾, and atomistic simulations ⁽¹⁶⁶⁾ are employed to this end. Thermodynamic data such as density

⁽¹⁶⁵⁾, vapour pressure ⁽¹⁶⁵⁾, surface tension ⁽¹⁵⁾, and free energy of transfer between two different solvents ⁽¹⁶⁶⁾ can be used as reference data to match the force field parameters to. Top-down approaches are usually employed to parameterise the non-bonded interactions, as they do not usually yield information on the bonded interactions. To obtain the intramolecular interactions, a bottom-up method is used in conjunction with a top-down method ⁽¹⁶⁷⁾. The top-down methods can be grouped into two types: methods that optimise the force field parameters via iterative simulation, and optimisation by using theories that directly relate the force field parameters to the free energy or macroscopic properties of the system.

Optimisation through iterative simulation

This methodology can be used for both atomistic and CG potentials, and because it requires manual iterative adjustment of force field parameters it can become computationally intensive. In terms of CG potentials, the most common examples that use this method are the MARTINI force field ⁽¹⁶⁸⁾ and those of Klein et al ⁽¹⁶⁷⁾. The former method employs a 4:1 mapping and the non-bonded interactions are matched to partitioning free energies in water and organic phases. The estimation is performed systematically by varying the LJ σ_{ij} and ϵ_{ij} through a set of pre-determined combinations ⁽¹⁰⁴⁾, which drastically reduces the parameter space. The bonded parameters were obtained from matching the CG structure to the all-atomistic simulations using a bottom-up approach ⁽¹⁰⁴⁾.

In a similar fashion, the models of Klein et al are parameterised using a top-down method for the non-bonded interactions and a bottom-up method for the bonded interactions. In their models a mapping of 3:1 is often used. Experimental density, surface tension, compressibility, free energy of hydration, and/or free energy of transfer data were used to parameterise the non-bonded interactions. These parameters were further optimised by running single phase and vapour-liquid equilibrium simulations ⁽¹⁶⁷⁾. The bonded interactions were matched to the bond length and angle distributions obtained from atomistic simulations ⁽¹⁶⁹⁾. Klein et al use Mie potentials in various forms (9-6, 8-4, 10-4, and 12-4) and the ϵ_{ij} and σ_{ij} were optimised after selecting the exponent pair ⁽¹⁶⁷⁾. The form of the potential was validated by comparing CG radial distributions to those from atomistic simulations.

The above methods suffer from high computational cost since each trial set of parameters requires a simulation. The MARTINI model only allows several combinations of the LJ σ_{ij} and ϵ_{ij} , which can reduce the parameter precision. Despite the simplicity of the MARTINI model, it has been shown to capture biologically important structures like lipid bilayers and membrane protein assemblies ⁽¹⁷⁰⁾. The focus of the MARTINI model is in the transferability of groups to other compounds, and this leads to limited robustness of the model: only the liquid phase properties are captured, the accurate simulation of liquid-vapour interfaces is not possible ⁽¹⁷⁰⁾. The models of Klein et al are found to be transferable, and the ability to reproduce protein structural data not included in model parameterisation shows some degree of robustness ⁽¹⁷¹⁾. However, whilst the water model is parameterised to be in the liquid state between 273 K and 373 K, the surface tension and density are fit to a single temperature point of 303.15 K ⁽¹⁷²⁾. The representability of this model is therefore not guaranteed. The general advantage of the iterative simulation approach is that it allows flexibility of the form of potential. This contrasts with theory-based approaches, which typically are designed to work with one form only. Despite this, the MARTINI and Klein et al models limit themselves to the LJ and Mie potentials respectively.

Optimisation by SAFT theory

It has been established in section 2.3 that the SAFT equation of state provides an analytical relation between the non-bonded potential and the thermodynamic parameters. This places it well as a CG tool since it can be used alongside optimisation algorithms to optimise the intermolecular parameters to macroscopic thermodynamic data ^{(24) (93) (88) (103) (18) (165) (173) (30)}

⁽⁸⁹⁾. The optimisation using the SAFT equation of state is less computationally expensive than a purely iterative simulation route.

There are practical considerations when using the SAFT EoS as a CG methodology, since certain factors cannot be accounted for in molecular simulation. The association contribution A_{assoc} is set to 0, see equation (2.54), because the short-range potentials used to represent hydrogen bonding cannot be implemented easily in molecular simulations. The Born term A_{Born} is also set to 0 as an implicit representation of solvent polarity is taken in SAFT MD approaches for example the water models ⁽¹⁸⁾ are represented with non-polar effective Mie potentials. To ensure consistency with simulations the segments are treated as tangentially bonded. There is no distinction in the SAFT theory between branched and linear molecules, and so it provides no information about the bonded potentials. The approach then should be using SAFT for the non-bonded interactions, and a bottom-up method for the bonded interactions.

The SAFT equation of state is firmly rooted in statistical mechanics and attempts to create an accurate molecular description. This should improve the ability of the model to accurately predict state points and properties beyond those included in the parameterisation strategy ⁽²⁴⁾. The fast model parameterisation possible with the SAFT approach means that it is feasible to include data over a wide range of conditions, for multiple molecules, and of multiple properties simultaneously. This should improve the model's representability, robustness and transferability. The parameterisation process has been streamlined further through the implementation of a corresponding states correlation ⁽²⁸⁾, which as mentioned before has been ported to an online website ⁽²⁹⁾. This effectively reduces the number of necessary simulations in model development.

There are limitations with the SAFT theory, it is a fluid model and can only be used to study vapour, liquid and supercritical conditions. The SAFT equation of state typically over-estimates the critical point when the parameters are fit up to temperatures of $0.9 T_c$, hence the representation in the critical region may be limited as a result. The SAFT EoS is a homogeneous model, which means it cannot be directly applied to systems of strong heterogeneous character, for example the formation of lamella by amphiphilic molecules. This can be circumvented by fitting the polar and non-polar groups making up the amphiphilic molecules independently to systems with no heterogeneous character (e.g. liquid mixtures) ⁽⁹⁰⁾. These can then be combined to study the phase behaviour via simulation. The SAFT EoS describes molecules as fully-flexible tangentially bonded chains, which may not be applicable to molecules where local structuring is important, such as branched surfactants. The inclusion of bonded potentials should help to model these complex molecules more accurately ⁽¹⁶⁵⁾. The lack of explicit modelling of hydrogen bonding is a challenge for all CG models. This can severely impact the representability of these models, especially those for molecules where these interactions are important such as water. The robustness will also be impacted as many liquid-liquid equilibria and transport properties are strongly related to these short-ranged anisotropic interactions. Using spherical Mie beads to represent these interactions is not possible, but along small temperature ranges where the hydrogen bonding behaviour does not change significantly can these models capture properties of the system, such as the CGW2-bio model presented in ⁽¹⁸⁾. Another approach is to use temperature-dependent parameters such as the CGW1-ift and CGW1-vle models ⁽¹⁸⁾.

Chapter 3 Modelling the aqueous behaviour of AOT

3.1 Chapter overview

The combined SAFT- γ Mie and SAFT-VRE Mie force fields are used to develop a model for the aqueous mixtures of AOT in this chapter. The AOT surfactant is coarse-grained in a group-contribution fashion. Pre-existing models were used to represent water and the charged surfactant beads. Bottled SAFT is used to obtain the pure parameters of the uncharged surfactant beads. The unlike bead interactions are parameterised to reproduce either the vapour-liquid equilibria of a pure molecule that can be modelled by both beads, or the liquid-liquid equilibrium of the corresponding mixture. This allowed for the study of phase behaviour and structural properties of the surfactant-water mixture. MD simulations using these force field parameters showed the formation of a lamellar phase at ambient conditions. At high temperature a transition to an isotropic phase occurs. The MD simulations do not indicate a structural transition in the middle of the lamellar phase region, instead there is a transition from flexible to rigid bilayers. These observations, as well as the calculated bilayer thickness at room temperature, are in agreement with recent experimental data.

3.2 Introduction

Docosate sodium (Molar mass: 444.56 g/mol, CAS number: 577-11-7), also known as Sodium dioctyl sulphosuccinate, sodium bis(2-ethyl 1-hexyl) sulphosuccinate, and more commonly as AOT (Aerosol® OT brand), is an anionic surfactant with two hydrocarbon tails. Each tail is further branched with an additional ethyl chain. The general aqueous behaviour of AOT has been studied extensively and the phase diagram is well-established⁽⁵⁸⁾. At 25 °C, the CMC of AOT occurs at ca. 0.12 wt % AOT, and a micellar phase extends to 2.5 wt %. A two-phase region extends to 17.5 wt %, where the aqueous solution is in equilibrium with dispersed lamellar bilayers. The lamellar phase is the predominant phase that exists until 77 wt %, where reverse structures form. At the region 78-82 wt % AOT, a bicontinuous cubic phase occurs, and at 82 wt % and above a reverse hexagonal phase is present. The experimental phase diagram is illustrated in Figure 3.1:

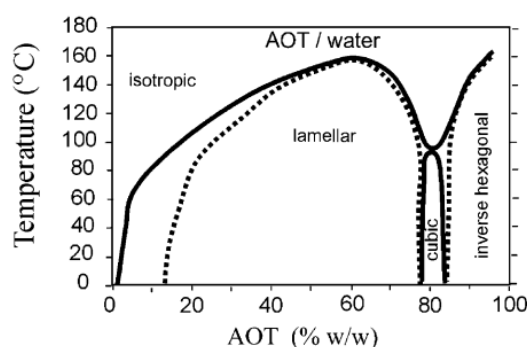


Figure 3.1 Experimental phase diagram of the AOT-water binary mixture. Taken from⁽⁵⁸⁾.

The preferential formation of lamellar and reverse phases with little or no interfacial curvature is related to the shape of the AOT molecule, which has a slightly bulkier hydrophobic region compared to the hydrophilic region. The liquid crystalline phases are of interest in research, with AOT-water formulations being some of the first experimental studies into such systems^(139, 174, 175). There is also interest in practical applications of AOT liquid crystalline phases, such as templating of functional materials including flat panel displays⁽¹⁷⁶⁾ and nanowires⁽¹⁷⁷⁾. The structures of the liquid crystalline phases can also be used to improve the delivery of drugs, and there are examples in the literature where the lamellar and cubic phase have enhanced the solubility of drugs used in anticancer, antibiotic and hypertension treatment purposes^(178, 179).

There have been multiple experimental investigations of the AOT-water system. Nave et al⁽¹³⁾ produced a series of surfactants analogous to AOT and studied the properties of dilute aqueous systems using drop volume tensiometry and neutron reflection. Interestingly no special effects were noted due to the 2-ethyl 1-hexyl chain structure found in AOT. Fontell⁽¹³⁹⁾ studied the entire lamellar phase via X-ray diffraction, and identified a structural rearrangement in the intermediate AOT concentration. This has been debated in the work of Fairweather⁽¹³⁸⁾, who related the anomalous result to an incorrect assumption in the experimental procedure, that when corrected shows a lamellar phase exists over the expected concentration range. AOT has been found in an experimental study to be toxic toward aquatic organisms⁽⁵²⁾, the measured toxicity for three aquatic organisms was higher compared to four perfluorinated surfactants. This study also found that when AOT is in mixtures with chlorinated compounds often used in water purification, the toxicity is higher than the individual molecules (synergism), highlighting the potential toxicological risk of co-occurrence. It is important to note that surfactant toxicity data is limited, indeed the authors noted that literature data for technical surfactants are scarce⁽⁵²⁾.

The number of molecular simulation studies of the AOT-water system are relatively few. Yang et al⁽¹⁸⁰⁾ studied the phase diagram of this system using the DPD (dissipative particle dynamics) method⁽¹⁵²⁾. In total 4 spherical particles were used to model the system, the AOT molecule was represented with 1 hydrophilic bead and 1 hydrophobic bead for each hydrocarbon tail, and the water was represented with 1 bead. The simulations contained AOT at 30 – 90 wt % in 10 wt % intervals. Overall, the structures observed were consistent with the experimental phase diagram, the lamellar, cubic, and reverse hexagonal phases observed were within the correct boundaries. The authors noted that at 40 wt % however there was a shift from the normal lamellar structure, which they deduced was due to a structural transition resulting in a new 'pseudo – reversed hexagonal phase' composed of rod – like micelles.

To study the micellar (1 wt% AOT), biphasic (7.2 wt% AOT) and bilayer (20 wt%) phases, Bhat et al⁽¹⁸¹⁾ used AA simulations, and hypothesised that the observed rod-like micelle structure in the biphasic system is a pre-cursor to lamellar microdomains found experimentally in biphasic dispersions. This is the only MD study which has attempted to investigate this phase region. The likely reason behind this is the required simulation size and time length required to achieve adequate statistics. In the work mentioned, the smallest initial cubic box length was 12 nm. The corresponding time for that system was 1500 ns. Even the authors note that the large number of water molecules required to simulate the dilute solutions led systems to be significantly larger compared to previous AA MD simulations.

Another simulation study by Poghosyan et al⁽²⁰⁾ used all-atomistic (AA) and united atom (UA) scale molecular dynamics (MD) simulations on a single AOT bilayer containing 50 wt % surfactant. Large undulation effects were observed in the AA representation alongside diffusion of single surfactants across the water space, forming curved barriers. It was noted by the investigators that larger systems would need to be simulated to validate the existence of these defects. The study of this system using AA and UA representation is limited in terms of simulation size. However, when using more aggressive CG methods such as DPD, the influence of tail structure on the AOT molecular and liquid crystalline behaviour, which is reported to be of strong influence⁽¹³⁸⁾, can be neglected. CG modelling should be used to model this system instead.

The overall aim of the work in this chapter is to develop the AOT-water model using force fields obtained via the SAFT route. To the author's knowledge, this has not been done before. The developed model will be applied to study the experimental phase diagram of the system, in order to assess the model's capability to capture the underlying physics. The advantage of using SAFT-based force fields combines the rapidity of obtaining parameters that are directly usable in molecular simulations and the ability to study properties of the AOT-water system not accessible to the SAFT theory, for example structural properties. The rest of the chapter

is set out as follows: the development of the model for the AOT-water system is covered in section 3.3. The details of the MD simulation method are given in section 3.4. The methods used to analyse the simulations are presented in section 3.5. The results of the validation simulations are given in section 3.6 and the main simulation results are discussed in section 3.7. Finally, the conclusions are presented in section 3.8.

3.3 Model parameterisation strategy

The AOT surfactant molecule is recast to a CG representation by employing a 3:1 mapping. The CG model for water already exists (details are given below) and is presented alongside the recast AOT in Figure 3.2. It is important to note that the atomistic structure presented is just a guide to the eye, the parameterisation does not follow the geometry or energetics of any atomistic model.

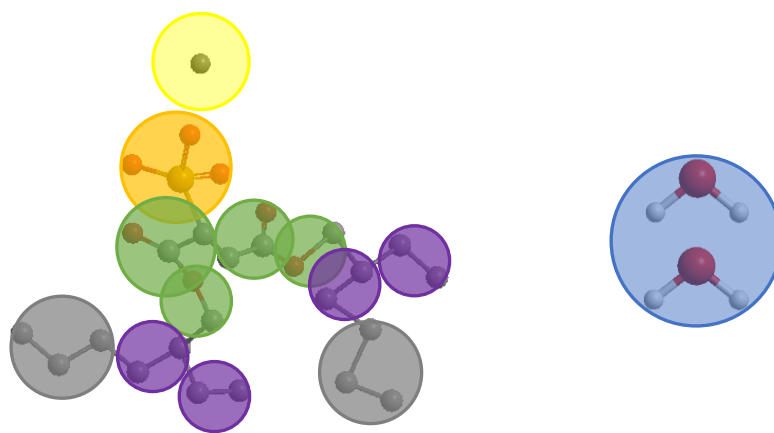


Figure 3.2 CG representations of the molecules used in this study: AOT (left) and water (right). The underlying atomistic structure is included as a guide to the eye. The hydrogens have been removed from the AOT model for clarity. These images are not to scale.

The resultant structure of AOT is composed of 12 beads of five different moieties: a grey bead CP comprising the terminal propyl group, 2 x purple beads CB representing a butyl group which includes the ethyl branch, 2 x green beads ES which represent a single ester group, an orange SO bead which represents the sulphonate ion, and a yellow bead NA which represents the sodium counter-ion, which is modelled as fully dissociated. It is acknowledged that this is not the only way of representing AOT, no attempt was made to optimise the mapping and the following approach is chosen without prejudice to the others.

The Bottled SAFT database ⁽²⁹⁾ is used to obtain pure-fluid force field parameters for the all the uncharged beads in the AOT model. It is acknowledged that assigning small molecules to the CG beads neglects connectivity for example the propyl group C_3H_7 is represented by propane C_3H_8 . It is assumed the difference in H atoms does not affect the energetics significantly. The force field parameters for the water model are taken from a previous study ⁽¹⁸⁾, wherein a single bead incorporates 2 water molecules and is parameterised to reproduce the liquid density and surface tension of pure water. This model was chosen because it allows for the simulation of larger systems with lower computational cost.

The force field parameters for the charged beads in the surfactant model are taken directly from a previous study of sodium chloride and sodium bisulphate in water ⁽³¹⁾, where the SAFT VRE Mie force field is used. Both salts were modelled as fully dissociated. Whilst the parameterisation process was not carried out in this study it will be included here for the sake of completion. Ionic species are not volatile, and so Rahman developed the force fields in the

presence of water. The water models ⁽¹⁸⁾ used in their study included the one used in this work. The need for mixture data, as well as the large number of parameters that need to be determined will cause degeneracy in the parameter space. To overcome this, a number of assumptions were made by Rahman. The first is that the repulsive and attractive exponents are the same as the water models. The remaining steps followed the procedure set out in Section 2.3.3. To optimise the ion-water cross-energetic interactions, the target macroscopic data for sodium chloride was liquid density ⁽¹⁸²⁾ and osmotic coefficient ⁽¹⁸³⁾. For the sodium bisulphate system, the liquid density was the target data ⁽¹⁸⁴⁾.

The SO and NA beads are assigned charges of -1 and +1 respectively, in keeping with the model of Rahman. Whilst the charges are the same, there are obvious differences in structure between the bisulphate ion (HSO_4^-) and sulphonate ion (SO_3^-). As no experimental data for the SO_3^- ion could be found, it was decided to take the HSO_4^- model as an initial approach to get an idea of the accuracy of the method. Indeed the bisulphate ion parameters have reproduced the behaviour of aqueous mixtures of sodium dodecyl sulphate (SO_4^-), including micelle aggregation number and bilayer thickness, with accuracy ⁽³¹⁾. The different CG beads are summarised in Table 3.1. There remain cross-interactions that need to be validated before studying the surfactant-water system, and this is accomplished by optimising the fit between MD simulations and macroscopic data.

The intramolecular interaction parameters are not provided within the SAFT formalism since they are averaged out in the coarse-graining procedure. The bond-stretching potentials are chosen so that the beads are bonded at a distance equal to σ and are rigid. The angle and dihedral potentials are adapted from an AOT model of a previous study where the 4:1 MARTINI model was employed ⁽¹⁹⁾. In this paper the parameters were obtained by matching the structural properties of an atomistic model, so it is a structure-based bottom-up method. Figure 3.3 gives a representation of the whole parameterisation strategy.

Table 3.1 List of the names of the CG beads used in the system, with the corresponding underlying chemical, number of CG beads m and the bead colour.

Bead name	Bead chemical	m	Colour
CP	Propane	1	Grey
CB	Butane	2	Purple
ES	Methyl acetate	2	Green
SO	Bisulphate ion	1	Orange
NA	Sodium ion	1	Yellow
W	Water	1	Blue

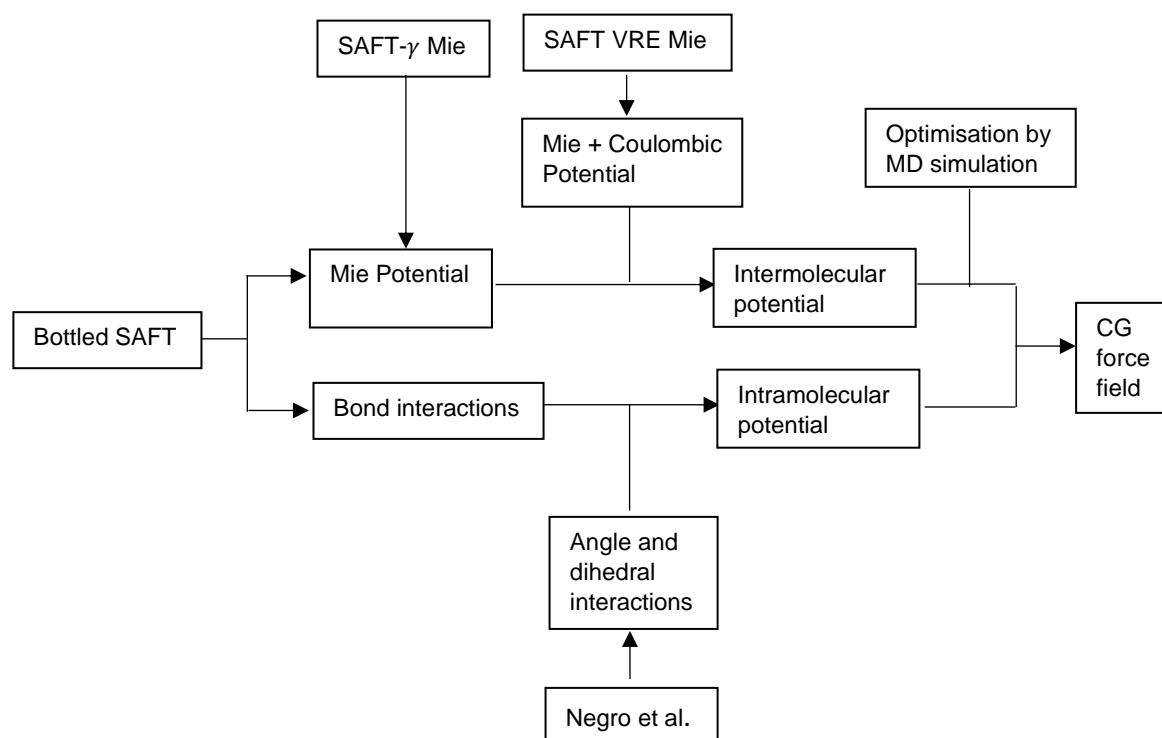


Figure 3.3 Flowchart of the coarse-graining methodology used in this work.

3.4 Molecular simulation details

All MD simulations in this study were performed using Gromacs 2019.2 ⁽⁷²⁾.

3.4.1 Alkane-ester simulations

The first cross-interaction to validate is that between both alkane beads in the AOT hydrophobic tail (CP and CB) with the methyl acetate bead ES in the intermediate section between surfactant head and tail. This is accomplished by parameterising the cross-interactions to reproduce macroscopic properties of molecules that contain both beads, in this case esters of varying alkyl chain length. Since the condensed phase of the binary system is to be studied, the target properties are the liquid density and surface tension of the pure esters. To ensure transferability, 4 different temperature points and 3 esters are included in the parameterisation strategy. Both the values of the bead bond distance $b_{0,ij}$ and ϵ_{ij} are varied to optimise the fit to experimental data.

NVT simulations are used to model the vapour-liquid equilibria of the selected esters. The number of butyl acetate (ES-ES-CP), pentyl acetate (ES-ES-CB-CB) and octyl acetate (ES-ES-CB-CB-CP) molecules were 4,000, 3,400 and 2,600 respectively. The molecules are abbreviated as BAC, PAC and OAC for butyl acetate, pentyl acetate and octyl acetate respectively. The molecular cut-off was set at 2.0 nm, as it is an aim that the resultant ester model can be used in conjunction with a water model for which this is the pre-requisite value ⁽¹⁸⁾. Periodic boundary conditions are applied in all directions. The box dimensions for each system are chosen such that $L_x = L_y$ and $L_z > 12 L_x$. This volume is too large for a pure liquid phase and so it coexists with a vapour phase, where there are two vapour-liquid interfaces. The temperature is varied from 293.15 K to 313.15 K, and the thermostat used is Nosé-Hoover with a time constant of 1.0 ps. The time step used is 0.01 ps, and the total simulation time is 40 ns. The averages are taken from the last half of the configurations. The liquid density is calculated from the corresponding density profile using the *gmx density* subroutine. The surface tension is calculated using the *gmx energy* subroutine, which employs the mechanical method which requires knowledge of the pressure tensor, as described in equation (2.78).

3.4.2 Ester-water simulations

The second cross-interaction to validate is between the ester bead ES and the water bead W. The same strategy as above is applied, except that the system property to compare with is the mutual solubility of the binary methyl acetate-water mixture across 4 different temperatures using NVT MD simulations. Prior to these simulations, an 80 ns NP_{zz}AT simulation was carried out to ensure the density was equilibrated. The pressure was set at 1 bar for all simulations. The barostat was Parrinello-Rahman with a time constant of 10.0 ps. The thermostat used is Nosé-Hoover with a time constant of 1.0 ps. The thermostat conditions are the same in the NVT simulations. The number of molecules for methyl acetate (ES-ES) and water (W) were 6,000 and 24,000 respectively. Note the 2:1 mapping for the water model⁽¹⁸⁾. This was chosen to ensure the initial volume fractions of both components were equal. The molecular cut-off was set at 2.0 nm, which is the pre-requisite value for using the water model⁽¹⁸⁾. Periodic boundary conditions are applied in all directions. The box dimensions for each system are chosen such that $L_x = L_y$ and $L_z > 7 L_x$. The initial configuration was a phase-separated system. The temperature is varied from 293.15 K to 313.15 K. The time step used is 0.01 ps, and the total simulation time is at least 240 ns, where the averages are taken from the last half of the configurations. The solubility, measured in mole fraction, is taken from the corresponding density profile of both components using *gmx density*.

3.4.3 AOT-water simulations

Table 3.2 lays out all the simulations carried out to study this binary system. The ambient temperature isotropic and 2-phase regions contain very small fractions of AOT. As mentioned in Section 3.2, this would require excessively large simulation sizes and time lengths to capture. This was deemed beyond the scope of this work, and so the focus was drawn to the AOT concentration range above 25 wt %.

Table 3.2 List of the systems studied in this chapter. Note that the water model contains two molecules per bead.

AOT molecules	Water molecules	AOT content (wt %)
337	20,000	29.39
385	20,000	32.22
443	20,000	35.36
650	20,000	44.53
920	20,000	53.19
1,320	20,000	61.98
2,000	20,000	71.18
2,000	12,000	80.45
2,000	6,000	89.17

The initial simulation point was at 71.18 wt % AOT where the initial molecular configuration is randomly inserted molecules. Periodic boundary conditions are applied in all directions for all simulations. The NPT ensemble with semi-isotropic barostat is the ensemble, where the pressure in the x/y and z dimensions are controlled independently. The thermostat is Nosé-Hoover and the barostat is Parrinello-Rahman. In all simulations the temperature is 298.15 K, and the pressure is 1 bar. The time step is set to 0.01 ps and the molecular cut-off is set to 2.0 nm, because this is a pre-requisite of using the water model⁽¹⁸⁾. The electrostatic interactions are calculated using the Particle Mesh Ewald method with a grid spacing of 0.29 nm. Only the ionic beads are modelled with explicit charge. The dielectric constant is determined using the approach described in section 3.3.1. For a solvent composed of only water at 298.15 K, $d_V = 0.3777 \text{ dm}^3 \text{ mol}^{-1}$ and $d_T = 1403.0 \text{ K}$, which obtain an absolute average deviation (AAD%) of 0.97 % when compared to experimental values of ϵ_r in a temperature range 273 – 423 K. When considering a wider temperature range 273 – 773 K, the AAD% rises to an acceptable 5%⁽²⁷⁾. Inserting the d_V and d_T parameters into equation (2.67) results

in $d = 1.4 \text{ dm}^3 \text{ mol}^{-1}$. The density of water predicted by the water model used in this work is $55.50 \text{ mol dm}^{-3}$ ⁽¹⁸⁾, these values are substituted into equation (2.66), which yields a dielectric constant equal to 78.68. The simulations are run for 200 ns, and the last half of the configurations are used to calculate averages. The systems with 29.39 – 61.98 wt % AOT are simulated by reducing the number of AOT molecules from 71.18 wt % AOT, and the systems 80.45 wt % and 89.17 wt % AOT are simulated by reducing the number of water beads from the 71.18 wt % AOT system. All simulation images are produced using the VMD package ⁽¹⁸⁵⁾.

3.5 Analysis methods

To characterise the surfactant-water systems analytical methods are employed. The phase morphologies of each system are studied by analysing the molecular organisation using the second rank orientational order parameter S_2 . The calculation procedure is described in Section 2.4.6. In this work \mathbf{u}_i is defined as the end-to-end vector connecting the beads SO and CP, meaning an average is taken over both hydrocarbon tails in an AOT molecule.

The bilayer phase is characterised by calculating the bilayer thickness, which can be estimated from the electron density profile of the sulphonate headgroup bead SO along the direction perpendicular to the bilayer surface. This distribution is calculated using the *gmx density* sub-routine. The distance between the distribution peaks is equal to the bilayer thickness. In systems where multiple bilayers exists an arithmetic average of the thickness is calculated.

3.6 Validation and model creation

3.6.1 Alkane-ester interactions

The optimum force field parameters are defined as those that achieve the minimum absolute average deviation (%AAD) from the target data ⁽⁹⁴⁾. This is defined in equation (3.1). The liquid density is matched by varying the equilibrium bond length $b_{0,ij}$ between the beads of different nature. The surface tension is matched by varying the cross energetic parameter ϵ_{ij} . The optimum fit is found when $b_{0,CPCB} = 0.6 \sigma_{CPCB}$, and $b_{0,CPES} = 0.6 \sigma_{CPES}$ and $b_{0,CBES} = 0.6 \sigma_{CBES}$, and when $\epsilon_{CPES} = 302.09 \text{ K}$ and $\epsilon_{CBES} = 239.25 \text{ K}$. This was accomplished through extensive optimisation by MD simulation. In total 60 MD simulations were performed to find the optimised force field parameters.

As shown in Tables 3.3-3.5, by adjusting the cross-interactions to the same extent an accurate representation of the target properties is obtained for all esters. The system equilibrium is determined by monitoring the time evolution of the Mie potential energy between the ES and alkane beads. An example is presented in Figure 3.4 for the BAC system at 298.15 K. The energetics between the CP and ES bead fluctuate around a constant value of 5.62 kJ mol^{-1} (standard deviation 0.02 kJ mol^{-1}) indicating equilibrium. The density profile and time evolution of the surface tension for the BAC system at 298.15 K are shown in Figures 3.5 and 3.6 respectively. These are taken from the final 20 ns of MD simulation.

The surface tension time evolution contains large fluctuations, which is explained by virtue of the method employed. The average pressure tensor elements are required to determine surface tension. In MD codes, the most common implementation of this method is to calculate over the whole volume of the simulation box. It has been suggested the reason behind this is to follow the pressure calculation of homogeneous systems ⁽¹⁸⁶⁾. Despite this, an accurate value for surface tension can be calculated, 25.56 mN m^{-1} (compared to the experimental value of 24.78 mN m^{-1}), which is a consequence of correlation between fluctuations in the different directions. The density profile clearly illustrates two bulk regions of the liquid and vapour, with sharp continuous changes along the interfacial regions. The vapour-liquid equilibrium simulation image is displayed for each system at 298.15 K in Figure 3.7.

$$\%AAD = \sum_{i=1}^n \left(\frac{|X_{exp,i} - X_{sim,i}|}{X_{exp,i}} \right) \times 100 \quad (3.1)$$

It should be noted that no long-range corrections are included in the surface tension calculation. These are not recommended for MD simulations of simple inhomogeneous systems, particularly in applications to molecules in the vicinity of the interfacial region, where different environments are present at either end of the interface⁽¹⁸⁶⁾. Taking this into account, it has been recommended that the cut-off for accurate surface tension be kept at 6σ of the largest CG bead. However, in this work, the cut-off must be kept at 2.0 nm, as this is a prerequisite of the water model⁽¹⁸⁾. The limitations of this approach are noted; the ideal cut-off would be 2.93 nm based on the size of the CP bead. Indeed, future work will focus on finding a water model that does not have a pre-determined cut-off radius.

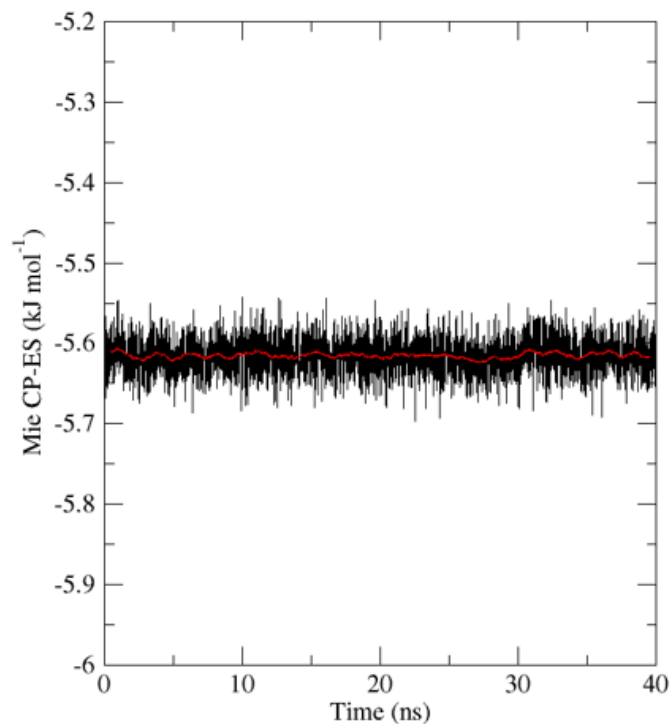


Figure 3.4 Plot of the potential energy between CP and ES beads for the BAC system at 298.15 K. The black line corresponds to the raw (unaveraged data), whilst the red line refers to the running average, every 100 configurations.

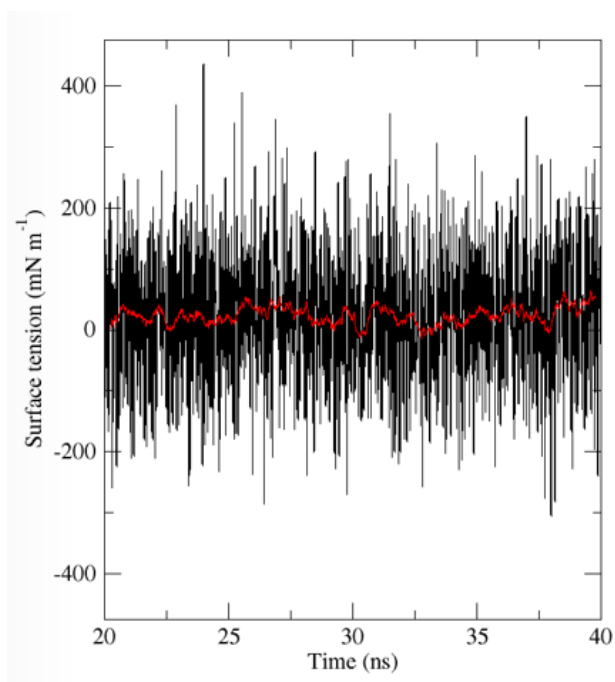


Figure 3.5 Plot of surface tension for the BAC system at 298.15 K over the last 20 ns of simulation. The black line corresponds to the raw (unaveraged data), whilst the red line refers to the running average, every 50 configurations.

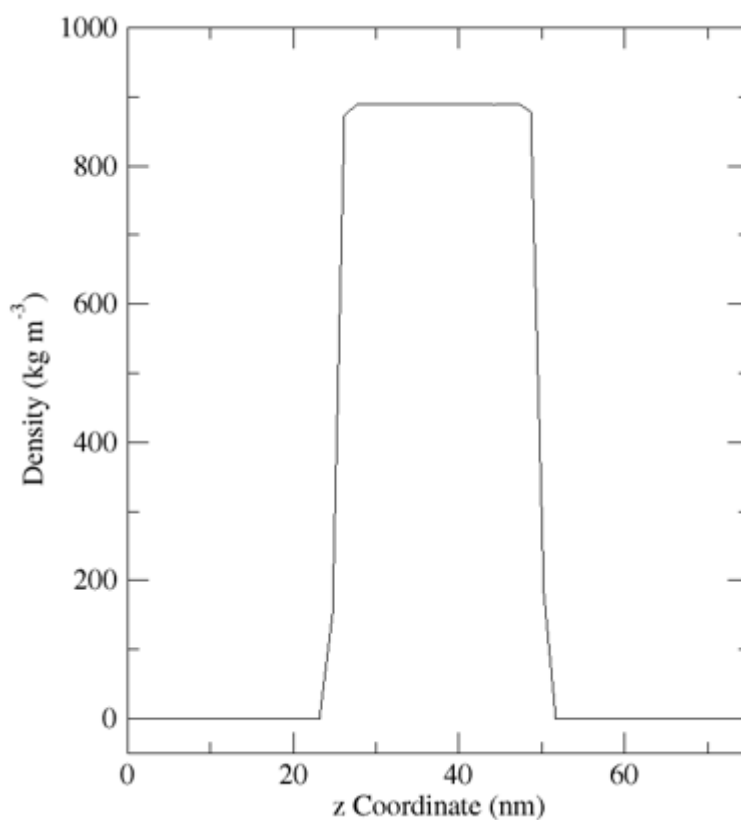


Figure 3.6 Equilibrated density profile of BAC at 298.15 K.

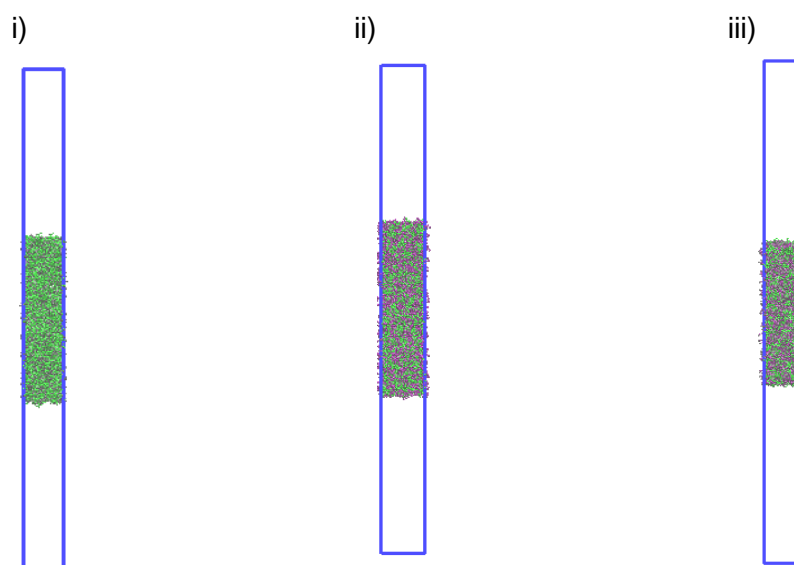


Figure 3.7 Equilibrated MD simulation images at 298.15 K for i) BAC, ii) PAC, and iii) OAC. The colour code is given in Table 3.1

Table 3.3 Comparison of experimental and optimised simulation values of liquid density (in kg m^{-3}) and surface tension (mN m^{-1}) for BAC.

Temperature (K)	Experimental		Simulation	
	Liquid density	Surface tension	Liquid density	Surface tension
293.15	881.16	25.31	894.81	26.36
298.15	876.00	24.78	889.24	25.56
303.15	870.81	24.24	883.54	25.45
313.15	860.32	23.18	872.18	24.01
%AAD			1.48	3.97

Table 3.4 Comparison of experimental and optimised simulation values of liquid density (in kg m^{-3}) and surface tension (mN m^{-1}) for PAC.

Temperature (K)	Experimental		Simulation	
	Liquid density	Surface tension	Liquid density	Surface tension
293.15	876.62	25.61	875.13	25.50
298.15	872.01	25.10	869.40	27.08
303.15	867.31	24.60	863.79	23.68
313.15	858.80	23.61	852.32	22.45
%AAD			0.41	4.25

Table 3.5 Comparison of experimental and optimised simulation values of liquid density (in kg m⁻³) and surface tension (mN m⁻¹) for OAC.

Temperature (K)	Experimental		Simulation	
	Liquid density	Surface tension	Liquid density	Surface tension
293.15	866.91	29.35	894.22	30.52
298.15	863.00	28.86	889.13	30.08
303.15	859.07	28.38	883.90	30.25
313.15	851.15	27.42	874.20	29.62
%AAD			2.94	5.71

3.6.2 Ester-water interactions

In these simulations a binary interaction parameter k_{ij} is used to adjust the cross energetic interactions to minimise %AAD between the experiment and MD simulations. The time evolution of the average interaction energy between the ES and W beads at 298.15 K is shown in Figure 3.8. After 175 ns the energetics reaches a steady value of -4.76 kJ mol⁻¹ (standard deviation 0.08 kJ mol⁻¹). The density profile for this system is presented in Figure 3.9, where two distinct bulk liquid phases can be observed, separated by an interfacial region. The best fit is obtained when $k_{ij} = 0.05$, for which the MD results are shown in Figure 3.10.

To fine-tune the k_{ij} parameter, the initial target data was the mutual solubility of the methyl acetate (1) – water (2) binary system at 298.15 K and 1 bar. The simulation settings were the same as in Section 3.4.2. The first simulation used $k_{ij} = 0$, to establish the magnitude of a needed binary interaction parameter. This simulation yielded a one-phase system, indicating that the k_{ij} should be positive. An initial guess was taken with $k_{ij} = 0.1$. Whilst this value provided a good estimate of x_1 in the methyl acetate-rich phase, the corresponding water-rich phase is represented poorly. To improve the representation of this phase, the simulations were repeated with k_{ij} in the range 0.04 – 0.07. For $k_{ij} < 0.04$, a one-phase system was generated. All the results are provided in Table 3.6, where the percentage absolute deviation (AD%) is reported.

Table 3.6 Absolute deviation from the mutual solubility data ⁽¹²⁹⁾ at 298.15 K and 1 bar

k_{ij}	%AD for x_1 , Water-rich	%AD for x_1 , Methyl acetate-rich
0.04	59.07	47.43
0.05	75.65	34.69
0.06	82.79	24.34
0.07	88.77	14.26
0.10	95.94	4.63

As shown, reducing k_{ij} leads to improved representation of the water-rich phase. Whilst $k_{ij} = 0.04$ yields the minimum %AD, the representation of the corresponding methyl acetate-rich phase is deemed too poor. Indeed, for this system the corresponding $x_{1, \text{Methyl acetate-rich}}$ is nearly half of the experimental value. Since it is desired to use this model in both water-rich and low-water systems, $k_{ij} = 0.05$ is taken as a compromise and used for all other simulations.

Before optimisation, the initial force field parameters would over-estimate the interactions between water and methyl acetate. Whilst the ester group would favour interactions with water due to the formation of hydrogen bonding, the presence of the alkyl groups would reduce this due to weaker dispersion forces. Hence a repulsive k_{ij} is not unexpected. Simulation images of each system are presented in Figure 3.11.

To the knowledge of the author, Feria et al ⁽¹⁸⁷⁾ reported the only other MD simulation study of the methyl acetate – water system, using a United Atom (UA) model. A contrast is provided between the SAFT CG model, the experimental data ⁽¹²⁹⁾ and the UA model in Figure 3.10. Compared to the UA model the CG model provides a better agreement with experimental data. The behaviour predicted by the UA model is similar to that exhibited by aqueous mixtures of CO₂ and methane ⁽¹⁷³⁾. These mixtures are dominated by large regions of immiscibility, and as such are categorised as Type III mixtures according to the classification of Scott and Van Konynenberg ⁽¹⁸⁸⁾ ⁽¹⁸⁹⁾. This is in contrast with experimental findings ⁽¹²⁹⁾, which would indicate Type II behaviour. The extent to which the intermolecular interactions differ between methyl acetate and water are less compared to the CO₂-water or methane-water systems. Whilst esters cannot form hydrogen bonds with themselves, the oxygen atom bonded to the carbonyl group allows hydrogen bonds with water. Compared to longer carbon-chain esters, this interaction will be quite prevalent in the methyl acetate-water mixture. This can also indicate why the system behaviour is difficult to capture quantitatively when using an isotropic Mie potential. Future work could investigate the explicit accounting of association sites in the CG model. Despite this, the model captures the Type II behaviour in a qualitative manner, as the solubility of water in the methyl acetate-rich phase does increase with increasing temperature. The SAFT CG model parameters therefore show some improvement compared to the UA model.

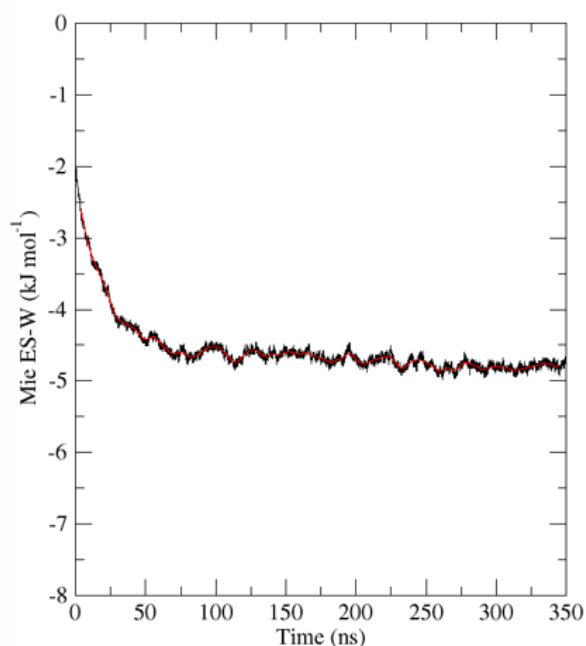


Figure 3.8 Plot of potential energy between ES and W beads for the system at 298.15 K. The black line corresponds to the raw (unaveraged data), whilst the red line refers to the running average, every 800 configurations.

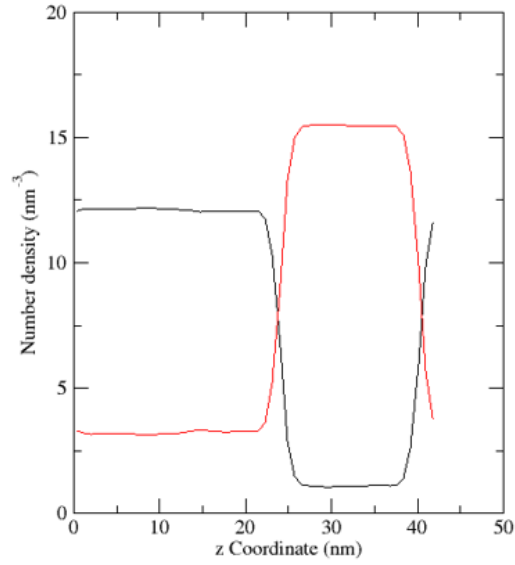


Figure 3.9 The particle number density profile of the MAC (black line) and water (red line) system at 298.15 K taken from the last 175 ns of simulation.

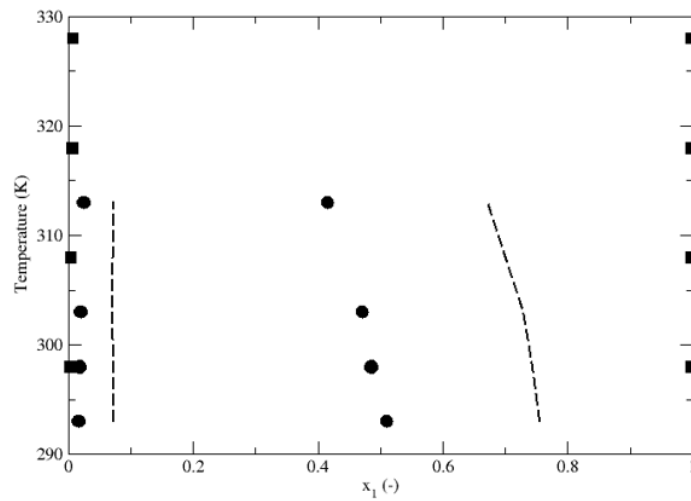


Figure 3.10 T-x liquid-liquid phase diagram at 1 bar for the binary mixture methyl acetate (x_1) and water. The SAFT CG model is shown as solid circles while the UA model by Feria et al ⁽¹⁸⁷⁾ is shown as solid squares. Experimental data ⁽¹²⁹⁾ is shown as dashed lines.

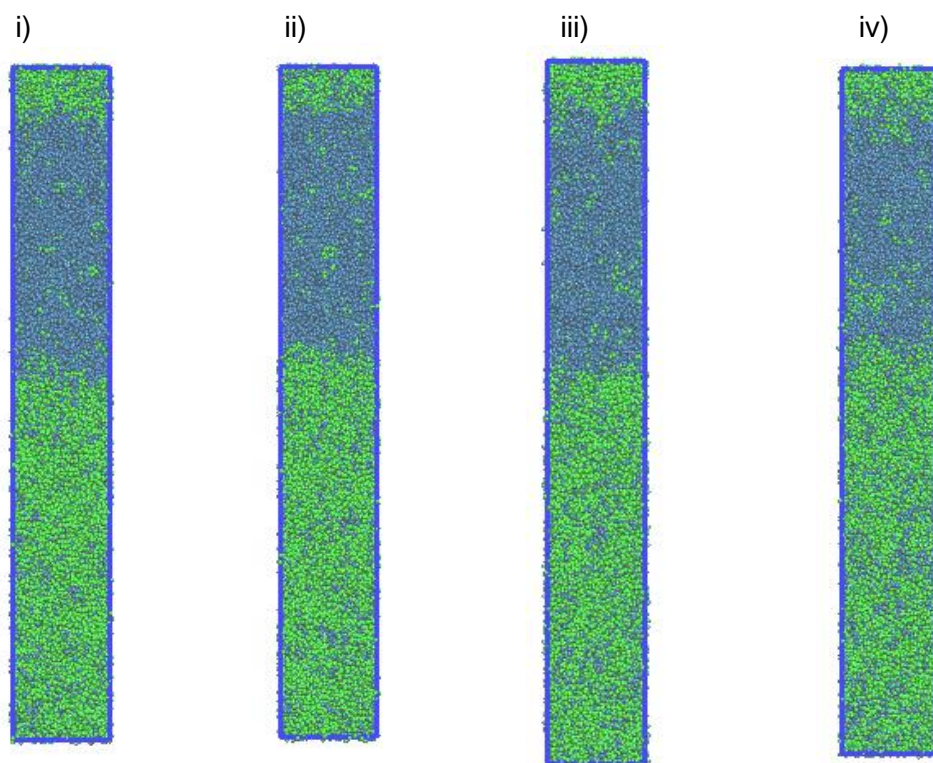


Figure 3.11 Equilibrated MD simulation images for the methyl acetate – water system at i) 293.15 K, ii) 298.15 K, iii) 303.15 K and iv) 313.15 K. The colour code is provided in Table 3.1.

3.6.3 Remaining cross-interactions

The cross-interactions between water (W) and the alkane beads propane (CP), and butane (CB) are parameterised by incorporating the k_{ij} value of 0.3205, which is taken from a previous study where the interfacial tension between water and a series of alkanes was the target property⁽¹⁹⁰⁾. In following with the work of Rahman⁽³¹⁾, the interactions between the charged beads (SO and NA) and the uncharged beads are expected to be few and of little relevance to the outcome of the binary interaction parameters. Therefore as an initial approach, the combining rules set out in equations (2.62)-(2.64) are used with no further parameterisation ($k_{ij} = 0$). The list of all intermolecular interaction parameters is provided in Table 3.7, and Table 3.8 summarises how each interaction was derived. ‘M&M’ refers to the M&M correlation, ‘Lafitte’ refers to the Lafitte combining rules, ‘VLE’ refers to vapour-liquid equilibrium data, ‘VRE Mie’ refers to the SAFT VRE Mie equation of state, ‘IFT’ refers to the interfacial tension, and ‘LLE’ refers to the liquid-liquid equilibrium. The development of the validated model permits application to the main AOT-water simulations.

Table 3.7 List of non-bonded intermolecular interaction parameters

Bead – Bead interaction	σ_{ij} (nm)	ε_{ij}/k_B (K)	λ_{ij}^r (-)	k_{ij} (-)
CP – CP	0.4871	426.08	34.29	-
CP – CB*	0.4416	325.25	20.94	-
CP – ES*	0.4355	302.09	27.39	-
CP – SO	0.4346	174.18	15.51	-
CP – NA	0.3596	50.39	15.51	-
CP – W	0.4311	273.44	15.51	0.3205
CB – CB	0.3961	256.36	13.29	-
CB – ES*	0.3900	239.25	16.99	-
CB – SO	0.3891	138.06	10.17	-
CB – NA	0.3141	43.01	10.17	-
CB – W	0.3856	217.35	10.17	0.3205
ES – ES	0.3839	397.25	22.01	-
ES – SO	0.3830	171.94	12.75	-
ES – NA	0.3080	54.18	12.75	-
ES – W	0.3795	378.61	12.75	0.0500
SO – SO	0.3820	74.42	8.00	-
SO – NA	0.3070	12.11	8.00	-
SO – W	0.3785	600.00	8.00	-
NA – NA	0.2320	8.92	8.00	-
NA – W	0.3035	179.76	8.00	-
W – W	0.3750	400.00	8.00	-

* The bead bond length is constrained to a constant value so that $b_{0,ij} = 0.6\sigma_{ij}$

Table 3.8 Parameter matrix indicating how each intermolecular interaction was derived.

	CP	CB	ES	SO	NA	W
CP	M&M	Lafitte	VLE	Lafitte	Lafitte	IFT
CB		M&M	VLE	Lafitte	Lafitte	IFT
ES			M&M	Lafitte	Lafitte	LLE
SO				VRE Mie	VRE Mie	VRE Mie
NA					VRE Mie	VRE Mie
W						VLE

3.7 Results and discussion

3.7.1 AOT-water phase diagram at room temperature

The energetics between the surfactant head bead SO and the W beads for the system with 29.39 wt% AOT is shown in Figures 3.12. The equilibrium value is $-1.85 \text{ kJ mol}^{-1}$ (standard deviation 0.01 kJ mol^{-1}). One of the main pre-requisites of an accurate AOT-water model is the ability to reproduce the phase boundaries and the mesostructures of the binary system. A high S_2 value would indicate the presence of an ordered phase. In particular the simulation value of S_2 has been reported to range between 0.3 – 0.5^(168, 191) for a bilayer. The time variation for the 29.39 wt% system is shown in Figure 3.13. The value reported is the average of both CP-SO vectors for each AOT molecule, and the time-average value is 0.5, indicative of a surfactant bilayer.

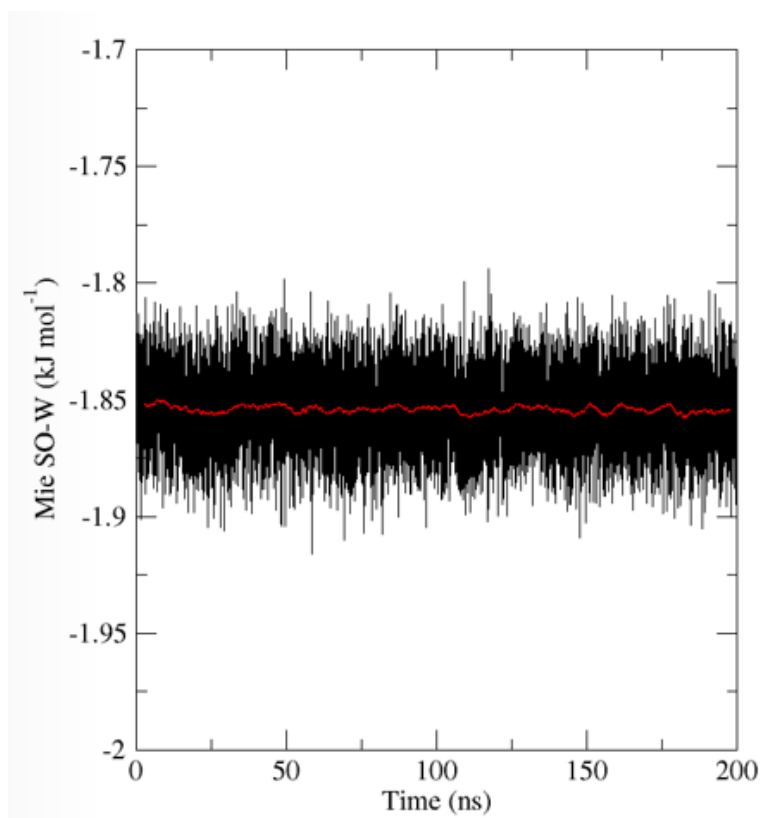


Figure 3.12 Potential energy between the SO and W beads at 29.39 wt % AOT. The black line corresponds to the raw (unaveraged data), whilst the red line refers to the running average, every 500 configurations

The variation of S_2 , averaged across both AOT tails, for all systems is shown in Figure 3.14. For systems with AOT content from 29.39 – 61.98 wt%, the average S_2 value increases from 0.47 to 0.57, before falling to 0.43 at 71.18 wt% AOT. Overall, the average S_2 values indicate the presence of a lamellar phase across this concentration range, which is confirmed by the final simulation snapshot images shown in Figure 3.15. The final simulation image at 71.18 wt% AOT reveals the developed lamellar phase forms curved domains which restrict the water layers. This is a consequence of the thin water layer thickness encountered at high AOT concentration, resulting in strong short-range steric hydration forces preventing close approach of the bilayers. This effect has been observed experimentally ⁽¹³⁸⁾ at AOT concentration above 60 wt %, and is reported to likely be a factor behind the cubic phase formation.

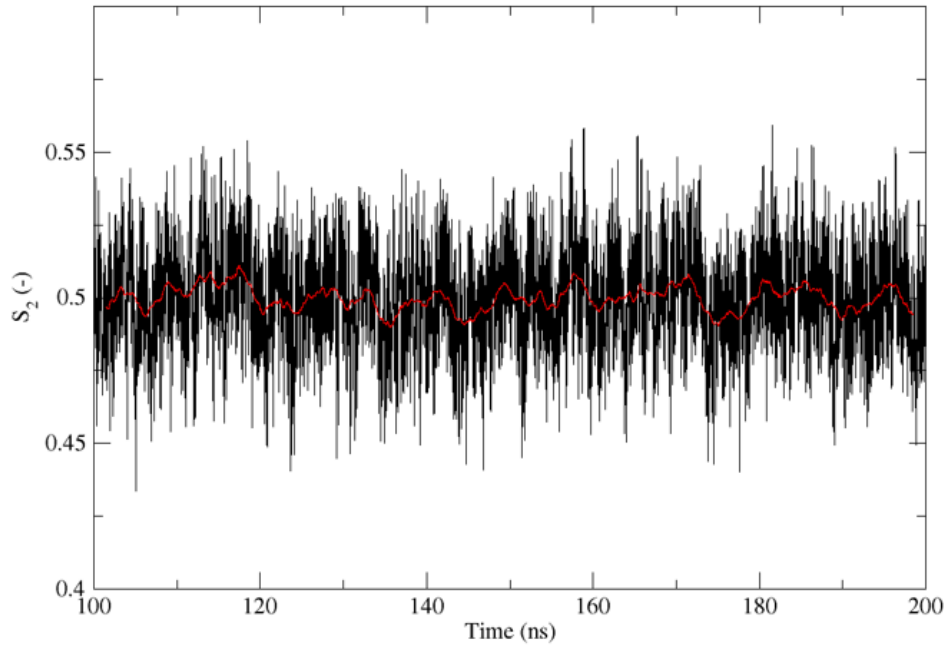


Figure 3.13 Time variation of tail-averaged S_2 for the 29.39 wt % system over the last 100 ns of simulation. The black line corresponds to the raw (unaveraged data), whilst the red line refers to the running average, every 300 configurations

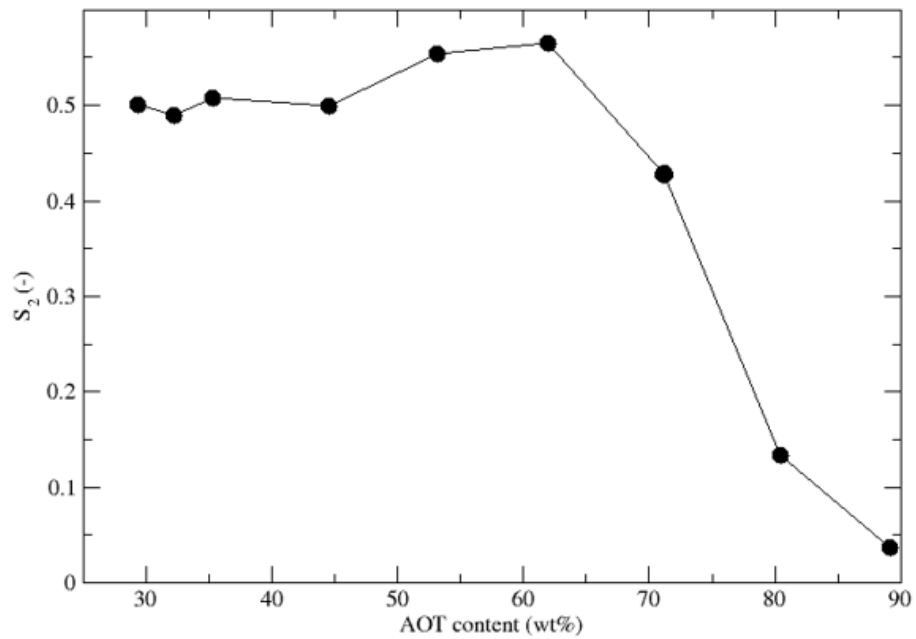


Figure 3.14 Variation of nematic order parameter S_2 for each system studied. The line is added as a guide to the eye.

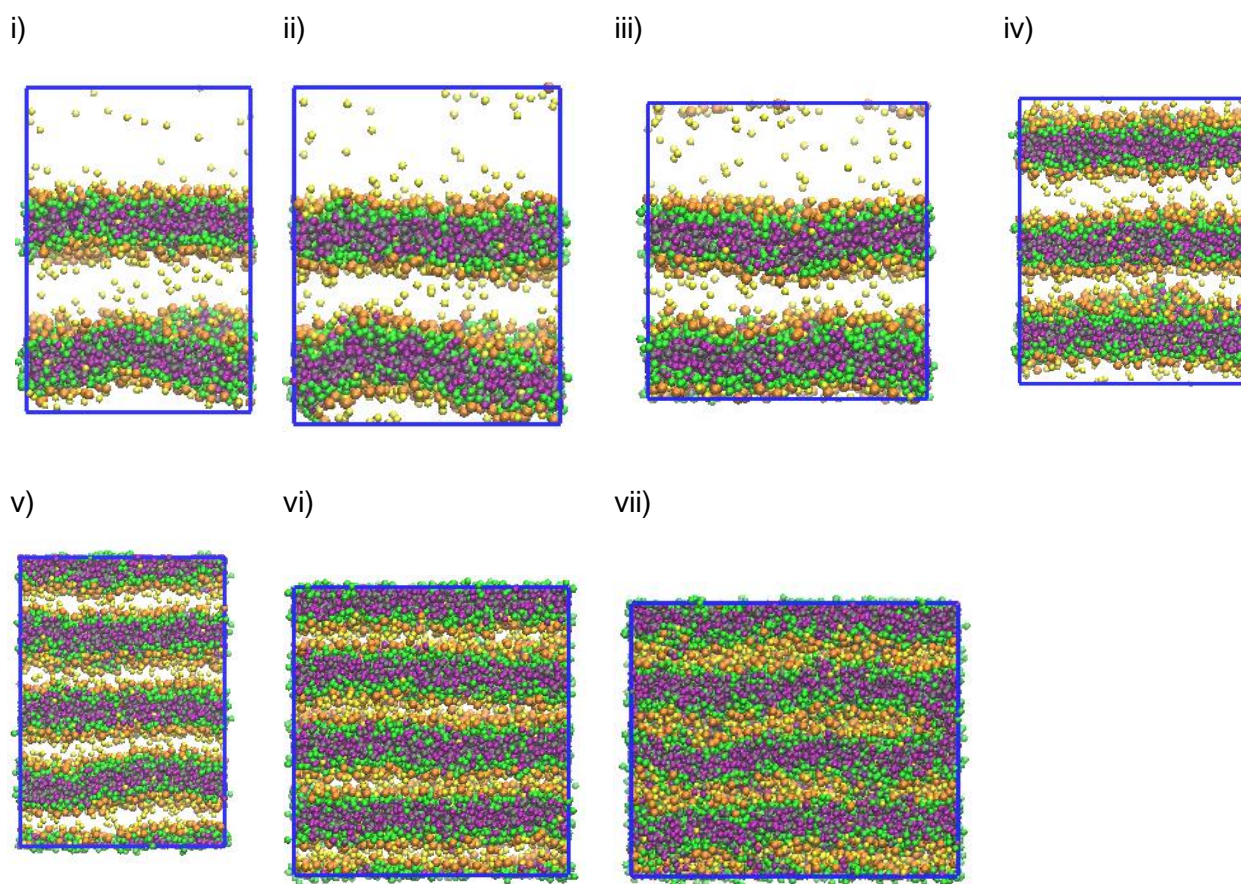


Figure 3.15 Equilibrated MD simulation images at AOT content of i) 29.39 wt%, ii) 32.22 wt %, iii) 35.36 wt % , iv) 44.53 wt %, v) 53.19 wt %, vi) 61.98 wt %, and vii) 71.18 wt %. The colour code is provided in Table 3.1. Water beads have been removed for clarity.

The reduction of S_2 that starts at 71.18 wt% continues until 89.17 wt%, indicating a change in phase morphology which is in agreement with the simulation images presented in Figure 3.16, where a reverse hexagonal and isotropic structures are present at 80.45 wt% and 89.17 wt% respectively. This is not in agreement with the experimental phase diagram, the reverse hexagonal phase is expected at system 89.17 wt%, and at 80.45 wt% the structure should consist of a bicontinuous cubic phase. The reason for this difference is likely due to system size, at such concentrations the ratio of surfactant to water molecules is very high. The amount of water present in these simulations may not be enough to lead to the assembly of these complicated structures. A similar issue was encountered in the work of Lindeboom⁽⁶⁵⁾ who tried to recreate similar phase morphologies for monoglycerides in aqueous solution using the SAFT- γ Mie force field. Larger system sizes would need to be simulated to investigate this further. Another issue may arise because of the nature of the water model: the polar interactions are not accounted for explicitly. These interactions may indeed be necessary to capture both the reverse phases and work would need to be carried out to create such a CG water model. To address these issues is deemed beyond the scope of this work.

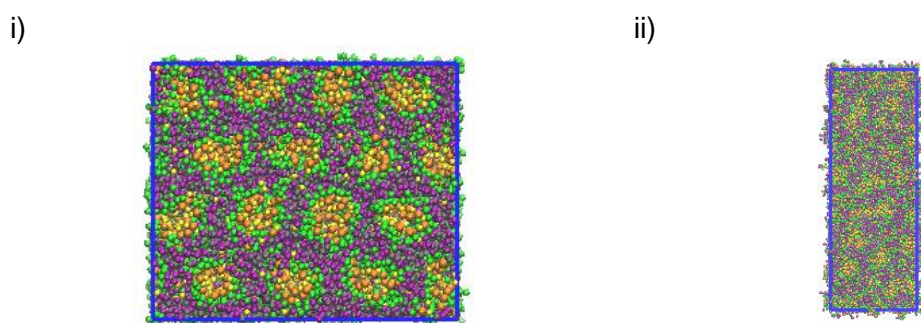


Figure 3.16 Equilibrated MD simulation images for systems with AOT content of i) 80.45 wt% and ii) 89.17 wt%. The colour code is provided in Table 3.1. Water beads have been removed for clarity.

3.7.2 Influence of AOT concentration on bilayer properties

The reproduction of the experimentally observed lamellar phase within the correct phase boundaries is an encouraging output of this methodology. Clearly the simulation images do not match with the X-ray scattering findings of Fontell⁽¹³⁹⁾, which indicated a structural transition within the concentration range of 33 – 45 wt % AOT. This finding led Fontell to characterise this phase in terms of 3 distinct regions, the low concentration (17.5 – 32 wt %, LCR), intermediate concentration (33 – 45 wt %, ICR) and high concentration (46 – 77 wt %, HCR) regions to take this into account. Going by the above convention, two systems (29.39 wt% and 32.22 wt%) are approximately in the LCR, two (35.36 wt% and 44.53 wt%) are in the ICR and three (53.19 – 71.18 wt%) are in the HCR. As the simulation images show in Figure 3.15, a lamellar phase exists in all regimes, which is not in agreement with the findings of Fontell⁽¹³⁹⁾ and DPD simulation studies^{(180) (140)}. The results in this work indicate there is no utility to describing the lamellar phase in this three – regime way. Indeed the findings by Fontell⁽¹³⁹⁾ were reported in the thesis of Fairweather⁽¹³⁸⁾ to be due to the mis-identification of the first-order Bragg peak, when performing the SAXS experiments no such anomalous behaviour is found when this procedural error is not repeated. Instead Fairweather⁽¹³⁸⁾ noted there to be a transition in lamellar phase structure: below 43 wt % the bilayers experience significant undulation due to dominant Helfrich forces related to large water layer thickness. Above 43 wt % bilayers become more rigid as the energy cost associated with deformation increases. The effect of concentration on the lamellar phase structure indicated by the results in this work can be analysed by exploring the S_2 value of each tail in an AOT molecule, which is presented in Figure 3.17.

It is observed that there is a difference between the S_2 value for Tail 1, which is defined as the shorter tail of the AOT molecule, as it contains the CP bead that is 3 beads away from the SO head bead, and Tail 2 which is longer (the CP bead is 4 beads away from the SO bead). This difference is more pronounced in the systems with 29.39 – 44.53 wt% AOT. After this, the individual S_2 values become closer in value, for example at 53 wt % the difference in value is 0.04. This contrasts with the values for system with 29.39 wt %, where the difference is 0.07. The increase in Tail 2 S_2 values indicates a closer alignment with the molecular director, which can be interpreted as a more upright tail orientation on average. The observed reduction in Tail1-Tail2 S_2 difference indicates both tails display the same extent of alignment as well at high concentration. As such these findings are in close agreement with the experimental findings⁽¹³⁸⁾ discussed above, with the MD simulations predicting the transition from flexible to rigid bilayer at 45 wt % compared to the experimental finding of 43 wt %.

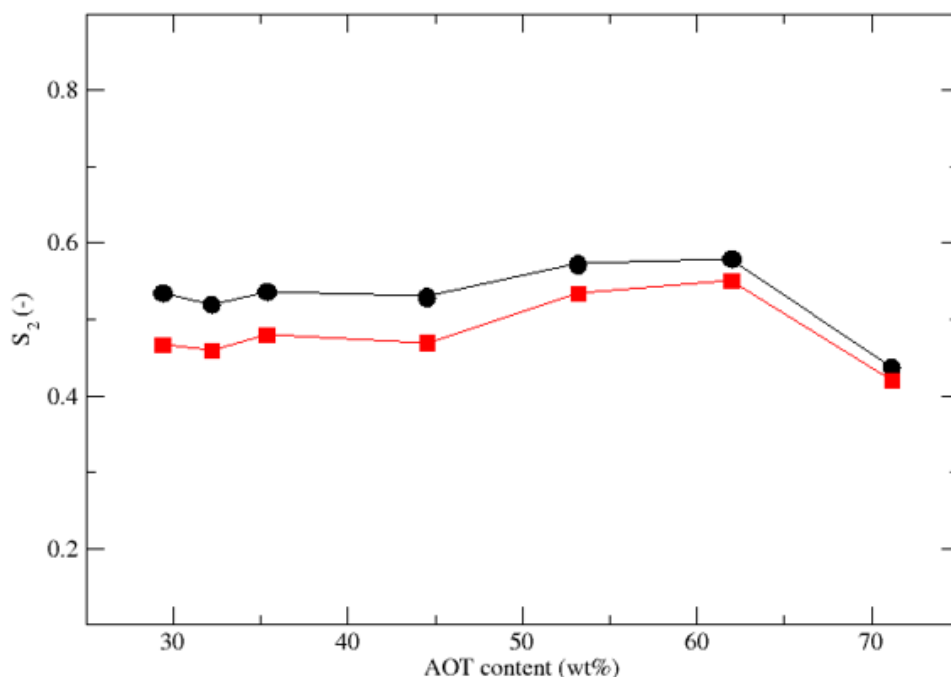


Figure 3.17 Variation of nematic order parameter S_2 for Tail 1 (black circles) and Tail 2 (red squares) for all bilayer systems. The lines are added as a guide to the eye.

The electron density distribution along the z dimension of the simulation box for systems at 29.39 wt% and 61.98 wt% are presented in Figures 3.18 and 3.19 respectively. The different number of peaks are due to the number of bilayers present in each system. The different magnitudes of the distribution peaks indicate an uneven distribution of surfactants in each bilayer. In Figure 3.19 the discontinuity is because, of the four bilayers present, the top bilayer is split across the periodic boundary. The average bilayer thickness for each simulation is presented in Figure 3.20, where there is very little change in the values across the systems studied. This analysis does not include the 71.18 wt % AOT system, due to the curved domains present which would influence the thickness calculation. The average value from the MD simulations is 2.05 nm, which is in reasonable agreement with experimental findings that the AOT bilayer thickness remains approximately within the range 1.8 – 2.0 nm in the lamellar phase⁽¹³⁸⁾. It is encouraging that the model can capture this property, because it was not included in the parameterisation strategy.

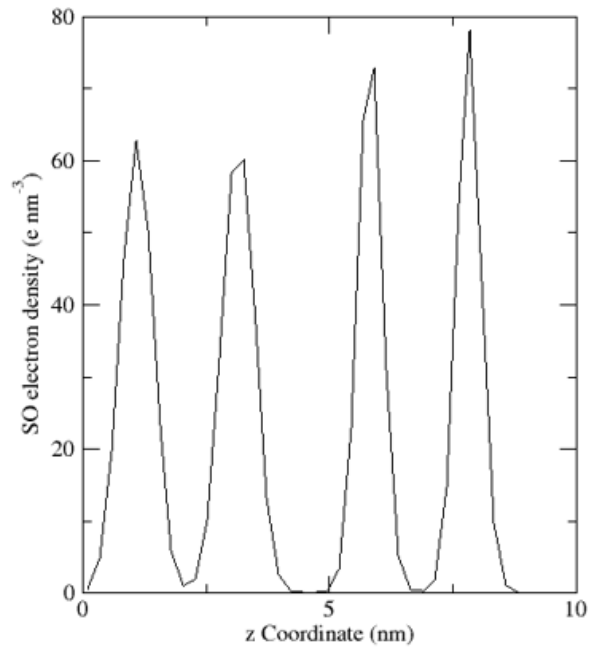


Figure 3.18 Average electron density distribution of the SO bead across the z dimension of the simulation box at 29.39 wt % AOT.

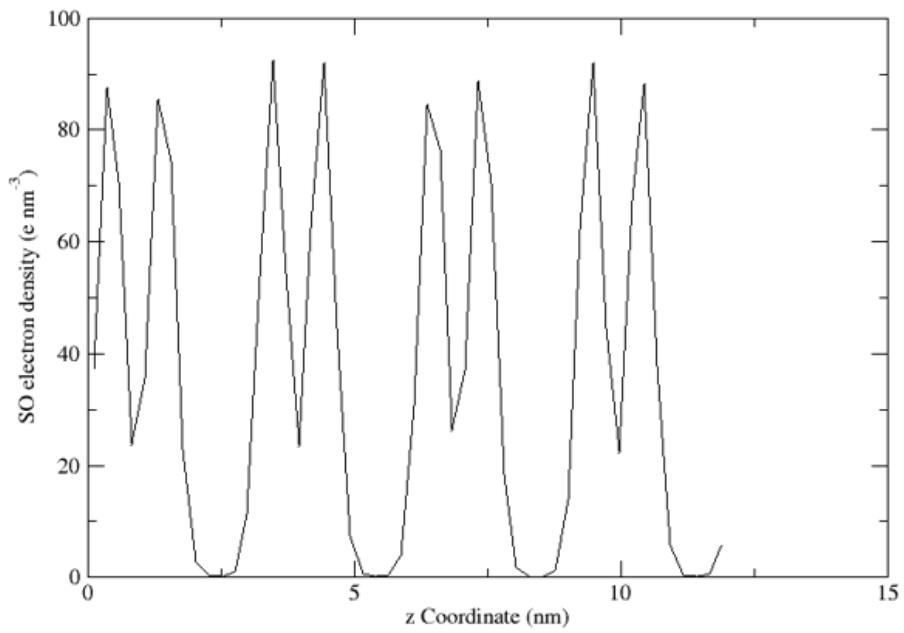


Figure 3.19 Average electron density distribution of the SO bead across the z dimension of the simulation box at 61.98 wt % AOT.

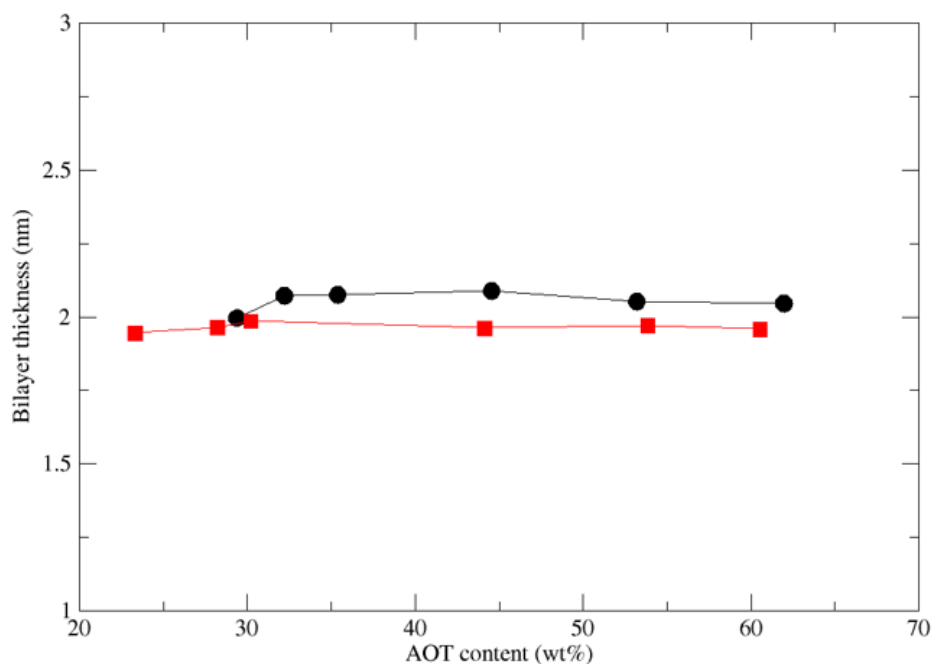


Figure 3.20 Average bilayer thickness as a function of AOT weight percentage. The MD simulations are represented by black circles and the experimental data by Fontell⁽¹³⁹⁾ (red squares) is included for comparison. The lines are added as a guide to the eye.

3.7.3 Ordered-isotropic transition

A further test for the model is the simulation of these systems at 433.15 K, as this is within the temperature region where for all concentration points there is a transition to an isotropic phase according to the experimental phase diagram⁽⁵⁸⁾. In these simulations the pressure control is isotropic, and the dielectric is set to 42.26 to account for the change in temperature. All other MD simulation conditions are the same. Whilst the water model used in this work has been parameterised to match water density and surface tension within the temperature range 293 – 313 K⁽¹⁸⁾, an investigation into aqueous solutions of polyethylene glycol found it performs well outside of this temperature range⁽⁶⁵⁾. Indeed, at 433.15 K, the density of water calculated by NPT MD simulation using these parameters is 48.79 mol dm⁻³, in close agreement with the NIST value of 50.41 mol dm⁻³⁽¹⁹²⁾. The final simulation images for systems of 29.39 wt% and 71.18 wt% AOT are shown below, showcasing the transition to isotropic from the lamellar phase. The corresponding average S_2 values are 0.048 (29.39 wt%) and 0.019 (71.18 wt%), which are indicative of the absence of an ordered phase. Therefore, the model presented in this work is able to capture some of the phase boundaries and morphologies specified by the experimental phase diagram.

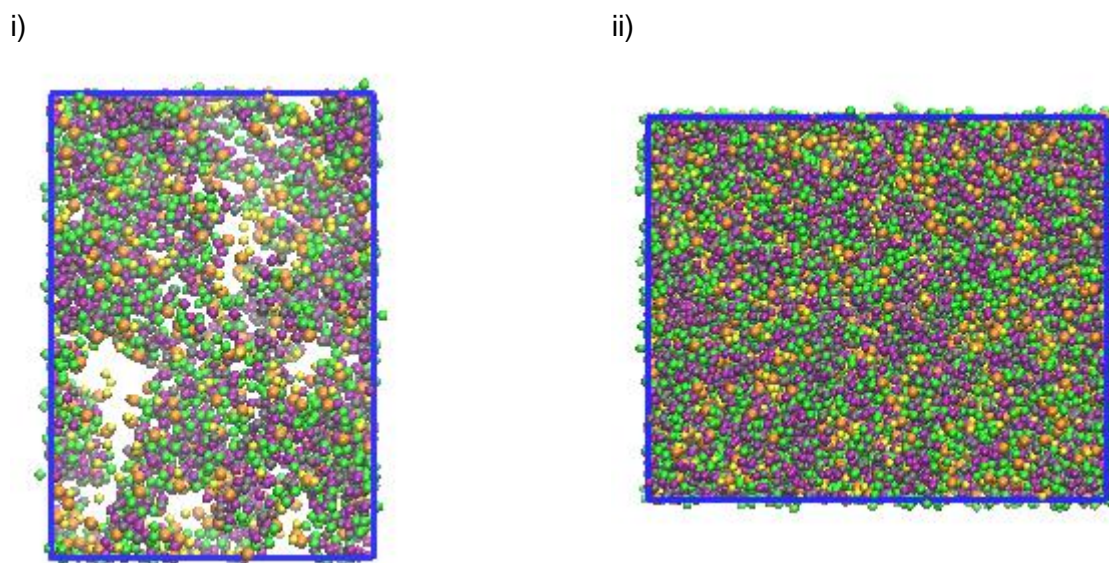


Figure 3.21 Equilibrated MD simulation images for systems with AOT wt% of i) 29.39 wt% and ii) 71.18 wt% at 433.15 K. The colour code is given in Table 3.1. Water beads have been removed for clarity.

3.8 Conclusions and outlook

A SAFT model for the aqueous mixtures of the ionic surfactant AOT is presented in this chapter. The surfactant molecule is represented in a group contribution manner, consisting of alkyl, ester and charged moieties. The force field parameters for the water and charged beads are taken from previous studies ⁽¹⁸⁾ ⁽³¹⁾. The remaining pure interactions and bonded interactions are obtained from Bottled SAFT. The other intramolecular parameters were assigned based on a previous CG MD study of AOT ⁽¹⁹⁾, which used a bottom-up structural-based method. The surfactant-surfactant and surfactant-water unlike interactions were validated by considering models of systems that contain both individual beads. The ester-water cross-interactions were scaled to the corresponding liquid-liquid equilibria data, where a qualitative fit was achieved via a single binary interaction parameter. Good agreement was achieved with the vapour-liquid equilibria data of 3 different esters of varying hydrocarbon chain length, with the maximum absolute average deviation being 5.71 % and 2.94 % for pure ester surface tension and density respectively.

The resultant AOT-water model was used to study the phase behaviour and structural properties. Figure 3.22 shows the experimental phase diagram with equilibrated MD simulation images super-imposed. MD simulations using these force field parameters showed the formation of a lamellar phase at ambient conditions from 29.39 wt% to 71.18 wt% AOT. The average calculated bilayer thickness at these conditions is 2.05 nm. By increasing the temperature to 433.15 K, a transition from lamellar to isotropic phase was observed. At 71.18 wt% the bilayers form curved domains due to the thin water layer thickness encountered at these conditions. These observations are in agreement with experimental data ⁽¹³⁸⁾ ⁽⁵⁸⁾. The room temperature transition from lamellar to reverse structures at high AOT content is not captured, which can be either due to system size limitations or the implicit modelling of the polarity of water. The MD simulations do not indicate a structural transition from 34 to 42 wt% AOT, instead there is a transition to more rigid bilayers at 45 wt %, as indicated by S_2 values. The data supporting structural realignment ⁽¹³⁹⁾ is then likely to be based on incorrect experimental procedure ⁽¹³⁸⁾.

The SAFT model has shown levels of representability, robustness and transferability. This is illustrated by the ability to capture information not included in the parameterisation strategy. The use of CG approaches with a strong link to the molecular theory, such as the SAFT approach, allow for the exploration of meaningful system sizes and times. This gives confidence in the use of the model to study surfactant systems, in particular incorporation of the model to study ternary systems. This is further encouraged by the CG nature of the force fields, which can overcome the computational limitations encountered by atomistic-scale simulations in studying surfactant self-assembly. A further benefit of the work completed in this chapter is that it reduces the number of necessary simulations to validate more complex ternary systems. This is because the cross-interactions between the surfactant hydrophilic sections and the hydrocarbon phase can be modelled in the same way as the interactions between the surfactant hydrophilic and hydrophobic sections. The creation and application of the AOT ternary system is presented in Chapter 4.

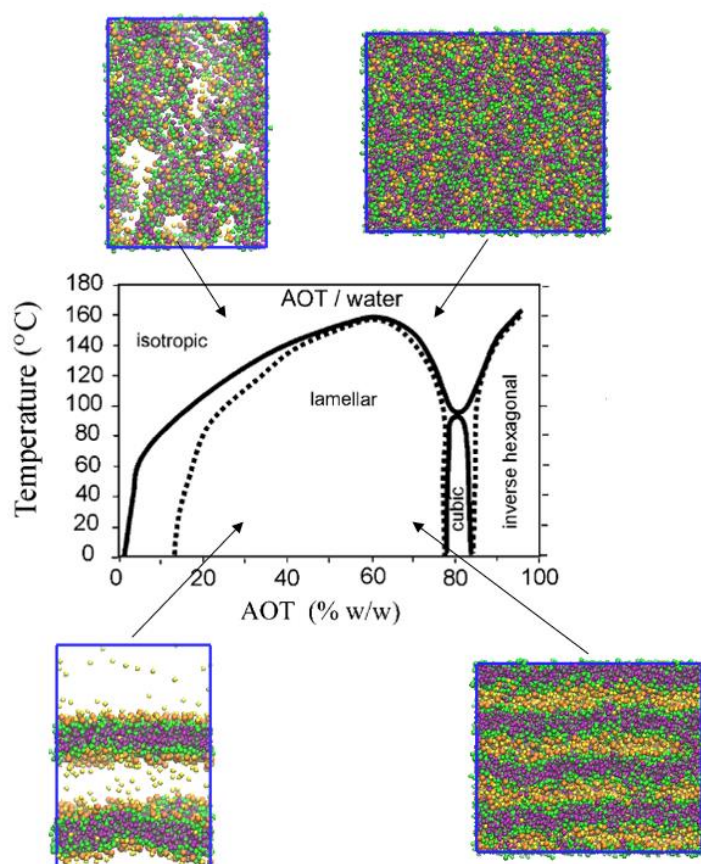


Figure 3.22 The experimental phase diagram for the AOT-water system ⁽⁵⁸⁾, with equilibrated MD simulation images for 29.39 wt% and 71.18 wt% at 298.15 K and 433.15 K super-imposed.

Chapter 4 Water effect in the reverse micellar formation of AOT

4.1 Chapter overview

In this chapter the ternary AOT-water-cyclohexane system is studied using the combined SAFT- γ Mie and SAFT VRE Mie force field. The model parameters for the AOT-water interactions have already been validated in Chapter 3. The cyclohexane model is obtained from Bottled SAFT. Due to the group contribution nature of the SAFT force fields, many of the intermolecular interactions were simply transferred from the AOT-water model. The resultant model is able to capture both phase morphologies and structural properties. The MD simulations reveal a transition from phase-separated systems to isotropic reversed micelle (RM) phases at low water content. The calculated average cluster size is in good agreement with experimental findings. The relationship between water content and RM morphology was studied. The reduction of water content results in a sharp reduction in average cluster size, highlighting its importance when considering RM stability. The water content does not significantly impact RM shape, since a predominant spherical shape exists for all RM systems investigated. The gained molecular insights can be further exploited for the design of more efficient, effective and non-toxic surfactants.

4.2 Introduction

AOT is commonly used as a stabiliser of water and hydrocarbon emulsions⁽¹³⁾. This is because it does not require a co-surfactant to be present to form stable emulsions. At low water fractions, the AOT surfactants spontaneously self-assemble around water droplets in such a way that the hydrophilic part surrounds the aqueous core, and the hydrophobic part forms the outer layer. The structure of these aggregates is the reverse of a normal micelle structure, and so it is termed a 'reverse micelle' (RM).

These aggregates find use in many industrial applications, for example the aqueous core can be a reaction medium for the synthesis of nanoparticles⁽³²⁾. Added polar or ionic components will become compartmentalised into the central cores. Due to the dynamic nature of these systems, the RMs will frequently collide via random Brownian motion and coalesce, allowing for the exchange of contents before breaking up again. This results in the mixture of any inorganic reagents resulting in reaction. RMs hence provide a suitable environment for controlled nanoparticle nucleation and growth, as steric stabilisation provided by the surfactant layer prevents separate nanoparticles from aggregating. Nanoparticles synthesised by this method are used in biocatalyst, food, biotechnology and pharmaceutical industries⁽¹⁹³⁾⁽¹⁹⁴⁾. Control parameters have been identified that influence the nanoparticle size and shape, including the water to surfactant molar ratio ($w_0 = [water]/[surfactant]$)⁽¹⁹⁵⁾, solvent type⁽¹⁹⁶⁾ and surfactant structure⁽¹⁹⁵⁾⁽¹⁹⁷⁾.

RMs can also be used to control the distribution of charged particles in non-polar fluids⁽¹⁹⁸⁾, where separation can be necessary for both stabilising components⁽¹⁹⁹⁾ and preventing explosions⁽²⁰⁰⁾ as is the case in the petroleum industry. Applications that rely on charges in non-polar fluids include the development of toner for printers and photocopiers⁽²⁰¹⁾, as well as measuring the activity of enzymes⁽²⁰²⁾. A more recent application is the electrophoretic displays found in e-Reader devices⁽²⁰³⁾, which can have the appearance of paper but can be refreshed to display different images, providing the benefits of both books and electronic displays. Non-polar fluids, such as cyclohexane, are characterised with low dielectric constants ($\epsilon_r \sim 2$)⁽²⁰⁴⁾. The inclusion of a charge in a non-polar fluid has a much longer-range effect compared to an aqueous medium ($\epsilon_r \sim 80$), as captured by the Bjerrum length⁽²⁰⁵⁾ which is the distance between two charges where the Coulombic energy is equal to the thermal energy, and is inversely proportional to ϵ_r . It has been noted⁽¹⁹⁸⁾ that expanding understanding of RM formation will enable improvement of surfactant ability to stabilise charge and find use in applications.

RMs can also be used in liquid-liquid extraction to separate bio-molecules from aqueous solution. In this process⁽²⁰⁶⁾ an aqueous phase containing the target molecules are brought

into contact with an organic phase containing RMs. Phase mixing is achieved by external agitation, during which the target molecule is solubilised in the water cores of the RMs, after which the phases are left to separate. The RM-rich phase is then mixed with a new aqueous phase which may contain salts or co-solvents to either destabilise the RMs or salt out the target molecules. Example target bio-molecules obtained by this route include: amoxicillin⁽²⁰⁷⁾, β -glucosidase⁽²⁰⁸⁾, chitosanases⁽²⁰⁹⁾, laccase⁽²¹⁰⁾, lipase⁽²¹¹⁾ and penicillin G⁽²¹²⁾. The advantages of this route include high selectivity, mild thermal operating conditions, low energy consumption and potential for large scale continuous operation⁽²⁰⁶⁾. Multiple factors affect extraction efficiency, including the pH of the aqueous phase⁽²¹³⁾, concentration⁽²¹⁴⁾ and choice of surfactant(s)⁽²¹⁵⁾, as well as salt concentration⁽²¹⁶⁾.

Experimental techniques employed to study microemulsions include small angle neutron scattering (SANS)⁽¹¹⁾⁽⁴⁶⁾, small angle x-ray scattering (SAXS)⁽¹⁹⁾ and conductivity⁽¹⁹⁾. With regards to AOT, Nave et al⁽⁴⁶⁾ studied the effect of changing the AOT structure on the packing in curved interfacial films at the oil-water interface. Both single-tailed and double-tailed analogues were investigated, and it was found that only double-tailed surfactants could form stable microemulsions without the presence of a co-surfactant. No special properties were noticed with AOT, but it was confirmed that the unique hydrocarbon tail structure gives optimum aqueous phase solubility at room temperature⁽⁴⁶⁾. Smith et al⁽¹¹⁾ investigated using SANS the effect of water content on the RM morphology at water to surfactant molar ratio $w_0 = 0.8$) and reported a monomer-to-aggregate transition, which indicates a critical micelle concentration exists for AOT in non-polar solvents.

There have been multiple investigations to study surfactant-water-hydrocarbon ternary systems using molecular simulation. Industrially-relevant systems studied include AOT-n-heptane-water⁽¹⁹⁾ using CG molecular dynamics (MD) simulation, where the non-bonded interactions were obtained from the MARTINI force field, and the bonded interactions were matched to geometry results from atomistic simulations. Water content was varied at a constant surfactant:oil mass ratio, and averaged diffusion coefficients calculated for all charged species were used to rationalise experimental conductivity data. The $C_{10}E_4$ -n-decane-water system has been studied using the dissipative particle dynamics (DPD)⁽¹⁵²⁾ method and was able to capture the phase transition from 3-phase to 1-phase microemulsion at a constant water:oil ratio⁽²¹⁷⁾. The effect of 3 different-length alkanes on the phase structure of $C_{12}E_6$ in water which showcase the destabilisation of phases with non-zero surface curvature⁽²¹⁸⁾ has been studied using DPD simulation. It was also identified that the longer the alkane, the more pronounced the effect. All mentioned studies report a high level of accuracy with respect to the experimental data. It is of interest to note that all mentioned examples employ either CG or DPD-level modelling.

The reverse micellar phase is a subject of great interest in molecular simulation. The first study to develop a full molecular model for AOT reverse micelles in non-polar solvent was claimed by Abel and co-workers⁽²¹⁹⁾. They studied the shape of single RMs with water-to-surfactant molar ratios of 3, 5 and 7 and found the equilibrated structures to be nonspherical with elliptical shape. Other papers which have explored single AOT RMs in non-polar solvent have investigated additional factors such as the influence of polar phase composition⁽²¹⁾, different force fields⁽²²⁰⁾ and the presence of metal salt ions⁽²²¹⁾ on RM systems. In the previous investigations mentioned, either all-atomistic or united atom scale descriptions have been used to model the relevant systems. These studies are thus limited to single monodisperse RMs when experimental results suggest that RMs of AOT-water-oil systems should be polydisperse⁽¹¹⁾. To study a system with multiple RMs, Khoshnood and Firoozabadi used a simplified CG model to study a theoretical surfactant-water-oil system⁽²²²⁾. Here two different particles, hydrophobic and hydrophilic, were used to represent the different components. The authors were able to study the influence of water content and surfactant tail length on the RM properties, identifying that RM shape depends on the size of the polar core: for large cores it is spherical and for small cores it is ellipsoidal. However, models such as these are too simple

and more accurate CG models are required to allow for direct quantitative comparison with experimental data.

The underlying aim of this chapter is to create a molecular model for the AOT-water-cyclohexane ternary system using the SAFT force field. To the author's knowledge, this is the first attempt to use SAFT to model not only this system, but microemulsion systems in general. The model's accuracy is assessed by its ability to predict the experimental phase diagram. It is then used to study the effect of varying water content on RM properties to improve understanding of this system. The parameters from the AOT-water interactions have been validated in Chapter 3, and so the only new interactions to parameterise relate to cyclohexane. The rest of this Chapter is set out as follows: the cyclohexane model development is covered in section 4.3. The details of the MD simulations are set out in section 4.4. The methods used to analyse the simulations are given in section 4.5. In section 4.6, the results of this Chapter are discussed. Finally, in section 4.7 the conclusions of this Chapter are presented.

4.3 Cyclohexane model parameterisation strategy

4.3.1 Pure interactions

The SAFT- γ Mie and the SAFT VRE-Mie models and force fields for the AOT and water interactions have already been validated in Chapter 3. The remaining model to create is thus that for cyclohexane. In keeping with the 3:1 CG mapping, it is chosen to model cyclohexane as a dimer ($m = 2$), illustrated in Figure 4.1. The pure fluid interactions for cyclohexane are obtained from Bottled SAFT⁽²⁹⁾. The beads are illustrated by a red colour.

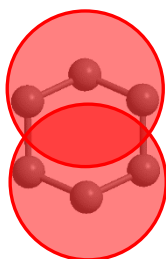


Figure 4.1 CG representation of cyclohexane. The underlying atomistic representation is included for comparison purposes. The hydrogen atoms have been removed for clarity. This image is not to scale.

4.3.2 Cross-interactions

Due to cyclohexane (CH) belonging to the same homologous series as propane (CP) and butane (CB), i.e. alkanes, the cross-interactions regarding cyclohexane are treated in the same way. The cross-interactions between water (W) and cyclohexane are parameterised by incorporating the k_{ij} value of 0.3205. The interactions between the ionic beads (SO and NA) and cyclohexane are calculated using the combining rules set out in equations (2.68-2.70) with no further parameterisation ($k_{ij} = 0$). The ϵ_{ij} between the methyl acetate (ES) beads in the surfactant intermediate section and the cyclohexane beads (CH) is adjusted to the same extent as the ES-CP and ES-CB cross-interactions, and so $\epsilon_{ESCH} = 277.03$ K. The optimised intermolecular interaction parameters are shown in Table 4.1 and a summary of where each interaction was derived is provided in Table 4.2. Please refer to Section 3.6.3 for the meaning of each term.

Table 4.1 List of cyclohexane non-bonded intermolecular interaction parameters

Bead-Bead interaction	σ_{ij} (nm)	ε_{ij}/k_B (K)	λ_{ij}^r (-)	k_{ij} (-)
CP – CH	0.4553	381.11	21.59	-
CB – CH	0.4098	297.31	13.66	-
ES – CH	0.4037	277.03	17.49	-
SO – CH	0.4027	159.82	10.43	-
NA – CH	0.3277	48.60	10.43	-
W – CH	0.3992	251.37	10.43	0.3205
CH – CH	0.4234	345.94	14.05	-

Table 4.2 Parameter matrix indicating how each cyclohexane intermolecular interaction was derived

	CP	CB	ES	SO	NA	W	CH
CH	Lafitte	Lafitte	VLE	Lafitte	Lafitte	IFT	M&M

This validated model is subsequently applied alongside the AOT and water models to simulate the ternary system.

4.4 Molecular simulation details

Table 4.3 presents all the simulations carried out in this study. Included is the dielectric constant ε_r , which is determined using the methodology included in the SAFT VRE Mie theory described in Section 2.3.3. This requires an estimation of the mixture density, which in this work is determined by MD simulation. The methodology is described in Section 4.4.1. The experimental phase diagram⁽⁵⁹⁾ in Figure 4.2 shows the phase boundaries and which phase structure should be expected. The approximate positions of each simulation are included as a guide. The phase diagram shows that there are two distinct regions, separated by a phase boundary. Near the cyclohexane-rich region there exists the reverse micellar L_2 phase, and it is reported that at equimolar amounts of cyclohexane and water ordered phases such as bicontinuous phases predominantly exist.

4.4.1 Water-cyclohexane density simulations

NPT simulations were performed with water and cyclohexane in the same proportion as described for each system. The thermostat used is Nosé-Hoover and the barostat is Parrinello-Rahman. In all simulations the temperature is 298.15 K and the pressure is 1 bar. The time step is set to 0.01 ps and the molecular cut-off is set to 2.0 nm, because this is a pre-requisite of using the water model⁽¹⁸⁾. Periodic boundary conditions are applied in all directions. The binary systems are run for 40 ns, and the last half of the configurations are used to calculate the average density, using the sub-routine gmx density. The initial system contained 25,600 water molecules and 5,600 cyclohexane molecules, which matches the cyclohexane:water molar ratio for system f. The number of water and cyclohexane molecules are then adjusted to achieve the desired composition, and the simulation procedure repeated. The density of pure cyclohexane is obtained by this procedure by removing all water molecules from the system. This permits the calculation of the d parameter for cyclohexane to substitute into equation (2.70). The d_V and d_T parameters for cyclohexane (see equation (2.67)) have not been published, in this work an estimate of d for cyclohexane was obtained based on the experimental dielectric constant at 298.15 K⁽²²³⁾, so $\varepsilon_r = 1.98$. By re-arranging equation (2.66) and knowing that the density of cyclohexane predicted by MD simulation is 9.17 mol dm^{-3} , it is obtained that for cyclohexane, $d = 0.11 \text{ dm}^3 \text{ mol}^{-1}$ at this temperature. The density predicted by MD simulation is close to the NIST value of 9.20 mol dm^{-3} ⁽¹⁹²⁾.

4.4.2 AOT-water-cyclohexane ternary simulations

The initial simulation point for the ternary simulations is system *f* where the initial molecular configuration is random. The MD simulation conditions are similar to the mixed solvents, with a few exceptions. The ionic beads (SO and NA) are modelled with explicit charge. The dielectric constant is determined using the method described in the previous section. The electrostatic interactions are calculated using the Particle Mesh Ewald method with a grid spacing of 0.29 nm. The simulations are run for at least 60 ns, and the last half of the configurations are used to calculate averages. The systems *a*-*e* are simulated by reducing the number of cyclohexane beads from system *f*, and the systems *g*-*p* are simulated by reducing the number of water beads from system *f*.

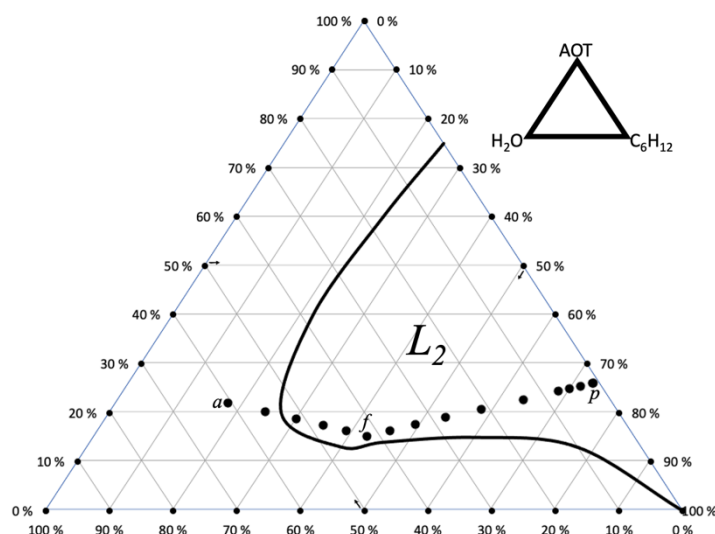


Figure 4.2 Phase diagram of the AOT-water-cyclohexane ternary system ⁽⁵⁹⁾. The solid continuous curve denotes the phase boundary, obtained by experiment. Included are the approximate positions of each system studied. Compositions are given in weight percentage.

4.5 Analysis methods

The nematic phase order parameter S_2 is used to characterise the phase, for the specific procedure please refer to Section 3.5.

The RM systems are studied by calculating the cluster size distribution, using the *gmx clustsize* subroutine. RM cluster size is defined as the number of AOT molecules per RM. A cluster cut-off method is used where two or more surfactant molecules are identified as belonging to the same aggregate if they are found within a cut-off distance of each other. Instead of the whole AOT molecule, the sulphonate bead SO is used as the reference point considering the structure of RMs. This also avoids accidentally counting the hydrocarbon tail-tail contacts which will occur in highly concentrated AOT systems. Since the aqueous core, and not the surfactant head groups, is the centre of the RM, the assignment of the cluster cut-off distance is not simple. In this work it is determined based on the final simulation snapshot for each system. For example, if the snapshot shows four distinct RMs, then a range of cut-off distances are trialled to ensure the resulting analysis does produce the same number of clusters at the final time step. To study the RM morphologies, a single RM is extracted from the corresponding bulk simulation and a variety of properties are calculated. The shape of the RMs is obtained from the principal moments of inertia I_1^2 , I_2^2 , I_3^2 and the relative shape anisotropy κ^2 , which are defined Section 2.4.7. The subroutine *gmx gyrate* is used to calculate these properties.

Table 4.3 AOT-water-cyclohexane systems, number of molecules, and estimated dielectric constant ϵ_r , calculated using equation (2.66).

System	AOT	Water*	Cyclohexane	ϵ_r (-)
a	400	25,600	1,600	57.09
b	400	25,600	2,400	50.47
c	400	25,600	3,200	45.28
d	400	25,600	4,000	41.08
e	400	25,600	4,800	37.63
f	400	25,600	5,600	34.77
g	400	21,600	5,600	31.64
h	400	17,600	5,600	28.03
i	400	13,600	5,600	23.80
j	400	9,600	5,600	18.80
k	400	5,600	5,600	12.71
l	400	2,800	5,600	7.75
m	400	2,000	5,600	6.19
n	400	1,200	5,600	4.56
o	400	400	5,600	2.85
p	400	320	5,600	2.69

*The water model contains two molecules per bead

4.6 Results and discussion

4.6.1 Ternary phase diagram

The equilibrium is noted by observing the energetics between the surfactant head group SO and the water beads. An example is presented for system a in Figure 4.3. The equilibrium values of the SO-W, interaction energy is $-1.69 \text{ kJ mol}^{-1}$, with a standard deviation of 0.03 kJ mol^{-1} .

High S_2 values are seen in Figure 4.4 for systems a – f, which range from ca. 0.15 – 0.45, indicating there is still some degree of nematic order even at the lowest content of cyclohexane explored in this work. The final simulation images for a and f confirm that the phases resemble

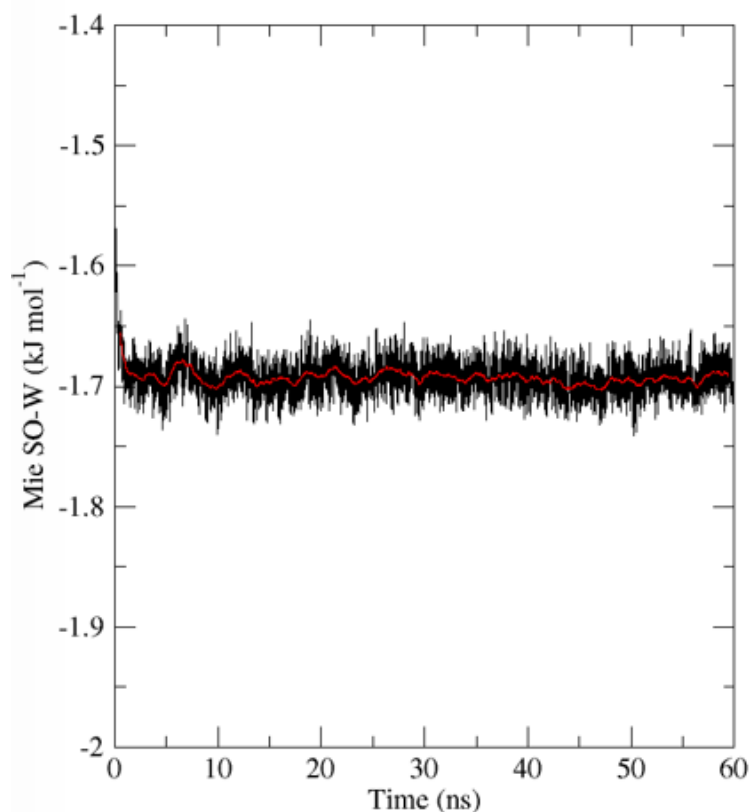


Figure 4.3 Plot of potential energy between the SO and W beads for system a. The black line corresponds to the raw (unaveraged data), whilst the red line refers to the running average, every 100 configurations

a bicontinuous and lamellar phase respectively. The reduction of water leads to a similar reduction in S_2 , but across systems i, j and k there is a clear transition in the structure, which after system k remains stable just above $S_2 = 0.03$, indicating isotropic systems. This transition is visualised in Figure 4.5 via the simulation images.

Overall, the simulations reproduce to a degree of accuracy the experimental phase diagram in Figure 4.2, whilst the transition between ordered structures and RMs would be expected by system c, the MD simulations predict it occurs by system i. The intramolecular potential of a surfactant model has been reported to affect the oil-water interfacial tension in DPD simulation⁽²²⁴⁾. Hence it was decided to see if there was any such effect in this work. The bond constant $k_{bond,ij}$ was increased from 20,000 to 70,000 $\text{kJ mol}^{-1} \text{nm}^{-2}$, to observe any changes in phase behaviour in system c. The impact was minimal, with S_2 varying from 0.221 to 0.225. This is in agreement with the work of Rahman et al⁽¹⁶⁵⁾, who carried out a detailed assessment of the impact of the intramolecular potential in the SAFT- γ Mie force field. Intramolecular interactions described by harmonic potentials were compared to rigid and fully flexible models. It was found that whilst the reproduction of thermodynamic properties was comparable, the former approach is better at capturing structural properties.

It should be considered that the reported experimental error with the phase boundaries is $\pm 5\%$. It should also be noted that systems c to h are very close to the phase boundary and there may occur coexistence between the RM and ordered phases. Unfortunately the experimental phase diagram does not provide in-depth information of the ordered phases, nor of the transition region⁽⁵⁹⁾. Despite this, the simulations are likely not to be able to capture phase coexistence easily due to finite size effects of the simulation box, which may explain the discrepancy between the MD simulations and experiment. The capturing of RM formation at low water content is still in qualitative agreement with experimental findings.

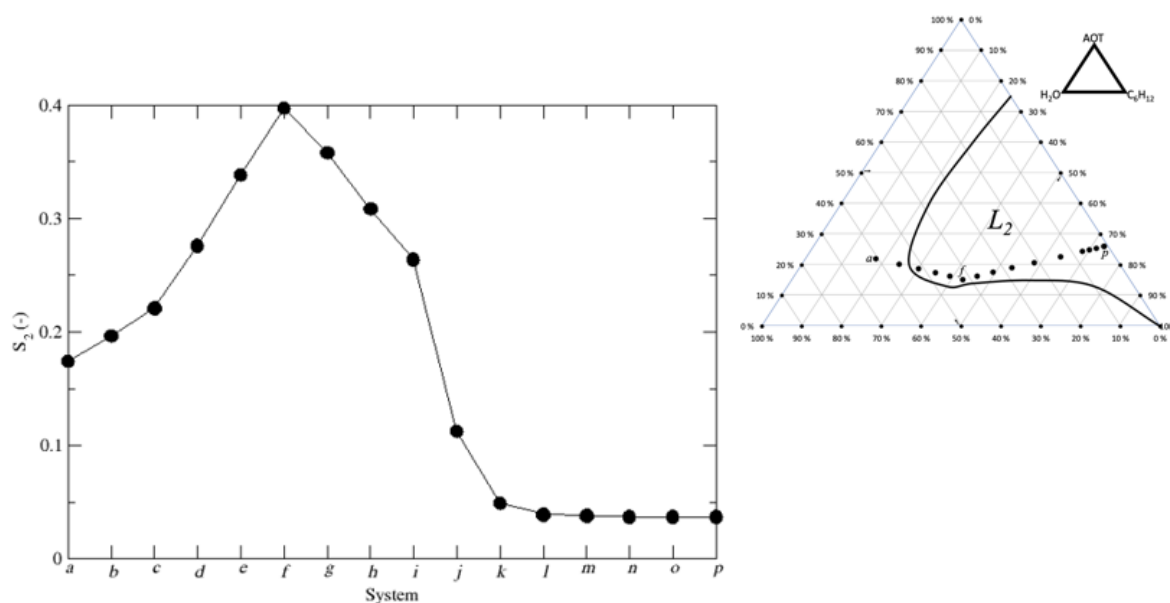


Figure 4.4 Variation of the average nematic order parameter, S_2 , with each system studied. The line is added to guide the eye. The experimental phase diagram⁽⁵⁹⁾ is included for reference.

4.6.2 Influence of water content on RM properties

RM size

The attention for the rest of this Chapter is turned to analysing the simulations where RMs are present (systems k – p). The RM cluster size distributions are presented below for systems k (Figure 4.6) and p (Figure 4.7). It is clear to see the amount of water in the system plays a significant role in the morphology of the resultant RMs. At system k the average water to surfactant molar ratio w_0 is 14 and the average size distribution is narrow, indicating that there are large swollen RMs present in the system. At system p however the w_0 is 0.8 and the RM aggregation number on average varies from 7 to 23. It is of note that for all RM systems there are no single-dispersed AOTs in the solution. The concentration of surfactant monomers is sharply reduced by the most moderate of increases in water content⁽²²²⁾. This also links to the broadening of size distributions seen from systems k-p, increasing the amount of water also reduces the average number of smaller aggregate sizes since the reduced number of free surfactants reduces the probability of exchange between the RM and the solution. This relationship has been investigated by Hirai et al⁽²²⁵⁾, who identified by synchrotron radiation small angle x-ray scattering that AOT RMs form a distinct monomeric (narrow size distribution) phase when $w_0 > 16$. The hydrocarbon phases included in this study were n-hexane, n-heptane and n-octane. In comparison, the MD simulations predict a monomeric phase by $w_0 = 14$ for a cyclohexane continuous phase.

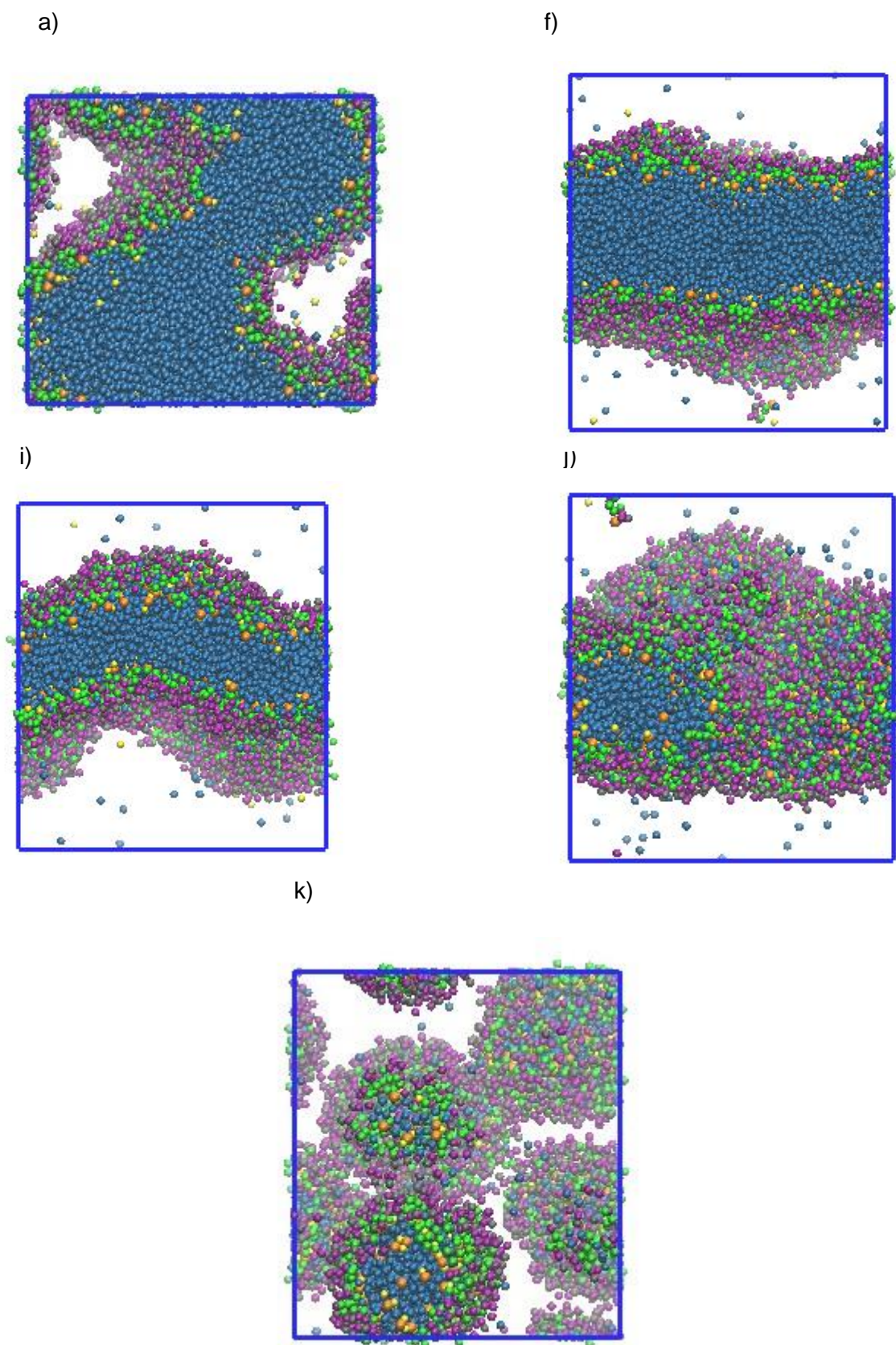


Figure 4.5 Equilibrated MD simulation images, from left to right, for the systems a, f, i, j, and k. The cyclohexane beads have been removed for clarity. The colour code is given in Table 3.1.

The cluster cut-off method permits the calculation of the average RM cluster size, which is presented for all RM systems in Table 4.4. At system k the average RM cluster size is 102 (standard deviation 8) despite the average size distribution reported. Fluctuations in average RM cluster size are to be expected due to Ostwald ripening where larger aggregates form due to being more energetically favourable. The time variation of average RM cluster size in system k, shown in Figure 4.8, confirms this. The narrow size distribution of this system means the average is more sensitive to fluctuations. This effect is not so significant for the other systems with broader size distributions, as evidenced by the difference in standard deviation. It is noted that the experimental aggregation number obtained using SANS for system p ($w_0 = 0.8$), is 23⁽¹¹⁾. This value is obtained by fitting the SANS curves for various AOT concentration points to a non-interacting polydisperse sphere model. The aggregation number is then obtained from an estimate of the micellar volume assuming it is of spherical shape. It is encouraging that the MD simulation of system p predicts a value that is close, 16.7 (standard deviation 0.1), as this was not a property included in the force field parameterisation strategy.

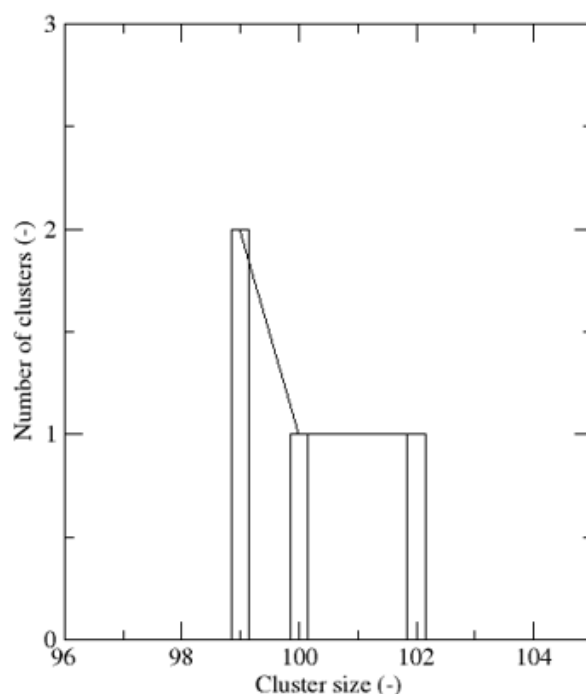


Figure 4.6 The average cluster size distribution for system k.

As indicated by Table 4.4, the reduction of water content results in a sharp reduction of the average RM cluster size. This agrees with the findings of Day et al⁽²²⁶⁾ who determined aggregation number at a range of w_0 from 1 to 8 for the same system at 293.3 K. In this investigation it was assumed that the AOT-water-cyclohexane system was an ideal solution of non-interacting dispersed spherical RMs, allowing aggregation number to be determined using the intrinsic viscosity. The aggregation numbers obtained by experiment ranged from 27 ($w_0 = 1$) to 114 ($w_0 = 8$). Whilst the difference in temperature prevents a direct comparison, it is still encouraging that the RM aggregation numbers in Table 4.4 are of the same magnitude for a similar w_0 range (0.8 – 14). The results hence support the finding that the w_0 ratio is the primary factor when considering RM stability, as opposed to total concentration.

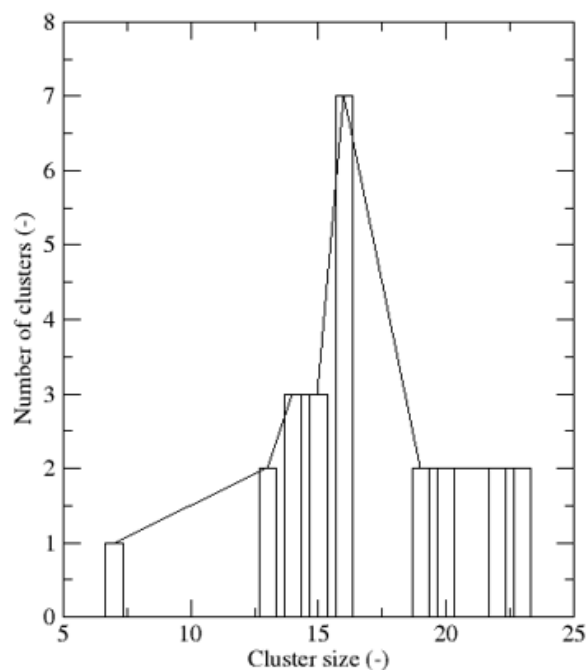


Figure 4.7 The average cluster size distribution for system p.

Table 4.4. Average cluster size, taken over the last half of the simulations.

System	Cluster size (-)	Standard deviation (-)
<i>k</i>	102.0	8.0
<i>l</i>	44.4	0.1
<i>m</i>	33.3	0.1
<i>n</i>	22.2	0.1
<i>o</i>	16.7	0.2
<i>p</i>	16.7	0.1

RM shape

It is of interest to explore the shape of RMs at these conditions, on the basis that analysis of the experimental data mentioned above requires a prior assumption of geometry. In the shape analysis, it was chosen to study single RMs with aggregation numbers representative of the corresponding bulk simulation distribution. For example, to resemble the aggregates found in system *k*, the single RM system contains 100 AOT molecules. The w_0 ratio is kept the same as the corresponding bulk simulation. It is noted here that in previous RM MD investigations⁽²¹⁹⁾ the polar phase is constrained to stay within a spherical shell during the simulation. Here no constraint is imposed, and it is assumed that most of the water molecules in the simulations remain in the RM core. The initial single RM system is obtained by removing the appropriate number of AOT and water molecules from the final configuration of system *k*. The number of

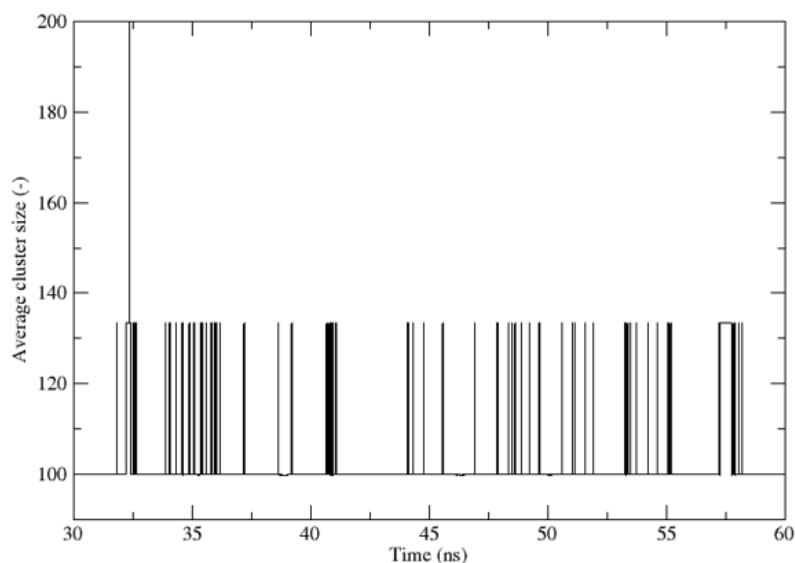


Figure 4.8 Variation of the average cluster size over the last 30 ns for system k

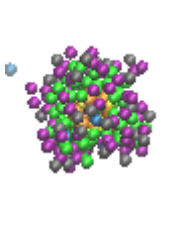
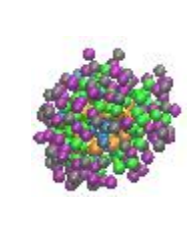
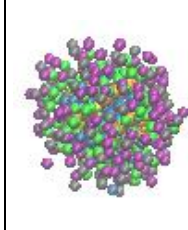
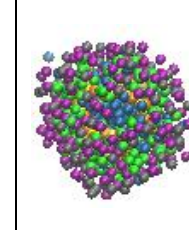
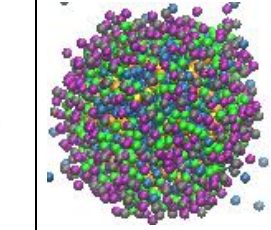
cyclohexane molecules are kept the same to ensure the system remains in the L_2 phase. The dielectric constant is calculated using the method described previously. Compositions of the single RM systems are given in Table 4.5. The other single RM systems are obtained by deleting the appropriate number of water and AOT molecules from the RM100 system. The single RM simulations are run for at least 400 ns, and average properties are taken from the last 100 ns of the trajectory. Equilibrated simulation snapshots are presented alongside the average κ^2 value in Table 4.6, which are calculated with respect to the surfactant layer only. The time variation of the SO-W Mie potential energy and κ^2 for system RM100 is provided in Figure 4.9 and 4.10 respectively. The average of the SO-W Mie potential energy over the last 100 ns is $-5.50 \text{ kJ mol}^{-1}$ (standard deviation 0.09 kJ mol^{-1}). Despite the κ^2 fluctuations, with lower and upper limits of 0.001 and 0.006, the results indicate that across the range of w_0 investigated the RMs have a predominant spherical shape, as the average κ^2 value is 0.003.

Table 4.5 List of all single RM systems studied and estimated dielectric constant ϵ_r , calculated using equation (2.66).

System	AOT	Water	Cyclohexane	ϵ_r (-)
RM17	17	16	5,600	2.02
RM22	22	66	5,600	2.13
RM33	33	166	5,600	2.35
RM44	44	310	5,600	2.67
RM100	100	1,400	5,600	5.00

*The water model contains two molecules per bead

Table 4.6 The average anisotropic shape factor for a variety of RM sizes, with the corresponding simulation image.

RM aggregation size (-)	17	22	33	44	100
w_0 (-)	1	3	5	7	14
κ^2 (-)	0.002 ± 0.001	0.003 ± 0.002	0.003 ± 0.003	0.003 ± 0.002	0.003 ± 0.002
					

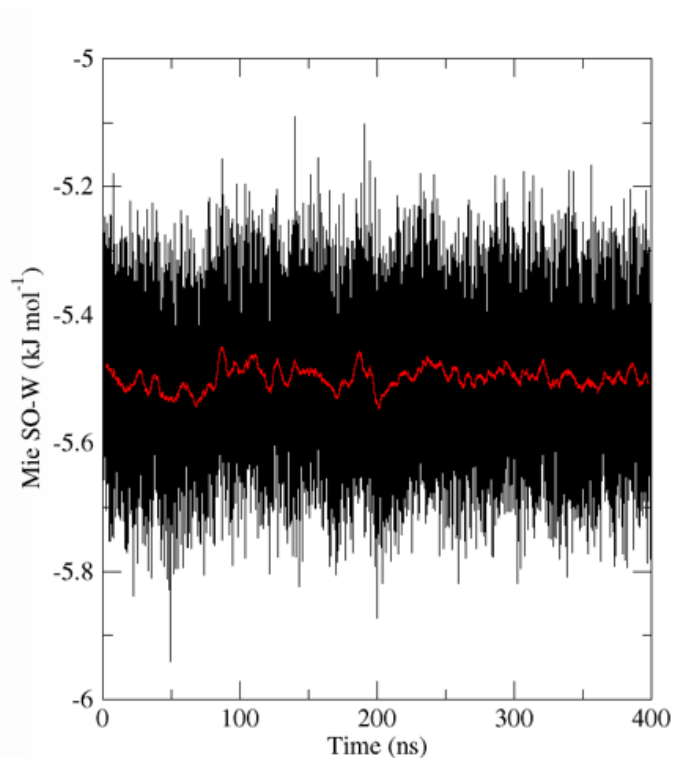


Figure 4.9 Plot of potential energy between the SO and W beads for the RM100 system. The black line corresponds to the raw (unaveraged data), whilst the red line refers to the running average, every 500 configurations

Previous atomistic MD simulations of RMs start with a pre-assembled spherical shape for AOT RMs. Multiple investigations have revealed that when constraints are removed, deviations from the original shape occur and the equilibrated RM is nonspherical at low water content;^(21, 219) in those works the w_0 was less than 10. However, both references assume an overall ellipsoidal geometry in their shape analysis, making comparisons to the results presented here difficult, as no such assumption is made. Salanwai *et al.* noted using molecular simulation of

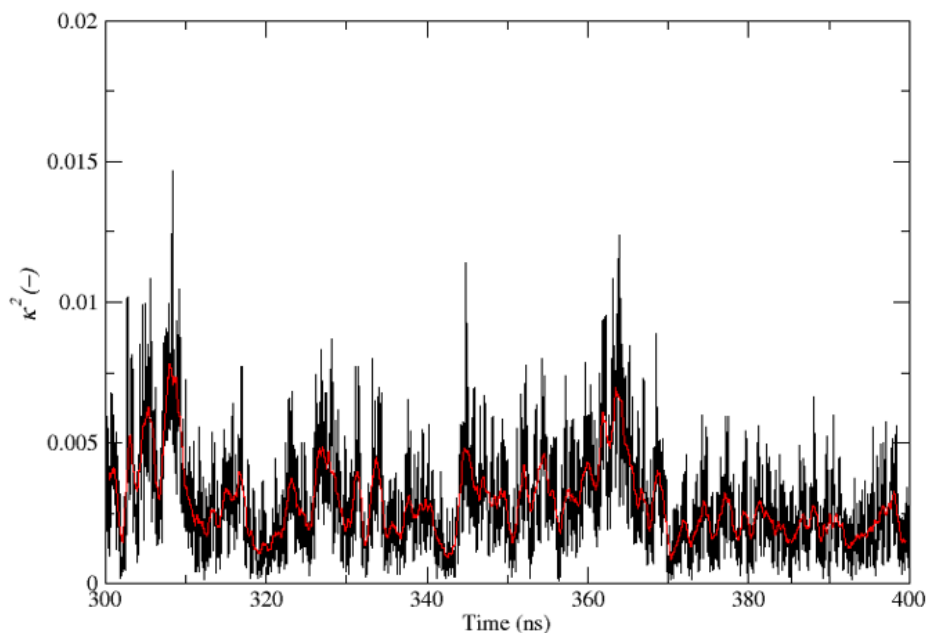


Figure 4.10 Variation of the relative shape anisotropy over the last 100 ns for the RM100 system. The black line corresponds to the raw (unaveraged data), whilst the red line refers to the running average, every 100 configurations

dichain surfactant-water-CO₂ RMs when w_0 is changed from 4 to 35, the departure from sphericity of the whole RM reduces at higher w_0 .⁽²²⁷⁾ They put forward that larger water core volumes afforded by higher water fractions facilitate a low packing density of surfactants around the aqueous core. Whilst another molecular simulation study of AOT-water-cyclohexane RM shape could not be found, a similar pattern was reported by Gardner et al.⁽²²¹⁾ for RMs in the AOT-water-isooctane system at a w_0 range of 3-20. They attributed this to the dispersion of surfactant Coulombic interactions with the water molecules. They also noted significant oscillations in the geometry of the RMs at low w_0 values, causing uncertainty in knowing whether these systems converged to a well-defined geometry. Oscillations of κ^2 in the present work are evident looking at the order of standard deviation for each system in Table 4.6, as well as in Figure 4.10. This is despite simulations being run on the order of 500 ns, as recommended in Vasquez et al⁽²²⁸⁾.

The experimental studies previously mentioned in the RM size distribution analysis^{(11) (226)} assumed a spherical aggregate geometry exists even at very dry conditions (average w_0 as low as 0.8). The assumption of spherical geometry is common in AOT RM experimental studies. Kotlarchyk et al⁽²²⁹⁾ found close agreement between the radius of an AOT RM in n-decane estimated via SANS, with that extracted from the measured radius of gyration, both approaches assuming a spherical geometry. The corresponding w_0 of that experiment was 0.7 ± 0.2 . Kotlarchyk et al concluded that AOT RMs are only slightly aspherical in shape at these conditions. Other investigations that have reported similar findings used techniques such as light and x-ray scattering^{(230) (174)}. In the previous two references, the nonaqueous solvents ranged from n-hydrocarbons, benzene, toluene, carbon tetrachloride and p-xylene. Despite this, in a dynamic light scattering study by Vasquez et al⁽²²⁸⁾ it was found that AOT RMs in iso-octane adopt non-spherical shapes at low w_0 . Another study using the same experimental technique concluded that deformation in the spherical shape only occurs at $w_0 > 20$ ⁽²³¹⁾. Despite extensive use in research, there is still continued debate on the shape of AOT RMs⁽²³²⁾, which makes comparison to experiment difficult.

Accurate knowledge of the RM shape is beneficial in product design. In a nanoparticle synthesis context, the shape of the RM template has been argued to influence the nanoparticle

shape,⁽³²⁾ which in turn will affect the mechanical, chemical and biochemical properties.⁽²³³⁾ When biological systems are considered, nanoparticle shape directly influences uptake into cells, with rods showing greater uptake than spheres, cylinders and cubes.⁽²³⁴⁾ The advantage of this MD methodology is that no assumptions must be made about the RM shape for analysis.

4.7 Conclusions and outlook

A molecular model has been successfully created for the AOT-water-cyclohexane ternary system and has been applied in MD simulations to study RM formation. This has used the models for AOT and water developed in Chapter 3 and reference ⁽¹⁸⁾ respectively. The model for cyclohexane was obtained from Bottled SAFT ⁽²⁹⁾, and the cross-interactions were transferred from Chapter 3.

The resultant model was used to study both phase morphologies and structural properties. This was to test the model capability to capture the balance between energetic and entropic contributions. Figure 4.11 shows the experimental phase diagram with equilibrated MD simulation images super-imposed. The MD simulations reveal a transition from phase-separated systems to isotropic reversed micelle (RM) phases when the water content is reduced to 27 wt%. The relationship between water content and RM morphology was studied. The reduction of water content results in a sharp reduction in average cluster size, from 102 surfactants per RM to 16.7 surfactants per RM when the w_0 ratio is reduced from 14 to 0.8. This highlights the importance of w_0 when considering RM stability. The RM cluster size value obtained at $w_0 = 0.8$, 16.7 is in close agreement with the value obtained by SANS experiment, 23 ⁽¹¹⁾. The results suggest there is little influence on the RM shape and w_0 since a predominant spherical shape exists over the systems studied, with the average κ^2 being 0.003. Significant oscillations are reported in the κ^2 values however, despite the systems being run for long simulation periods. The presence of spherical RMs, even at low water content, is in agreement with assumptions of some experimental investigations ^{(11) (226) (229)}. The advantage of this MD methodology is that no assumptions must be made about the RM shape for analysis.

Despite the acknowledged limitations, the agreement that is achieved between the model predictions and some experimental investigations is encouraging. It gives confidence in the use of SAFT force fields to be used in the discovery of non-toxic microemulsion formulations. The benefits of integral design include better tuning of the structures formed and enablement of efficient use of surfactants. This is further encouraged by the CG nature of the force fields, which can overcome the computational limitations encountered by atomistic-scale simulations in studying RMs. The mechanical, chemical and biochemical properties of nanoparticles can be tuned by adjusting the microemulsion composition. The MD simulations could hence be used to screen different compositions to ensure the optimal RM morphology is achieved. In this thesis the focus is turned to using the presented methodology i) to explore the effect of changing the surfactant hydrophobic tail structure on the resultant properties of the water-in-supercritical CO₂ RMs, and ii) to study the influence of adding groups that reduce the free volume between surfactant tails, which should affect the ability of the surfactant to separate the dispersed and continuous phase, towards the discovery of non-fluorinated CO₂-philic surfactants. The preliminary progress of this work is presented in Chapter 6.

Water effect in the reverse micellar formation of AOT

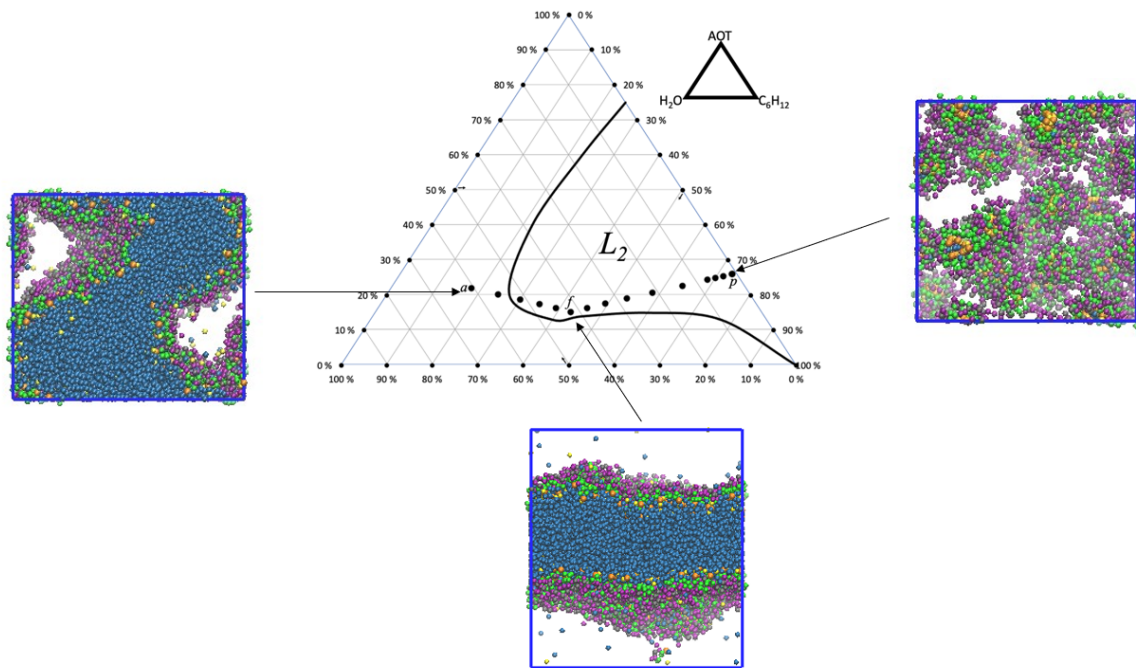


Figure 4.11 The experimental phase diagram for the AOT-water-cyclohexane system ⁽⁵⁹⁾, with equilibrated MD simulation images for systems a, f and p super-imposed.

Chapter 5 Conclusions

5.1 Conclusions

In this thesis a methodology to study surfactant-stabilised microemulsions has been created, that can aid in the design of more efficient and environmentally friendly surfactants. MD simulations using a combination of the SAFT- γ Mie⁽²⁶⁾ and SAFT VRE Mie⁽²⁷⁾ force fields underline the method. All models are coarse-grained since atomistic details have been removed, allowing system sizes and times relevant to surfactant self-assembly to be studied. The approach exploits the previous progress made in extending SAFT force fields to various systems of industrial interest^{(93) (88) (103) (18) (165) (173) (30) (89)}. The parameterisation strategy uses the SAFT M&M correlation⁽²⁸⁾ to derive the pure fluid intermolecular interactions. This has the effect of reduction in force field development time, as many of the force fields have already been recorded in the Bottled SAFT database⁽²⁹⁾. As such, the initial parameterisation stage involves using open-source software. If the force field for the desired chemical is not already in the online database, then it can be created by substituting the acentric factor, critical temperature and characteristic liquid density. The first two properties can be readily found in common databases, for example Yaws book of thermodynamical properties⁽²³⁵⁾. If the liquid density cannot be found, the Bottled SAFT database can provide an approximation using a Rackett-type equation⁽²³⁶⁾. This has an advantage over the SAFT EoS route, where the vapour liquid equilibria data is the target, and may not be readily available for all chemicals. The focus in this work is on using the MD method to assess how well the SAFT force fields can represent the phase behaviour, structure and interfacial properties of surfactant ternary systems.

The first system studied with this route was the binary mixtures of AOT and water. AOT is an industrially-relevant surfactant as it can form oil/water emulsions without the presence of a co-surfactant⁽⁴⁶⁾. Establishing a SAFT AOT-water model that can reproduce the underlying physics is a necessary first step to studying the relevant microemulsions. The corresponding states correlation was used to obtain the intermolecular and bond parameters for the uncharged beads of the AOT model. The charged bead intermolecular parameters were obtained from a previous SAFT study⁽³¹⁾. The remaining intramolecular parameters were assigned based on a previous CG MD study of AOT⁽¹⁹⁾, which used a bottom-up structural-based method. It was chosen to use a pre-existing SAFT model for water that employs a 2:1 mapping⁽¹⁸⁾, because this allows for the simulation of larger systems with lower computational cost. Further parameterisation was performed by optimising the interaction parameters between beads of different nature to reproduce macroscopic properties of either heteronuclear chain molecules that contain both beads, or binary mixtures of the constituent molecules, using MD simulation. Good agreement was achieved with a variety of experimental data including liquid density, surface tension and mutual solubility. MD simulations of the AOT-water system using the optimised force field can capture some of the binary phase behaviour. The room temperature transition from lamellar to reverse structures at high AOT content is not captured, which can be either due to system size limitations or the implicit modelling of the polarity of water. The lamellar phase is captured well, and the bilayer thicknesses estimated by MD simulation show quantitative agreement with the experimental values. Interestingly, the results do not show AOT molecules undergoing structural re-alignment in the intermediate lamellar concentration region. Instead, a lamellar phase is present throughout the expected region, which at low concentration is slightly less ordered than at high concentration. The data supporting structural realignment⁽¹³⁹⁾ is then likely to be based on incorrect experimental procedure⁽¹³⁸⁾. The transition from lamellar to isotropic phase at high temperature is also captured by this model, which is encouraging as this was outside the temperature range the surfactant-water model is parameterised for. The model hence shows some level of transferability, robustness and representability.

The ternary mixture AOT-water-cyclohexane at room temperature has been studied which allowed the performance of the SAFT force fields in modelling microemulsions to be assessed. The cyclohexane model was obtained from Bottled SAFT⁽²⁹⁾, and the cross-interactions

between the surfactant hydrophilic groups and cyclohexane are treated the same way as those between the surfactant hydrophilic and hydrophobic groups. The cyclohexane-related cross-interactions have been optimised either by transferring from the AOT-water system or in a previous study⁽⁹⁰⁾, and so no further validation work was required for this system. MD simulations of the phase diagram showed the model was able to predict the transition from ordered phases to RM phases with some agreement to experiment. Further analysis on the RM systems revealed quantitative agreement with experimental aggregation number, and simulations predict that a predominant spherical shape exists even at low water content in agreement to the shape assumed in some experimental SANS^{(11) (229)} investigations. Significant oscillations in the RM shape are reported in the MD simulations. The disagreement between experimental studies means the shape of AOT RMs remains a subject of continued debate, despite their extensive use in research. This microemulsion system can be used as the template in the synthesis of nanoparticles. The mechanical, chemical and biochemical properties of the nanoparticle can be tuned by adjusting the microemulsion composition. The MD simulations could hence be used to screen different compositions to ensure the optimal RM morphology is achieved. This work is, to the authors knowledge, the first time SAFT models have been used to study surfactant ternary systems.

Overall, the work presented in this thesis has achieved objectives 1 and 2 set out in Section 1.3. Preliminary progress has been achieved for objective 3, which is presented in Chapter 6. The results accomplished in this thesis allow progress to be made in achieving objective 4. Through additional tuning, the SAFT force fields obtained by Bottled SAFT and previous SAFT work have demonstrated accuracy in reproducing macroscopic properties for binary and ternary ionic surfactant systems. Simulation at the molecular scale with an accurate model will allow a more rigorous understanding of the role of structure on phase behaviour. The SAFT MD-based methodology that has been created can hence be used as a screening tool in the design of tailor-made surfactant products for a variety of industrial applications. This methodology can hence be expanded to other microemulsion systems to discover non-toxic and/or biodegradable surfactants.

5.2 Future work

Despite the progress made in this work, there are still many areas to expand on and areas not yet explored. Firstly, the surfactant-water interactions can be optimised in a more rapid fashion by using the $\Gamma - \gamma$ method described in Section 2.4.4. However, this method assumes that bulk surfactant concentration is negligible, which is not applicable to ionic surfactants. Whilst attempts were made during this study to adapt the $\Gamma - \gamma$ method to accurately represent the AOT-water surface tension isotherm⁽¹³⁾, certain practical issues were also revealed. The sodium counter-ions diffuse across the entire simulation box when they are expected to mostly remain solvated in the bulk water. Above the reported maximum surface excess, the AOT molecules do not form micelles, but instead assemble into a bilayer. It is believed that the second problem is likely due to the first one. In these simulations a dielectric constant is applied throughout the box, but it is questionable if this is truly an accurate representation of the underlying physics. The low density of air means that in these MD simulations it is not modelled explicitly, so using a mixed dielectric as is the approach in the ternary systems is not a viable option. One way to overcome this could be to create an MD code where the dielectric constant is shifted so that it is the value of air within the vapour regions, and the value of water within the liquid slab. There will likely be issues regarding the discontinuity of the dielectric constant at each phase, which will need to be overcome. The ionic bead parameters could also be re-adjusted to take into account the vapour pressure of the corresponding aqueous electrolyte as well, which will likely help to recreate a more accurate counter-ion distribution. Another, more challenging route, would be to develop ion models without explicit charge. This would have the benefit of reducing simulation time, due to no Coulombic interactions and hence no reciprocal space calculations. The challenge would lie in representing strong anisotropic forces with a simple isotropic Mie potential and would give insight into how coarse the CG models can go without losing the ability to describe a range of properties. The

representation of like-like charge repulsion at short-range would be one of the main challenges of this work.

The water model that is used in the $\Gamma - \gamma$ method must be able to reproduce the surface tension. Unfortunately, the two SAFT models⁽¹⁸⁾ (CGW1-ift and CGW2-bio) that can do this also over-estimate the vapour pressure of water. Note that the CGW2-bio model is the one used in this work. This can be explained by considering the strong anisotropic hydrogen bonds that give water its unique properties. As such, a purely isotropic Mie potential cannot accurately reproduce all the thermodynamic properties. The restriction of the cut-off potential to 2.0 nm, as is the case of the water model, can restrict the accuracy of simulating molecules with beads of certain size. A study by Duque and Vega⁽²³⁷⁾ found when calculating surface tension, the cut-off should be at least six times the size of the largest CG bead. Taking the AOT-water system as an example, the largest bead is CP ($\sigma = 0.4871$ nm), the cut-off radius should then be no less than 2.93 nm. When this is considered, the ability of the CGW2-bio model-enforced cut-off radius to provide an accurate representation of the intermolecular interactions may not be optimal. There is hence a need to develop a more robust water model with no cut-off specifications. One potential route to do this is incorporating association sites to represent more accurately hydrogen bonding, which has been done on a theoretical level using the SAFT VR SW equation of state⁽²³⁸⁾. The limitation here is that discontinuous square-well potentials are difficult to represent in MD simulations, due to complications in solving the equations of motion. It should be noted that adding association sites will likely significantly increase the computational expense, especially for large-scale surfactant simulations. A Mie potential with an appropriately deep ϵ could be used to model a single water molecule instead. Alternatively, a two-site CG model formed from beads with very different energetic interactions to model more explicitly the dipolar-like directional interactions could be used. This would again incur a higher computational cost, especially when compared to the CGW2-bio model.

The development of the ester models can be expanded by considering longer chain molecules, where it can be assessed if the current cross-interactions are still transferable. For longer chain molecules the torsion potential is an important factor, and so this can be studied. This will allow the simulation of the equivalent aqueous binary mixtures, where again the transferability of the ester-water cross interactions can also be studied.

Transport properties of the AOT binary and ternary systems can be studied using MD simulation. These can include diffusivity of the counter-ion and water beads, as well as the conductivity of the mixtures. The CG nature of these models means that transport properties will likely be over-estimated, due to many interactions being integrated out. However, this would be a good test of the robustness of the CG models, and further optimisation could lead to improved representation of the experimental phenomena.

The use of GPUs (graphic processing units) to study large-scale surfactant systems can reduce the simulation time but will usually incur an additional cost. Studies can be carried out to benchmark the use of GPUs in future systems and improve understanding of how the performance scales with cost.

The MD methodology can also be applied to other industrial systems where microemulsions are present. Their stability makes them promising tools as drug targeting and controlled drug release⁽²³⁹⁾. Whilst hydrophilic drugs can be carried in the aqueous phase of a water-in-oil microemulsion, hydrophobic drugs can be solubilised within the oil cores of an oil-in-water microemulsion, giving them a wide range of applicability. In the food industry, microemulsion technology can be used for delivery of poorly soluble and/or sensitive compounds and bioactives such as natural oils⁽²⁴⁰⁾. Here it is necessary to use only food-safe surfactants in product formulation. In the oil and gas industry, microemulsion flooding is one technique used in the latter stages of oil recovery, used to reduce interfacial tension between water and oil, which decreases capillary pressure, removing the trapped oil⁽²⁴¹⁾. Collaborations between academic/industrial organisations working in these areas can be sought and identified non-

toxic surfactants could be studied using the simulation method to assess performance and compare to the current standards. The simulations can also be used to identify potential surfactants that can then be validated by experimental techniques.

The list of potential future applications using knowledge gained from this work is by no means exhaustive. It instead gives an idea of what is necessary to move the research field forward.

Chapter 6 Toward design of non-toxic surfactants for enhancing scCO₂ as a green solvent

6.1 Chapter overview

The MD simulation methodology developed and tested in Chapters 3 and 4 can be applied further to study water-in-supercritical CO₂ (water-in-scCO₂) microemulsions. This is a growing area of microemulsion technology and is attractive since CO₂ is non-toxic and naturally abundant in the environment, making it a green solvent that could replace petroleum-derived organic solvents. In this case the methodology can be used as a screening tool to discover new surfactants with improved microemulsion stabiliser properties whilst avoiding the need for fluorinated groups in the structure, which are environmentally harmful. The preliminary AOTSiC-water-scCO₂ model is presented in this Chapter. Bottled SAFT was used to obtain the new pure force field parameters. The interactions between water and scCO₂ have been optimised by fitting to the liquid-liquid equilibrium, using a single binary interaction parameter. The future work necessary to apply the methodology is detailed at the end of this Chapter.

6.2 Introduction

Volatile organic compounds (VOCs) are organic chemicals that evaporate easily at room temperature. A wide range of chemicals fall into this class, including aromatic and aliphatic hydrocarbons, oxygenates such as alcohols, ketones, esters and chlorinated hydrocarbons⁽²⁴²⁾. They are commonly used as solvents in the formulation of paints, inks and adhesives⁽²⁴³⁾, extraction of vegetable oil from oil seeds⁽²⁴⁴⁾, manufacture of pharmaceuticals⁽²⁴⁵⁾, cleaning of metal and plastic components⁽²⁴⁵⁾, dry cleaning of textiles⁽²⁴⁶⁾ and formulation of consumer products such as aerosols, cosmetics, and household paints⁽²⁴⁵⁾. The use of VOC solvents in industry are associated with waste emissions that are harmful to the environment⁽²⁴⁷⁾. These include contributing to climate change and carcinogenic effects to humans⁽²⁴⁸⁾.

The philosophy of green chemistry sets out guidance regarding the reduction/elimination of toxic and hazardous reagents/products, minimising the energy required for chemical processes, and avoiding the use or production of waste where possible⁽²⁴⁹⁾⁽²⁵⁰⁾. These steps also form part of the Chemical Engineering Inherent Safety Principles⁽²⁵¹⁾ first put forward by Trevor Kletz⁽²⁵²⁾. It is in accordance with these principles that viable alternatives to VOCs should be found. Supercritical fluids are an attractive option because of the ease of removal, recyclability and tuneability of fluid properties such as density and solvent quality by controlling temperature and pressure⁽⁶⁰⁾.

By definition, a supercritical fluid refers to any fluid above the critical temperature and pressure (termed the critical point)⁽²⁵³⁾. The critical temperature of a substance is the temperature when heating a liquid and vapour in equilibrium, the surface between the two phases disappears as the densities are equal. The critical pressure is the pressure required to liquefy a gas at the critical temperature. The resultant supercritical fluid will have unique properties that can be exploited, including densities like a liquid, with the lower viscosity (and higher diffusivity) of a gas. The critical point of most common solvents is however too demanding, for example the critical point for water is around 647 K and 220 bar⁽²⁵⁴⁾. In contrast the critical point of CO₂ is more conveniently accessible at around 304 K and 72.8 bar⁽⁶⁰⁾⁽²⁵⁴⁾. Supercritical CO₂ (sc-CO₂) offers both green and energy-saving properties, and is cheap, non-toxic and non-flammable⁽⁶⁰⁾, placing it as a potential replacement of harmful VOC solvents.

ScCO₂ is routinely employed as a solvent for various commercial processes, for example coffee decaffeination which employs a liquid-liquid extraction between scCO₂ and water to recover caffeine (molar mass 194.19 g mol⁻¹)⁽²⁵⁵⁾. It has also been used as the continuous phase in nanomaterial synthesis⁽³²⁾⁽²⁵⁶⁾, where materials produced have included silver nanoparticles⁽²⁵⁷⁾, and even drugs such as Ibuprofen and Naproxen⁽²⁵⁸⁾. Another application of scCO₂ is in cleaning, where the advantage over conventional aqueous-based systems include energy savings as no drying step is required, scCO₂ has higher affinity for oils and

other lipophilic materials, and improved cleaning efficiency because of higher diffusivity and lower viscosity ⁽²⁵⁹⁾.

The issue with scCO₂ is that due to its non-polar nature, polar and high-molecular weight compounds are only sparingly soluble ⁽²⁵⁵⁾ ⁽²⁶⁰⁾. For example the non-steroidal inflammatory inhibitory drug ketoprofen (Molar mass 254.29 g mol⁻¹) has a solubility of 7.98 x 10⁻⁵ by mole fraction in scCO₂ at 312.5 K and 220 bar ⁽²⁶¹⁾, which the authors claim is a 'relatively high' value. However, eflucimibe (Molar mass 469.73 g mol⁻¹), a drug that has shown anti-atherosclerotic properties, has a lower solubility of 5.71 x 10⁻⁷ by mole fraction at 308.15 K and 274 bar ⁽²⁶²⁾. A key research goal is thus to broaden the universality of scCO₂ as an industrial solvent. One route is to incorporate surfactants in a continuous scCO₂ phase to form water-in-scCO₂ (W/scCO₂) microemulsions ⁽²⁶⁰⁾. The advantages of this approach include enhanced flexibility for modification of CO₂ properties such as wettability, viscosity and interfacial tension ⁽²⁶³⁾ ⁽²⁶⁴⁾ ⁽²⁶⁵⁾. Hence much research has been performed to design CO₂-philic surfactants which are efficient stabilisers of W/CO₂ microemulsions ⁽⁶⁰⁾. Surfactant molecular design has revealed that surfactants which achieve low surface tension at the air-water interface (high surfactant effectiveness) are also efficient stabilisers for W/scCO₂ microemulsions ⁽²⁶⁶⁾. Surfactants with high levels of fluorination have demonstrated strong affinity for scCO₂ ⁽²⁶⁷⁾ ⁽²⁶⁸⁾ ⁽²⁶⁹⁾, however these are also associated with high expense and negative environmental impacts, including persistence, bioaccumulation and toxicity ⁽²⁷⁰⁾. It has recently been reported that exposure to fluorinated chemicals may reduce the effectiveness of certain vaccines, which may have knock-on consequences for responding to the Covid-19 Pandemic ⁽²⁷¹⁾. Attention in this field has therefore turned to the design of scCO₂-philic surfactants with little to no fluorination.

Investigation into the compatibility of many commercially available hydrocarbon surfactants has revealed that the majority are not CO₂-philic ⁽²⁷²⁾. Surfactant structure has been found to play a role in increasing CO₂-philicity, for example increased tail branching and methylation have been shown to lead to formation of W/scCO₂ microemulsions with increased stability ⁽²⁷³⁾. This can be explained by weaker interactions between surfactant tails as well as lower surfactant affinity for water. In the work of Pitt et al ⁽²⁷⁴⁾, it was noted that for hydrocarbon surfactants, those with *tert*-butyl tipped chains achieve the lowest surface energy. Following from this, Mohamed et al ⁽²⁷⁵⁾ studied two variations of AOT with *tert*-butyl tipped chains which were observed to have low water-CO₂ interfacial tensions. By comparison, AOT cannot stabilise W/scCO₂ microemulsions without co-surfactants ⁽²⁷⁶⁾. Surfactants with three hydrocarbon chains, each with extensive methylation have also been investigated with the aim to enhance CO₂-philicity and reduce surface tension. TC14 (sodium 1,4-bis(neopentyloxy)-3-(neopentyloxycarbonyl)-1,4-dioxobutane-2-sulphonate) was solubilised in water, heptane and scCO₂ and the aggregates were characterised by SANS ⁽²⁷⁷⁾ ⁽²⁷⁸⁾. Tensiometry results showed a reduction in surface tension as the number of tails is increased. This is attributed to hydrocarbon tail packing efficiency balanced against head-group repulsions, alongside the increased number of low surface energy methyl groups per headgroup.

In the work of Czajka et al ⁽²⁷⁹⁾, a novel class of hydrocarbon surfactants called trimethylsilane hedgehogs (TMS hedgehogs) was tested and showed good performance at reducing the surface tension at the air-water interface. The term 'hedgehog' refers to the spiky brush-like structure of the surfactant tails. Hill et al ⁽³³⁾ investigated the ability of the best performing surfactant, AOTSiC (sodium bis (3-(trimethylsilyl)-1-propanol) sulphosuccinate), to stabilise W/scCO₂ microemulsions. They recorded the maximum water to surfactant molar ratio (w_0) at which stable W/scCO₂ microemulsions form, which in effect indicates the maximum water solubilisation capacity. By adding a third TMS tail to AOTSiC, the highest w_0 obtained was 25, which they noted as 'very rare for non-fluorinated surfactants'. However, they put forward that three-tail surfactants, due to the inherent tail bulkiness will not be able to form water/scCO₂ microemulsions with lower curvature (higher water content). This will limit their water solubilisation capacity, even with the appropriate CO₂-philicity. It was concluded that the focus

should be shifted to finding double-tail surfactants which can solubilise larger amounts of water, with the sufficient scCO₂-philicity easily found in three-tail surfactants.

When trying to predict the CO₂-philicity of a surfactant, one approach is to use the fraction free volume (FFV) of an adsorbed monolayer defined by Stone et al ⁽²⁸⁰⁾:

$$FFV = 1 - \frac{V_{tail}}{L_{tail}A_{cmc}} \quad (6.1)$$

where V_{tail} is the surfactant tail volume, L_{tail} is the surfactant tail length, and A_{cmc} is the area of the surfactant headgroup at the critical micelle concentration. Surfactants with lower FFV values are expected to be CO₂-philic, corresponding to improved solubility of surfactants and therefore increased stability with the formation of W/scCO₂ microemulsions. This is because when considering surfactants with hydrocarbon tails, the CO₂-tail interactions are weaker than if an oil continuous phase is considered. scCO₂ has a higher diffusivity than an oil phase, and so reducing the free volume between surfactants plays a greater role as this determines the efficiency of separation between scCO₂ and water. Indeed, many factors that have been shown to increase scCO₂-philicity also reduce FFV . Fluorinated surfactants which have a larger tail volume compared to an equivalent hydrocarbon, hydrocarbon surfactants with increased branching and surfactants with three tails compared to two have all been shown to be more CO₂-philic ⁽²⁷⁸⁾ ⁽²⁷⁷⁾ ⁽²⁷⁴⁾. A reduced FFV value leads to a more densely packed interfacial film and therefore a decrease in both CO₂ and water penetration into the surfactant film, which can destabilise the aggregates.

Salaniwal et al ⁽²⁸¹⁾ used MD simulation to study the structural properties of a dichain surfactant-water-scCO₂ system, where the surfactant formula was [(C₇F₁₅)(C₇H₁₅)CHSO₄⁻Na⁺], i.e. it contained both an alkane and perfluoroalkane tail. A combination of UA and AA models were used to represent the various moieties. It was identified that the two distinct tails exhibit different conformations indicating contrasting CO₂-philicity. Particularly, the fluoroalkane tails assumed more extended conformations than the alkane tails. Mudzhikova and Brodskaya ⁽²⁸²⁾ carried out CG simulations of the AOT-water-scCO₂ system, claiming it to be the first of its kind. It should be noted in this case a pre-arranged RM was the starting molecular configuration. They remarked that due to the mutual dissolution of water and scCO₂, the surfactant layer is thicker compared to an aggregate formed in hexane ⁽²⁸³⁾, resulting in a reduced deviation from sphericity. Neither of the above studies investigated the impact of surfactant structure. Using AA simulations, Wang et al ⁽²⁸⁴⁾ explored the effect of changing the hydrocarbon chain length of hybrid surfactants, defined as containing hydrocarbon and fluorocarbon chains, on CO₂ philicity. They noted there are two competing mechanisms with shortening the hydrocarbon chain length: first the tail volume is reduced, which decreases the efficiency to separate CO₂ from water. However, this can also result in a broader distribution of fluorocarbon chain conformations, due to reduction of steric effects and resultant increase in free space, which could enhance the separation efficiency. All the simulations in their work contained 20 surfactant molecules, 100 water molecules and 3000 CO₂ molecules, only single RMs were studied.

In this Chapter the aim is to use CG MD simulations to design more efficient non-fluorinated scCO₂-philic surfactants. This will be achieved by expanding the knowledge on TMS hedgehog surfactant architecture, in particular the AOTSiC surfactant at 318.15 K and 350 bar ⁽³³⁾. To the knowledge of the author, there have been no previous attempts to do this. Whilst King ⁽¹²⁷⁾ carried out MD simulations to study the relationship between ethoxylated surfactant tail architecture and surfactant effectiveness to replace perfluorinated surfactants, their approach uses the Γ - γ method ⁽¹⁵⁾ (c.f. Chapter 2.4.4) which is not appropriate for ionic surfactants. Instead, the ternary system will be simulated directly using the SAFT force field, which has been shown to be possible in Chapter 4. This will be accomplished by first creating the molecular models of the chemicals involved. The new CG pure-fluid force fields can be

obtained from Bottled SAFT⁽²⁹⁾, and the cross-interactions are parameterised to re-create selected experimental data. These include the water-scCO₂ liquid-liquid equilibrium⁽²⁸⁵⁾, as well as the maximum water solubilisation capacity of AOTSiC⁽³³⁾. The validated model can then be applied to find surfactants that can form more stable W/scCO₂ microemulsions. An advantage of this approach is that due to the similarity of AOT and AOTSiC, some of the CG bead interactions used previously can simply be transferred over to the new surfactant. In MD simulations, structural variation can be carried out in a trivial manner, hence there is no limit to the number of different surfactants possible. The current progress of the AOTSiC-water-scCO₂ model parameterisation is presented in Section 6.3. The molecular simulation details are given in Section 6.4. The preliminary validation results and force field parameters are detailed in Section 6.5. The Chapter concludes with a report of the preliminary progress and potential future work in Section 6.6.

6.3 Model parameterisation strategy

The CG model for water is the same as used in Chapters 3 and 4. CO₂ is modelled as a dimer because it has been reported that the use of a geometry more closely aligned to the actual molecule helps to capture both thermophysical and transport properties with lower deviation to the experiment⁽³¹⁾. It is presented alongside the recast AOTSiC in Figure 6.1.

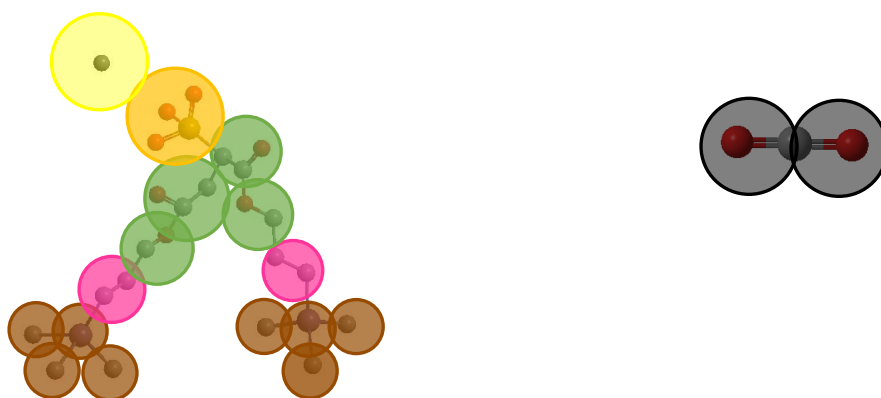


Figure 6.1 CG representations of the molecules used in this study: AOTSiC and CO₂. The underlying atomistic representation is included for comparison purposes. In the AOTSiC model the hydrogen atoms have been removed for clarity. These images are not to scale.

The resultant CG structure of AOTSiC is composed of 15 beads of five different moieties: 4 x brown beads termed TMS comprising the terminal trimethyl silane group, 1 x pink CE bead representing an ethyl group in the tail. The remaining beads (ES, SO and NA) represent the same groups as in the AOT model in Chapters 3 and 4. It is acknowledged that this is not the only way of representing AOTSiC, no attempt was made to optimise the mapping and the following approach is chosen without prejudice to the others.

The force field parameters for the groups ES, SO, NA and W are the same as in Chapters 3 and 4. Bottled SAFT⁽²⁹⁾ is used to obtain pure-fluid force field parameters for the remaining non-ionic beads in the AOTSiC model, as well as the CO₂ model. It is acknowledged that assigning small molecules to the CG beads neglects connectivity for example the ethyl group C₂H₅ is represented by ethane C₂H₆. It is assumed the difference in H atoms does not affect the energetics significantly. A summary of the system model is provided in Table 6.1.

Table 6.1 List of the new CG beads used in the study, with the corresponding chemical, number of segments m and the colour.

Bead name	Bead chemical	m	Colour id
TMS	Trimethyl silane	4	Brown
CE	Ethane	1	Pink
CO	CO ₂	2	Black

The intramolecular parameters are obtained in the same fashion for AOT in Chapter 3. The solvent specific parameters necessary to calculate the dielectric constant, d_V and d_T , for water have already been presented in Chapter 3. The equivalent parameters for CO₂ are $d_V = -0.025 \text{ dm}^3 \text{ mol}^{-1}$ and $d_T = 0$, as it was found that the dielectric constant is not dependent on the temperature⁽²⁷⁾. These parameters achieve an AAD% of 1.45 % when 107 data points are considered. The temperature and solvent composition would be varied in these simulations, and so the dielectric constant for the mixed scCO₂ – water solvent could be calculated using the same method described in Chapter 4.

6.4 Molecular simulation details

6.4.1 Water – CO₂ simulations

The cross-interactions are parameterised by fitting to the mutual solubility data⁽²⁸⁵⁾ of the binary mixture at 383.15 K and at four different pressure points: 200, 300, 400 and 500 bar. Simulations were first carried out in the NP_{zz}AT ensemble to ensure the density was equilibrated. The thermostat is Nosé-Hoover with a time constant of 1.0 ps. The barostat used is Parrinello-Rahman with the time constant set at 10.0 ps. The barostat is used in a semi-isotropic fashion such that L_x and L_y are constant, and so the box area A will remain constant. L_z will fluctuate to maintain the specified pressure, which corresponds to the diagonal z component of the pressure tensor P_{zz} . This was followed by an NVT simulation, using the same thermostat conditions. The number of molecules of CO₂ were kept constant at 5,000, but the number of water molecules were adjusted at different pressures to ensure the initial volume fractions were the same. The molecular cut-off was set to 2.0 nm as this is a prerequisite of the water model⁽¹⁸⁾. Periodic boundary conditions are applied in all directions. The initial box dimensions are chosen such that $L_x = L_y$ and $L_z > 4 L_x$. The time step used is 0.005 ps, and each simulation was run for 80 ns, with averages taken from the last half of the configurations. The system compositions are summarised in Table 6.2:

Table 6.2 List of all the water-CO₂ binary mixtures studied via MD simulation

Pressure (bar)	Number of CO ₂ molecules	Number of Water molecules
200	5,000	24,000
300	5,000	20,000
400	5,000	18,000
500	5,000	16,000

6.5 Validation and model creation

6.5.1 Water – CO₂ interactions

The energetics between the W and CO beads were used to study the simulation progress, an example is shown in Figure 6.2 which is for the system at 200 bar. A stable value is found at around $-0.44 \text{ kJ mol}^{-1}$ (standard deviation 0.02 kJ mol^{-1}). This value is indicative of the difference in intermolecular interactions between both water and CO₂. The density profile of

this system is provided in Figure 6.3, where two distinct bulk liquid phases can be identified. The peaks at either end of the scCO₂ phase (black line) are indicative of accumulation at the interface region, specifically adsorption. This is due to the differences in surface tension between water and CO₂. At these conditions the surface tension of water will be around 54 mN m⁻¹ ⁽²⁸⁶⁾. For scCO₂ the surface tension will be negligible ⁽²⁸⁷⁾ since the properties of the liquid and vapour phase are similar. Hence scCO₂, the phase with lower surface tension will adsorb in the interfacial regions.

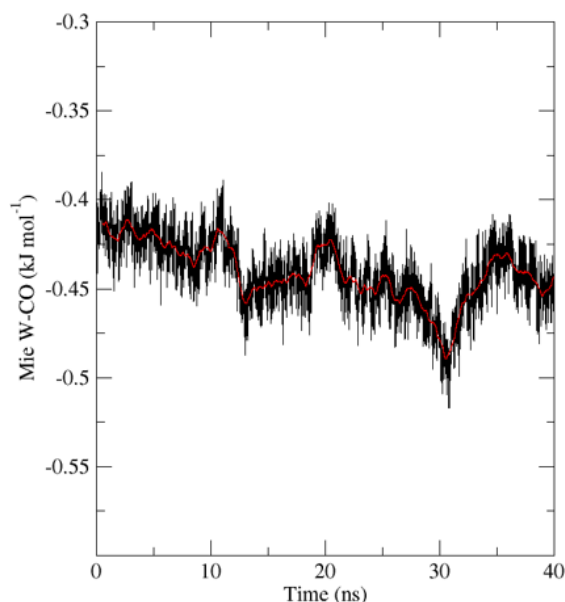


Figure 6.2 Plot of potential energy between W and CO beads for the system at 200 bar. The black line corresponds to the raw (unaveraged data), whilst the red line refers to the running average, every 200 configurations

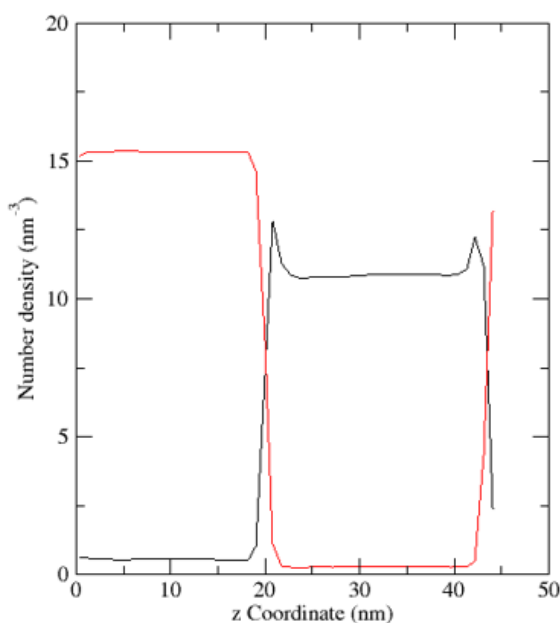


Figure 6.3 The particle number density profile of the water (red line) and scCO₂ (black line) system at 200 bar taken from the last 40 ns of the simulation.

The best fit to the mutual solubility is achieved when $k_{ij} = 0.3$, the results of this fitting are shown in Figure 6.4. The value implies that the cross-energetic parameters derived from the Lafitte combining rules would over-estimate the interaction energy between water and CO₂. Both components contain different intermolecular forces, water interactions are dominated by hydrogen bonds whilst CO₂ interactions result from a combination of both dispersion forces and permanent quadrupole forces. It is therefore not unexpected that a positive (i.e. repulsive) k_{ij} improves the fit to experimental data. It is worth noting that Lobanova et al investigated the water-scCO₂ binary system using the CGW1-vle model⁽¹⁸⁾, and the monomer model for CO₂⁽⁸⁸⁾. The optimum k_{ij} value was calculated as -0.07⁽¹⁷³⁾. In this case both the equation of state and MD simulations were employed. The difference in k_{ij} can be explained in the different data used to parameterise the model: the CGW1-vle was created to reproduce the density and vapour pressure of water, whereas the model used in this work, (the 'CGW2-bio' model) reproduces the density and surface tension⁽¹⁸⁾. Therefore, the reported difference is not unexpected. Despite this, the results are in agreement that both fluids are highly immiscible. The equilibrated MD snapshots for each system are shown in Figure 6.5.

6.5.2 Remaining cross-interactions

The cross-interactions established from Chapters 3 and 4 are carried over to this system. The cross-energetic parameter ε_{ij} between the ES and CE beads are adjusted in the same way as the other hydrocarbon bead – ester bead interactions were in Chapter 3. The cross-interactions between the CE beads and the CO₂ beads is adjusted by using a k_{ij} of 0.08 which was found to reproduce the VLE data for a variety of CO₂ – n-alkane binary mixtures⁽¹⁷³⁾. The list of all intermolecular interactions is provided in Table 6.3, with an accompanying Table 6.4 which describes how each interaction was derived.

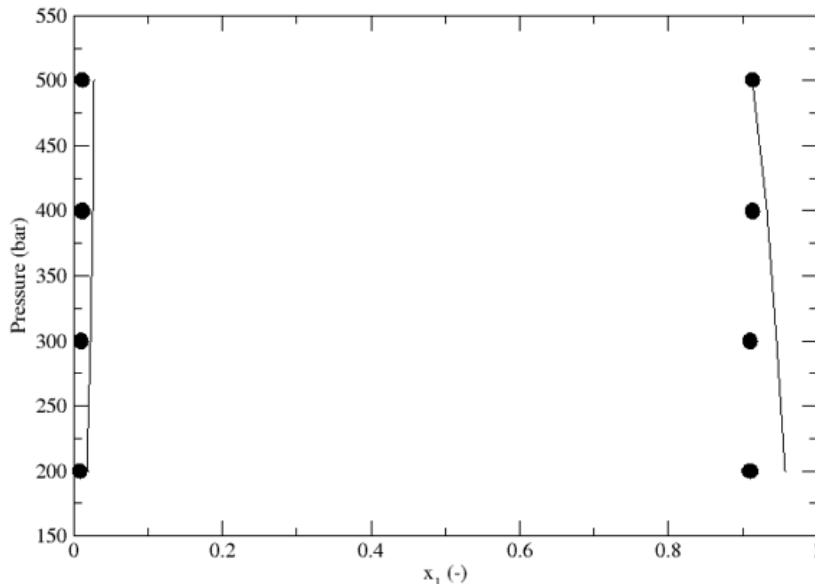


Figure 6.4 P-x liquid-liquid phase diagram at 383.15 K for the binary mixture scCO₂ (x_1) and water. The SAFT CG model is shown as solid circles, while the experimental data⁽²⁸⁵⁾ is shown as solid lines.

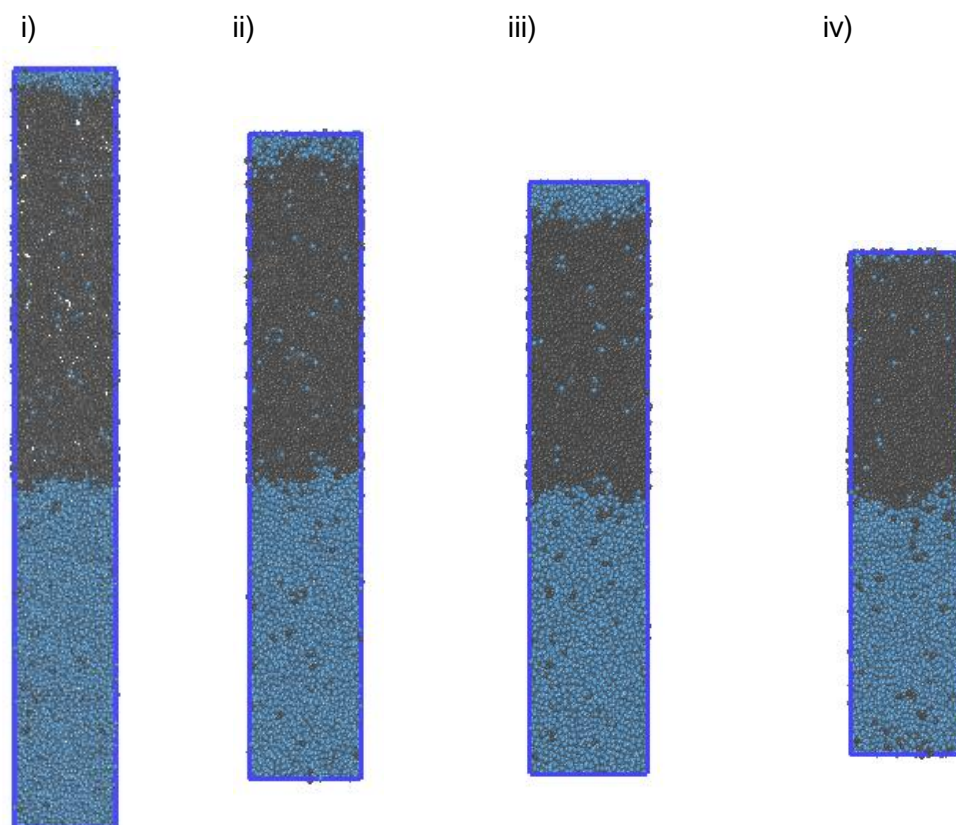


Figure 6.5 Equilibrated MD simulation images for the scCO₂ – water system at i) 200 bar, ii) 300 bar, iii) 400 bar and iv) 500 bar. The temperature is 383.15 K for all systems. The colour code is provided in Table 5.1 and Table 3.1.

Table 6.3 List of the new non-bonded intermolecular interaction parameters

Bead – Bead interaction	σ_{ij} (nm)	ε_{ij}/k_B (K)	λ_{ij}^r (-)	k_{ij} (-)
TMS – TMS	0.3327	134.05	8.55	-
TMS – CE	0.3780	203.52	14.62	-
TMS – ES	0.3533	228.17	13.27	-
TMS – SO	0.3524	98.82	8.27	-
TMS – NA	0.2774	33.20	8.27	-
TMS – W	0.3489	229.61	8.27	-
TMS – CO	0.3042	161.42	11.11	-
CE – CE	0.4349	330.25	27.30	-
CE – ES*	0.4094	270.07	24.49	-
CE – SO	0.4085	155.79	14.02	-
CE – NA	0.3335	46.92	14.02	-
CE – W	0.4050	244.94	14.02	0.3205
CE – CO	0.3603	219.47	19.97	0.0800
ES – CO	0.3348	270.45	18.01	-
SO – CO	0.3338	117.19	10.70	-
NA – CO	0.2588	41.20	10.70	-
W – CO	0.3303	190.92	10.70	0.3000
CO – CO	0.2857	196.55	14.85	-

* The bead bond length is constrained to a constant value so that $b_{0,ij} = 0.6\sigma_{ij}$

Table 6.4 Parameter matrix indicating how each new intermolecular interaction was derived.

	TMS	CE	ES	SO	NA	W	CO
TMS	M&M	Lafitte	Lafitte	Lafitte	Lafitte	Lafitte	Lafitte
CE		M&M	VLE	Lafitte	Lafitte	IFT	VLE
CO			Lafitte	Lafitte	Lafitte	LLE	M&M

6.6 Concluding remarks and future work

Preliminary steps have been completed to study the AOTSiC-water-scCO₂ system using the SAFT-based MD methodology. Due to the similarity in structure to AOT, many of the force field parameters were carried over from Chapters 3 and 4. The new CG beads created were assigned force field parameters using Bottled SAFT⁽²⁹⁾. The water-scCO₂ cross-interactions were optimised by MD simulation to match the binary mixture solubility at various pressures using a single binary interaction parameter. The results show good agreement to experimental values. The benefits of molecular simulation include the ability to study systems which can be expensive and time-consuming via purely experimental routes. As shown with the W/scCO₂ microemulsions, high pressures (e.g. 350 bar) are encountered in these systems, which require access to specialist equipment⁽³³⁾. With molecular simulations, this is not an issue as changing pressure is just a case of changing a line in the MD code.

This work provides an initial molecular model to study the ternary system, which can be compared to the experimental HP SANS data⁽³³⁾. The analytical techniques described in Chapters 3 and 4 can be used to calculate the equivalent MD values. For example, multiple MD simulations can be carried out where the water content is gradually reduced, and the nematic order parameter can establish the phase boundary between stable W/scCO₂ microemulsions (low S_2 values), and bicontinuous/phase separated systems (high S_2 values). The relative shape anisotropy κ^2 can be used to determine the shape of the resultant RMs.

An accurate model can then be used to investigate the impact of surfactant structure on CO₂-philicity, to design more effective non-fluorinated microemulsion stabilisers, with higher maximum amounts of water that can be solubilised. It has been suggested in the work of Hill et al⁽³³⁾ that the substitution of silicon for carbon atoms has an effect of increasing the minimum area occupied by a surfactant at the water-scCO₂ interface, which in turn has a positive effect on the maximum w_0 . One approach is then to study the effect of increasing the number of silicon atoms in the surfactant tail, by adding more silane CG groups. For example the CE bead can be replaced with a bead representing disilane (Si₂H₆). This will have the effect of increasing the tail volume resulting in a surfactant with a lower FFV . Other groups can be added to the structure, for example it has been shown that incorporating oxygen into the surfactant tails significantly improves CO₂-philicity, for example by a carbonyl group⁽²⁸⁸⁾. In the CG MD simulation this can be achieved by adding a formaldehyde CG bead to the tail. The number of methyl branches in the tail structure have been shown to affect CO₂-philicity⁽²⁸⁹⁾, and this can be explored by adding methane CG beads to varying positions on the surfactant tail. Tail length can impact CO₂ philicity due to increased flexibility⁽²⁷⁹⁾ allowing for a greater packing efficiency, and this can be explored by adding more alkyl beads to the main tail structure. Sagisaka et al⁽²⁹⁰⁾ identified that changing counter-ions of TMS surfactants from Na⁺ to Mg²⁺ results in a reduction of minimum air-water surface tension, implying enhanced CO₂-philicity. This can be tested using the MD simulation method, where the parameters for the Mg²⁺ counter-ion would be obtained from the SAFT VRE Mie equation of state^{(27) (106)}. The abundance of force field parameters in Bottled SAFT⁽²⁹⁾ means a variety of different functional groups can be investigated. The results of this study can point to new design approaches for CO₂-philic surfactants, widening the potential of scCO₂ as a green processing, cleaning, and separation medium.

References

1. Houston J. Surfactant Market Overview: Importance in Different Industries. In: Farn RJ, editor. *Chemistry and Technology of Surfactants* 2006.
2. Sarkar A, Singh H. Emulsions and Foams Stabilised by Milk Proteins. In: McSweeney PLH, O'Mahony JA, editors. *Advanced Dairy Chemistry*. New York: Springer Science+Business Media; 2016.
3. Research AM. Surfactant Market Size, Share | Industry Analysis & Forecast, 2027: Allied Market Research; [14/04/2022]. Available from: <https://www.alliedmarketresearch.com/surfactant-market>.
4. IHS Markit. Surfactants: Speciality Chemicals Update Program [16/04/2022]. Available from: <https://ihsmarkit.com/products/chemical-surfactants-scup.html>.
5. Jackson M, Eadsforth C, Schowanek D, Delfosse T, Riddle A, Budgen N. Comprehensive review of several surfactants in marine environments: Fate and ecotoxicity. *Environmental toxicology and chemistry*. 2016;35(5):1077-86.
6. Kruszelnicka I, Ginter-Kramarczyk D, Wyrwas B, Idkowiak J. Evaluation of surfactant removal efficiency in selected domestic wastewater treatment plants in Poland. *Journal of environmental health science and engineering*. 2019;17(2):1257-64.
7. Badmus SO, Amusa HK, Oyehan TA, Saleh TA. Environmental risks and toxicity of surfactants: overview of analysis, assessment, and remediation techniques. *Environmental science and pollution research international*. 2021.
8. Petrie B, Barden R, Kasprzyk-Hordern B. A review on emerging contaminants in wastewaters and the environment: Current knowledge, understudied areas and recommendations for future monitoring. *Water research (Oxford)*. 2015;72:3-27.
9. Zhu F-J, Ma W-L, Xu T-F, Ding Y, Zhao X, Li W-L, et al. Removal characteristic of surfactants in typical industrial and domestic wastewater treatment plants in Northeast China. *Ecotoxicology and environmental safety*. 2018;153:84-90.
10. Bragin GE, Warren Davis C, Kung MH, Kelley BA, Sutherland CA, Lampi MA. Biodegradation and Ecotoxicity of Branched Alcohol Ethoxylates: Application of the Target Lipid Model and Implications for Environmental Classification. *J Surfact Deterg*. 2020;23:383–403.
11. Smith GN, Brown P, Rogers SE, Eastoe J. Evidence for a Critical Micelle Concentration of Surfactants in Hydrocarbon Solvents. *Langmuir*. 2013;29:3252-8.
12. Shang T, Smith KA, Hatton TA. Photoresponsive Surfactants Exhibiting Unusually Large, Reversible Surface Tension Changes under Varying Illumination Conditions. *Langmuir*. 2003;19:10764-73.
13. Nave S, Eastoe J, Penfold J. What Is So Special about Aerosol-OT? 1. Aqueous Systems. *Langmuir*. 2000;16:8733-40.
14. Herdes C, Pàmies JC, Marcos RM, Vega LF. Thermodynamic properties and aggregate formation of surfactant-like molecules from theory and simulation. *JOURNAL OF CHEMICAL PHYSICS*. 2004;120:9822-30.
15. Herdes C, Santiso EE, James C, Eastoe J, Müller EA. Modelling the interfacial behaviour of dilute light-switching surfactant solutions. *Journal of Colloid and Interface Science*. 2015;445:16-23.
16. Wong-ekkabut J, Karttunen M. The good, the bad and the user in soft matter simulations. *Biochimica et Biophysica Acta*. 2016;1858:2529–38.
17. Gubbins KE, Moore JD. Molecular Modeling of Matter: Impact and Prospects in Engineering. *Ind Eng Chem Res*. 2010;49:3026–46.
18. Lobanova O, Avendaño C, Lafitte T, Müller EA, Jackson G. SAFT- γ force field for the simulation of molecular fluids: 4. A single-site coarse-grained model of water applicable over a wide temperature range. *Molecular Physics*. 2015;113(9-10):1228-49.

19. Negro E, Latsuzbaia R, De Vries AH, Koper GJM. Experimental and molecular dynamics characterization of dense microemulsion systems: morphology, conductivity and SAXS. *Soft Matter*. 2014;10:8685.
20. Poghosyan AH, Adamyan MP, Shahinyan AA. A rippled defective phase of AOT lamella: A molecular dynamics study. *Colloids and Surfaces A*. 2019;578.
21. Pomata MHH, Laria D, Skaf MS, Elola MD. Molecular dynamics simulations of AOT-water/formamide reverse micelles: Structural and dynamical properties. *J Chem Phys*. 2008;129.
22. Israelachvili JN. *Special Interactions: Hydrogen-Bonding and Hydrophobic and Hydrophilic Interactions*. Intermolecular and Surface Forces 2011.
23. Noid WG. Perspective: Coarse-grained models for biomolecular systems. *J Chem Phys*. 2013;139.
24. Müller EA, Jackson G. Force-Field Parameters from the SAFT- γ Equation of State for Use in Coarse-Grained Molecular Simulations. *Annual Review of Chemical and Biomolecular Engineering*. 2014;5:405-27.
25. Chapman WG, Gubbins KE, Jackson G, Radosz M. SAFT: Equation-of-state solution model for associating fluids. *Fluid Phase Equilibria*. 1989;52:31-8.
26. Papaioannou V, Lafitte T, Avendaño C, Adjiman CS, Jackson G, Müller EA, et al. Group contribution methodology based on the statistical associating fluid theory for heteronuclear molecules formed from Mie segments. *J Chem Phys*. 2014;140.
27. Schreckenber J, Dufal S, Haslam AJ, Adjiman CS, Jackson G, Galindo A. Modelling of the thermodynamic and solvation properties of electrolyte solutions with the statistical associating fluid theory for potentials of variable range. *Molecular Physics*. 2014;112(17):2339-64.
28. Mejía A, Herdes C, Müller EA. Force Fields for Coarse-Grained Molecular Simulations from a Corresponding States Correlation. *Industrial & Engineering Chemistry Research*. 2014;53:4131-41.
29. Ervik Å, Mejía A, Müller EA. Bottled SAFT: A Web App Providing SAFT- γ Mie Force Field Parameters for Thousands of Molecular Fluids. *Journal of Chemical Information and Modelling*. 2016;56:1609-14.
30. Lobanova O, Herdes C, Jackson G, Müller EA. SAFT- γ Force Field for the Simulation of Molecular Fluids: 7. A Coarse Grained Model for Non-Ionic Surfactant Solutions (In preparation).
31. Rahman S. Development of coarse-grained models of ionic and non-ionic surfactants for the molecular simulation of structural, thermodynamic and dynamical properties. United Kingdom: Imperial College London; 2016.
32. Eastoe J, Hollamby MJ, Hudson L. Recent advances in nanoparticle synthesis with reversed micelles. *Advances in Colloid and Interface Science*. 2006;128-130:5-15.
33. Hill C, Umetsu Y, Fujita K, Endo T, Sato K, Yoshizawa A, et al. Design of Surfactant Tails for Effective Surface Tension Reduction and Micellization in Water and/or Supercritical CO₂. *Langmuir*. 2020;36(48):14829-40.
34. Eastoe J. Surfactant Aggregation and Adsorption at Interfaces. In: Cosgrove T, editor. *Colloid Science: Principles, Methods and Applications* 2005.
35. Tanford C. *The Hydrophobic Effect: Formation of Micelles and Biological Membranes*. New York: Wiley; 1978.
36. Israelachvili JN. *Thermodynamic Principles of Self-Assembly*. Intermolecular and Surface Forces 2011.
37. Algaba J, Míguez JM, Gómez-Álvarez P, Mejía A, Blas FJ. Preferential Orientations and Anomalous Interfacial Tensions in Aqueous Solutions of Alcohols. *The Journal of Physical Chemistry B*. 2020;124(38):8388-401.
38. McBain JW, Martin HE. XCII.—Studies of the constitution of soap solutions: the alkalinity and degree of hydrolysis of soap solutions. *J Chem Soc, Trans*. 1914;105:957-77.
39. Holmberg K. Surfactants. *Ullmann's Encyclopedia of Industrial Chemistry* Weinheim: Wiley-VCH; 2019.

40. Israelachvili JN. *Soft and Biological Structures. Intermolecular and Surface Forces*2011.
41. Mitchell DJ, Tiddy GJT, Waring L, Bostock T, McDonald MP. Phase behaviour of polyoxyethylene surfactants with water. Mesophase structures and partial miscibility (cloud points). *Journal of the Chemical Society, Faraday Transactions 1: Physical Chemistry in Condensed Phases.* 1983;79(4):975-1000.
42. Nave S. *Phase Behaviour and Interfacial Properties of Double-chain Anionic Surfactants*: University of Bristol; 2001.
43. Danielsson I, Lindman B. The definition of microemulsion. *Colloids and Surfaces.* 1981;3(4).
44. Eastoe J. Microemulsions. In: Cosgrove T, editor. *Colloid Science: Principles, Methods and Applications*2005.
45. Winsor PA. Hydrotropy, solubilisation and related Emulsification processes. Part I. *Transactions of the Faraday Society.* 1948;44:376-98.
46. Nave S, Eastoe J, Heenan RK, Steytler D, Grillo I. What Is So Special about Aerosol-OT? 2. Microemulsion Systems. *Langmuir.* 2000;16(23):8741-8.
47. Holmberg K, Jönsson B, Kronberg B, Lindman B. *Surfactants and Polymers in Aqueous Solution.* Second ed: John Wiley & Sons; 2003.
48. OECD. *OECD Guidelines for testing of chemicals.* 1995;305:1-68.
49. Ellis AJ, Hales SG, Ur-Rehman A, White GF. Novel Alkylsulfatases Required for Biodegradation of the Branched Primary Alkyl Sulfate Surfactant 2-Butyloctyl Sulfate. *APPLIED AND ENVIRONMENTAL MICROBIOLOGY.* 2002;68(1):31–6.
50. Begum F, Xu L, Amin S. Surfactants. *Kirk-Othmer Encyclopedia of Chemical Technology*2020.
51. Jardak K, Drogui P, Daghrir R. Surfactants in aquatic and terrestrial environment: occurrence, behavior, and treatment processes. *Environmental science and pollution research international.* 2016;23(4):3195-216.
52. Rosal R, Rodea-Palomares I, Boltes K, Fernández-Piñas F, Leganés F, Petre A. Ecotoxicological assessment of surfactants in the aquatic environment: Combined toxicity of docusate sodium with chlorinated pollutants. *Chemosphere.* 2010;81:288-93.
53. Blasco J, Moreno-Garrido I. Chapter 7 Toxicity of surfactants. *Comprehensive Analytical Chemistry.* 2003.
54. Rebello S, Asok AK, Mundayoor S, Jisha MS. Surfactants: Chemistry, Toxicity and Remediation. In: Lichtfouse E, editor. *Pollutant Diseases, Remediation and Recycling. Environmental Chemistry for a Sustainable World.* 4. Switzerland: Springer International Publishing; 2013.
55. Rosen MJ, Kunjappu JT. *Surfactants and Interfacial Phenomena.* Fourth ed. New Jersey: Wiley; 2012.
56. Miller DJ, McWilliams P. Octanol-Water Partition Coefficients of Surfactants: Slow Stirring/Surface Tension Method. *Tenside Surfactants Detergents.* 2010;47.
57. Hodges G, Eadsforth C, Bossuyt B, Bouvy A, Enrici M-H, Geurts M, et al. A comparison of log Kow (n-octanol–water partition coefficient) values for non-ionic, anionic, cationic and amphoteric surfactants determined using predictions and experimental methods. *Environmental sciences Europe.* 2019;31(1).
58. Petrov PG, Ahir SV, Terentjev EM. Rheology at the Phase Transition Boundary: 1. Lamellar L α Phase of AOT Surfactant Solution. *Langmuir.* 2002;18:9133-9.
59. Leser ME, Kooijman M, Pollitte J, Magid LJ. Effect of the Macrobicyclic Ligand Kryptofix 222 on AOT/Water/Cyclohexane Microemulsions. *The Journal of Physical Chemistry.* 1991;95(22):9013-9.
60. Peach J, Eastoe J. Supercritical carbon dioxide: A solvent like no other. *Beilstein journal of organic chemistry.* 2014;10(1):1878-95.
61. Prausnitz JM, Lichtenthaler RN, de Azevedo EG. *Molecular thermodynamics of fluid-phase equilibria.* Prentice-Hall, editor1986.
62. Braun E, Gilmer J, Mayes HB, Mobley DL, Monroe JL, Prasad S, et al. Best Practices for Foundations in Molecular Simulations [Article v1.0]. *Living J Comp Mol Sci.* 2019;1(1).

63. Allen MP, Tildesley DJ. *Computer Simulation of Liquids*. Oxford: Oxford University Press; 1987.
64. Sadus RJ. *Molecular Simulation of Fluids* 1999.
65. Lindeboom T. *Molecular Origins of the Thermodynamic Properties, Phase Separation Behaviour and Structure of Biomolecules in Aqueous Solutions*: Imperial College London; 2020.
66. Grüneisen E. Theorie des festen Zustandes einatomiger Elemente. *Annalen der Physik*. 1912;344(12):257-306.
67. Mie G. Zur kinetischen Theorie der einatomigen Körper. *Annalen der Physik*. 1903;11:657-97.
68. Eisenschitz R, London F. Über das Verhältnis der van der Waalsschen Kräfte zu den homöopolaren Bindungskräften. *Zeitschrift für Physik*. 1930;60(7):491-527.
69. Lennard-Jones JE. On the determination of molecular fields 1. From the variation of the viscosity of a gas with temperature. *Proc R Soc (London) A*. 1924;106(738):441-62.
70. Coulomb C. Premier mémoire sur l'électricité et le magnétisme. *Histoire de l'Académie royale des sciences*. 1785:569-77.
71. Reith D, Meyer H, Müller-Plathe F. Mapping Atomistic to Coarse-Grained Polymer Models Using Automatic Simplex Optimization To Fit Structural Properties. *Macromolecules*. 2001;34(7):2335-45.
72. van der Spoel D, Lindahl E, Hess B, Groenhof G, Mark AE, Berendsen HJC. GROMACS: Fast, Flexible, and Free. *Journal of Computational Chemistry*. 2005;26:1701-18.
73. Frenkel D, Smit B. *Understanding Molecular Simulation. From Algorithms to Applications*. Second ed. London: Academic Press; 2002.
74. Atkins P, de Paula J. *Atkins' Physical Chemistry*. Oxford: Oxford University Press; 2006.
75. Berendsen HJC, van Gunsteren WF. Practical Algorithms for Dynamic Simulation. In: *Molecular-Dynamics Simulations of Statistical-Mechanical Systems* [Internet]. Italy; [43-65].
76. Leach AR. *Molecular Modelling: Principles and Applications*. 2nd ed. Essex, England: Pearson Education Limited; 2001.
77. Darden T, York D, Pedersen L. Particle mesh Ewald: An N·log(N) method for Ewald sums in large systems. *The Journal of chemical physics*. 1993;98(12):10089-92.
78. Hünenberger PH. Thermostat Algorithms for Molecular Dynamics Simulations. *Advanced Computer Simulation*. 2005:105-49.
79. Bussi G, Donadio D, Parrinello M. Canonical sampling through velocity rescaling. *Journal of Chemical Physics*. 2007;126(1):014101--7.
80. Nosé S. A unified formulation of the constant temperature Molecular Dynamics methods. *Journal of Chemical Physics*. 1984;81(1):511-9.
81. Hoover WG. Canonical dynamics - equilibrium phase-space distributions. *Physical Review A*. 1985;31(3):1695 - 7.
82. Parrinello M, Rahman A. Polymorphic transitions in single crystals: A new molecular dynamics method. *J Appl Phys*. 1981;52:7182-90.
83. Wertheim WS. Fluids with highly directional attractive forces. 1. Statistical thermodynamics. *Journal of Statistical Physics*. 1984;35(1-2):19-34.
84. McCabe C, Galindo A. SAFT Associating Fluids and Fluid Mixtures. In: Goodwin ARH, Sengers JV, Peters CJ, editors. *Applied Thermodynamics of Fluids*: Royal Society of Chemistry; 2010.
85. Gil-Villegas A, Galindo A, Whitehead PJ, Mills SJ, Jackson G, Burgess AN. Statistical associating fluid theory for chain molecules with attractive potentials of variable range. *The Journal of chemical physics*. 1997;106(10):4168-86.
86. Johnson JK, Müller EA, Gubbins K. Equation of state for Lennard-Jones chains. *J Phys Chem*. 1994;98:6413-19.
87. Lafitte T, Apostolakou A, Avendaño C, Galindo A, Adjiman CS, Müller EA, et al. Accurate statistical associating fluid theory for chain molecules formed from Mie segments. *J Chem Phys*. 2013;139.

88. Avendaño C, Lafitte T, Adjiman CS, Galindo A, Müller EA, Jackson G. SAFT- γ Force Field for the Simulation of Molecular Fluids: 2. Coarse-Grained Models of Greenhouse Gases, Refrigerants, and Long Alkanes. *The journal of physical chemistry B*. 2013;117(9):2717-33.
89. Morgado P, Lobanova O, Müller EA, Jackson G, Almeida M, Filipe EJM. SAFT- γ force field for the simulation of molecular fluids: 8. Hetero-segmented coarse-grained models of perfluoroalkylalkanes assessed with new vapour-liquid interfacial tension data. *Molecular physics*. 2016;114(18):2597-614.
90. Lobanova O. Development of coarse-grained force fields from a molecular based equation of state for thermodynamic and structural properties of complex fluids. London: Imperial College London; 2014.
91. Lafitte T, Papaioannou V, Dufal S, Pantelides CC. gSAFT: Advanced physical property prediction for process modelling. *Computer Aided Chemical Engineering*. 2017;40:1003-8.
92. Reed TMK, Gubbins KE. *Applied Statistical Mechanics: Thermodynamic and Transport Properties of Fluids*: McGraw-Hill; 1973.
93. Avendaño C, Lafitte T, Galindo A, Adjiman CS, Jackson G, Müller EA. SAFT- γ Force Field for the Simulation of Molecular Fluids. 1. A Single-Site Coarse Grained Model of Carbon Dioxide. *The journal of physical chemistry B*. 2011;115(38):11154-69.
94. Yaws CL. *Thermophysical properties of chemicals and hydrocarbons (Electronic Edition)*. 2010.
95. Herdes C, Totton TS, Müller EA. Coarse grained force field for the molecular simulation of natural gases and condensates. *Fluid Phase Equilibria*. 2015;406:91-100.
96. Herdes C, Ervik Å, Mejía A, Müller EA. Prediction of the water/oil interfacial tension from molecular simulations using the coarse-grained SAFT- γ Mie Force Field. *Fluid Phase Equilibria*. 2018;476:9-15.
97. Lorentz HA. Ueber die Anwendung des Satzes vom Virial in der kinetischen Theorie der Gase. *Annalen der Physik*. 1881;248(1):127-36.
98. Berthelot D. Sur le mélange des gaz. *Comptes rendus hebdomadaires des séances de l'Académie des Sciences*. 1898;126:1703-855.
99. London F. The general theory of molecular forces. *Transactions of the Faraday Society*. 1937;33(0):8b-26.
100. Lennard-Jones JE. On the determination of molecular fields II. From the equation of state of a gas. *Proc R Soc (London) A*. 1924;106(738):463-77.
101. Haslam AJ, Galindo A, Jackson G. Prediction of binary intermolecular potential parameters for use in modelling fluid mixtures. *Fluid Phase Equilibria*. 2008;266(1):105-28.
102. Hudson GH, McCoubrey JC. Intermolecular forces between unlike molecules. A more complete form of the combining rules. *Transactions of the Faraday Society*. 1960;56(0):761-6.
103. Lafitte T, Avendaño C, Papaioannou V, Galindo A, Adjiman C, Jackson G, et al. SAFT- γ force field for the simulation of molecular fluids: 3. Coarse-grained models of benzene and hetero-group models of n-decylbenzene. *Molecular Physics*. 2012;110(11-12):1189-203.
104. Marrink SJ, Risselada HJ, Yefimov S, Tieleman DP, de Vries AH. The MARTINI force field: Coarse grained model for biomolecular simulations. *Journal of Physical Chemistry B*. 2007;111(27):7812-24.
105. Shinoda W, Devane R, Klein ML. Coarse-grained force fields for ionic surfactants. *Soft Matter*. 2011;7:6178.
106. Eriksen DK, Lazarou G, Galindo A, Jackson G, Adjiman CS, Haslam AJ. Development of intermolecular potential models for electrolyte solutions using an electrolyte SAFT-VR Mie equation of state. *Molecular Physics*. 2016.
107. Blum L. Mean spherical model for asymmetric electrolytes. *Molecular Physics*. 1975;30(5):1529-35.
108. Blum L, Hoeye JS. Mean spherical model for asymmetric electrolytes. 2. Thermodynamic properties and the pair correlation function. *Journal of physical chemistry (1952)*. 1977;81(13):1311-6.
109. Born M. *Z Phys*. 1920;1(45).

110. Uematsu M, Frank EU. Static Dielectric Constant of Water and Steam. *Journal of physical and chemical reference data*. 1980;9(4):1291-306.
111. Kwak TY, Mansoori GA. Van der waals mixing rules for cubic equations of state. Applications for supercritical fluid extraction modelling. *Chemical engineering science*. 1986;41(5):1303-9.
112. Shannon R. Revised effective ionic radii and systematic studies of interatomic distances in halides and chalcogenides. *Acta Crystallographica Section A*. 1976;32(5):751-67.
113. Marcus Y. Ionic radii in aqueous solutions. *Chemical Reviews*. 1988;88(8):1475-98.
114. Lide ER. *CRC Handbook of Chemistry and Physics*. 86th ed. London, UK: CRC Press; 2005.
115. Jungwirth P, Curtis JE, Tobias DJ. Polarizability and aqueous solvation of the sulfate dianion. *Chemical Physics Letters*. 2003;367(5):704-10.
116. Wang X-B, Nicholas JB, Wang L-S. Photoelectron Spectroscopy and Theoretical Calculations of SO₄⁻ and HSO₄⁻: Confirmation of High Electron Affinities of SO₄ and HSO₄. *The Journal of Physical Chemistry A*. 2000;104(3):504-8.
117. BRAND™ BLAUBRAND™ Borosilicate Glass Calibrated Density Bottles: fisher scientific; [14/04/2022]. Available from: <https://www.fishersci.co.uk/shop/products/blaubrand-borosilicate-glass-calibrated-density-bottle/p-8000978>.
118. Gibbs JW. *The Collected Works of J. W. Gibbs*. New York: Longmans, Green; 1931.
119. Dukhin SS, Kretzschmar G, Miller R. Introduction. *Dynamics of Adsorption at Liquid Interfaces*1995.
120. von Helmholtz H. *Physical memoirs, selected and translated from foreign sources*: Taylor & Francis; 1882.
121. KRÜSS. Drop volume tensiometer [14/04/2022]. Available from: <https://www.kruss-scientific.com/en/know-how/glossary/drop-volume-tensiometer>.
122. KRÜSS. Drop Volume Tensiometer DVT50 [14/04/2022]. Available from: <https://www.kruss-scientific.com/en/products-services/products/dvt50>.
123. Kirkwood JG, Buff FP. *J Chem Phys*. 1949;17:338.
124. Eastoe J, Nave S, Downer A, Paul A, Rankin A, Tribe K, et al. Adsorption of Ionic Surfactants at the Air-solution Interface. *Langmuir*. 2000;16:4511-8.
125. Eastoe J. Surfactant Aggregation and Adsorption at Interfaces. In: Cosgrove T, editor. *Colloid Science: Principles, Methods and Applications*2009.
126. Atkins P, de Paula J. *Atkins' Physical Chemistry Oxford*: Oxford University Press 2006.
127. King MJ. *Theoretical Analysis of Interfacial Phenomena during Thin Film Growth and Surfactant Characterization*: North Carolina State University; 2018.
128. Goral M, Wisniewska-Gocłowska B, Skrzecz A, Owczarek I, Blazej K, Haulait-Pirson M-C, et al. IUPAC-NIST Solubility Data Series. 81. Hydrocarbons with Water and Seawater—Revised and Updated. Part 3. C₆H₈–C₆H₁₂ Hydrocarbons with Water and Heavy Water. *Journal of physical and chemical reference data*. 2005;34(2):657-708.
129. Góral M, Shaw DG, Mączyński A, Wiśniewska-Gocłowska B, Jezierski A. IUPAC-NIST Solubility Data Series. 88. Esters with Water—Revised and Updated. Part 1. C₁ to C₄ Esters. *J Phys Chem Ref Data*. 2009;38.
130. Eppenga R, Frenkel D. Monte Carlo study of the isotropic and nematic phases of infinitely thin hard plates. *Molecular Physics*. 1984;52(6):1303-34.
131. McGibbon RT, Beauchamp KA, Harrigan MP, Klein C, Swails JM, Hernandez CX, et al. MDTraj: A Modern Open Library for the Analysis of Molecular Dynamics Trajectories. *Biophysical Journal*. 2015;109(8):1528-32.
132. Vermeer LS, de Groot BL, Réat V, Milon A, Czaplicki J. Acyl chain order parameter profiles in phospholipid bilayers: computation from molecular dynamics simulations and comparison with 2H NMR experiments. *European biophysics journal*. 2007;36(8):919-31.
133. Theodorou DN, Suter UW. Shape of Unperturbed Linear Polymers: Polypropylene. *Macromolecules*. 1985;18:1206-14.

134. Velinova M, Sengupta D, Tadjer AV, Marrink S-J. Sphere-to-Rod Transitions of Nonionic Surfactant Micelles in Aqueous Solution Modeled by Molecular Dynamics Simulations. *Langmuir*. 2011;27(23):14071-7.
135. Richardson R. Scattering and Reflection Techniques. In: Cosgrove T, editor. *Colloid Science: Principles, methods and applications*. Second ed: John Wiley & Sons, Ltd; 2010.
136. Moseley HGJ. XCIII. The high-frequency spectra of the elements. *The London, Edinburgh, and Dublin Philosophical Magazine and Journal of Science*. 1913;26(156):1024-34.
137. Bacon GE. *Neutron Scattering in Chemistry*. London: Butterworths; 1977.
138. Fairweather GS. *Investigations into the Mesophase Behaviour and Equilibrium Dynamics of a Family of Aerosol OT-related Surfactants*: Victoria University of Wellington; 2017.
139. Fontell K. The Structure of the Lamellar Liquid Crystalline Phase in Aerosol OT-Water System. *Journal of Colloid and Interface Science*. 1973;44(2).
140. Zhuang W, Chen X, Yang C, Wang L, Chai Y. Study of Ordering for AOT/Water Lamellar Lyotropic Liquid Crystal: Small-angle X-ray Scattering Experiments. *Acta Phys -Chim Sin*. 2005;21(9):1055-8.
141. Klauda JB, Venable RM, Freites JA, O'Connor JW, Tobias DJ, Mondragon-Ramirez C, et al. Update of the CHARMM All-Atom Additive Force Field for Lipids: Validation on Six Lipid Types. *The journal of physical chemistry B*. 2010;114(23):7830-43.
142. Best RB, Zhu X, Shim J, Lopes PEM, Mittal J, Feig M, et al. Optimization of the Additive CHARMM All-Atom Protein Force Field Targeting Improved Sampling of the Backbone ϕ , ψ and Side-Chain $\chi(1)$ and $\chi(2)$ Dihedral Angles. *Journal of chemical theory and computation*. 2012;8(9):3257-73.
143. Dickson CJ, Madej BD, Skjevik ÅA, Betz RM, Teigen K, Gould IR, et al. Lipid14: The Amber Lipid Force Field. *Journal of chemical theory and computation*. 2014;10(2):865-79.
144. Duan Y, Wu C, Chowdhury S, Lee MC, Xiong G, Zhang W, et al. A point-charge force field for molecular mechanics simulations of proteins based on condensed-phase quantum mechanical calculations. *Journal of computational chemistry*. 2003;24(16):1999-2012.
145. Jorgensen WL, Maxwell DS, Tirado-Rives J. Development and Testing of the OPLS All-Atom Force Field on Conformational Energetics and Properties of Organic Liquids. *Journal of the American Chemical Society*. 1996;118(45):11225-36.
146. Kaminski GA, Friesner RA, Tirado-Rives J, Jorgensen WL. Evaluation and Reparametrization of the OPLS-AA Force Field for Proteins via Comparison with Accurate Quantum Chemical Calculations on Peptides. *The journal of physical chemistry B*. 2001;105(28):6474-87.
147. Yang L, Tan C-h, Hsieh M-J, Wang J, Duan Y, Cieplak P, et al. New-Generation Amber United-Atom Force Field. *The journal of physical chemistry B*. 2006;110(26):13166-76.
148. Lee S, Tran A, Allsopp M, Lim JB, Hénin Jrm, Klauda JB. CHARMM36 United Atom Chain Model for Lipids and Surfactants. *The journal of physical chemistry B*. 2014;118(2):547-56.
149. Poger D, Van Gunsteren WF, Mark AE. A new force field for simulating phosphatidylcholine bilayers. *Journal of computational chemistry*. 2010;31(6):1117-25.
150. Brini E, Algaer EA, Ganguly P, Li C, Rodriguez-Ropero F, van der Vegt NFA. Systematic coarse-graining method for soft matter simulations - a review. *Soft Matter*. 2013;9:2108.
151. DeVane RH, Wagner MS, Murch BP. The Procter and Gamble Company: Current State and Future Needs in Materials Modeling. In: Madsen LD, Svedberg EB, editors. *Materials Research for Manufacturing*. Switzerland: Springer International Publishing; 2016.
152. Groot RD, Warren PB. Dissipative particle dynamics: Bridging the gap between atomistic and mesoscopic simulation. *J Chem Phys*. 1997;107.
153. Vishnyakov A, Talaga DS, Neimark AV. DPD Simulation of Protein Conformations: From α -Helices to β -Structures. *The journal of physical chemistry letters*. 2012;3(21):3081-7.

154. Ingólfsson HI, Lopez CA, Uusitalo JJ, de Jong DH, Gopal SM, Periole X, et al. The power of coarse graining in biomolecular simulations. *WIREs Comput Mol Sci*. 2014;4:225-48.
155. van der Kamp MW, Shaw KE, Woods CJ, Mulholland AJ. Biomolecular simulation and modelling: status, progress and prospects. *Journal of the Royal Society interface*. 2008;5(Suppl 3):173-90.
156. Arnarez Cm, Uusitalo JJ, Masman MF, Ingólfsson HI, de Jong DH, Melo MN, et al. Dry Martini, a Coarse-Grained Force Field for Lipid Membrane Simulations with Implicit Solvent. *Journal of chemical theory and computation*. 2015;11(1):260-75.
157. Lee H, de Vries AH, Marrink S-J, Pastor RW. A Coarse-Grained Model for Polyethylene Oxide and Polyethylene Glycol: Conformation and Hydrodynamics. *The journal of physical chemistry B*. 2009;113(40):13186-94.
158. Wagner JW, Dama JF, Durumeric AEP, Voth GA. On the representability problem and the physical meaning of coarse-grained models. *J Chem Phys*. 2016;145(044108).
159. Reith D, Putz M, Müller-Plathe F. Deriving effective mesoscale potentials from atomistic simulations. *Journal of Computational Chemistry*. 2003;24(13):1624-36.
160. Henderson RL. Uniqueness theorem for fluid pair correlation-functions. *Physics Letters A*. 1974;49(3):197-8.
161. Lyubartsev AP, Laaksonen A. Calculation of effective interaction potentials from radial-distribution functions - A reverse Monte-Carlo approach. *Physical Review E*. 1995;52(4):3730-7.
162. Izvekov S, Voth GA. Modeling real dynamics in the coarse-grained representation of condensed phase systems. *The Journal of chemical physics*. 2006;125(15):151101--4.
163. Shell M. The relative entropy is fundamental to multiscale and inverse thermodynamic problems. *Journal of Chemical Physics*. 2008;129(14).
164. Shell MS. Coarse graining and multiscale techniques: University of California Santa Barbara; 2019.
165. Rahman S, Lobanova O, Jiménez-Serratos G, Braga C, Raptis V, Müller EA, et al. SAFT- γ Force Field for the Simulation of Molecular Fluids. 5. HeteroGroup Coarse-Grained Models of Linear Alkanes and the Importance of Intramolecular Interactions. *The Journal of Physical Chemistry B*. 2018;122(9161-9177).
166. Grunewald F, Rossi G, de Vries AH, Marrink SJ, Monticelli L. Transferable MARTINI Model of Poly(ethylene Oxide). *The journal of physical chemistry B*. 2018;122(29):7436-49.
167. Shinoda W, Devane R, Klein ML. Multi-property fitting and parameterization of a coarse grained model for aqueous surfactants. *Molecular Simulation*. 2007;33(1-2):27-36.
168. Marrink SJ, de Vries AH, Mark AE. Coarse Grained Model for Semiquantitative Lipid Simulations. *J Phys Chem B*. 2004;108:750-60.
169. Nielsen SO, Lopez CF, Srinivas G, Klein ML. A coarse grain model for n-alkanes parameterized from surface tension data. *The Journal of chemical physics*. 2003;119(14):7043-9.
170. Marrink SJ, Tieleman DP. Perspective on the Martini model. *Chemical Society reviews*. 2013;42(16):6801-22.
171. Shinoda W, Devane R, Klein ML. Coarse-grained molecular modelling of non-ionic surfactant self-assembly. *Soft Matter*. 2008;4(12):2454-62.
172. He X, Shinoda W, Devane R, Klein ML. Exploring the utility of coarse-grained water models for computational studies of interfacial systems. *Molecular Physics*. 2010;108(15):2007-20.
173. Lobanova O, Mejía A, Jackson G, Müller EA. SAFT- γ force field for the simulation of molecular fluids 6: Binary and ternary mixtures comprising water, carbon dioxide, and n-alkanes. *J Chem Thermodynamics*. 2016;93:320-36.
174. Ekwall P, Mandell L, Fontell K. Some Observations on Binary and Ternary Aerosol OT Systems. *Journal of Colloid and Interface Science*. 1970;33.
175. Park D, Rogers J, Toft RW, Winsor PW. The Structure of Micellar Solutions of Ionic Amphiphiles: The Lamellar Phase. X-Ray Diffraction Measurements with the Aerosol OT/Water System. *Journal of Colloid and Interface Science*,. 1970;32.

176. Chien W. Synthesis of Y₂O₃:Eu phosphors by bicontinuous cubic phase process. *Journal of Crystal Growth*. 2006;290:554–9.
177. Huang L, Wang H, Wang Z, Mitra A, Zhao D, Yan Y. Cuprite Nanowires by Electrodeposition from Lyotropic Reverse Hexagonal Liquid Crystalline Phase. *Chem Mater*. 2002;14:876-80.
178. Tavano L, Gentile L, Rossi CO, Muzzalupo R. Novel gel-niosomes formulations as multicomponent systems for transdermal drug delivery. *Colloids and Surfaces B: Biointerfaces*. 2013;110:281-8.
179. Ranneh A, Iwao Y, Noguchi S, Oka T, Itai S. The use of surfactants to enhance the solubility and stability of the water-insoluble anticancer drug SN38 into liquid crystalline phase nanoparticles. *International Journal of Pharmaceutics*. 2016;515:501–5.
180. Yang C, Chen X, Qiu H, Zhuang W, Chai Y, Hao J. Dissipative Particle Dynamics Simulation of Phase Behaviour of Aerosol OT/Water System. *J Phys Chem B*. 2006;110:21735-40.
181. Bhat A, Harris MT, Jaeger VW. Structural Insights into Self-Assembled Aerosol-OT Aggregates in Aqueous Media Using Atomistic Molecular Dynamics. *The journal of physical chemistry*. 2021;125(50):13789-803.
182. Al Ghafri S, Maitland GC, Trusler JPM. Densities of Aqueous MgCl₂(aq), CaCl₂(aq), KI(aq), NaCl(aq), KCl(aq), AlCl₃(aq), and (0.964 NaCl + 0.136 KCl)(aq) at Temperatures Between (283 and 472) K, Pressures up to 68.5 MPa, and Molalities up to 6 mol·kg⁻¹. *Journal of Chemical & Engineering Data*. 2012;57(4):1288-304.
183. Hamer WJ, Wu YC. Osmotic Coefficients and Mean Activity Coefficients of Uni-univalent Electrolytes in Water at 25°C. *Journal of Physical and Chemical Reference Data*. 1972;1(4):1047-100.
184. Zaitsev I, Mozharova G, Vernigora I, Makarovskaya N, Tsurko N, Pavlyuchenko E, et al. Physico-chemical properties of binary aqueous solutions of electrolytes in wide ranges of concentrations and temperatures (hand-book): Karbonat; 1988.
185. Humphrey W, Dalke A, Schulten K. VMD - Visual Molecular Dynamics. *J Molec Graphics*. 1996;14.1:33-8.
186. Müller EA, Ervik Å, Mejía A. A Guide to Computing Interfacial Properties of Fluids from Molecular Simulations [Article v1.0]. *Living J Comp Mol Sci*. 2021;2:1-27.
187. Feria E, Algaba J, Míguez JM, Mejía A, Blas FJ. Molecular dynamics of liquid–liquid equilibrium and interfacial properties of aqueous solutions of methyl esters. *Physical chemistry chemical physics*. 2022;24(9):5371-82.
188. Scott RL, van Konynenburg PH. Static properties of solutions. Van der Waals and related models for hydrocarbon mixtures. *Discussions of the Faraday Society*. 1970;49:87.
189. Van Konynenburg PH, Scott RL. Critical Lines and Phase Equilibria in Binary Van Der Waals Mixtures. *Philosophical transactions of the Royal Society of London Series A: Mathematical, physical, and engineering sciences*. 1980;298(1442):495.
190. Ervik Å, Lysgaard MO, Herdes C, Jiménez-Serratos G, Müller EA, Munkejord ST, et al. A multiscale method for simulating fluid interfaces covered with large molecules such as asphaltenes. *Journal of Computational Physics*. 2016;327:576–611.
191. Curtis EM, Hall CK. Molecular Dynamics Simulations of DPPC Bilayers Using “LIME”, a New Coarse-Grained Model. *J Phys Chem B*. 2013;117:5019–30.
192. Thermophysical Properties of Fluid Systems in NIST Chemistry WebBook, NIST Standard Reference Database Number 69 [Internet]. [cited 25/04/2022]. Available from: <http://webbook.nist.gov>.
193. Jalali-Jivan M, Garavand F, Jafari SM. Microemulsions as nano-reactors for the solubilization, separation, purification and encapsulation of bioactive compounds. *Advances in colloid and interface science*. 2020;283:102227-.
194. Wolf S, Feldmann C. Microemulsions: Options To Expand the Synthesis of Inorganic Nanoparticles. *Angewandte Chemie (International ed)*. 2016;55(51):15728-52.
195. Gradzielski M, Duvail M, Zemb T, Gradzielski M, Duvail M, de Molina PM, et al. Using Microemulsions: Formulation Based on Knowledge of Their Mesosstructure. *Chemical reviews*. 2021;121(10):5671-740.

196. Dib N, Girardi VR, Silber JJ, Correa NM, Falcone RD. How the external solvent in biocompatible reverse micelles can improve the alkaline phosphatase behavior. *Organic & biomolecular chemistry*. 2021;19(22):4969-77.
197. Sunaina, Mehta SK, Vaidya S, Mehta SK, Ganguli AK, Vaidya S. Small-angle X-ray scattering as an effective tool to understand the structure and rigidity of the reverse micelles with the variation of surfactant. *Journal of molecular liquids*. 2021;326:115302.
198. Smith GN, Eastoe JE. Controlling colloid charge in nonpolar liquids with surfactants. *Phys Chem Chem Phys*. 2013;15:424-39.
199. Leon O, Rogel E, Lucas A, Leon O, Rogel E, Torres G, et al. ELECTROPHORETIC MOBILITY AND STABILIZATION OF ASPHALTENES IN LOW CONDUCTIVITY MEDIA. *Petroleum science and technology*. 2000;18(7-8):913-27.
200. Hu YQ, Wang DS, Gao JS, Hu Y, Wang D, Liu J, et al. A case study of electrostatic accidents in the process of oil-gas storage and transportation. *Journal of physics*. 2013;418:012037.
201. Farrokhbin M, Stojimirovic B, Trefalt G, Farrokhbin M, Stojimirović B, Galli M, et al. Surfactant mediated particle aggregation in nonpolar solvents. *Physical chemistry chemical physics PCCP*. 2019;21(35):18866-76.
202. Leiske DL, Chow A, Farinas J, Leiske DL, Chow A, Dettloff R, et al. Single-molecule enzymology based on the principle of the Millikan oil drop experiment. *Analytical biochemistry*. 2014;448:30-7.
203. Wang YY, Nie H, Zhang SXA, Han J, An Y, Zhang Y. Green revolution in electronic displays expected to ease energy and health crises. *Light: science & applications*. 2021;10.
204. Rumble JR. *CRC Handbook of Chemistry and Physics*. Boca Raton, FL: CRC Press/Taylor & Francis 2021.
205. Israelachvili JN. *Electrostatic Forces between Surfaces in Liquids*. Intermolecular and Surface Forces 2011.
206. Chuo SC, Ahmad A, Mohd-Setapar SH, Ripin A. Reverse micelle extraction-an alternative for recovering antibiotics. *Der Pharma Chemica*. 2014;6:37-44.
207. Chuo SC, Abd-Talib F, Mohd-Setapar SH, Hassan H, Mohd-Nasir H, Ahmad A, et al. Reverse micelle Extraction of Antibiotics using an Eco-friendly Sophorolipids Biosurfactant. *Scientific Reports*. 2018;8(477).
208. Hemavathi AB, Hebbar HU, Raghavarao KSMS. Mixed reverse micellar systems for extraction and purification of β -glucosidase. *Separation and purification technology*. 2010;71(2):263-8.
209. Chen Y-L, Su C-K, Chiang B-H. Optimization of reversed micellar extraction of chitosanases produced by *Bacillus cereus*. *Process biochemistry (1991)*. 2006;41(4):752-8.
210. Peng X, Yuan X-z, Zeng G-m, Huang H-j, Zhong H, Liu Z-f, et al. Extraction and purification of laccase by employing a novel rhamnolipid reversed micellar system. *Process biochemistry (1991)*. 2012;47(5):742-8.
211. Gaikawai RP, Wagh SA, Kulkarni BD. Efficient lipase purification using reverse micellar extraction. *Bioresource technology*. 2012;108:224-30.
212. Mohd-Setapar SH, Mohamad-Aziz SN. Backward Extraction of Penicillin G Using AOT Reverse Micelles. *Adv Sci Lett*. 2013;19:3688-94.
213. Chuo SC, Mohd-Setapar SH, Mohamad-Aziz SN, Starov VM. A new method of extraction of amoxicillin using mixed reverse micelles. *Colloids and surfaces A, Physicochemical and engineering aspects*. 2014;460:137-44.
214. Mohd-Setapar SH, Mohamad-Aziz SN, Harun NH, Hussin SH. Reverse Micelle Liquid-Liquid Extraction of a Pharmaceutical Product. *Advanced Materials Research*. 2012;545:240-4.
215. Mohamad-Aziz SN, Mohd-Setapar SH, Rahman RA. Characteristic of Binary Mixtures AOT/TWEEN 85 Reverse Micelle for Amoxicillin Solubilisation. *Journal of Bionanoscience*. 2013;7:1-7.
216. Juang R-S, Chen H-L, Tsao S-C. Recovery and separation of surfactin from pretreated *Bacillus subtilis* broth by reverse micellar extraction. *Biochemical engineering journal*. 2012;61:78-83.

217. Schulz SG, Kuhn H, Schmid G, Mund C, Venzmer C. Phase behavior of amphiphilic polymers: A dissipative particles dynamics study. *Colloid Polym Sci.* 2004;283:284–90.
218. Denham N, Holmes MC, Zvelindovsky AV. The Phases in a Non-Ionic Surfactant (C12E6)-Water Ternary System: A Coarse-Grained Computer Simulation. *J Phys Chem B.* 2011;115:1385–93.
219. Abel S, Sterpone F, Bandyopadhyay S, Marchi M. Molecular Modeling and Simulations of AOT-Water Reverse Micelles in Isooctane: Structural and Dynamic Properties. *J Phys Chem B.* 2004;108:19458-66.
220. Martinez AV, Dominguez L, Malolepsza E, Moser A, Ziegler Z, Straub JE. Probing the Structure and Dynamics of Confined Water in AOT Reverse Micelles. *J Phys Chem B.* 2013;117:7345–51.
221. Gardner A, Vásquez VR, Clifton A, Graeve OA. Molecular dynamics analysis of the AOT/water/isooctane system: Effect of simulation time, initial configuration, and model salts. *Fluid Phase Equilibria.* 2007;262:264–70.
222. Khoshnood A, Firoozabadi A. Polar Solvents Trigger Formation of Reverse Micelles. *Langmuir.* 2015;31:5982-91.
223. George J, Sastry NV. Densities, Excess Molar Volumes, Viscosities, Speeds of Sound, Excess Isentropic Compressibilities, and Relative Permittivities for $C_mH_{2m+1}(OCH_2CH_2)_nOH$ ($m = 1$ or 2 or 4 and $n = 1$) + Benzene, + Toluene, + (o-, m-, and p-) Xylenes, + Ethylbenzene, and + Cyclohexane. *J Chem Eng Data.* 2003;48:977-89.
224. Deguillard E, Pannacci N, Creton B, Rousseau B. Interfacial tension in oil–water–surfactant systems: On the role of intra-molecular forces on interfacial tension values using DPD simulations. *The Journal of Chemical Physics.* 2013;138(14):144102.
225. Hirai M, Kawai-Hirai R, Sanada M, Iwase H, Mitsuya S. Characteristics of AOT Microemulsion Structure Depending on Apolar Solvents. *The Journal of Physical Chemistry B.* 1999;103(44):9658-62.
226. Day RA, Robinson BH, Clarke JHR, Doherty JV. Characterisation of water-containing reversed micelles by viscosity and dynamic light scattering methods. *Journal of the Chemical Society, Faraday Transactions 1: Physical Chemistry in Condensed Phases.* 1979;75(0):132-9.
227. Salanwai S, Cui ST, Cochran HD, Cummings PT. Molecular Simulation of a Dichain Surfactant/Water/Carbon Dioxide System. 1. Structural Properties of Aggregates. *Langmuir.* 2001;17:1773-83.
228. Vasquez VR, Williams BC, Graeve OA. Stability and Comparative Analysis of AOT/Water/Isooctane Reverse Micelle System Using Dynamic Light Scattering and Molecular Dynamics. *The Journal of Physical Chemistry B.* 2011;115(12):2979-87.
229. Kotlarchyk M, Huang JS, Chen SH. Structure of AOT reversed micelles determined by small-angle neutron scattering. *The Journal of Physical Chemistry.* 1985;89(20):4382-6.
230. Peri JB. The state of solution of aerosol OT in nonaqueous solvents. *Journal of Colloid and Interface Science.* 1969;29(1):6-15.
231. Bohidar HB, Behboudnia M. Characterization of reverse micelles by dynamic light scattering. *Colloids and Surfaces A: Physicochemical and Engineering Aspects.* 2001;178(1):313-23.
232. Gale CD, Derakhshani-Molayousefi M, Levinger NE. How to Characterize Amorphous Shapes: The Tale of a Reverse Micelle. *The Journal of Physical Chemistry B.* 2022;126(4):953-63.
233. Arsene M-L, Răut I, Călin M, Jecu M-L, Doni M, Gurban A-M. Versatility of Reverse Micelles: From Biomimetic Models to Nano (Bio)Sensor Design. *Processes.* 2021;9.
234. Albanese A, Tang PS, Chan WCW. The Effect of Nanoparticle Size, Shape, and Surface Chemistry on Biological Systems. *Annu Rev Biomed Eng.* 2012;14:1-16.
235. Yaws CL. *YAWS' thermophysical properties of chemicals and hydrocarbons*: Knovel; 2010.
236. Rackett HG. Equation of state for saturated liquids. *Journal of chemical and engineering data.* 1970;15(4):514-7.

237. Duque D, Vega LF. Some issues on the calculation of interfacial properties by molecular simulation. *J Chem Phys.* 2004;121.
238. Clark GNI, Haslam AJ, Galindo A, Jackson G. Developing optimal Wertheim-like models of water for use in Statistical Associating Fluid Theory (SAFT) and related approaches. *Molecular physics.* 2006;104(22-24):3561-81.
239. Sharma AK, Garg T, Goyal AK, Rath G. Role of microemulsions in advanced drug delivery. *Artificial cells, nanomedicine, and biotechnology.* 2016;44(4):1177-85.
240. Xavier-Junior FH, Vauthier C, Morais ARV, Alencar EN, Egito EST. Microemulsion systems containing bioactive natural oils: an overview on the state of the art. *Drug development and industrial pharmacy.* 2017;43(5):700-14.
241. Negin C, Ali S, Xie Q. Most common surfactants employed in chemical enhanced oil recovery. *Petroleum.* 2017:197-211.
242. Hester RE, Harrison RM. 4.1 Introduction. *Volatile Organic Compounds in the Atmosphere: Royal Society of Chemistry.* p. 51-3.
243. Zhu L, Shen D, Luo KH. A critical review on VOCs adsorption by different porous materials: Species, mechanisms and modification methods. *Journal of hazardous materials.* 2020;389:122102.
244. Pateiro M, Gomez-Salazar JA, Lorenzo JM, Pateiro M, Gómez-Salazar JA, Jaime-Patlán M, et al. Plant Extracts Obtained with Green Solvents as Natural Antioxidants in Fresh Meat Products. *Antioxidants.* 2021;10(2):181.
245. Kamal MS, Razzak SA, Hossain MM, Kamal MS, Razzak SA, Hossain MM. Catalytic oxidation of volatile organic compounds (VOCs) – A review. *Atmospheric environment.* 2016;140:117-34.
246. Lee H, Kim K, Choi Y, Kim D. Emissions of Volatile Organic Compounds (VOCs) from an Open-Circuit Dry Cleaning Machine Using a Petroleum-Based Organic Solvent: Implications for Impacts on Air Quality. *Atmosphere.* 2021;12(5):637.
247. Lipshutz BH, Gallou F, Handa S. Evolution of Solvents in Organic Chemistry. *ACS sustainable chemistry & engineering.* 2016;4(11):5838-49.
248. Manisalidis I, Stavropoulou E, Bezirtzoglou E. Environmental and Health Impacts of Air Pollution: A Review. *Frontiers in public health.* 2020;8.
249. Poliakov M, Fitzpatrick JM, Farren TR, Anastas PT. *Green Chemistry: Science and Politics of Change.* Science (American Association for the Advancement of Science). 2002;297(5582):807-10.
250. Anastas PT, Warner JC. *Green Chemistry: Theory and Practice, 12 Principles of Green Chemistry: Oxford University Press; 1998.*
251. Amyotte PR, Khan FI. The role of inherently safer design in process safety. *Canadian journal of chemical engineering.* 2021;99(4):853-71.
252. Mannan MS. Trevor Kletz's impact on process safety and a plea for good science – An academic and research perspective. *Process safety and environmental protection.* 2012;90(5):343-8.
253. Atkins PW. *Physical transformations.* In: De Paula J, editor. *Elements of physical chemistry.* Oxford: Oxford: Oxford University Press 2017.
254. Yaws CL. *Critical Properties and Acentric Factors - Elements and Inorganic Compounds.* YAWS' thermophysical properties of chemicals and hydrocarbons: Knovel; 2010.
255. Beckman EJ. Supercritical and near-critical CO₂ in green chemical synthesis and processing. *The Journal of supercritical fluids.* 2004;28(2-3):121-91.
256. Reverchon E, Adami R. Nanomaterials and supercritical fluids. *The Journal of supercritical fluids.* 2006;37(1):1-22.
257. Sun Y-P, Atornjitjawat P, Meziani MJ. Preparation of Silver Nanoparticles via Rapid Expansion of Water in Carbon Dioxide Microemulsion into Reductant Solution. *Langmuir.* 2001;17(19):5707-10.
258. Pathak P, Meziani MJ, Desai T, Sun Y-P. Nanosizing Drug Particles in Supercritical Fluid Processing. *Journal of the American Chemical Society.* 2004;126(35):10842-3.

259. Jackson K, Fulton JL. Surfactants and Microemulsions in Supercritical Fluids. 1998. In: Supercritical Fluid Cleaning: Fundamentals, Technology and Applications [Internet].
260. Goetheer ELV, Vorstman MAG, Keurentjes JTF. Opportunities for process intensification using reverse micelles in liquid and supercritical carbon dioxide. *Chemical engineering science*. 1999;54(10):1589-96.
261. Macnaughton SJ, Kikic I, Foster NR, Alessi P, Cortesi A, Colombo I. Solubility of Anti-Inflammatory Drugs in Supercritical Carbon Dioxide. *Journal of chemical and engineering data*. 1996;41(5):1083-6.
262. Saucéau M, Letourneau JJ, Freiss B, Richon D, Fages J. Solubility of eflucimibe in supercritical carbon dioxide with or without a co-solvent. *The Journal of supercritical fluids*. 2004;31(2):133-40.
263. Johnston KP. Water-in-carbon dioxide microemulsions: An environment for hydrophiles including proteins. *Science*. 1996;271(5249):624-7.
264. Cooper AI. Polymer synthesis and processing using supercritical carbon dioxide. *Journal of materials chemistry*. 2000;10(2):207-34.
265. Zielinski RG, Kline SR, Kaler EW, Rosov N. A Small-Angle Neutron Scattering Study of Water in Carbon Dioxide Microemulsions. *Langmuir*. 1997;13(15):3934-7.
266. Girard E, Tassaing T, Marty J-D, Destarac M. Structure–Property Relationships in CO₂-philic (Co)polymers: Phase Behavior, Self-Assembly, and Stabilization of Water/CO₂ Emulsions. *Chemical reviews*. 2016;116(7):4125-69.
267. Peach J, Czajka A, Hazell G, Hill C, Mohamed A, Pegg JC, et al. Tuning Micellar Structures in Supercritical CO₂ Using Surfactant and Amphiphile Mixtures. *Langmuir*. 2017;33(10):2655-63.
268. Eastoe J, Gold S, Steytler DC. Surfactants for CO₂. *Langmuir*. 2006;22(24):9832-42.
269. Sagisaka M, Ono S, James C, Yoshizawa A, Mohamed A, Guittard F, et al. Anisotropic reversed micelles with fluorocarbon-hydrocarbon hybrid surfactants in supercritical CO₂. *Colloids and surfaces, B, Biointerfaces*. 2018;168:201-10.
270. Giesy JP. Perfluorochemical Surfactants in the Environment. *Environmental Science & Technology*. 2002;36(7):147A.
271. Beans C. News Feature: How "forever chemicals" might impair the immune system. *Proceedings of the National Academy of Sciences - PNAS*. 2021;118(15).
272. Consan KA, Smith RD. Observations on the solubility of surfactants and related molecules in carbon dioxide at 50°C. *The Journal of Supercritical Fluids*. 1990;3(2):51-65.
273. Trickett K, Xing D, Enick R, Eastoe J, Hollamby MJ, Mutch KJ, et al. Rod-Like Micelles Thicken CO₂. *Langmuir*. 2010;26(1):83-8.
274. Pitt AR, Morley SD, Burbidge NJ, Quickenden EL. The relationship between surfactant structure and limiting values of surface tension, in aqueous gelatin solution, with particular regard to multilayer coating. *Colloids and surfaces A, Physicochemical and engineering aspects*. 1996;114:321-35.
275. Mohamed A, Sagisaka M, Hollamby M, Rogers SE, Heenan RK, Dyer R, et al. Hybrid CO₂-philic Surfactants with Low Fluorine Content. *Langmuir*. 2012;28(15):6299-306.
276. Eastoe J, Paul A, Nave S, Steytler DC, Robinson BH, Rumsey E, et al. Micellization of Hydrocarbon Surfactants in Supercritical Carbon Dioxide. *Journal of the American Chemical Society*. 2001;123(5):988-9.
277. Mohamed A, Trickett K, Chin SY, Cummings S, Sagisaka M, Hudson L, et al. Universal Surfactant for Water, Oils, and CO₂. *Langmuir*. 2010;26(17):13861-6.
278. Gold S, Eastoe J, Grilli R, Steytler DC. Branched trichain sulfosuccinates as novel water in CO₂ dispersants. *Colloid and polymer science*. 2006;284(11):1333-7.
279. Czajka A, Hill C, Peach J, Pegg JC, Grillo I, Guittard F, et al. Trimethylsilyl hedgehogs – a novel class of super-efficient hydrocarbon surfactants. *Physical chemistry chemical physics*. 2017;19(35):23869-77.
280. Stone MT, Smith PG, da Rocha SRP, Rossy PJ, Johnston KP. Low Interfacial Free Volume of Stubby Surfactants Stabilizes Water-in-Carbon Dioxide Microemulsions. *The journal of physical chemistry B*. 2004;108(6):1962-6.

281. Salaniwal S, Cui ST, Cochran HD, Cummings PT. Molecular Simulation of a Dichain Surfactant/Water/Carbon Dioxide System. 1. Structural Properties of Aggregates. *Langmuir*. 2001;17(5):1773-83.
282. Mudzhikova GV, Brodskaya EN. An AOT reverse micelle in a medium of supercritical carbon dioxide. *Colloid journal*. 2015;77(3):306-11.
283. Brodskaya EN, Mudzhikova GV. Molecular dynamics simulation of AOT reverse micelles. *Molecular physics*. 2006;104(22-24):3635-43.
284. Wang MH, Fang TM, Liu B, Wang M, Fang T, Wang P, et al. The self-assembly structure and the CO₂-philicity of a hybrid surfactant in supercritical CO₂: effects of hydrocarbon chain length. *Soft matter*. 2016;12(39):8177-85.
285. Takenouchi S, Kennedy GC. The binary system H₂O-CO₂ at high temperatures and pressures. *American Journal of Science*. 1964;262:1055-74.
286. Yaws CL. *Surface Tensions - Elements and Inorganic Compounds*. YAWS' thermophysical properties of chemicals and hydrocarbons: Knovel; 2010.
287. Yaws CL. *Surface Tensions - Organic Compounds*. YAWS' thermophysical properties of chemicals and hydrocarbons: Knovel; 2010.
288. Eastoe J, Gold S, Rogers S, Wyatt P, Steytler DC, Gurgel A, et al. Designed CO₂-Philes Stabilize Water-in-Carbon Dioxide Microemulsions. *Angewandte Chemie (International ed)*. 2006;45(22):3675-7.
289. Sagisaka M, Kudo K, Nagoya S, Yoshizawa A. Highly Methyl-Branched Hydrocarbon Surfactant as a CO₂-philic Solubilizer for Water/Supercritical CO₂ Microemulsion. *J Oleo Sci*. 2013;62(7):481-8.
290. Sagisaka M, Endo T, Fujita K, Umetsu Y, Osaki S, Narumi T, et al. Very low surface tensions with "Hedgehog" surfactants. *Colloids and surfaces A, Physicochemical and engineering aspects*. 2021;631:127690.

Appendices

Appendix A User-defined functions in Gromacs

Gromacs allows the user to define their own potential functions. In this study the Mie potential, described in section 2.2.1, is the specific potential function. In Gromacs the intermolecular interaction parameters of two atoms i and j are split in three parts: the electrostatic, the dispersion and the short-range repulsion:

$$V(r_{ij}) = \frac{z_i z_j}{4\pi\epsilon_0\epsilon_r} f(r_{ij}) + Cg(r_{ij}) + Ah(r_{ij}) \quad (\text{A.1})$$

Where $f(r)$, $g(r)$ and $h(r)$ are the so-called ‘user-defined functions’. In principle, for the Mie potential in Gromacs, only the last two functions are needed, however one must provide meaningful (non-zero) data for the electrostatic function.

The user-defined functions to describe any Mie potential will be:

$$f(r_{ij}) = \frac{1}{r_{ij}} \quad (\text{A.2})$$

$$g(r_{ij}) = -\frac{1}{r_{ij}^a} \quad (\text{A.3})$$

$$h(r_{ij}) = \frac{1}{r_{ij}^r} \quad (\text{A.4})$$

The constants A and C are defined as:

$$A = \left(\frac{\lambda_{ij}^r}{\lambda_{ij}^r - \lambda_{ij}^a} \right) \left(\frac{\lambda_{ij}^r}{\lambda_{ij}^a} \right)^{\frac{\lambda_{ij}^a}{\lambda_{ij}^r - \lambda_{ij}^a}} \epsilon_{ij} \sigma_{ij}^{\lambda_{ij}^r} \quad (\text{A.5})$$

$$C = \left(\frac{\lambda_{ij}^r}{\lambda_{ij}^r - \lambda_{ij}^a} \right) \left(\frac{\lambda_{ij}^r}{\lambda_{ij}^a} \right)^{\frac{\lambda_{ij}^a}{\lambda_{ij}^r - \lambda_{ij}^a}} \epsilon_{ij} \sigma_{ij}^{\lambda_{ij}^a} \quad (\text{A.6})$$

With this knowledge, a tabulated potential that contains the evaluation of $f(r_{ij})$, $g(r_{ij})$, $h(r_{ij})$ and their negative first derivatives at a series of values of r_{ij} must be constructed. This will be used by Gromacs to calculate the values of the functions for any values of r_{ij} , using a cubic splines algorithm to interpolate the table. The format of this table should be the following:

r_{ij}	$f(r_{ij})$	$-f'(r_{ij})$	$g(r_{ij})$	$-g'(r_{ij})$	$h(r_{ij})$	$-h'(r_{ij})$
#	$\frac{1}{r_{ij}}$	$\frac{1}{r_{ij}^2}$	$-\frac{1}{r_{ij}^a}$	$-\frac{\lambda_{ij}^a}{r_{ij}^{\lambda_{ij}^a+1}}$	$\frac{1}{r_{ij}^r}$	$\frac{\lambda_{ij}^r}{r_{ij}^{\lambda_{ij}^r+1}}$

Where r_{ij} should range from 0 to $r_c + 1$. A C++ code, mie2gmx.cpp, has been written by Herdes to create a tabulated potential upon specifying λ_{ij}^r , λ_{ij}^a and r_c . It should be noted in this script λ_{ij}^r and λ_{ij}^a are referred to as n and m respectively. The code is presented in Figure A.1.

```
// Tabulated Mie Potential For GROMACS
// Date and comments:
// Aug 03 2012 at Imperial College London, Hello World, C.Herdes
// Oct 09 2012 at Imperial College London, restriction max energy

#include <iostream>
#include <ctype.h>
#include <math.h>
#include <sstream>
#include <string>
using namespace std;

int main()
{
    FILE *fout;
    double r;
    double cutoff;
    double n;
    double m;
    stringstream myfile;
    cout << "This program generates a tabulated Mie potential for GROMACS,\nplease read http://www.sklogwiki.org/Sklogwiki/index.php/Mie_potential_for_notation.\n#\nPlease, enter a value for n = ";
    cin >> n;
    cout << "Please, enter a value for m = ";
    cin >> m;
    cout << "Please, enter a value for the cut-off = ";
    cin >> cutoff;
    myfile << "tableMIE_" << n << "_" << m << ".xvg";
    string mytable(myfile.str());
    const char* cstr1 = mytable.c_str();
    fout = fopen(cstr1, "w");
    double c_mie = n/(n-m)*pow(n/m,m/(n-m));
    fprintf(fout, "# C.Herdes Imperial College London 2012\n# Tabulated Mie Potential n:%f and m:%f\n# Please calculate your A = %f x Epsilon x Sigma^%f and C = %f x Epsilon x Sigma^%f.\n", n, m, c_mie, n, c_mie, m);
    for (r=0; r<=cutoff+1; r+=0.002) {
        double f = 1/r;
        double fprime = 1/(pow(r,2));
        double g = -1/(pow(r,m));
        double gprime = -m/(pow(r,m+1));
        double h = 1/(pow(r,n));
        double hprime = n/(pow(r,n+1));
        /* print output */
        if (hprime>1e27) {
            fprintf(fout, "%12.10e %12.10e %12.10e %12.10e %12.10e %12.10e\n", r,0,0,0,0,0,0,0,0,0);
        }
        else {
            fprintf(fout, "%12.10e %12.10e %12.10e %12.10e %12.10e %12.10e\n", r,f,fprime,g,gprime,h,hprime);
        }
    }
    fclose(fout);
    cout << myfile.str() << "\n now can be found in the current directory, enjoy!\n";
    return(0);
}
```

Figure A.1 C++ code lines for mie2gmx.cpp

This can be compiled in Linux OS with the line:

```
$ g++ mie2gmx.cpp -o mie2gmx.exe
```

The resultant file can then be executed by the line:

```
$ ./mie2gmx.exe
```

Upon successful execution, a table will be generated in the current work directory called *tableMIE_n_m.xvg*. This must be renamed appropriately before using it in Gromacs. The comment lines at the header of each table will specify the used λ_{ij}^r and λ_{ij}^a , as well as the needed pre-factors to set A and C detailed in equations x and y: It should be noted that the same table can be used for different molecular species, provided λ_{ij}^r and λ_{ij}^a are the same. The units of A and C are $\text{kJ mol}^{-1} \text{nm}$, where nm is raised to the power of λ_{ij}^r and λ_{ij}^a (in this work it is set to 6) respectively.

Appendix B Input interaction parameters

Butyl acetate

Table B.1 Intermolecular interaction parameters for a butyl acetate molecule

Interaction ($i - j$)	σ_{ij} (nm)	ε_{ij}/k_B (K)	λ_{ij}^r	C (kJ mol ⁻¹ nm ⁶)	A (kJ mol ⁻¹ nm ⁴ λ_{ij}^r)
CP – CP	0.4871	426.08	34.29	8.3009×10^{-2}	1.2074×10^{-10}
CP – ES	0.4355	302.09	27.39	3.3594×10^{-2}	6.3765×10^{-10}
ES – ES	0.3839	397.25	22.01	2.3658×10^{-2}	5.2157×10^{-9}

Table B.2 Structure of a butyl acetate molecule

Bead index	Corresponding bead
1	ES
2	ES
3	CP

Table B.3 Intramolecular interaction parameters for a butyl acetate molecule

Bonds		
Bond ($i - j$)	$b_{0,ij}$ (nm)	$k_{bond,ij}$ (kJ mol ⁻¹ nm ⁻²)
1 – 2	0.384	20,000
2 – 3	0.261	20,000
Angles		
Angle ($i - j - k$)	$\theta_{0,ijk}$ (deg)	$k_{angle,ijk}$ (kJ mol ⁻¹ rad ⁻²)
1 – 2 – 3	157	22.18

Pentyl acetate

Table B.4 Intermolecular interaction parameters for a pentyl acetate molecule

Interaction ($i - j$)	σ_{ij} (nm)	ε_{ij}/k_B (K)	λ_{ij}^r	C (kJ mol ⁻¹ nm ⁶)	A (kJ mol ⁻¹ nm ⁴ λ_{ij}^r)
CB – CB	0.3961	256.36	13.29	2.8878×10^{-2}	3.3773×10^{-5}
CB – ES	0.3900	239.25	16.99	1.9105×10^{-2}	6.1450×10^{-7}
ES – ES	0.3839	397.25	22.01	2.3658×10^{-2}	5.2157×10^{-9}

Table B.5 Structure of a pentyl acetate molecule

Bead index	Corresponding bead
1	ES
2	ES
3	CB
4	CB

Table B.6 Intramolecular interaction parameters for a pentyl acetate molecule

Bonds		
Bond ($i - j$)	$b_{0,ij}$ (nm)	$k_{bond,ij}$ (kJ mol ⁻¹ nm ⁻²)
1 - 2	0.384	20,000
2 - 3	0.234	20,000
3 - 4	0.396	20,000
Angles		
Angle ($i - j - k$)	$\theta_{0,ijk}$ (deg)	$k_{angle,ijk}$ (kJ mol ⁻¹ rad ⁻²)
1 - 2 - 3	157	22.18
2 - 3 - 4	157	22.18

Octyl acetate

Table B.7 Intermolecular interaction parameters of an octyl acetate molecule

Interaction ($i - j$)	σ_{ij} (nm)	ε_{ij}/k_B (K)	λ_{ij}^r	C (kJ mol ⁻¹ nm ⁶)	A (kJ mol ⁻¹ nm ⁴ λ_{ij}^r)
CP - CP	0.4871	426.08	34.29	8.3009×10^{-2}	1.2074×10^{-10}
CP - CB	0.4416	325.25	20.94	4.6431×10^{-2}	2.3028×10^{-7}
CP - ES	0.4355	302.09	27.39	3.3594×10^{-2}	6.3765×10^{-10}
CB - CB	0.3961	256.36	13.29	2.8878×10^{-2}	3.3773×10^{-5}
CB - ES	0.3900	239.25	16.99	1.9105×10^{-2}	6.1450×10^{-7}
ES - ES	0.3839	397.25	22.01	2.3658×10^{-2}	5.2157×10^{-9}

Table B.8 Structure of an octyl acetate molecule

Bead index	Corresponding bead
1	ES
2	ES
3	CB
4	CB
5	CP

Table B.9 Intramolecular interaction parameters of an octyl acetate molecule

Bonds		
Bond ($i - j$)	$b_{0,ij}$ (nm)	$k_{bond,ij}$ (kJ mol ⁻¹ nm ⁻²)
1 - 2	0.384	20,000
2 - 3	0.234	20,000
3 - 4	0.396	20,000
4 - 5	0.265	20,000
Angles		
Angle ($i - j - k$)	$\theta_{0,ijk}$ (deg)	$k_{angle,ijk}$ (kJ mol ⁻¹ rad ⁻²)
1 - 2 - 3	157	22.18
2 - 3 - 4	157	22.18
3 - 4 - 5	157	22.18

AOT – water – cyclohexane

Table B.10 Intermolecular interaction parameters for the AOT-water-cyclohexane system. The SO and NA beads are assigned a charge of -1 and +1 respectively.

Interaction (<i>i</i> – <i>j</i>)	σ_{ij} (nm)	ε_{ij}/k_B (K)	λ_{ij}^r	C (kJ mol ⁻¹ nm ⁶)	A (kJ mol ⁻¹ nm ^{λ_{ij}^r})
CP – CP	0.4871	426.08	34.29	8.3009×10^{-2}	1.2074×10^{-10}
CP – CB	0.4416	325.25	20.94	4.6431×10^{-2}	2.3028×10^{-7}
CP – ES	0.4355	302.09	27.39	3.3594×10^{-2}	6.3765×10^{-10}
CP – SO	0.4346	174.18	15.51	2.8959×10^{-2}	1.0478×10^{-5}
CP – NA	0.3596	50.39	15.51	2.6879×10^{-3}	1.6054×10^{-7}
CP – W	0.4311	273.44	15.51	4.3308×10^{-2}	1.4510×10^{-5}
CP – CH	0.4553	381.11	21.59	6.3937×10^{-2}	2.9946×10^{-7}
CB – CB	0.3961	256.36	13.29	2.8878×10^{-2}	3.3773×10^{-5}
CB – ES	0.3900	239.25	16.99	1.9105×10^{-2}	6.1450×10^{-7}
CB – SO	0.3891	138.06	10.17	2.0731×10^{-2}	4.0343×10^{-4}
CB – NA	0.3141	43.01	10.17	1.7868×10^{-3}	1.4227×10^{-5}
CB – W	0.3856	217.35	10.17	3.0916×10^{-2}	5.7936×10^{-4}
CB – CH	0.4098	297.31	13.66	3.9731×10^{-2}	4.2635×10^{-5}
ES – ES	0.3839	397.25	22.01	2.3658×10^{-2}	5.2157×10^{-9}
ES – SO	0.3830	171.94	12.75	1.6645×10^{-2}	2.5572×10^{-5}
ES – NA	0.3080	54.18	12.75	1.4183×10^{-3}	5.0043×10^{-7}
ES – W	0.3795	378.61	12.75	3.4688×10^{-2}	5.0089×10^{-5}
ES – CH	0.4037	277.03	17.49	2.6511×10^{-2}	7.8534×10^{-7}
SO – SO	0.3820	74.42	8.00	1.8230×10^{-2}	2.6602×10^{-3}
SO – NA	0.3070	12.11	8.00	7.9926×10^{-4}	7.5329×10^{-5}
SO – W	0.3785	600.00	8.00	1.3908×10^{-1}	1.9925×10^{-2}
SO – CH	0.4027	159.82	10.43	2.8200×10^{-2}	5.0016×10^{-4}
NA – NA	0.2320	8.92	8.00	1.0965×10^{-4}	5.9018×10^{-8}
NA – W	0.3035	179.76	8.00	1.1075×10^{-2}	1.0202×10^{-3}
NA – CH	0.3277	48.60	10.43	2.4900×10^{-3}	1.7713×10^{-5}
W – W	0.3750	400.00	8.00	8.7692×10^{-2}	1.2332×10^{-2}
W – CH	0.3992	251.37	10.43	4.2092×10^{-2}	7.1822×10^{-4}
CH – CH	0.4234	345.94	14.05	5.4531×10^{-2}	5.3950×10^{-5}

Table B.11 Structure of an AOT molecule. The NA bead is modelled as fully dissociated.

Bead index	Corresponding bead
1	CP
2	CB
3	ES
4	ES
5	ES
6	ES
7	CB
8	CP
9	CB
10	SO
11	CB

Table B.12 Intramolecular interaction parameters for an AOT molecule.

Bonds			
Bond ($i - j$)	$b_{0,ij}$ (nm)	$k_{bond,ij}$ ($\text{kJ mol}^{-1} \text{nm}^{-2}$)	
1 - 2	0.265	20,000	
2 - 3	0.234	20,000	
3 - 4	0.384	20,000	
4 - 5	0.384	20,000	
4 - 10	0.383	20,000	
5 - 6	0.384	20,000	
6 - 7	0.234	20,000	
7 - 8	0.265	20,000	
2 - 9	0.396	20,000	
7 - 11	0.396	20,000	
Angles			
Angle ($i - j - k$)	$\theta_{0,ijk}$ (deg)	$k_{angle,ijk}$ ($\text{kJ mol}^{-1} \text{rad}^{-2}$)	
1 - 2 - 3	100	65	
1 - 2 - 9	90	45	
2 - 3 - 4	60	45	
3 - 4 - 5	70	45	
10 - 4 - 3	60	45	
4 - 5 - 6	80	25	
5 - 6 - 7	70	45	
6 - 7 - 11	90	45	
6 - 7 - 8	100	45	
Dihedrals			
Dihedral ($i - j - k - l$)	$\phi_{0,ijkl}$ (deg)	$k_{dihedral,ijkl}$ (kJ mol^{-1})	n (-)
2 - 3 - 4 - 10	0	0.12	4
7 - 6 - 5 - 4	0	0.12	4

Table B.13 Structure of a cyclohexane molecule

Bead index	Corresponding bead
1	CH
2	CH

Table B.14 Intramolecular interaction parameters for a cyclohexane molecule

Bond ($i - j$)	$b_{0,ij}$ (nm)	$k_{bond,ij}$ ($\text{kJ mol}^{-1} \text{nm}^{-2}$)
1 - 2	0.423	20,000

AOTSiC – water – scCO₂Table B.15 Intermolecular interaction parameters for the ternary AOTSiC – water – scCO₂ system. The SO and NA beads are assigned a charge of -1 and +1 respectively.

Interaction (<i>i</i> – <i>j</i>)	σ_{ij} (nm)	ε_{ij}/k_B (K)	λ_{ij}^r	C (kJ mol ⁻¹ nm ⁶)	A (kJ mol ⁻¹ nm ⁶ λ_{ij}^r)
TMS – TMS	0.3227	134.05	8.55	9.7010 x 10 ⁻³	5.4048 x 10 ⁻⁴
TMS – CE	0.3788	203.52	14.62	1.5765 x 10 ⁻²	3.6741 x 10 ⁻⁶
TMS – ES	0.3533	228.17	13.27	1.2961 x 10 ⁻²	6.6936 x 10 ⁻⁶
TMS – SO	0.3524	98.82	8.27	1.3380 x 10 ⁻²	1.2544 x 10 ⁻³
TMS – NA	0.2774	33.20	8.27	1.0693 x 10 ⁻³	5.8237 x 10 ⁻⁵
TMS – W	0.3489	229.61	8.27	2.9282 x 10 ⁻²	2.6837 x 10 ⁻³
TMS – CO	0.3042	161.42	11.11	4.7645 x 10 ⁻³	1.0882 x 10 ⁻⁵
CE – CE	0.4349	330.25	27.30	3.6488 x 10 ⁻²	7.2418 x 10 ⁻¹⁰
CE – ES	0.4094	270.07	24.49	2.2103 x 10 ⁻²	1.4858 x 10 ⁻⁹
CE – SO	0.4085	155.79	14.02	1.9835 x 10 ⁻²	1.5056 x 10 ⁻⁵
CE – NA	0.3335	46.92	14.02	1.7864 x 10 ⁻³	2.6364 x 10 ⁻⁷
CE – W	0.4050	244.94	14.02	2.9618 x 10 ⁻²	2.0982 x 10 ⁻⁵
CE – CO	0.3603	219.47	19.97	9.5632 x 10 ⁻³	6.1488 x 10 ⁻⁹
ES – ES	0.3839	397.25	22.01	2.3658 x 10 ⁻²	5.2157 x 10 ⁻⁹
ES – SO	0.3830	171.94	12.75	1.6645 x 10 ⁻²	2.5572 x 10 ⁻⁵
ES – NA	0.3080	54.18	12.75	1.4183 x 10 ⁻³	5.0043 x 10 ⁻⁷
ES – W	0.3795	378.61	12.75	3.4688 x 10 ⁻²	5.0089 x 10 ⁻⁵
ES – CO	0.3348	270.45	18.01	8.2228 x 10 ⁻³	1.6195 x 10 ⁻⁸
SO – SO	0.3820	74.42	8.00	1.8230 x 10 ⁻²	2.6602 x 10 ⁻³
SO – NA	0.3070	12.11	8.00	7.9926 x 10 ⁻⁴	7.5329 x 10 ⁻⁵
SO – W	0.3785	600.00	8.00	1.3908 x 10 ⁻¹	1.9925 x 10 ⁻²
SO – CO	0.3338	117.19	10.70	6.4292 x 10 ⁻³	3.7217 x 10 ⁻⁵
NA – NA	0.2320	8.92	8.00	1.0965 x 10 ⁻⁴	5.9018 x 10 ⁻⁸
NA – W	0.3035	179.76	8.00	1.1075 x 10 ⁻²	1.0202 x 10 ⁻³
NA – CO	0.2588	41.20	10.70	4.9102 x 10 ⁻⁴	8.6050 x 10 ⁻⁷
W – W	0.3750	400.00	8.00	8.7692 x 10 ⁻²	1.2332 x 10 ⁻²
W – CO	0.3303	190.92	10.70	4.2092 x 10 ⁻²	7.1822 x 10 ⁻⁴
CO – CO	0.2857	196.55	14.85	2.7553 x 10 ⁻³	4.2380 x 10 ⁻⁸

Table B.16 Structure of an AOTSiC molecule. The NA bead is modelled as fully dissociated.

Bead index	Corresponding bead
1	TMS
2	TMS
3	CE
4	ES
5	ES
6	ES
7	ES
8	CE
9	TMS
10	TMS
11	TMS
12	SO
13	TMS
14	TMS
15	TMS

Table B.17 Intramolecular interaction parameters for AOTSiC

Bonds			
Bond ($i - j$)	$b_{0,ij}$ (nm)	$k_{bond,ij}$ (kJ mol ⁻¹ nm ⁻²)	
1 - 2	0.323	20,000	
2 - 3	0.379	20,000	
3 - 4	0.246	20,000	
4 - 5	0.384	20,000	
5 - 6	0.384	20,000	
6 - 7	0.384	20,000	
7 - 8	0.246	20,000	
8 - 9	0.379	20,000	
9 - 10	0.323	20,000	
2 - 11	0.323	20,000	
2 - 14	0.323	20,000	
5 - 12	0.383	20,000	
9 - 13	0.323	20,000	
9 - 15	0.323	20,000	
Angles			
Angle ($i - j - k$)	$\theta_{0,ijk}$ (deg)	$k_{angle,ijk}$ (kJ mol ⁻¹ rad ⁻²)	
1 - 2 - 3	100	65	
2 - 3 - 4	100	65	
3 - 4 - 5	60	45	
4 - 5 - 6	70	45	
5 - 6 - 7	70	45	
6 - 7 - 8	60	45	
7 - 8 - 9	100	65	
8 - 9 - 10	100	65	
1 - 2 - 11	90	45	
1 - 2 - 14	90	45	
12 - 4 - 5	60	45	
10 - 9 - 13	90	45	
10 - 9 - 15	90	45	
Dihedrals			
Dihedral ($i - j - k - l$)	$\phi_{0,ijkl}$ (deg)	$k_{dihedral,ijkl}$ (kJ mol ⁻¹)	n (-)
3 - 4 - 5 - 12	0	1.96	4
3 - 4 - 5 - 6	0	1.96	4
7 - 6 - 5 - 12	0	1.96	4
8 - 7 - 6 - 5	0	1.96	4

Table B.18 Structure of a CO₂ molecule

Bead index	Corresponding bead
1	CO
2	CO

Table B.19 Intramolecular interaction parameters for a CO₂ molecule

Bond ($i - j$)	$b_{0,ij}$ (nm)	$k_{bond,ij}$ (kJ mol ⁻¹ nm ⁻²)
1 - 2	0.286	20,000

Appendix C Example Gromacs input files

C.1 NVT simulations

```
;VARIOUS PREPROCESSING OPTIONS =  
  
include          =  
  
define           = -DPOSRES  
  
  
;RUN CONTROL PARAMETERS =  
  
integrator       = md  
  
; start time and timestep in ps =  
  
tinit           = 0  
  
dt              = 0.01  
  
nsteps          = 4000000  
  
; For exact run continuation or redoing part of a run  
  
init_step       = 0  
  
; number of steps for center of mass motion removal =  
  
nstcomm        = 1000  
  
comm_grps      =  
  
  
; OUTPUT CONTROL OPTIONS =  
  
; Output frequency for coords (x), velocities (v) and forces (f) =  
  
nstxout        = 1000  
  
nstvout        = 1000  
  
nstfout        = 1000  
  
; Output frequency for energies to log file and energy file =  
  
nstlog         = 1000  
  
nstenergy      = 1000  
  
; Output frequency and precision for xtc file =  
  
nstxtcout      = 1000  
  
xtc-precision  = 1000  
  
; This selects the subset of atoms for the xtc file. You can =  
  
; select multiple groups. By default all atoms will be written. =  
  
xtc-grps       =  
  
; Selection of energy groups =
```

```
energygrps          = CP ES
energygrp_table     = CP CP CP ES ES ES

; NEIGHBORSEARCHING PARAMETERS =
; cutoff-scheme =
cutoff-scheme = group
; nblast update frequency =
nblast            = 5
; ns algorithm (simple or grid) =
ns-type           = grid
pbc               = xyz
; nblast cut-off     =
rlist             = 2.0

; OPTIONS FOR ELECTROSTATICS AND VDW =
; Method for doing electrostatics =
coulombtype       = cut-off
rcoulomb-switch   = 0
rcoulomb          = 2.0
; Dielectric constant (DC) for cut-off or DC of reaction field =
epsilon-r         = 1
; Method for doing Van der Waals =
vdwtype           = user
; cut-off lengths    =
rvdw-switch       = 0
rvdw              = 2.0
; Apply long range dispersion corrections for Energy and Pressure =
DispCorr          = no
; Spacing for the PME/PPPM FFT grid =
fourierspacing    = 0.12
; FFT grid size, when a value is 0 fourierspacing will be used =
fourier_nx        = 0
```

```

fourier_ny      = 0
fourier_nz      = 0
; EWALD/PME/PPPM parameters =
pme_order       = 4
ewald_rtol      = 1e-05
optimize_fft    = yes

; OPTIONS FOR WEAK COUPLING ALGORITHMS =
; Temperature coupling =
tcoupl          = nose-hoover
; Groups to couple separately =
tc-grps        = CP ES
; Time constant (ps) and reference temperature (K) =
tau-t          = 1.0 1.0
ref-t          = 298.15 298.15
; Pressure coupling =
pcoupl         = no
pcoupltype     = semiisotropic
; Time constant (ps), compressibility (1/bar) and reference P (bar) =
tau-p         = 10.0
compressibility = 0 4.50E-5
ref-p         = 1.01325 1.01325

; GENERATE VELOCITIES FOR STARTUP RUN =
gen-vel        = no
gen-temp       = 298.15
gen-seed       = 173539

```

C.2 Isotropic NPT simulations

```

;VARIOUS PREPROCESSING OPTIONS =
;From surface excess to surface tension
;old fashion entry cpp = /lib/cpp

```

```
include      =
define      = -DPOSRES

;RUN CONTROL PARAMETERS =
integrator   = md
; start time and timestep in ps =
tinit       = 0
dt          = 0.01
nsteps      = 5000000
; For exact run continuation or redoing part of a run
init_step   = 0
; number of steps for center of mass motion removal =
nstcomm     = 1000
comm_grps   =

; OUTPUT CONTROL OPTIONS =
; Output frequency for coords (x), velocities (v) and forces (f) =
nstxout     = 1000
nstvout     = 1000
nstfout     = 1000
; Output frequency for energies to log file and energy file =
nstlog      = 1000
nstenergy   = 1000
; Output frequency and precision for xtc file =
nstxtcout   = 1000
xtc-precision = 1000
; This selects the subset of atoms for the xtc file. You can =
; select multiple groups. By default all atoms will be written. =
xtc-grps    =
; Selection of energy groups =
energygrps  = CP CB ES SO NA W CH
```

```
energygrp_table      = CP CP CP CB CP ES CP SO CP NA CP W CP CH CB CB CB ES
CB SO CB NA CB W CB CH ES ES ES SO ES NA ES W ES CH SO SO SO NA SO W SO
CH NA NA NA W NA CH W W W CH CH CH
```

```
; NEIGHBORSEARCHING PARAMETERS =
```

```
;cutoff-scheme =
```

```
cutoff-scheme = group
```

```
; nblast update frequency =
```

```
nstlist          = 5
```

```
; ns algorithm (simple or grid) =
```

```
ns-type          = grid
```

```
pbcs             = xyz
```

```
; nblast cut-off =
```

```
rlist           = 2.0
```

```
; OPTIONS FOR ELECTROSTATICS AND VDW =
```

```
; Method for doing electrostatics =
```

```
coulombtype     = PME
```

```
rcoulomb-switch = 0
```

```
rcoulomb        = 2.0
```

```
; Dielectric constant (DC) for cut-off or DC of reaction field =
```

```
epsilon-r       = 34.77
```

```
; Method for doing Van der Waals =
```

```
vdwtype         = user
```

```
; cut-off lengths =
```

```
rvdw-switch     = 0
```

```
rvdw            = 2.0
```

```
; Apply long range dispersion corrections for Energy and Pressure =
```

```
DispCorr        = no
```

```
; Spacing for the PME/PPPM FFT grid =
```

```
fourierspacing  = 0.29
```

```
; FFT grid size, when a value is 0 fourierspacing will be used =
```

```
fourier_nx      = 0
```

```

fourier_ny      = 0
fourier_nz      = 0
; EWALD/PME/PPPM parameters =
pme_order       = 4
ewald_rtol      = 1e-05
optimize_fft    = yes

; OPTIONS FOR WEAK COUPLING ALGORITHMS =
; Temperature coupling =
tcoupl          = nose-hoover
; Groups to couple separately =
tc-grps         = CP CB ES SO NA W CH
; Time constant (ps) and reference temperature (K) =
tau-t           = 1.0 1.0 1.0 1.0 1.0 1.0 1.0
ref-t           = 298.15 298.15 298.15 298.15 298.15 298.15 298.15
; Pressure coupling =
pcoupl          = Parrinello-Rahman
pcoupltype      = isotropic
; Time constant (ps), compressibility (1/bar) and reference P (bar) =
tau-p           = 10.0
compressibility = 4.50E-5
ref-p           = 1.01325

; GENERATE VELOCITIES FOR STARTUP RUN =
gen-vel         = no
gen-temp        = 298.15
gen-seed        = 173539

```

C.3 Semi-isotropic NPT simulations

```

;VARIOUS PREPROCESSING OPTIONS =
;From surface excess to surface tension
;old fashion entry cpp = /lib/cpp

```

```

include          =
define          = -DPOSRES

;RUN CONTROL PARAMETERS =
integrator      = md
; start time and timestep in ps =
tinit          = 0
dt             = 0.01
nsteps         = 20000000
; For exact run continuation or redoing part of a run
init_step      = 0
; number of steps for center of mass motion removal =
nstcomm        = 1000
comm_grps     =

; OUTPUT CONTROL OPTIONS =
; Output frequency for coords (x), velocities (v) and forces (f) =
nstxout        = 1000
nstvout        = 1000
nstfout        = 1000
; Output frequency for energies to log file and energy file =
nstlog         = 1000
nstenergy      = 1000
; Output frequency and precision for xtc file =
nstxtcout      = 1000
xtc-precision  = 1000
; This selects the subset of atoms for the xtc file. You can =
; select multiple groups. By default all atoms will be written. =
xtc-grps       =
; Selection of energy groups =
energygrps     = CP CB ES SO NA W
energygrp_table = CP CP CP CB CP ES CP SO CP NA CP W CB CB CB ES CB SO
CB NA CB W ES ES ES SO ES NA ES W SO SO SO NA SO W NA NA NA W W W

```

```
; NEIGHBORSEARCHING PARAMETERS =  
;cutoff-scheme =  
cutoff-scheme = group  
; nblast update frequency =  
nblast          = 5  
; ns algorithm (simple or grid) =  
ns-type         = grid  
pbc             = xyz  
; nblast cut-off      =  
rlist          = 2.0  
  
; OPTIONS FOR ELECTROSTATICS AND VDW =  
; Method for doing electrostatics =  
coulombtype     = PME  
rcoulomb-switch = 0  
rcoulomb        = 2.0  
; Dielectric constant (DC) for cut-off or DC of reaction field =  
epsilon-r      = 78.68  
; Method for doing Van der Waals =  
vdwtype        = user  
; cut-off lengths      =  
rvdw-switch    = 0  
rvdw           = 2.0  
; Apply long range dispersion corrections for Energy and Pressure =  
DispCorr       = no  
; Spacing for the PME/PPPM FFT grid =  
fourierspacing = 0.29  
; FFT grid size, when a value is 0 fourierspacing will be used =  
fourier_nx     = 0  
fourier_ny     = 0  
fourier_nz     = 0
```



```

; EWALD/PME/PPPM parameters =
pme_order          = 4
ewald_rtol         = 1e-05
optimize_fft       = yes

; OPTIONS FOR WEAK COUPLING ALGORITHMS =
; Temperature coupling =
tcoupl            = nose-hoover
; Groups to couple separately =
tc-grps          = CP CB ES SO NA W
; Time constant (ps) and reference temperature (K) =
tau-t            = 1.0 1.0 1.0 1.0 1.0 1.0
ref-t            = 298.15 298.15 298.15 298.15 298.15 298.15
; Pressure coupling =
pcoupl           = Parrinello-Rahman
pcoupltype       = semiisotropic
; Time constant (ps), compressibility (1/bar) and reference P (bar) =
tau-p            = 10.0
compressibility   = 4.50E-5 4.50E-5
ref-p            = 1.01325 1.01325

; GENERATE VELOCITIES FOR STARTUP RUN =
gen-vel          = no
gen-temp         = 298.15
gen-seed        = 173539

```

C.4 NP_{zz}AT simulations

```

;VARIOUS PREPROCESSING OPTIONS =
include          =
define          = -DPOSRES

;RUN CONTROL PARAMETERS =

```

```

integrator          = md
; start time and timestep in ps =
tinit              = 0
dt                 = 0.005
nsteps             = 4000000
; For exact run continuation or redoing part of a run
init_step          = 0
; number of steps for center of mass motion removal =
nstcomm            = 1000
comm_grps          =

; OUTPUT CONTROL OPTIONS =
; Output frequency for coords (x), velocities (v) and forces (f) =
nstxout            = 1000
nstvout            = 1000
nstfout            = 1000
; Output frequency for energies to log file and energy file =
nstlog             = 1000
nstenergy          = 1000
; Output frequency and precision for xtc file =
nstxtcout          = 1000
xtc-precision      = 1000
; This selects the subset of atoms for the xtc file. You can =
; select multiple groups. By default all atoms will be written. =
xtc-grps           =
; Selection of energy groups =
energygrps         = W CO
energygrp_table    = W W W CO CO CO

; NEIGHBORSEARCHING PARAMETERS =
;cutoff-scheme =
cutoff-scheme = group

```

```
; nblast update frequency =
nblast          = 5
; ns algorithm (simple or grid) =
ns-type         = grid
pbc             = xyz
; nblast cut-off =
rlist           = 2.0

; OPTIONS FOR ELECTROSTATICS AND VDW =
; Method for doing electrostatics =
coulombtype     = cut-off
rcoulomb-switch = 0
rcoulomb        = 2.0
; Dielectric constant (DC) for cut-off or DC of reaction field =
epsilon-r       = 1
; Method for doing Van der Waals =
vdwtype        = user
; cut-off lengths =
rvdw-switch     = 0
rvdw            = 2.0
; Apply long range dispersion corrections for Energy and Pressure =
DispCorr       = no
; Spacing for the PME/PPPM FFT grid =
fourierspacing = 0.12
; FFT grid size, when a value is 0 fourierspacing will be used =
fourier_nx     = 0
fourier_ny     = 0
fourier_nz     = 0
; EWALD/PME/PPPM parameters =
pme_order      = 4
ewald_rtol     = 1e-05
optimize_fft   = yes
```

```

; OPTIONS FOR WEAK COUPLING ALGORITHMS =
; Temperature coupling =
tcoupl          = nose-hoover
; Groups to couple separately =
tc-grps         = W CO
; Time constant (ps) and reference temperature (K) =
tau-t           = 1.0 1.0
ref-t           = 383.15 383.15
; Pressure coupling =
pcoupl          = Parrinello-Rahman
pcoupltype      = semiisotropic
; Time constant (ps), compressibility (1/bar) and reference P (bar) =
tau-p           = 10.0
compressibility  = 0 4.50E-5
ref-p           = 200 200

; GENERATE VELOCITIES FOR STARTUP RUN =
gen-vel         = no
gen-temp        = 248.15
gen-seed        = 173539

```

Appendix D Example MDTraj script

This code is written in Python and requires two input files: the trajectory to compute the ordering in, and the structure file of the specific group to consider. The indices of the atoms in the group of interest, termed the 'chain indices' must also be specified. For example, if 400 surfactant molecules, each with a chain consisting of 2 atoms are considered, then the chain indices must be specified from 1 to 800 (the total number of atoms). This code returns the nematic order parameter (termed S2 in this code) in each trajectory frame. To obtain each data point, the Python package pandas is used, and the resultant data is transferred to an Excel file. This code can be run in a Jupyter notebook, with the Anaconda Scientific Python package.

```
>>>import mdtraj as md
>>>from mdtraj.testing import get_fn
>>>t = md.load('trajectory.xtc', top='structure.pdb')
>>>chain_indices = [[n+x for x in range('number of atoms in a chain')] for n in range(0, 'total
number of atoms', 'number of atoms in a chain')]
>>>S2 = md.compute_nematic_order(t, indices=chain_indices)
>>>import matplotlib.pyplot as plt
>>>plt.plot(S2)
>>>import pandas as pd
>>>pd.set_option("display.max_rows", None, "display.max_columns", None)
>>>dataframe = pd.DataFrame(S2)
>>>print(dataframe)
```

Appendix E SO electron density distributions for the AOT – water system at 298.15 K and 1 bar

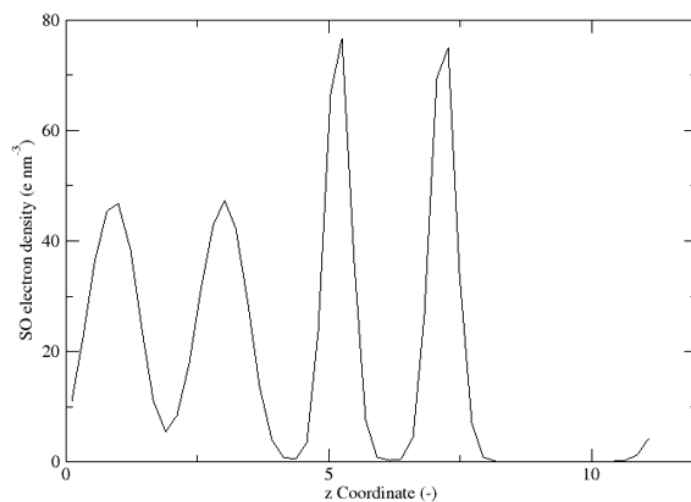


Figure E.1 Average electron density distribution of the SO bead across the z dimension of the simulation box at 32.22 wt % AOT

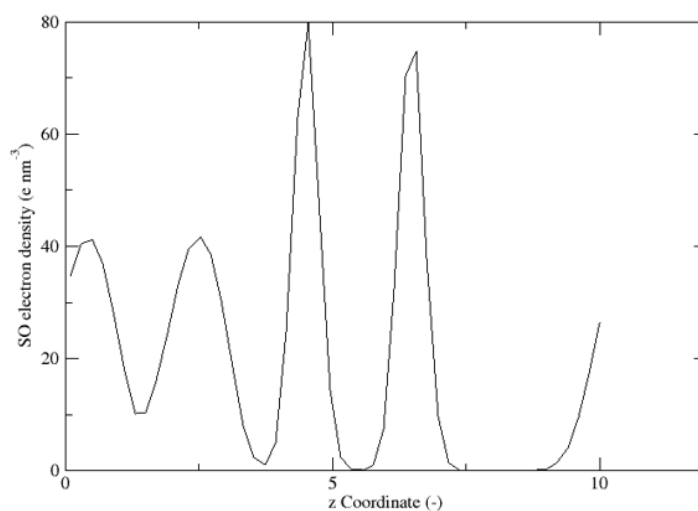


Figure E.2 Average electron density distribution of the SO bead across the z dimension of the simulation box at 35.36 wt % AOT

SO electron density distributions for the AOT – water system at 298.15 K and 1 bar

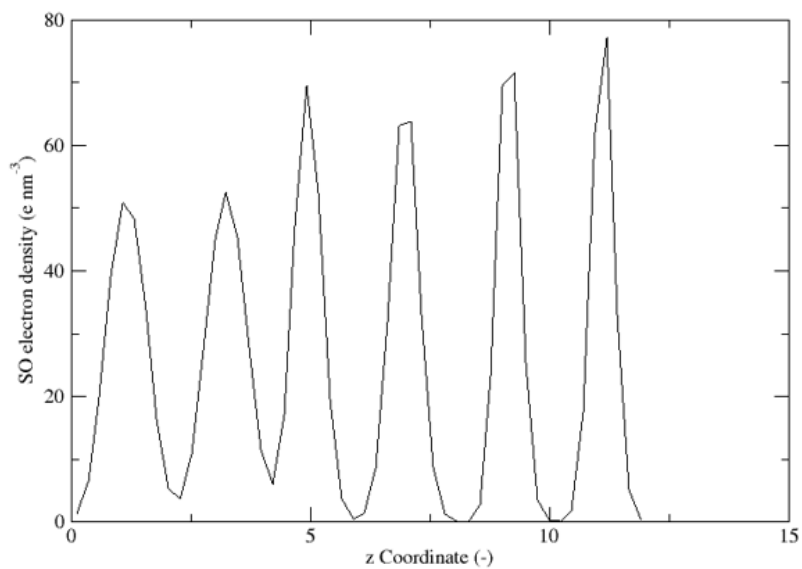


Figure E.3 Average electron density distribution of the SO bead across the z dimension of the simulation box at 44.53 wt % AOT

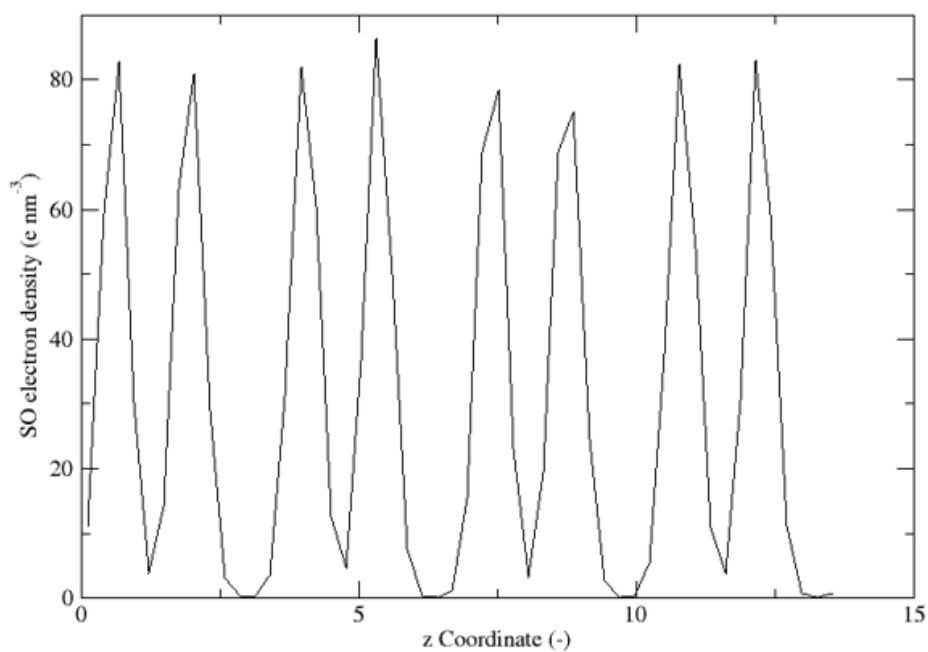


Figure E.4 Average electron density distribution of the SO bead across the z dimension of the simulation box at 53.19 wt % AOT

Appendix F RM size distributions for the AOT – water – cyclohexane system at 298.15 K and 1 bar

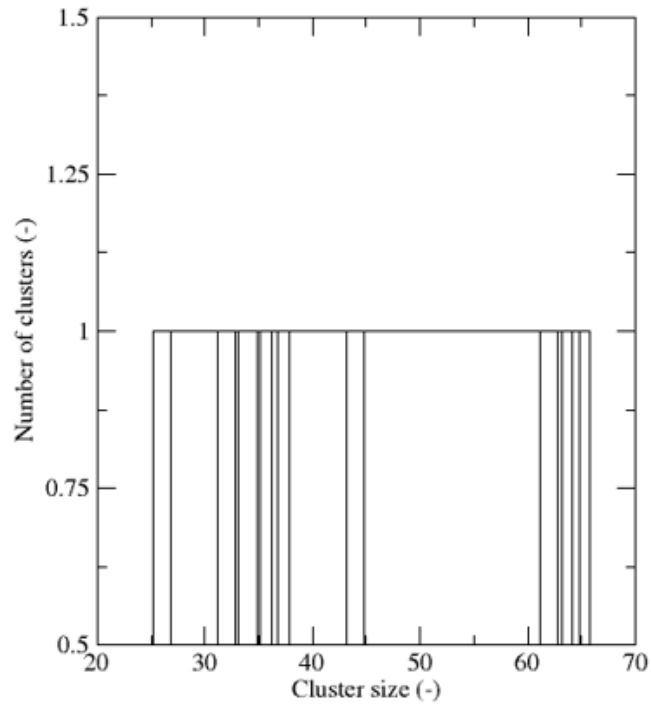


Figure F.1 The average cluster size distribution for system l

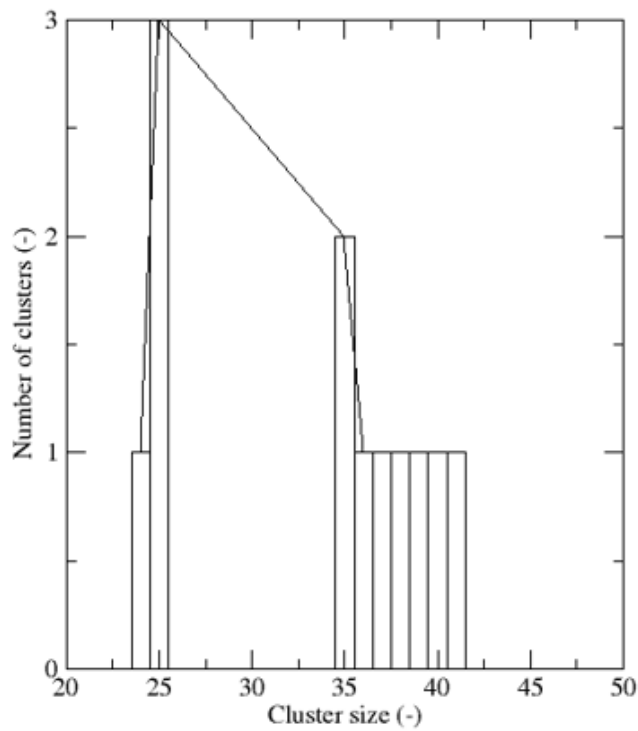


Figure F.2 The average cluster size distribution for system m

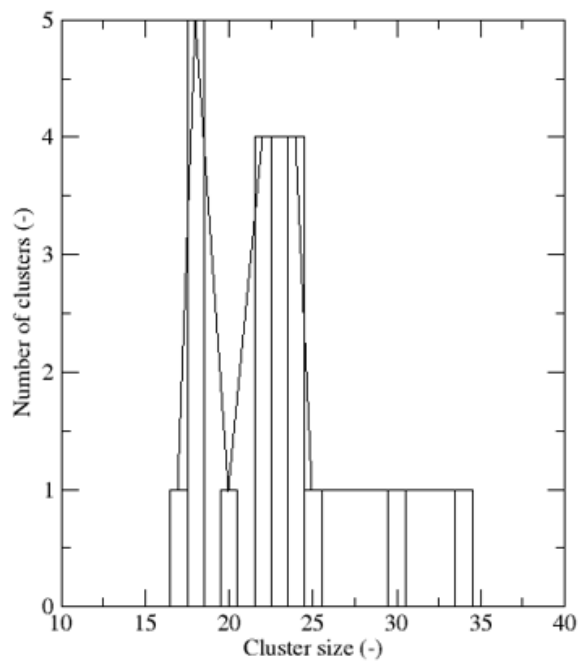


Figure F.3 The average cluster size distribution for system n

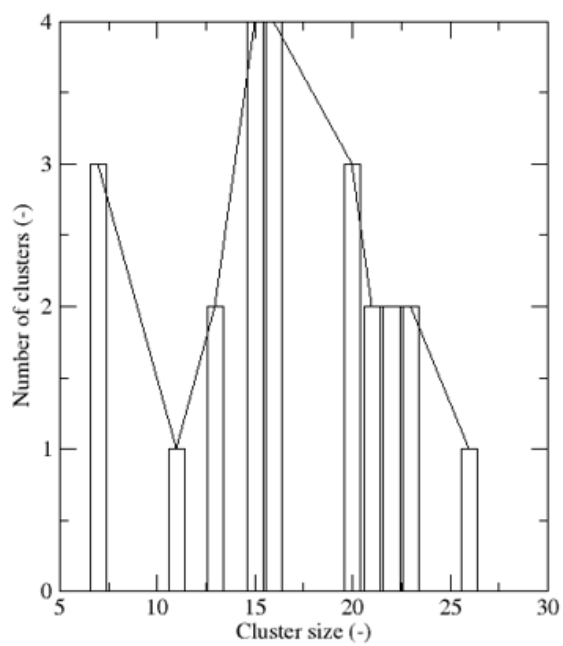


Figure F.4 The average cluster size distribution for system o

Appendix G Balena and Janus technical information

High Performance Computing (HPC) refers to the practice of aggregating computing power in a way that delivers much higher performance than one could get out of a typical desktop computer or workstation in order to solve large-scale problems in science, engineering or business.

The University of Bath has a High-Performance Computing facility, called Balena with 3,480 general purpose Intel 'Ivybridge' and 'Skylake' compute cores, with 16 and 24 cores per node, respectively. There is over 23 TiB of distributed memory, with 4 or 8 GiB/core, and 2 nodes have 512 GiB each for large memory-intensive jobs. In addition there are a range of Nvidia P100 and K20x GPGPUs and Intel Xeon Phi (5110P) co-processors. The system has 0.7 PBs of BeeGFS high-performance parallel file system. The entire system is connected by low-latency Intel TrueScale Infiniband at 40 GB/sec. The service offers a dedicated development zone and high-end visualisation suite designed for interacting with workloads and models. It is classed as a Research Facility charged under the Directly Incurred model.

The University has recently obtained a cloud HPC environment, Janus, which is hosted on the highly scalable Microsoft Azure program. Compute capacity ranges from the Fsv2 series offering from 2 to 72 cpus per node, to the HBv3 series which can offer from 12 to 120 AMD cpus per node. The cloud environment is still under development, before it can be made available to fully replace the Balena environment.